LEABHARLANN CHOLÁISTE NA TRÍONÓIDE, BAILE ÁTHA CLIATH | TRINITY COLLEGE LIBRARY DUBLIN
Ollscoil Átha Cliath | The University of Dublin

Terms and Conditions of Use of Digitised Theses from Trinity College Library Dublin

Copyright statement

All material supplied by Trinity College Library is protected by copyright (under the Copyright and Related Rights Act, 2000 as amended) and other relevant Intellectual Property Rights. By accessing and using a Digitised Thesis from Trinity College Library you acknowledge that all Intellectual Property Rights in any Works supplied are the sole and exclusive property of the copyright and/or other IPR holder. Specific copyright holders may not be explicitly identified. Use of materials from other sources within a thesis should not be construed as a claim over them.

A non-exclusive, non-transferable licence is hereby granted to those using or reproducing, in whole or in part, the material for valid purposes, providing the copyright owners are acknowledged using the normal conventions. Where specific permission to use material is required, this is identified and such permission must be sought from the copyright holder or agency cited.

Liability statement

By using a Digitised Thesis, I accept that Trinity College Dublin bears no legal responsibility for the accuracy, legality or comprehensiveness of materials contained within the thesis, and that Trinity College Dublin accepts no liability for indirect, consequential, or incidental, damages or losses arising from use of the thesis for whatever reason. Information located in a thesis may be subject to specific use constraints, details of which may not be explicitly described. It is the responsibility of potential and actual users to be aware of such constraints and to abide by them. By making use of material from a digitised thesis, you accept these copyright and disclaimer provisions. Where it is brought to the attention of Trinity College Library that there may be a breach of copyright or other restraint, it is the policy to withdraw or take down access to a thesis while the issue is being resolved.

Access Agreement

By using a Digitised Thesis from Trinity College Library you are bound by the following Terms & Conditions. Please read them carefully.

I have read and I understand the following statement: All material supplied via a Digitised Thesis from Trinity College Library is protected by copyright and other intellectual property rights, and duplication or sale of all or part of any of a thesis is not permitted, except that material may be duplicated by you for your research use or for educational purposes in electronic or print form providing the copyright owners are acknowledged using the normal conventions. You must obtain permission for any other use. Electronic or print copies may not be offered, whether for sale or otherwise to anyone. This copy has been supplied on the understanding that it is copyright material and that no quotation from the thesis may be published without proper acknowledgement.

Boundary Element Methods for the Prediction of Aircraft Noise Shielding in Flight

Cathal Clancy

Department of Mechanical & Manufacturing Engineering

Parsons Building

Trinity College

Dublin 2

Ireland

May 2011

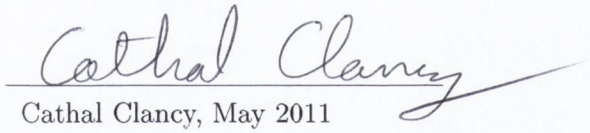
A thesis submitted to the University of Dublin in partial fulfillment of the requirements for the degree of Ph.D.

TRINITY COLLEGE
21 JUL 2011
LIBRARY DUBLIN
THOSIS
9138

Declaration

I declare that I am the author of this thesis and that all work described herein is my own, unless otherwise referenced. Furthermore, this work has not been submitted in whole or part, to any other university or college for any degree or qualification.

I authorise the library of Trinity College, Dublin to lend or copy this thesis.



Cathal Clancy, May 2011

Abstract

Aircraft noise emissions may be significantly reduced by positioning the aeroengines above the wings or fuselage so as to utilize the shielding effect of the airframe. Computational tools are likely to play a key role in the design of future low noise aircraft that maximize this shielding effect.

The Boundary Element Method (BEM) is ideally suited as a prediction tool for medium to high frequency shielding calculations, provided the acoustic medium is uniform. The drawback of the standard BEM is that the effects of flight on the propagation of sound are left as an uncertainty in the prediction of shielding. In this work, the standard BEM is extended to include the flight effect of a low Mach number lifting flow. The acoustic field is modeled by the convected wave equation for the acoustic velocity potential under the assumption that the mean flow is irrotational and homentropic everywhere except for a thin wake extending from the trailing edge. A novel transformation method has been developed to solve an acoustic BEM problem that includes the lowest order convection terms of a small-disturbance low Mach number expansion.

Shielding predictions of a lift producing wing insonified by monopole sources are presented for the novel BEM. These predictions are compared with a high fidelity method based on the Linearized Euler Equations, and with a ray-tracing approach for both lifting and non-lifting flow conditions. The main benefit of the novel BEM approach over the standard formulation is the ability to predict the refraction of sound by the wingtip vortices. This effect was shown to dominate over other flow scattering effects when the Mach number is small.

Acknowledgments

This thesis would not have been possible without the help and support of many people. First and foremost, I sincerely thank my supervisor Henry Rice whose help and guidance has been invaluable. I would also like to thank Professor John Fitzpatrick, Craig Meskell and Gar Bennett who have always been open and willing when it comes to offering assistance in all topics of fluid mechanics and acoustics.

To my workmates and friends in the Fluids lab, I thank everyone for making my time at Trinity so enjoyable. I wish you all the best in everything you pursue.

To my parents, Jerry and Marian and my brothers Niall and Robert I would like to express my deepest gratitude. You have always offered encouragement and support whenever it was needed. Robert, your expertise in all areas of mathematics and computing has been a lifeline.

To Ruth, this thesis simply wouldn't exist without you.

Contents

Nomenclature **xiii**

1 Introduction **1**

1.1 Background 1

1.2 Progress in Aircraft Noise Abatement 2

1.3 Aircraft Engine Noise Shielding 4

1.4 Objectives and Scope of the Thesis 5

1.5 Structure of the Thesis 9

2 Acoustic Propagation in Non-Uniform Flows **11**

2.1 Linearized Euler Equations 12

2.1.1 Kelvin-Helmholtz Type Instability 13

2.1.2 Developments in LEE solvers 14

2.2 Convected Wave Equation 16

2.2.1 Helmholtz Integral Equation 18

2.2.2 CHIEF Formulation 20

2.2.3 Burton-Miller Formulation 21

2.2.4 Modeling Convection Effects with the BEM 22

2.2.5 Fast Summation Acceleration 24

2.3 High Frequency Methods 26

2.3.1 Ray Tracing 26

2.3.2 Kirchhoff Approximation 28

2.4 Potential Models for Scattering of Sound by Vorticity 29

2.4.1 The Influence of Vortex Shedding at a Trailing Edge 31

2.5 Discussion 32

3 BEM Models for Acoustic Scattering in Low Mach Number Flows 35

3.1 Analysis of Convected Helmholtz Equation 36

3.1.1 Small-Disturbance Low Mach Number Approximation 38

3.1.2 Comparison with Taylor's Low Mach Approximation 39

3.2 Transformation Method for Non-Uniform Flows 40

3.2.1 Transformation of Boundary Conditions 42

3.2.2 Higher Order Transformation 44

3.2.3 Comparison of Error Terms 48

3.2.4 Implications for Lifting Flows 53

3.3 Scattering of Sound by Steady Vorticity 54

3.4 BEM Formulation in a Steady Lifting Flow 58

3.4.1 Planar Surface BEM Discretization 63

3.4.2 Boundary Conditions 64

3.4.3 BEM Equations 68

3.4.4 Vortex Scattering Correction 71

3.4.5 Artificial Truncation of the Wake 73

3.4.6 Mean Flow BEM 74

3.5 Iterative Solution Strategies for Planar BEM Formulations 75

3.5.1 Fast Summation Algorithm 76

3.5.2 One Dimensional Fast Convolution 76

3.5.3 Two Dimensional Fast Convolution 78

3.5.4 Solution Procedure for Non-Rectangular Geometries 79

3.5.5 Dimensionless Formulation 80

3.6 Propagation of the Solution to the Field Points 80

4 Scattering of Monopole Sources by a Half-Plane in Flow 83

4.1 Problem Description 84

4.2 Solutions 87

4.2.1 No Kutta Condition Solutions 87

4.2.2 Jones' Two Dimensional Vortex Shedding Solution 88

4.2.3 Point Source Extension to Jones' Solution 89
4.3 Computation of Solutions 92
4.3.1 Computation of Jones' Kutta Condition Solution 94
4.3.2 Point Source Extension to Jones' Solution 95
4.4 Far-field Asymptotic Solution 97
4.4.1 Comparison with Balasubramanyam's Solution 98
4.5 Ray Tracing Solution for a Planar Acoustic Shield 99

5 Assessment of the BEM formulations 103
5.1 Description of Model Problem 104
5.1.1 Wing Geometry 104
5.1.2 Symmetry Planes and Source Position 106
5.1.3 Far-Field Coordinates 107
5.2 Steady Flow Simulations 108
5.2.1 RANS Simulations 108
5.2.2 BEM Flow Simulations 110
5.3 Solution Procedures 115
5.3.1 BEM Solution 115
5.3.2 LEE Solution 115
5.4 Scattering Predictions in Non-Lifting Flow 118
5.4.1 Convergence Studies 119
5.4.2 Effect of Kutta Condition in non-lifting Flow 122
5.5 Scattering Predictions in Lifting Flows 131
5.5.1 Convergence Studies 131
5.5.2 Near-field BEM solution 135
5.5.3 Near-field Comparison of BEM and LEE solutions 137
5.5.4 Far-field Comparison of BEM and LEE Solutions 151
5.5.5 Frequency Averaged Shielding Factor 158
5.6 Performance of BEM solver 165
5.7 Discussion 169
5.7.1 Scattering Mechanisms in Low Mach Number Flow 169

5.7.2 Limitations of the PGT Transformation Method 172

6 Conclusions **175**

A Singular Integrals **189**

A.1 Derivation of Integral Kernels 189

A.2 Extraction of Free Terms 191

A.3 Hypersingular Integration for Constant Elements 194

A.4 Hypersingular Integration for Plane Wave Elements 195

Nomenclature

Abbreviations	
BEM	Boundary Element Method
BIE	Boundary Integral Equation
CAA	Computational Aeroacoustics
CEM	Computational Electromagnetics
CHE	Convected Helmholtz Equation
DGM	Discontinuous Galerkin Method
DRP	Dispersion Relation Preserving
FD	Finite Difference
FMM	Fast Multipole Method
FV	Finite Volume
GTD	Geometrical Theory of Diffraction
HHIE	Hypersingular Helmholtz Integral Equation
HIE	Helmholtz Integral Equation
KA	Kirchhoff Approximation
KH	Kelvin-Helmholtz
KJ	Kutta-Joukowski
LEE	Linearized Euler Equations
PG	Prandtl-Glauert
PGT	Prandtl-Glauert-Taylor
PO	Physical Optics
PTD	Physical Theory of Diffraction
SPL	Sound Pressure Level

Notation	Description
f_0	Mean value of f
f_∞	Free stream value of f
f'	Perturbation of f about f_0
f'^i	Incident Perturbation field
f^+	Value of f on the upper side of a surface of discontinuity
f^-	Value of f on the lower side of a surface of discontinuity
$\Sigma f = f^+ + f^-$	Sum of f across a surface of discontinuity
$\delta f = f^+ - f^-$	Difference of f across a surface of discontinuity
$\hat{\mathbf{n}}$	Surface Unit Normal Vector
$\frac{\partial f}{\partial n} \equiv \nabla f \cdot \hat{\mathbf{n}}$	Surface normal derivative of f
$x_l \equiv \mathbf{x}$	Cartesian coordinates
$\eta_l \equiv \boldsymbol{\eta}$	Generalized coordinates
$\tilde{f}$	Value of f after transformation to generalized coordinates

Symbol	Description
j	Unit Imaginary Number $= \sqrt{-1}$
ρ	Density
$\mathbf{u}$	Velocity
p	Pressure
s	Entropy
h	Stagnation Enthalpy
ϕ	Velocity Potential
ω	Angular Frequency

Symbol	Description
C_v	Constant Volume Specific Heat
C_p	Constant Pressure Specific Heat
γ	Ratio of Specific Heats $= C_p/C_v$
c	Speed of Sound
$\mathbf{M} \equiv M_l \equiv \mathbf{u}_0/c_\infty$	Mean Flow Mach Number
k	Wavenumber $= \omega/c$
$\boldsymbol{\gamma}$	Vorticity
Γ	Circulation of a Vortex Filament
κ	Coupling Constant in Burton Miller BEM Formulation
$\mathcal{F}$	Acoustic Source Term
L_a	Characteristic Acoustic Length Scale
L_m	Characteristic Hydrodynamic Length Scale
Ψ	Stream Function
$\beta = (1-M^2)^{-1/2}$	Prandtl-Glauert Factor
τ	Phase Factor
φ	Transformed Acoustic Velocity Potential
J_{lm}	Jacobian Matrix
A_{lm}	Coefficients of Second Order Derivatives in the CHE
B_l	Coefficients of First Order Derivatives in the CHE
C	Coefficient of Zeroth Order Derivatives in the CHE
$G(\mathbf{x};\mathbf{y})$	Free-Space Green's Function
S	Surface of Scattering Structure
V	Volume External to Scattering Structure
σ_ϵ	Surface of Half-Ball Enclosing BIE Singular Point
ϵ	Radius of Half-Ball Enclosing BIE Singular Point

Chapter 1

Introduction

1.1 Background

Environmental noise has long been a source of annoyance to the general public and particularly to residents near major noise polluters such as airports. As scientific evidence has accumulated, a clearer picture of the negative impact of noise exposure has emerged. According to World Health Organization guidelines, exposure to excessive noise has been shown to have a number of negative effects including [1]

- Hearing Impairment
- Annoyance/Stress
- Sleep Disturbance
- Interference with Speech Communication

There is also some evidence that noise exposure is linked to a number of other physiological and psychological problems such as

- Mental health problems
- Decreased educational performance
- Cardiovascular/stress related illnesses

The authorities have responded to the increasing sensitivity of public opinion on this issue by issuing stricter noise regulations. In the U.S., the first regulations governing aircraft noise emissions were introduced in 1969 by the Federal Aviation Administration (FAA) [2]. This was followed closely by the Annex 16 regulation issued by the International Civil Aviation Organization (ICAO) in 1971 [3]. The most recent revision to Annex 16 was adopted in 2006 with the introduction of Chapter 4 regulations for subsonic jets. ICAO noise limits are specified in terms of effective perceived noise level (EPNL) at three certification locations, referred to as *flyover*, *sideline* and *approach* (see Fig. 1.1). On a local level, individual airports may restrict noise emissions to levels significantly lower than ICAO limits. In the UK, the BAA discounts the landing charge for quieter aircraft by up to one third, relative to the noisiest aircraft, which provides a strong financial incentive for airlines to transition to low noise aircraft. Although noise from individual aircraft may have reduced greatly over the last 60 years, this progress has been masked by the rapid growth in air traffic. Historically, global air traffic has grown at approximately 4.5% per annum on average over the last decade. Unless low noise aircraft are developed, the aircraft industry will face a crisis as regulations become stricter in a time of increasing air traffic and expanding airports. It is clear that from both the environmental and economic perspectives, the development of noise reducing technologies will continue to be of critical importance to the aircraft industry.

1.2 Progress in Aircraft Noise Abatement

In the early years of civil jet development, progressive generations of aircraft benefited from lower noise emissions as an after-effect of advances in high bypass engines. Current engine designs, with bypass ratios of 9 or higher, have dramatically lower jet noise emissions in comparison to older turbojet designs. As the jet noise component has been lowered, the other major sources such as fan noise and airframe noise have become more dominant contributors. In Europe, the Advisory Council for Aeronautical Research in Europe (ACARE) has set an ambitious target of reducing noise levels by 10dB EPNL from 2001 levels by 2020. Looking at the progression of aircraft noise lev-

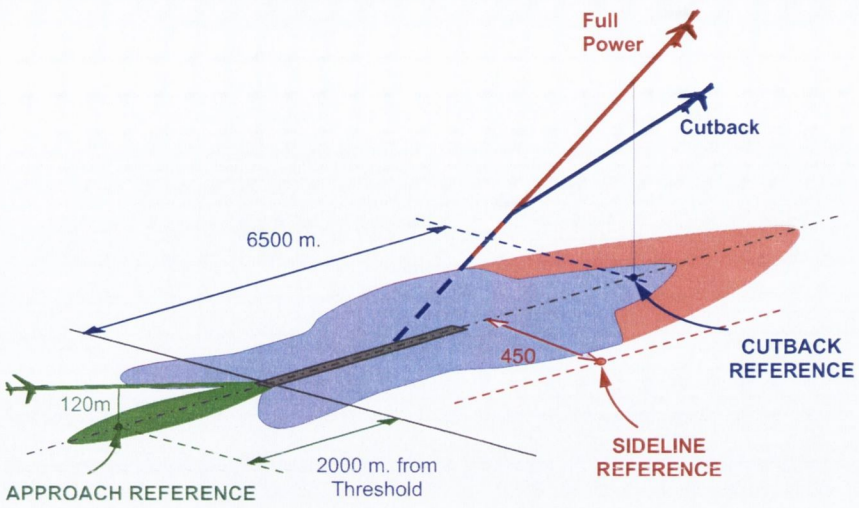


Figure 1.1: FAA certification points.
(Reproduced from [4])

els over the last sixty years (see Fig. 1.2), this target is certainly a challenging one. In setting this goal, the ACARE anticipates the development of new noise reducing technologies, most likely in the form of novel engine and aircraft configurations rather than through incremental improvement of existing designs. New technologies are also constrained by economic and environmental demands for lower fuel consumption, which places certain limitations on the scope of viable noise reducing technologies. Furthermore, future low fuel burn engine architectures such as the open rotor designs may actually increase noise emissions relative to traditional ducted turbofan designs, which makes the aircraft noise problem even more challenging.

Significant advances have been made within a number of areas of aircraft noise research [4]. Highly efficient acoustic liners are in development with the potential to reduce the radiated acoustic power by 10-20dB. The zero-splice liner, developed by Airbus within the SILENCER project [5], has been successfully applied on the A380. Advances in nozzle design have incorporated adjustable chevrons that may potentially be used to control the source of noise in a turbulent jet. This technology has been introduced on commercial aircraft in the GEnx engine for the Boeing 787 and 747-8. Highly swept fan blades, quiet slat and flap designs have also contributed to low noise designs.

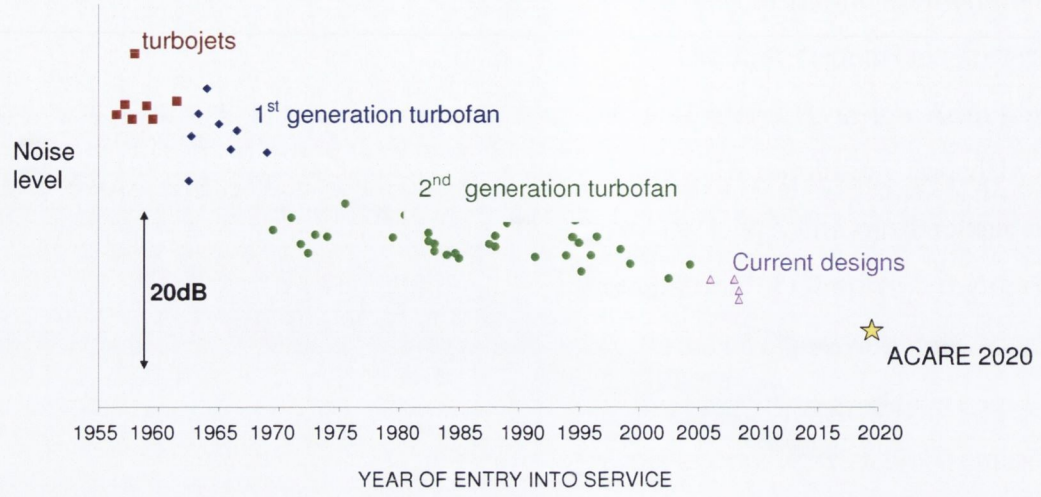


Figure 1.2: Progression in aircraft noise emmisions.
(Reproduced from [4])

1.3 Aircraft Engine Noise Shielding

Another approach to noise reduction is to shield the dominant sources from the observer on the ground by positioning the engines above the airframe. Early in-flight and wind tunnel tests of Jeffery and Holbeche [6] on a delta-winged aircraft demonstrated the potential for shielding a high frequency compact source with the airframe. They reported a 20dB reduction in sound in the deep shadow region. More recently, the ROSAS project [7], the NACRE project [8] and the Silent Aircraft Initiative [9] [10], have examined the use of acoustical shielding in novel aircraft configurations (see Fig. 1.3). Preliminary experimental and computational testing show encouraging signs that shielding is a viable method for reducing the fan noise component, and to a lesser extent the jet component [7].

The basic principle of acoustic shielding is technologically simple. An obstacle is placed between the sound source and the receiver so as to obstruct the direct path of sound propagation. Future novel aircraft configurations may be designed to make use of the airframe itself as an acoustic shield by positioning the engines, which constitute the dominant noise sources, above the fuselage, wings or tailplane. Secondary sound fields will always diffract around an obstacle to produce a non-zero sound field at the receiver point, even in the deep shadow region where the direct path propagation is

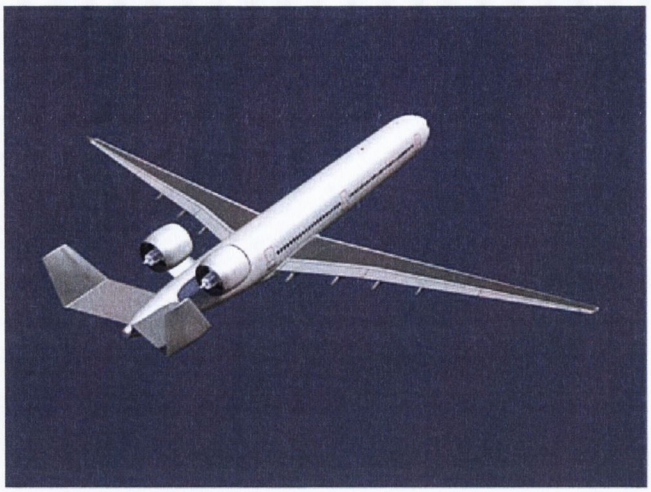


Figure 1.3: Rear fuselage mounted engine configuration (NACRE).
(http://www.x-noise.net/OtherNoiseProjects)

completely obscured by the shield (see the schematic in Fig. 1.4). The assessment of a particular shielding configuration requires a good measurement, or ideally a prediction, of the magnitude of these diffracted sound fields at a variety of receiver points below the aircraft. Different shielding configurations may be compared in their effectiveness, in a source independent way, by comparing a shielding factor for each configuration at specific points in the sound field. The shielding factor, defined as the ratio of the shielded acoustic pressure to the unshielded acoustic pressure, accounts for variations in source strength between different tests in a simple way and is often used as the only measurement of shielding effectiveness. As a noise metric, shielding factor does not take into account the quality of the sound, in terms of spectral content and transient character and does not give a direct measure of the impact of a noise shield on the perceived noise level at a particular location on the ground. Nevertheless, it can be used as a measure of the angular redistribution of acoustic energy due to the introduction of a noise shield, relative to the unshielded configuration.

1.4 Objectives and Scope of the Thesis

Computational tools play an ever increasing role in many areas of engineering design, mainly due to the rapid growth in available computing power over the past few decades. Computational design packages, are now considered a fundamental part of the design

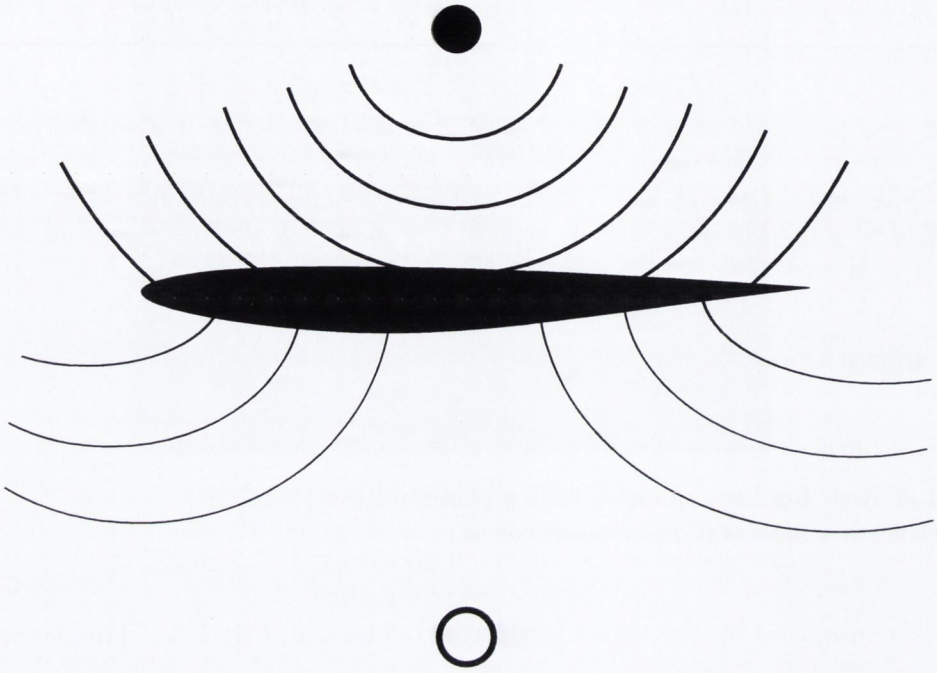


Figure 1.4: Schematic diagram of acoustic shielding by a simple source. The solid circle denotes a source and the hollow circle denotes an observer. The direct field is indicated by the thick lines and the secondary fields by the thin lines.



Figure 1.5: BEM simulation of forward radiating fan noise shielded by the wings and fuselage. Blue contours show regions of low pressure, while red denotes a region of high acoustic pressure. Simulation carried out by the author under the NACRE program.

process, from the conceptual through to the detailed stages. In this respect, it could be argued that aeroacoustics is still lagging slightly behind other fields such as aerodynamics, with fewer accurate physics-based computational tools available to designers. In the case of acoustic shield design, a careful balance is required between aerodynamic constraints on the positioning of engines, the acoustic requirement of high shield effectiveness and the many other constraints such as mechanical and structural limitations. As a result, fast and accurate acoustic predictions of shielding patterns are likely to play a major role in the optimization of low noise configurations. It is worth noting that aeroacoustic scattering tools are also useful for assessing standard configurations under the general topic of engine installation effects. Under-wing mounted engines tend to radiate more noise to the ground below when compared against engines tested in isolation. This effect is partly due to the downward reflection of sound by the wing, which is essentially the same process as acoustic shielding, only with amplification of sound rather than attenuation.

The physics of sound propagation in static fluids is well understood and was one of the first problems to be tackled by numerical analysis. Consequently, the task of computing the shielding pattern of a novel aeroengine configuration could be overlooked as a straightforward problem in computational analysis. In practice, the difference in scale between the characteristic wavelength of sound and the characteristic length of the aircraft structure, combined with the inhomogeneity of the acoustic medium, makes for a challenging computational problem.

Currently, there are many CAA codes available that could potentially be used to calculate aeroacoustic scattering of engine noise sources by full aircraft geometries. In particular, the time-domain Linearized Euler Equations (LEE) solvers scale well in computational memory, and can be applied to very large problems provided that suitable computational resources are available to reduce the computation time to within acceptable limits. In this work it is assumed that computational resources are constrained to the typical level of resources found at industry, meaning that calculations are required to run on tens of cpus rather than hundreds, and run times are limited to days rather than weeks. With these limitations in mind, the LEE solvers become impractical for design stage calculations, where speed of computation is of critical

importance in order to explore the impact of multiple parameters over the full range of a design space. While LEE calculations may play an important role in validating faster more approximate methods, with current computational resources it is clear that design stage calculations would be limited to low frequency ranges on the order of a few hundreds Hz, when simulating scattering over full aircraft geometries.

On the other hand, very fast methods exist for the scalar wave equation and the Helmholtz equation in a homogeneous medium that remain practical up to much higher frequencies. An example of a BEM calculation on a representative shielding configuration for a low noise aircraft is shown in Fig. 1.5. Boundary Element Methods (BEM) for acoustic and electromagnetic scattering calculations have been applied to problems where the characteristic dimensions of the aircraft are on the order of hundreds of wavelength in scale. The major advantage of the BEM approach is the availability of highly efficiency acceleration strategies that dramatically reduce the computational complexity of the problem. As far back as 2000, Song and Chew demonstrated the feasibility of calculating electromagnetic scattering on full aircraft geometries at high frequencies using the FISC solver [11]. They computed a radar cross section of a full aircraft geometry at 8GHz, which is equivalent to solving an acoustic scattering problem at a frequency close to 7KHz. Unfortunately, the BEM approach has so far only been applied to static or uniform media, which limits the possibility to capture the effect of flight on the propagation of sound.

With these limitations in mind, the major objectives of this work are:

- To develop and assess a practical method for shielding calculations that is similar to the fast methods with respect to computational load but incorporates some of the physical accuracy of the LEE codes. Fast propagation codes that can accommodate flow effects will aid in the analysis of future low noise aircraft designs.

- To investigate three-dimensional steady flow interactions with acoustic scattering. The limited computational investigations of aeroacoustical shielding available in the literature are entirely based on truncated shielding geometries or overly simplified steady flow fields. Early experimental investigations of Jeffrey

et. al. reported an additional 8dB of shielding in the sideline due to vortex refraction effects [12]. This effect has largely been ignored by more recent investigations but may be important to include in an analysis where sound propagates through a region of rotational flow.

The intellectual contribution of this thesis may be summarized as follows:

1. The formulation of a new transformation that combines elements of the Prandtl-Glauert and Taylor transformations, which is used to simplify the convected Helmholtz equation.

2. The formulation of a novel accelerated BEM for scattering by planar geometries, that utilizes the above transformation to account for mean flow convection effects. Additionally, the BEM scheme accounts for unsteady vortex shedding at a trailing edge and the interaction of the acoustic field with steady vorticity.

3. The derivation of a new analytical solution for scattering of a monopole source by a half-plane in a uniform flow, treating vortex shedding at the trailing edge correctly.

4. A comparison of a three dimensional LEE scattering solution for a symmetric wing in a lifting flow against BEM solution based on the above formulation and also against a ray theory approach derived from the above analytical solution.

1.5 Structure of the Thesis

Chapter. 2 reviews computational methods for simulating acoustic propagation and scattering. The current state of the art as found in the literature is critically examined in the context of practical methods for aeroacoustic shielding calculation, and deficiencies in current methodologies are highlighted.

Chapter. 3, the transformation approach to modeling propagation through flow is revisited. A framework of analysis of the convected wave equation is laid out, from which a novel Boundary Element Method is developed, for the purpose of predicting aeroacoustic shielding.

In Chapter. 4, the problem of sound scattering of a monopole source by a half plane in uniform flow is solved. This reference solution is used to validate the BEM solver developed in the preceding chapter. The solution itself validates the numerical implementation of the Kutta condition for the BEM approach, while the asymptotic form of the reference solution provides the diffraction coefficients for a ray-tracing approach to modeling diffraction of sound at a cusped trailing edge.

Chapter. 5, the novel BEM approach is applied to a model shielding problem. The shielding results are compared with a commercial LEE solver and a basic ray tracing solver. The results are discussed in the context of practical methods for calculating shielding on realistic geometries and in the context of scattering mechanisms that have been neglected in previous analyses.

Chapter. 6 summaries the various observations of the studies presented. Conclusions are drawn and directions for further exploration are suggested.

Chapter 2

Acoustic Propagation in Non-Uniform Flows

The prediction of aircraft noise in the far-field is generally considered as a two stage or multistage problem in which sound generation is considered separately from propagation. This thesis focuses on the propagation step, in that it is assumed that the sources are known in advance. The remaining problem involves simulating the interaction of linear sound waves with the airframe and the non-uniform flow surrounding it.

Away from a turbulent source region, the time dependent part of the flow can be modeled as a small amplitude perturbation of an otherwise steady flow. Since the disturbances are small, the products of small terms may be neglected. Also, the effect of viscosity on the near field propagation of acoustic waves is limited and may be neglected in the flow equations. The influence of viscosity in damping acoustic propagation over long distances may be treated at a later stage by applying a correction to the Green's function during the far-field propagation stage of the calculation. With these simplifications, the equations of motion for the small amplitude perturbations of an ideal gas are reduced to the Linearized Euler Equations (LEE) [13].

From a numerical perspective, the LEEs are considerably more challenging to solve than the ordinary wave equation for stationary acoustic media. Aside from the increase in computational load on changing from one to five dependent variables, the LEEs are also susceptible to unstable propagation modes associated with the onset of turbulence.

Further assumptions about the nature of the background flow and the nature of the perturbation field can be incorporated into the propagation model to greatly simplify the governing equations and also to improve the stability of numerical solutions. In the sections that follow, a hierarchy of assumptions and propagation models are discussed with reference to the current state of the art solvers and in particular, where they have been applied to the prediction of acoustic shielding.

2.1 Linearized Euler Equations

The state of a fluid can be completely described at any time t and position $\mathbf{x}$ by specifying the velocity $\mathbf{u}$, and any two thermodynamic variables such as pressure p, density ρ, or entropy s [13]. The evolution of these fields in time are described by the equations of mass continuity, conservation of momentum and conservation of energy. An equation of state is required to close the system.

If viscous stresses and body forces are ignored, the governing equations reduce to the Euler equations.

$$\frac{1}{\rho}\frac{D\rho}{Dt} + \nabla \cdot \mathbf{u} = 0 \tag{2.1}$$

$$\frac{D\mathbf{u}}{Dt} = -\frac{1}{\rho}\nabla p \tag{2.2}$$

$$\frac{Ds}{Dt} = 0 \tag{2.3}$$

where $D/Dt \equiv \partial/\partial t + \mathbf{u} \cdot \nabla$. These equations can be linearized about a steady mean flow. Substituting

$$\begin{aligned} \mathbf{u}(\mathbf{x},t) &= \mathbf{u}_0(\mathbf{x}) + \mathbf{u}'(\mathbf{x},t), \qquad & p(\mathbf{x},t) &= p_0(\mathbf{x}) + p'(\mathbf{x},t), \\ \rho(\mathbf{x},t) &= \rho_0(\mathbf{x}) + \rho'(\mathbf{x},t), \qquad & s(\mathbf{x},t) &= s_0(\mathbf{x}) + s'(\mathbf{x},t) \end{aligned} \tag{2.4}$$

into Equations (2.1-2.3) and neglecting products of small quantities yields the Linearized Euler Equations for the perturbation terms,

$$\frac{D_0\rho'}{Dt} + \rho'\nabla \cdot \mathbf{u}_0 + \nabla \cdot (\rho_0 \mathbf{u}') = 0 \tag{2.5}$$

$$\rho_0 \left(\frac{D_0 \mathbf{u}'}{Dt} + (\mathbf{u}' \cdot \nabla) \mathbf{u}_0 \right) + \rho' (\mathbf{u}_0 \cdot \nabla) \mathbf{u}_0 + \nabla p' = 0 \tag{2.6}$$

$$\frac{D_0 s'}{Dt} + \mathbf{u}' \cdot \nabla s_0 = 0 \tag{2.7}$$

where D_0/Dt denotes the convective derivative in the steady flow field. For an ideal gas with constant specific heats, C_v and C_p, the entropy fluctuations can be expressed in terms of pressure and density perturbations by

$$s' = -\rho' \frac{C_p}{\rho_0} + p' \frac{C_v}{p_0} \tag{2.8}$$

which closes the system.

2.1.1 Kelvin-Helmholtz Type Instability

Equations (2.5-2.7) describe the propagation of all small amplitude disturbances in an inviscid flow. This may include vortical and entropy disturbances in addition to acoustic perturbations. A downside of the LEE model of acoustic propagation is that the system also supports hydrodynamic instabilities that can swamp the acoustic field in a numerical simulation. The Kelvin-Helmholtz type instability of a perturbed shear layer is a typical example of where numerical solutions of the LEEs run into difficulty. The physical solution contains a convective instability that grows exponentially in the downstream direction. In a Navier-Stokes model, these perturbations would show initial rapid growth, followed by saturation due to non-linear roll-up and viscous dissipation (Fig. 2.1). However, the linear model contains no such mechanisms to limit the growth of the instability and these perturbation modes continue to grow unbounded without special treatment by artificial damping. Agarwal et al. have given a detailed review of the implications of the KH instability for the numerical solution of the LEEs and on techniques to alleviate the problem [14]. They concluded that the appropriate way to suppress the unstable behavior is to solve in the frequency domain with a direct solver. It was demonstrated, by comparison with a semi-analytical solution of a benchmark problem, that the frequency domain solver captures the non-causal

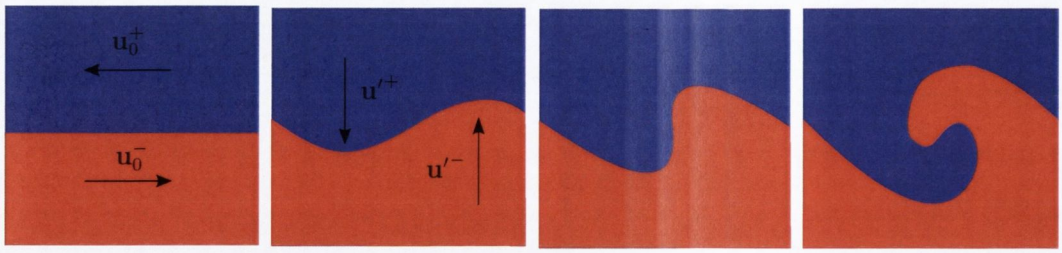


Figure 2.1: Onset of Kelvin-Helmholtz instability

solution, in which an incoming wave enters the computational domain that cancels the instability wave that would normally appear in the causal solution. However, this principle was only demonstrated for the specific case of two-dimensional parallel shear flow and the validity of the approach for fully three dimensional flows and flows over scattering bodies has yet to be demonstrated. Various other suppression techniques have been suggested, such as the removal of shear terms from the governing equations [15] and the use of filtered equations [16]. In the case of the Discontinuous Galerkin Methods, explicit suppression of hydrodynamic instabilities is rarely needed because of the inherent damping of short wave length flow disturbances. An appropriate selection of grid resolution is usually sufficient to suppress the vortex instability waves while maintaining a good resolution of the acoustic wave phenomena. It is important to note that the instability of the LEEs is a fundamental problem for numerical solution techniques because the instability is a feature of the physics of linearized fluid motion and independent of the solution method. The techniques listed in the literature are simply a means of suppressing this behavior. The approach adopted in this study is to start from a stable equation system, in the form of the convected wave equation. This provides the robustness that is required for routine use in industry.

2.1.2 Developments in LEE solvers

Historically, LEE numerical solvers were based on finite difference (FD) and finite volume (FV) schemes that were derived from existing fluid dynamics Euler codes [17],[18],[19]. For aeroacoustic calculations, the dominant requirement for numerical schemes is that waves should propagate with minimal dispersion and diffusion error. By relaxing the formal order of convergence of the finite difference approximation, Tam

derived a set of coefficients for an FD stencil that are optimal in terms of numerical wave propagation [20]. These dispersion relation preserving schemes (DRP) have been widely used with structured FD grids in industrial and academic codes, such as the *PIANO* code developed at DLR [21] and the *sAbrinA* solver developed at ONERA [22]. More recently, Ashcroft and Zhang developed optimized prefactored compact schemes that provide similar high accuracy wave resolution but with much smaller stencil size than the classical DRP schemes [23]. Further improvements in acoustic LEE solvers have been made through the development of accurate non-reflective and buffer type boundary conditions [15], [24], [25] . High order FD and FV methods are usually necessary for good wave propagation characteristics in structured mesh solvers but these codes tend to be more sensitive to the smoothness of the grid metrics for boundary fitted meshes. Often, singular points in the boundary geometry and at block interfaces cause problems with the smoothness in the grid metrics. These problems can be somewhat alleviated by improving the interface conditions between neighbouring blocks [26], through the use of coupled overlapping grids [27], or simply by increasing numerical damping at problem points.

Ideally, user intervention should not be required to get accurate results from a automated simulation tool. From this perspective, the finite element method is more flexible in the handling of complex geometries and is a natural choice for fully three dimensional calculations on awkward geometries. Recent developments have seen an increase in the popularity of the Discontinuous Galerkin Methods (DGM) for the LEEs. Unlike classical continuous Galerkin FEM schemes, the DGM has good stability properties, has low dispersion and diffusion errors and and is generally competitive with FD methods for time-domain implementations [28],[29]. By allowing the solution to have discontinuities across inter-element boundaries, the discretized equation may be solved locally in each element. Inter-element communication is then achieved by calculation of a flux through neighbouring element boundaries. The inherently local nature of the solution procedure allows for local adaption and efficient parallel implementation. The development of highly scalable parallel DGM codes may be viewed as a step towards the capability to simulate in-flight acoustic shielding on full aircraft configurations.

A small number of computational studies of acoustic shielding have been carried out

with the Euler equations on three dimensional geometries. Redonett et al. simulated the installation effect on aft-fan radiated noise [27]. They found that the full Euler perturbation equations did not suffer from the Kelvin-Helmholtz type instabilities, to which the linear equations are susceptible. By adopting an overlapping grid approach, body fitted grids were used on both the airfoil and the engine nozzle. A high degree of shielding was reported for this configuration. Although the calculations were carried out on 3D grids, this configuration could not be regarded as a fully three dimensional simulation since the flow results were projected from 2D and axisymmetric calculations. Stanescu solved the LEEs over a representative high shielding configuration with a discontinuous Galerkin spectral element method [30],[31],[32]. Shielding values of 10-15 dB were reported for low frequency calculations with no mean flow. Frequency domain calculations were also performed with incompressible mean flow. However, a velocity potential formulation was used for these simulations with no correction to account for mean flow vorticity.

2.2 Convected Wave Equation

A linear wave equation for inhomogeneous potential flows may be derived by linearizing the full velocity potential equation about a steady value (see Howe [13]). Splitting the full potential, ϕ, into a steady component plus a time-unsteady perturbation

$$\phi(\mathbf{x}, t) = \phi_0(\mathbf{x}) + \phi'(\mathbf{x}, t) \tag{2.9}$$

,the acoustic perturbation velocity potential ϕ' satisfies the convected wave equation

$$\frac{D_0}{Dt}\left(\frac{1}{c_0^2}\frac{D_0\phi'}{Dt}\right) - \frac{1}{\rho_0}\nabla\cdot(\rho_0\nabla\phi') = 0. \tag{2.10}$$

The restriction of irrotational isentropic mean flow is limiting in practice since most engineering applications involve at least a minor deviation from potential mean flow. Pierce showed that the wave operator in Eq. 2.10 may be derived as an approximation for acoustic propagation in general rotational flows when the wavelength of sound is

smaller than the characteristic length scale of the steady flow features [33]. Defining the wavelength of sound, λ, as the relevant acoustic length scale and defining a characteristic length scale of the mean flow as L_m, Pierce's derivation proceeds by neglecting terms of order

$$\mathcal{O}(\frac{\lambda}{L_m})^2$$

or higher.

Howe showed that a non-homogeneous form of the convected wave equation may be derived directly from the Navier-Stokes equations [13] when the stagnation enthalpy, h, is considered as the acoustic variable. For homentropic flow, Howe's analogy takes the form

$$\frac{D}{Dt}\left(\frac{1}{c^2}\frac{Dh}{Dt}\right) - \frac{1}{\rho}\nabla\cdot(\rho\nabla h) = \frac{1}{\rho}\nabla\cdot(\rho(\boldsymbol{\gamma}\times\mathbf{u})) \tag{2.11}$$

where $\boldsymbol{\gamma} = \nabla\times\mathbf{u}$ is the vorticity of the flow field. The above equation may be linearized for a time-unsteady perturbation about a steady mean flow. Substituting the following,

$$h(\mathbf{x},t) = h_0(\mathbf{x}) + h'(\mathbf{x},t) \tag{2.12}$$

$$\gamma(\mathbf{x},t) = \gamma_0(\mathbf{x}) + \gamma'(\mathbf{x},t) \tag{2.13}$$

$$\mathbf{u}(\mathbf{x},t) = \mathbf{u}_0(\mathbf{x}) + \mathbf{u}'(\mathbf{x},t) \tag{2.14}$$

into (2.11), and neglecting terms containing the products of perturbation quantities and finally noting that noting that for a homentropic flow

$$\nabla h_0 = -\boldsymbol{\gamma}_0\times\mathbf{u}_0 \tag{2.15}$$

the linear form of Howe's analogy becomes

$$\frac{D_0}{Dt}\left(\frac{1}{c_0^2}\frac{D_0h'}{Dt}\right) - \frac{1}{\rho_0}\nabla\cdot(\rho_0\nabla h') = \frac{1}{\rho_0}\nabla\cdot(\rho_0(\boldsymbol{\gamma_0}\times\mathbf{u}' + \boldsymbol{\gamma}'\times\mathbf{u}_0)) \tag{2.16}$$

This equation explicitly demonstrates the interaction between the hydrodynamic components and acoustic components of the time-varying perturbations when linearized

about a rotational steady flow. For irrotational flow, the right hand side of Eq. 2.16 vanishes and Howe's analogy reduces to the convected wave equation. When the base flow is rotational, the right hand side source term accounts for scattering of sound by the mean flow vorticity and the interaction of the time-varying vorticity with the mean flow field. When time-varying vorticity is present, the momentum equation is also required to solve for the unsteady vortex dynamics.

At low Mach numbers, the mean flow density and the speed of sound may be assumed to be constant. These assumptions reduce the linearized velocity potential wave equation to the convected wave equation.

$$\frac{D_0^2\phi'}{Dt^2} - c_0^2\nabla^2\phi' = 0 \tag{2.17}$$

This has the same form as the ordinary wave equation with the time derivatives $\partial/\partial t$ replaced by the material derivative D_0/Dt. The assumption of incompressibility is approximately valid when $U^2/c_\infty^2 = M^2 \ll 1$, which limits the use of Eq. 2.17 to low subsonic applications.

The frequency domain equivalents of the LEE or the wave equations above may be obtained by replacing the $\partial/\partial t$ operator by $j\omega$. In the case of a static ambient medium, the frequency domain velocity potential obeys the Helmholtz equation.

$$\nabla^2\phi' + k^2\phi' = 0 \tag{2.18}$$

2.2.1 Helmholtz Integral Equation

The Helmholtz equation may be recast into Boundary Integral Equation (BIE) form with the use of Green's identity [34]. In an open external domain, Ω, the Helmholtz Integral Equation (HIE) is given by,

$$C(\mathbf{y})\,\phi'(\mathbf{y}) = -\int_S \left(\frac{\partial G(\mathbf{x};\mathbf{y})}{\partial n_\mathbf{x}}\phi'(\mathbf{x}) - G(\mathbf{x};\mathbf{y})\frac{\partial \phi'(\mathbf{x})}{\partial n_\mathbf{x}} \right) \mathrm{d}S(\mathbf{x}) + \phi'(\mathbf{y})^i \tag{2.19}$$

where ϕ' is the frequency domain acoustic velocity potential, ϕ'^i is the incident wave, S is the boundary of Ω and n is the unit inward normal on S. The function, G, is the

free-space Green's function that satisfies the inhomogeneous Helmholtz equation,

$$\nabla^2 G(\mathbf{x};\mathbf{y}) + k^2 G(\mathbf{x};\mathbf{y}) = -\delta(\mathbf{x}-\mathbf{y}). \tag{2.20}$$

For the 2D and 3D cases, G is given by,

$$\begin{aligned} G &= -j/4H_0^{(2)}(k|\mathbf{x}-\mathbf{y}|) && \text{2D} \\ G &= \frac{e^{-jk|\mathbf{x}-\mathbf{y}|}}{4\pi|\mathbf{x}-\mathbf{y}|} && \text{3D} \end{aligned} \tag{2.21}$$

where $H_0^{(2)}$ is the Hankel function of the second type. The value of C in Eq. 2.19 depends on the location of the field point. For a smooth boundary the three cases are given by

$$C(\mathbf{y}) = \begin{cases} 1 & \mathbf{y} \in \Omega \\ \frac{1}{2} & \mathbf{y} \in S \\ 0 & \mathbf{y} \in \Omega^c \end{cases}$$

where Ω^c is the open interior complement of Ω. If S is not smooth at $\mathbf{y}$ then c can be evaluated by

$$C(\mathbf{y}) = 1 - \int_S \frac{\partial G_0}{\partial n}\,\mathrm{d}S$$

where G_0 is the Green's function for the Laplace equation.

In many reference texts, a second linearly independent boundary integral equation is derived by taking the directional derivative of Eq. 2.19 with respect to the surface normal at the loading point $\mathbf{x}$,

$$C(\mathbf{y})\frac{\partial \phi'(\mathbf{y})}{\partial n_{\mathbf{y}}} = -\int_S \left(\frac{\partial^2 G(\mathbf{x};\mathbf{y})}{\partial n_{\mathbf{y}} \partial n_{\mathbf{x}}} \phi'(\mathbf{x}) - \frac{\partial G(\mathbf{x};\mathbf{y})}{\partial n_{\mathbf{y}}} \frac{\partial \phi'(\mathbf{x})}{\partial n_{\mathbf{x}}} \right) \mathrm{d}S(\mathbf{x}) + \frac{\partial \phi'(\mathbf{y})^i}{\partial n_{\mathbf{y}}} \tag{2.22}$$

This notation has unfortunately lead to a lot of confusion over the correct interpretation of the hypersingular integral operator,

$$\int_S \frac{\partial^2 G(\mathbf{x};\mathbf{y})}{\partial n_{\mathbf{y}} \partial n_{\mathbf{x}}} \phi'(\mathbf{x})\,\mathrm{d}S(\mathbf{x}) \tag{2.23}$$

which contains a singularity of order, $O(|\mathbf{x}-\mathbf{y}|^{-3})$, and is formally divergent. As described by Guigianni [35], a rigorous derivation of the hypersingular HIE requires a careful limiting procedure in which the derivatives are brought inside the integral sign *before* the limit to the boundary is taken. This topic is discussed further in the section that follows and in chapter 3.4.

A well known shortcoming of Eq. 2.19 and Eq. 2.22 is the non-uniqueness of the solution to the external problem when the frequency of excitation matches the internal resonance frequency of the scatterer.

As a classic example of the non-uniqueness difficulty, when Neumann boundary conditions are specified on the scatterer surface, the solution is non-unique at the eigenfrequencies of the internal Dirichlet problem [34]. Many treatments have been proposed to alleviate the non-uniqueness problem and a thorough examination of the topic is covered by Marburgh and Wu in chapter 15 of [36]. The two most commonly applied treatments, (1) the CHIEF formulation and (2) the Burton and Miller formulation are briefly discussed here.

2.2.2 CHIEF Formulation

A simple numerical treatment of the internal resonance problem was proposed by Schenk [37], decades before high frequency scattering calculations on three dimensional geometries were feasible. By explicitly constraining the field inside the scattering structure to zero, Schenk derived an overdetermined system of equations for the discrete HIE. Provided that the constraint collocation points do not lie on a node of the internal resonance solution, the external solution is specified uniquely by this system. The method is simple to implement in the sense that the underlying boundary integral equation remain unchanged. This implies that no new integral kernels are introduced and the method simply requires augmenting an existing equation system with some additional constraints. The major impact of adding the constraints is the requirement to solve a least squares problem rather than an ordinary linear system. Direct solvers for least squares problems are freely available in linear equation packages such as LINPACK, so this does not typically cause a problem for a the classical

BEM solution methods. When iterative solution methods are required, the variety of packaged solvers are much more limited. In practice, the CHIEF method leads to poorly conditioned linear systems for high frequency problems. These systems are slow to converge when iterative solvers are used even when large numbers of CHIEF points are utilized. Furthermore, devising a suitable strategy for selecting the location and number of CHIEF points so as to guarantee a unique solution remains an unsolved problem.

2.2.3 Burton-Miller Formulation

Burton and Miller derived a direct BIE formulation that is unique for all frequencies by considering a linear combination of the regular HIE and the hypersingular HIE [38],

$$\begin{aligned} 1/2\left(\phi' - j\kappa\frac{\partial\phi'}{\partial n_{\mathbf{y}}}\right) - \left(\phi'^{i} - j\kappa\frac{\partial\phi'^{i}}{\partial n_{\mathbf{y}}}\right) = &-\int_S \left(\frac{\partial G}{\partial n_{\mathbf{x}}} - j\kappa\frac{\partial^2 G}{\partial n_{\mathbf{y}}\partial n_{\mathbf{x}}}\right)\phi'\,\mathrm{d}S \\ &+\int_S \left(G - j\kappa\frac{\partial G}{\partial n_{\mathbf{y}}}\right)\frac{\partial\phi'}{\partial n_{\mathbf{x}}}\,\mathrm{d}S \end{aligned} \tag{2.24}$$

Kress demonstrated that a coupling parameter given by, $\kappa = 1/k$, is nearly optimal, in the sense of minimizing the condition number of the discretized integral operators, for the case of scattering by a sound hard sphere [39]. In practice, this choice works well for most geometries when the wavelength of sound is smaller than the characteristic dimension of the scatterer.

A frequently cited drawback of the Burton-Miller formulation is that the hypersingular integral kernel is difficult to treat numerically. Given the theoretical and numerical advances in hypersingular BIEs over the past two decades, this criticism is no longer valid. In their original paper, Burton and Miller suggested a regularization of the hypersingular integral by performing a convolution of the integral equation with the Laplace equation Green's function. This strategy is numerically expensive because of the need to evaluate double integrals in the entire domain. Several other authors have proposed alternative regularization schemes by applying Stoke's theorem to move the order of the derivative from the hypersingular kernel onto the potential or by adding identities involving the Laplace Green's function [40], [41], [42] (see the

review [43]), sometimes requiring an auxiliary Laplace problem to be solved. The other approach to the treatment of the hypersingularity is the direct evaluation of the integrals by semi-analytical methods [35], [44], [45]. This method is more desirable for large acoustic problems since there are fewer integral operators to be evaluated for the non-local interactions, when compared with a regularized scheme.

Although the theory cited above allows for the use of higher order curved boundary elements, from an engineering perspective, the use of planar constant elements is sufficiently accurate for many applications. For the special case of constant potential elements, simple analytical formulae are available for the singular integrals [46].

2.2.4 Modeling Convection Effects with the BEM

The Helmholtz integral equation has many advantages over its partial differential counterparts for the modeling of the external scattering problem in a uniform medium at rest. When it comes to aeroacoustic applications, the BIE approach is limited by the lack of flexibility to handle propagation through non-uniform flows. In specific cases, it is possible to apply a change of variables that recovers the wave equation in a medium at rest. Hence, the problem of obtaining a closed form Green's function for the integral kernel is avoided.

Given a set of cartesian coordinates $\mathbf{x}$, which are aligned to the flow along the x_1-axis, the Prandtl-Glauert transformation

$$\beta = (1 - M^2)^{-1/2}, \qquad \eta_1 = \beta x_1, \qquad \eta_2 = x_2, \qquad \eta_3 = x_3, \qquad \tilde{k} = \beta k, \tag{2.25}$$

$$\phi'(\mathbf{x}, k) = \varphi\left(\boldsymbol{\eta}, \tilde{k}\right) e^{j\tilde{k}M\eta_1}$$

reduces the frequency domain potential flow wave equation Eq. 2.10 to the Helmholtz equation.

For low Mach number flows, Taylor's transformation approximates more accurately the refractive effect of a non-uniform mean flow [47]. If the mean flow is homentropic

and irrotational with potential, ϕ_0, the transformation

$$\boldsymbol{\eta} = \mathbf{x}, \qquad \tilde{t} = t + \phi_0/c_\infty^2, \qquad \varphi\left(\boldsymbol{\eta}, \tilde{t}\right) = \phi'\left(\mathbf{x}, t\right) \tag{2.26}$$

recovers the ordinary wave equation from the convective wave equation correct to $O(M^2)$. The acoustic pressure may be obtained by the linearized form of Bernoulli's equation.

$$p' = \rho_0 \left(\frac{\partial \phi'}{\partial t} + \nabla \phi_0 \cdot \nabla \phi' \right) \tag{2.27}$$

Astley and Bain[48] performed a rigorous analysis of the truncated terms in the low Mach number approximation and found that there is an auxiliary condition that should be satisfied. This term depends on the ratio of the characteristic length scale of sound to the length scale of the flow field. Based on this result, they concluded that Taylor's approach is better suited to high frequency simulations. More recently, Agarwal and Dowling [49] analysed Taylor's transformations and concluded that the acoustic propagation problem becomes fully decoupled from the mean flow to order $O(M^2)$, when Taylor's transformation is applied to the convected Helmholtz equation and hard wall boundary conditions are applied on the scatterer surface. Following directly from this reasoning, they performed shielding calculations in the absence of mean flow for the Silent Aircraft airframe insonified by a monopole source. A procedure was outlined to correct the phase of a more general source term, in order to compensate for mean flow effects. In principle, the decoupling of acoustics and mean flow is valid for a low Mach number potential steady flow. However, this decoupling does not cover the class of quasi-potential steady flows that are commonly used to approximate lifting flows around aircraft wings when Laplace equation solvers are employed. For this class of flows, the discontinuity in the mean flow potential across the trailing edge vortex sheet implies that Green's identities are not valid on the surface of the vortex sheet and some correction must be made before the BEM can be used with Taylor's transformation.

2.2.5 Fast Summation Acceleration

The success of the BEM in handling large problems lies in the highly efficient acceleration techniques of the Fast Multipole Method (FMM) and its equivalents. Consider the matrix vector multiplication step in the iterative solution of a BEM problem. A direct evaluation of this step involves computing the influence of every element on every collocation point on the surface by summing over the individual pointwise interactions. The FMM accelerates this step by grouping the elements together and enabling groups that are far from one another to communicate via multipole expansions. The definition of "far" can be quantified by setting a global error constraint and then determining a distance between groups for which the multipole expansion error is low enough to satisfy the global error constraint. Usually, elements are grouped together by subdividing the scattering into discrete boxes. The ability to control global error is central to multipole type accelerators and may be handled in a consistent manner.

The basic operations required to perform the communication step are:

1. A computation of the multipole coefficients for each space partitioned source region.

2. A translation operation to move the location of the expansion centre to a far field box.

3. Evaluation of the field potentials in the far field box via the translated multiple expansion.

The translation operator is the most expensive part of the process because it must be carried out for every far field box pairing. Plane wave expansions have been used to speed up the translation cost from $O(p^4)$ to $O(p^3)$, where p is the number of coefficients in a multipole expansion. The development of fast translations for the FMM is an active area of research.

A simple far-field approximation that follows logically from plane wave translation operators is the idea of replacing the multipoles with plane waves from the outset. This approximation, first proposed by Lu and Chew [50], is known as the Fast Far Field Approximation (FAFFA). Generally, the FAFFA requires the computation of more

local interactions than the FMM because the criterion for what constitutes the"far field" is stricter for the FAFFA but the "far field" interactions are much faster to compute. It is reported that the best performance is obtained by a combined approach in which the FAFFA is employed only to speed up the most distant interactions [51].

Other acceleration techniques are available for the HIE such as Fast Fourier/Wavelet Transform based methods and wavelet compression techniques [52], [53], [54]. Many of these algorithms are not yet mature enough to be applied to complex geometries and, in any case, they do not appear to better the asymptotic complexity of the FMM. Time domain versions of these algorithms are available but the requirement to store the solution at every retarded time that can influence the current state of the surface potential makes these methods less attractive.

The FMM is a general purpose acceleration strategy that does not rely on assumptions about the nature of the solution or the scattering geometry. Its implementation is non-trivial and has a critical influence on efficiency. For the special case of a regularly-tiled planar geometry or a cascade of parallel planar geometries, the block Toeplitz structure of the BEM influence matrix may be exploited for fast matrix-vector products based on Fast Fourier Transforms (FFT) (see [55] for a complete description of the fast block Toeplitz multiplication algorithm). The block Toeplitz matrix structure arises naturally when solving integral equations on regular rectangular grids and has been exploited in the solution of electromagnetic scattering problems on rectangular structures, by the discrete dipole approximation [56]. Toeplitz matrices also arise in the fast computation of two dimensional muli-cylinder scattering problems [57]. Block Toeplitz acceleration may be implemented trivially and displays the same $O(n \log n)$ complexity as the FMM for a matrix problem of n unknowns. Hence, it is a useful tool for performing parametric testing and for examining convergence properties, when the scattering geometry can be approximated by planar surfaces.

2.3 High Frequency Methods

2.3.1 Ray Tracing

Ray tracing, has been used extensively in computational electromagnetics (CEM) for scattering computations and in computer graphics to render 3D images with lighting effects. The CEM formulation is much simpler than in the aeroacoustic case because the external medium can always be treated as uniform. In this case, the determination of ray paths is a purely geometric problem because the rays travel in straight lines. Data structures such as k-d trees and R trees play a large role in the efficient implementation of classical ray tracing codes. This is because the geometry is usually represented by a large number of planar facets and the most costly computation is the testing of ray intersections with planar faces. A good data structure minimizes the number of checks performed per ray by trimming the list of possible intersections.

In its basic form, ray tracing is unsuitable for acoustic shielding calculations because it does not predict a diffracted field in the shadow zone. Keller proposed an extension to geometrical acoustics, called the Geometrical Theory of Diffraction (GTD) that includes an additional set of rays that radiate from geometrical discontinuities such as edges and vertices and shadow boundaries [58]. Fermat's principle predicts additional ray paths that are not included in standard geometrical acoustics. Keller called these paths diffracted rays and constructed a systematic approach to obtain the amplitudes of these rays based on coefficients extracted from the asymptotic solutions of canonical problems. The first order diffraction coefficients depend solely on the local geometry of the scatterer so only a small number of coefficients are required to model a wide range of realistic geometries. Unfortunately, the GTD was developed almost exclusively for electromagnetics and, to the author's knowledge, there are no published diffraction coefficients for scattering in the presence of mean flow. Another problem with the GTD is that typical ray tracer codes are not well suited to the addition of diffraction theory. Edge diffraction does not generally cause difficulty but smooth surface diffraction effects are awkward to implement with a non-smooth representation of the geometry, such as planar faceted meshes. Attempts have been made to reconcile the GTD with

classical ray tracing by using heuristic criteria to distinguish a grazing angle from a reflecting angle [59]. The accuracy and robustness of such a scheme is highly dependent on the quality of the decision making routine.

More recent developments in the calculation of smooth surface diffraction by ray tracing methods have addressed some of the difficulties associated with the classical approach. Sefi et al., developed a novel ray tracing code to perform computations directly on the CAD representation of the geometry [60]. The formulation differs from the classical approach in that the paths are determined by direct application of Fermat's principle. A minimization routine is applied to candidate solutions of the ray path problem. Direct paths, reflected and diffracted rays are all computed by minimizing the path length from the source to the receiver and performing a check for intersections with other NURBS patches. Creeping rays are also calculated by a minimization procedure. In this case, the geodesic path connecting the source shadow boundary to the set of receiver detachment points, must be included in the minimization. This formulation based on Fermat's principle appears to be a considerable improvement on standard calculations. The method is reported to calculate scattering patterns for entire aircraft configurations within seconds or minutes when up to two diffraction/reflection interactions are considered.

Agarwal et al, extended the applicability of the above formulation to the case of the acoustic propagation through low Mach number homentropic flows. It was demonstrated in [61] that for such flows the Taylor transformed acoustic rays travel in straight lines when $O(M^2)$ terms are neglected. It was argued that this also justifies the use of GTD coefficients derived for a uniform medium. The predictions obtained for the shielding of a point monopole by a novel aircraft configuration showed a good match with experimental testing for the high frequency case reported. In general, where discrepancies occurred the method tended to over-predict the shielding by approximately 2-5dB.

2.3.2 Kirchhoff Approximation

The Kirchhoff Approximation (KA) is a method for determining the scattered field via the Helmholtz Integral Equation and an assumed surface distribution for the acoustic potential. A pointwise approximate solution for the surface potential is obtained by replacing the true geometry at each point with the local tangent plane. Hence, the surface potential for the Neumann problem is approximated as,

$$\phi' = \begin{cases} 2\phi'^{i} & \text{on illuminated side} \\ 0 & \text{on shadow side} \end{cases} \tag{2.28}$$

where ϕ'^{i} is the incident acoustic potential field. The Kirchhoff approximation may be considered an ad-hoc combination of infinite frequency and finite frequency theory that is convenient for computation but lacks any rigorous justification. Necessary and sufficient conditions for the validity of Eq. 2.28 cannot be stated. Nevertheless, the KA has seen widespread use in the electromagnetic community where it is called the Physical Optics (PO) approximation. An important distinction between KA based methods and Geometrical Acoustics is that the computational complexity of the KA integral is frequency dependent. Fast Multipole acceleration or a conversion to a contour integral is required to speed up the integration for high frequency applications.

Given the uncertainty over the applicability of KA it is often combined in some way with a boundary integral solver. PO-BEM hybrids are used in CEM to rapidly compute radar cross sections. The Kirchhoff Approximation is either substituted in the BEM as a high frequency ansatz or the domain is partitioned into a PO domain and a BEM domain and solved as a coupled system (see [62] and [63]). The KA solution may also be iterated by allowing the PO field to scatter onto the body [64]. This process is almost identical to solving the boundary integral equation by a Neumann series.

There is also a high frequency extension to the Physical Optics approximation known as the Physical Theory of Diffraction (PTD). Similar to the Geometrical Theory of Diffraction, the PTD adds new sources to the surface distribution in order to account for diffraction processes. The new sources are related to the incident field and the local

geometry by considering asymptotic solutions to canonical scattering problems [65].

2.4 Potential Models for Scattering of Sound by Vorticity

In the hierarchy of assumptions described in the preceding sections, perhaps the most limiting restriction is that of potential mean flow. In real aeroacoustic shielding configurations, the flow domain always includes a vortical region extending downstream of the lifting surfaces. Important scattering processes may be neglected if the interaction of the sound field with the mean flow vorticity is ignored. It may be argued that these vortex scattering phenomena are excluded, *a priori* from potential based methods, and may only be captured by an Euler simulation. However, some attempts have been made to incorporate vortex scattering effects directly into potential based methods by approximate models.

The first category of approximations includes the vortex sheet model of a thin shear layer. With the thin shear layer idealization, both the steady and fluctuating fields are permitted to be discontinuous across an interface. Conservation of mass and momentum must be specified as interface conditions across the surface of discontinuity. Several canonical problems with analytical solutions exist for this type of approximation. Jones examined the scattering of a point source by a planar vortex sheet [66]. Other analytical studies have extended these results to include thick shear layers with continuous and discontinuous vorticity profiles [67] [68]. These studies confirm the validity of vortex sheet model when the wavelength of sound is much greater than the thickness of the shear layer. Morgan considered the more complex case of a semi-infinite plate separating two flow streams, with a vortex sheet discontinuity along the extension of the plate [69]. The analysis of this type of problem is complicated by the presence of a Kelvin-Helmholtz instability of the vortex sheet in the causal solution. The axisymmetric equivalents to this configuration have also been studied extensively [70], [71], [72].

Eversman applied the vortex sheet methodology to the numerical simulation of

acoustic radiation from the aft-fan duct of a turbofan engine [73]. Continuity of particle displacement was implicitly satisfied by the finite element formulation while the penalty method was used to enforce continuity of pressure. Interestingly, there were no reported numerical difficulties relating to the instability of the shear layer for this method. A comparison between LEE and a wave equation method with the vortex sheet approximation for a shear layer was performed by Manera et al. [74]. The vortex sheet was implemented as a membrane of negligible mass and variable tension, through which damping of the Kelvin-Helmholtz instability could be controlled. Of the two flow conditions tested the "approach" condition showed better agreement with the LEE simulation for the modes that were simulated. The potential based calculation in a "cut-back" configuration differed slightly from the LEE simulation. The discrepancies in this case were attributed to the method of flow solution rather than on the inaccuracy of the shear layer approximation. For the turbine mode, the radiation patterns differed significantly, which is to be expected since the flow in the vicinity of the turbine exhaust contains strong entropy gradients which cannot be simulated by potential flow.

The second category of approximations for acoustic scattering by vorticity is the acoustic analogy methods. Lighthill's manipulation of the Navier-Stokes equations allows the perturbation density to be expressed in terms of a forced wave equation. Sakov[75], O'Shea[76] and Ford and Smith[77] have applied the Born approximation to Lighthill's acoustic analogy to analyse the scattering of sound by a discrete vortex in two dimensions. Howe has also applied the Born approximation with a similar acoustic analogy method, where the dependent variable is the perturbation stagnation enthalpy rather than acoustic density. One of the original difficulties that arose due to the Born approximation of vortex scattering is that the forward scattered field appears to be singular. This problem has been resolved by an appropriate treatment of a transition region that forms a parabolic arc in the forward scatter direction [75]. O'Shea pointed out that the singular behavior arises from the refraction of sound over long range and suggested that this effect should be treated as distinct and separate to the scattering by vorticity [76]. From this perspective, Howe's acoustic analogy is a more suitable starting point for vortex scattering analysis since the refractive effects are captured

by the wave operator while the source terms are confined to regions of mean flow vorticity. For the case of a plane wave scattered by a line vortex in two dimensions, Howe's analogy predicts a single dipole source on the vortex filament [78].

Ford and Smith investigated the validity of the acoustic analogy approach by direct comparison with the method of matched asymptotics and found that, despite the lack of *a priori* justification for the acoustic analogy approach, the leading order solution of the asymptotic expansion does match that obtained by the acoustic analogy [77], [79]. When higher order terms are neglected, the scattered field is independent of the internal structure of the vortex and only depends only on the incident acoustic field and on the circulation of the vortex. They also reported good agreement with the full non-linear solution obtained numerically by Collonius [80].

2.4.1 The Influence of Vortex Shedding at a Trailing Edge

The question of how strongly the shedding of vorticity at the trailing edge influences the acoustic pressure in the far field has yet to be answered definitively by theoretical or numerical investigation. A related question for linear perturbation theory is whether or not the Kutta condition is the appropriate model for the behavior of the velocity field at a trailing edge. In the case of LEE formulations, the Kutta condition is implicitly imposed by modeling the trailing edge as a sharp feature. Numerical diffusion is then sufficiently large to cause vorticity to be shed into flow domain at the trailing edge. When potential models are used, the Kutta condition must be explicitly imposed by maintaining finite velocity at the trailing edge. This can be achieved by relating the jump in potential across a vortex sheet to the difference in potential above and below the sharp edge.

The problem of trailing edge diffraction at a sound hard semi-infinite plate, due to a line source, has been treated by Jones [81], for a uniform flow, and by Morgan for a for the case in which the half plane separates a uniform flow stream from a quiescent medium [69]. Rienstra analysed the effect of the Kutta condition on the diffracted component of the far-field scattered sound for Jones' solution in a uniform flow [81], and derived a simple relation for the ratio of the Kutta solution to the no

Kutta solution in the far field shadow zone given by,

$$\frac{p'_{kutta}}{p'_{no_kutta}} = \frac{1 + M\left(\frac{\cos\theta_0}{\sqrt{1-M^2\sin^2\theta_0}}\right)}{1 - M\left(\frac{\cos\theta}{\sqrt{1-M^2\sin^2\theta}}\right)} \tag{2.29}$$

where θ_0 is the angle measured from the wake (in the positive x direction) to the source point and θ is defined similarly for the receiver point. This expression is valid for a source and receiver far from the scattering edge. Based on this approximation, the effect of shed vorticity is minimal for low Mach number. For example, considering a source point far upstream and a receiver point directly below the origin, the attenuation due to vortex shedding at Mach 0.3 is approximately 3 dB. This corresponds to the maximum attenuation that might be obtained by a wing in flight based on the semi-infinite model in uniform flow at low Mach number.

Gabard and Astley, obtained a semi-analytical solution to the problem of sound radiation from a semi-infinite duct with a centre body [71]. A vortex sheet extending from the duct edge was included in the model with an additional free parameter to control the phase and amplitude of shed vorticity. They performed a parametric study of the influence of the Kutta condition at the duct lip on the far-field radiation and found that the effect of varying the phase and amplitude of the shed vorticity was minimal for the frequencies tested. They concluded that its effect could be neglected when the far-field region of concern was near the maximum radiation lobe.

2.5 Discussion

Current techniques for the simulation of shielding effects in non-uniform flows are approaching the stage in development where they can be incorporated into automated design tools. At present, fully three dimensional shielding calculations with the Linearized Euler Equations still present a major computational challenge but recent developments in time-marching Discontinuous Galerkin Methods, running on unstructured grids, are promising to bridge the remaining gap in terms of simplicity of meshing and also in terms of parallel performance and computational efficiency. Despite these

improvements, the high cost of volume discretization methods and the relative insensitivity of the acoustic field to the mean flow effects at low mach number suggest that there is room for a lower fidelity approach that can operate at much lower computational cost than the LEE or other full field schemes. The high computational cost of full field methods is also reflected in the small number of three dimensional shielding studies found in the literature.

The Boundary Element Method for the Helmholtz equation is ideally suited to the external scattering problem in a quiescent medium but lacks the flexibility to handle non-uniform flows. Historical criticisms relating to the non-uniqueness problem have been fully resolved by theoretical advances in the understanding of the hypersingular operator and in the numerical evaluation of the hypersingular kernel on general curved surfaces. A wide variety of highly efficient acceleration strategies exist for both low frequency and high frequency applications which are unrivaled in asymptotic complexity by volume discretization methods, making the BEM an attractive option for scattering calculations.

High frequency methods offer even lower asymptotic complexity than BEM schemes but the implementation of these schemes on engineering geometries becomes increasingly complex as more accurate diffraction models are considered. Creeping wave diffraction is particularly challenging to compute on arbitrary curved surfaces, even more so when flow effects cause the ray paths to bend as they propagate. Since the asymptotic theory of diffraction in high Mach number flows is not well developed, the diffraction coefficients used to calculate sound amplitude on creeping waves may not be valid, even if the ray paths can be found. The difficulties of modeling flow effects in both BEM and ray tracing methods may be circumvented to some extent, by removing the convection effects with a transformation of the time variable. The transformation approach, as originally described by Taylor, is limited to low Mach number non-lifting potential flows.

In the chapters that follow, a flow correction to the standard BEM is developed with a view to simulating the shielding effect of a lift producing wing at low Mach number. It is assumed in this work that the most critical flight phase for noise shielding occurs at take-off and landing, which implies that the Mach number of the steady

flow can be assumed small. The flow correction is based on an extended form of Taylor's transformation for lifting flow. Simulations with the new formulation are compared against LEE simulations and a ray tracing method on a idealized shielding configuration.

A correction for vortex scattering and unsteady vortex shedding has also been accounted for in the formulation. The Born approximation to Howe's acoustic analogy has been utilized to capture the leading order vortex scattering term due to the interaction of the sound field with the steady vorticity that is shed from a lift producing wing in a pseudo-potential mean flow. Time-harmonic vortex shedding has been considered by applying a Kutta condition on the acoustic velocity field and then imposing a "frozen" vorticity model on the disturbances shed from the trailing edge.

Chapter 3

BEM Models for Acoustic Scattering in Low Mach Number Flows

The Boundary Element Method is well suited to external scattering problems when the acoustic medium is stationary and uniform. Unlike volume discretization methods such as the finite element method and finite difference method, the BEM relies on the existence of a closed form Green's function for the problem at hand. Green's functions are easily obtained for uniform media but for non-uniform flows, Green's functions can rarely be found and there is often no option but to abandon the BEM approach.

There have been several attempts to extend the BEM approach to general flows by either approximating the Green's function through a small Mach number expansion of the governing equations or by moving the non-uniform terms to the right hand side and performing a volume integral over these pseudo-source terms. Lee and Wu [82] solved the convected Helmholtz equation by boundary element methods, with a pseudo-source term included in the formulation to model the non-uniform flow terms. They reduced the volume integral involving these source terms to a surface integral by application of the dual reciprocity BEM. However, the usefulness of this formulation in aeroengine noise shielding prediction is questionable because of the reported ill-conditioning of the influence matrix at moderate frequencies, making the method

incompatible with iterative solution strategies. Taylor showed that a retardation of the time variable reduces the approximate convected wave equation to the ordinary wave equation [47]. Astley and Bain [48], and more recently Agarwal and Dowling [49], applied this technique to acoustic radiation and scattering problems at low Mach number.

In this chapter, Taylor's transformation method is analysed and extended to include refraction by steady vorticity and unsteady vortex shedding at a trailing edge. It is shown that additional terms, neglected in Taylor's original analysis may be accounted for by a simple modification of the transformation. Simulations performed with the addition of these terms tends to improve the agreement of the BEM approach with LEE calculations.

3.1 Analysis of Convected Helmholtz Equation

Consider the flow around an aircraft in subsonic flight. Outside the boundary layers and the wake region, the flow is essentially irrotational and homentropic. With the usual acoustic approximation of small amplitude time-varying perturbations of the flow variables about a steady mean value, the propagation of sound through this flow regime is governed by the convected wave equation (Eq. 2.10) for the acoustic velocity potential, $\phi'(\mathbf{x}, t)$. Since the steady component of flow is also irrotational and homentropic, the mean flow can be expressed as the gradient of the steady flow potential, $\mathbf{u}_0 = \nabla\phi_0(\mathbf{x})$, and the sound speed and density may be expressed in terms of the mean flow velocity by the relations

$$c_0^2 = c_\infty^2 - (\gamma - 1)/2(|\mathbf{u}_0|^2 - |\mathbf{u}_\infty|^2) \tag{3.1}$$

and

$$\rho_0 = \rho_\infty \left[1 - (\gamma - 1)/2c_\infty^2(|\mathbf{u}_0|^2 - |\mathbf{u}_\infty|^2)\right]^{1/(\gamma-1)} \tag{3.2}$$

where the subscript ∞ denotes the free stream value and the parameter γ is the adiabatic index of air. Using these relations, the coefficients of the convected wave equation may be written purely in terms of the mean flow velocity and the constants

c_∞ and γ. In cartesian coordinates aligned with the free stream flow, the convected Helmholtz equation for a time-harmonic disturbance may be expressed as

$$A_{lm}\frac{\partial^2\phi'}{\partial x_l \partial x_m} - 2jkB_m\frac{\partial\phi'}{\partial x_m} + k^2C\phi' = \mathcal{F}(x_m) \tag{3.3}$$

where the free stream velocity points in the direction of increasing x_1 coordinate and $\mathcal{F}(x_m)$ is a an acoustic source. The coefficients A_{lm}, B_m and C are given by

$$A_{lm} = \delta_{lm}(1 - \tfrac{1}{2}(\gamma-1)(M^2 - M_\infty^2)) - M_l M_m \tag{3.4}$$

$$B_m = M_m + \tfrac{1}{2}k^{-1}\frac{\partial M^2}{\partial x_m} + \tfrac{1}{2}k^{-1}(\gamma-1)\frac{\partial M_l}{\partial x_l}M_m \tag{3.5}$$

$$C = 1 - jk^{-1}(\gamma-1)\frac{\partial M_m}{\partial x_m} \tag{3.6}$$

where

$$M_l \equiv \mathbf{M} = \mathbf{u}_\infty / c_\infty \tag{3.7}$$

is a reference Mach vector for the steady flow and has magnitude M. The Kronecker delta is defined by

$$\delta_{lm} = \begin{cases} 0, & \text{if} \quad l \neq m \\ 1, & \text{if} \quad l = m \end{cases} \tag{3.8}$$

.

The mean flow velocity potential must satisfy the non-linear full potential equation

$$A_{lm}(\phi_0)\frac{\partial^2\phi_0}{\partial x_l \partial x_m} = 0 \tag{3.9}$$

which simplifies to Laplace's equation

$$\frac{\partial^2\phi_0}{\partial x_m \partial x_m} = 0 \tag{3.10}$$

for low Mach number flow.

Astley and Bain [48] provided a detailed analysis of the relative magnitudes of each of the terms in the convected wave equation. By introducing the characteristic length scales, L_M and L_A for the steady flow and the acoustic perturbation, they showed that

the terms containing derivatives of the mean flow are asymptotically negligible at high frequencies ($L_A/L_m \ll 1$). Since the problem at hand is essentially high frequency, in the sense that shielding is only obtained when the wavelength of sound is smaller than the characteristic dimensions of the scatterer, the steady flow gradient terms may be removed from the convected Helmholtz equation giving

$$A_{lm}\frac{\partial^2\phi'}{\partial x_l \partial x_m} - 2jkM_m\frac{\partial\phi'}{\partial x_m} + k^2\phi' = \mathcal{F}. \tag{3.11}$$

3.1.1 Small-Disturbance Low Mach Number Approximation

At this point, it is useful to consider a small disturbance expansion of the steady flow about a low Mach number uniform flow. Splitting the mean flow Mach vector into a uniform and a perturbation component

$$\begin{aligned} M_1(\mathbf{x}) = M_\infty + M_1'(\mathbf{x}), \qquad M_2(\mathbf{x}) = M_2'(\mathbf{x}), \qquad M_3(\mathbf{x}) = M_3'(\mathbf{x}) \\ \phi_0(\mathbf{x}) = c_\infty M_\infty x_1 + \phi_0'(\mathbf{x}) \end{aligned} \tag{3.12}$$

the following approximation can be made for small disturbance mean flow with low free stream Mach number

$$\begin{aligned} M^2 &= M_\infty^2 + 2M_\infty M_1' + M'^2 \\ &= M_\infty^2 + O(M_\infty M') + O(M'^2) \end{aligned} \tag{3.13}$$

Similarly, we may also expand the terms M_1^2, M_2^2 and M_3^2 to the same order, so that

$$\begin{aligned} M_1^2 &= M_\infty^2 + O(M_\infty M') + O(M'^2) \\ M_2^2 &= 0 \quad + O(M_\infty M') + O(M'^2) \\ M_3^2 &= 0 \quad + O(M_\infty M') + O(M'^2) \end{aligned} \tag{3.14}$$

These approximations may be used to simplify the coefficients A_{lm} in (3.11), which yields a simplified form of the convected Helmholtz equation that is valid in low Mach

number small disturbance mean flows. Consider the A_{11} coefficient which is given by

$$A_{11} = (1 - \tfrac{1}{2}(\gamma - 1)(M^2 - M_\infty^2)) - M_1^2 \tag{3.15}$$

then by the approximations (3.13) and (3.14) we have

$$M^2 - M_\infty^2 \approx 0, \quad M_1^2 \approx M_\infty^2 \tag{3.16}$$

when $O(M_\infty M')$ and $O(M'^2)$ are neglected, so that

$$A_{11} \approx 1 - M_\infty^2 \tag{3.17}$$

Similarly, it can be shown that the other terms simplify to

$$A_{22} \approx 1 \tag{3.18}$$

$$A_{33} \approx 1 \tag{3.19}$$

$$A_{12} \approx A_{23} \approx A_{13} \approx 0 \tag{3.20}$$

Hence, a small disturbance convected Helmholtz equation is obtained

$$\frac{\partial^2 \phi'}{\partial x_m \partial x_m} - M_\infty^2 \frac{\partial^2 \phi'}{\partial x_1^2} - 2jkM_m \frac{\partial \phi'}{\partial x_m} + k^2 \phi' = \mathcal{F} \tag{3.21}$$

It is important to note that the M' quantity in the formulae above, is a steady flow quantity that describes the deviation of the steady flow velocity from a uniform flow and is distinct from the time-unsteady component that describes the acoustic perturbation of the potential field.

3.1.2 Comparison with Taylor's Low Mach Approximation

In Taylor's original paper on low Mach number transformations for acoustics, a low Mach number Helmholtz equation is derived directly from the ordinary convected Helmholtz equation (CHE) Eq. 3.3, simply by stating that when $O(M^2)$ terms are

neglected the following equation is obtained

$$\frac{\partial^2 \phi'}{\partial x_m \partial x_m} - 2jkM_m \frac{\partial \phi'}{\partial x_m} + k^2 \phi' = \mathcal{F} \tag{3.22}$$

Although Taylor omitted the details of the low Mach number expansion of Eq. 3.3, Astley and Bain's analysis of the low Mach number approximation showed that Taylor's derivation of the low Mach number CHE must contain an implicit assumption in the scaling of the acoustics disturbance relative to the mean flow characteristic dimensions [48]. This scaling has been discussed earlier in this section, where it was explicitly stated that the ratio of the wavelength of sound to the characteristic dimension of the mean flow is small ($L_A/L_m \ll 1$), in the derivation of (3.11).

Comparing the small disturbance Helmholtz equation with Taylor's low Mach number Helmholtz equation [47] it is apparent that an extra term of order $O(M_\infty^2)$ is retained in the former equation. The advantage of the small disturbance approximation is a more accurate modeling of sound propagation in the far field where the small disturbance equation approaches the correct asymptotic behavior at large distances from the source of the flow disturbance while Taylor's approximation contains a long range error term of order $O(M_\infty^2)$ that is always present. The small disturbance equation also contains a term of order $O(M')$ that captures the dominant refraction effect of the perturbation mean flow. This term is not included in the convected wave equation for a uniform mean flow.

3.2 Transformation Method for Non-Uniform Flows

Taylor showed that a simple transformation of the time variable is sufficient to reduce the low Mach number convected wave equation to the ordinary wave equation when all $O(M^2)$ terms are neglected . A similar transformation may also be deduced for the small disturbance convected Helmholtz equation. Consider the following transforma-

tions

$$\eta_1 = \beta x_1, \quad \eta_2 = x_2, \quad \eta_3 = x_3, \quad \tilde{k} = \beta k, \quad \phi'(x_l) = e^{j\tau(x_l)}\,\varphi(\eta_l) \tag{3.23}$$

$$\beta = (1 - M_\infty^2)^{-\frac{1}{2}}, \quad \tau(x_l) = \beta\tilde{k}(M_\infty x_1 + \phi_0'/c_\infty) \tag{3.24}$$

where β is the usual Prandtl-Glauert factor that appears in the uniform flow Prandtl-Glauert transformation. Essentially, the transformations above consist of a Prandtl-Glauert stretching of the spatial coordinate in the free stream flow direction combined with Taylor's retardation of the time variable. A phase shift in the frequency-domain is the direct equivalent of a time delay when dealing with the time-domain. Hence, the application of Taylor's time-delay is implemented as a phase shift when solving in the frequency domain. The non-uniform flow refraction effects are modeled purely through this phase shift to the potential. From this point on, Eqn(3.23-3.24) is referred to as the Prandtl-Glauert-Taylor (PGT) transformation.

The following product and chain rules may be used to compute the spatial derivatives in the new coordinates

$$\frac{\partial\phi'}{\partial x_m} = e^{j\tau}\left[\frac{\partial\varphi}{\partial x_m} + j\frac{\partial\tau}{\partial x_m}\varphi\right] \tag{3.25}$$

$$\frac{\partial^2\phi'}{\partial x_l\partial x_m} = e^{j\tau}\left[\frac{\partial^2\varphi}{\partial x_l\partial x_m} + j\frac{\partial\tau}{\partial x_l}\frac{\partial\varphi}{\partial x_m} + j\frac{\partial\tau}{\partial x_m}\frac{\partial\varphi}{\partial x_l} + \left\{j\frac{\partial^2\tau}{\partial x_l\partial x_m} - \frac{\partial\tau}{\partial x_l}\frac{\partial\tau}{\partial x_m}\right\}\varphi\right] \tag{3.26}$$

$$\frac{\partial\varphi}{\partial x_m} = \frac{\partial\varphi}{\partial\eta_s}\frac{\partial\eta_s}{\partial x_m} \tag{3.27}$$

$$\frac{\partial^2\varphi}{\partial x_l\partial x_m} = \frac{\partial^2\varphi}{\partial\eta_r\partial\eta_s}\left(\frac{\partial\eta_r}{\partial x_l}\frac{\partial\eta_s}{\partial x_m}\right) + \frac{\partial^2\eta_s}{\partial x_l\partial x_m}\frac{\partial\varphi}{\partial\eta_s} \tag{3.28}$$

so that the transformed equation can be written as

$$\frac{\partial^2\varphi}{\partial\eta_s\partial\eta_s} - 2j\tilde{k}\widetilde{B}_s\frac{\partial\varphi}{\partial\eta_s} + \tilde{k}^2\widetilde{C}\,\varphi = \tilde{\mathcal{F}} \tag{3.29}$$

where

$$\tilde{\mathcal{F}} = e^{-j\tau}\mathcal{F} \tag{3.30}$$

$$\widetilde{B}_1 = 0, \quad \widetilde{B}_2 = \left(\beta^{-1} - \beta\right) M_2, \quad \widetilde{B}_3 = \left(\beta^{-1} - \beta\right) M_3 \tag{3.31}$$

$$\widetilde{C} = \beta^{-2} + M^2(2 - \beta^2) + \beta^2 M_\infty^2 M_1^2 + j\frac{\beta}{\tilde{k}c_\infty}\left[\frac{\partial^2 \phi_0'}{\partial x_s \partial x_s} - M_\infty^2 \frac{\partial^2 \phi_0'}{\partial x_1 \partial x_1}\right] \tag{3.32}$$

Comparing the last term in Eq. 3.32, with the continuity equation for the mean flow Eq. 3.9, it is clear that the term

$$\frac{\beta}{\tilde{k}c_\infty}\left[\frac{\partial^2 \phi_0'}{\partial x_s \partial x_s} - M_\infty^2 \frac{\partial^2 \phi_0'}{\partial x_1 \partial x_1}\right] \tag{3.33}$$

is of order $O(M^3 L_A/L_M)$, and may be neglected in the high frequency approximation. Then by neglecting all $O(M^3)$ terms and also terms of order $O(M_\infty M')$ and $O(M'^2)$, the transformed convected Helmholtz equation reduces to the ordinary Helmholtz equation in the new coordinate system

$$\frac{\partial^2 \varphi}{\partial \eta_s \partial \eta_s} + \tilde{k}^2 \varphi = \tilde{\mathcal{F}}. \tag{3.34}$$

Hence, the original problem may be solved by performing a transformation of the spatial coordinates and a change of dependent variable according to Eq. 3.23, and then solving an analogous problem in this transformed domain, in which there is no mean flow. A transformed set of boundary conditions must also be provided for a complete description of the scattering problem.

3.2.1 Transformation of Boundary Conditions

When considering boundary conditions on a sound scatterer, it is useful to interpret the transformed coordinates of the scattering surface as the *actual* cartesian coordinates of a deformed surface. This stretched surface is part of an analogous scattering problem in which there is no mean flow. Apart from the phase shift to the potential, introduced by the change of variables, the solutions of both problems are identical to the order of approximation of the small disturbance assumption. This approach allows for a natural interpretation of the potential flux term, appearing directly in the boundary integral formulation of Eq. 3.34, as the normal derivative of the transformed potential with respect to the deformed surface.

Given a surface S with unit surface normal $\mathbf{n}$, the sound hard boundary condition demands that the velocity normal to S is zero so that

$$\frac{\partial \phi'}{\partial x_l} n_l = 0 \tag{3.35}$$

When written in terms of the new coordinates, this condition becomes

$$\frac{\partial \varphi}{\partial \eta_s} \frac{\partial \eta_s}{\partial x_l} n_l + j\tilde{k}\beta\varphi M_l n_l = 0 \tag{3.36}$$

which reduces to

$$\frac{\partial \varphi}{\partial \eta_s} \frac{\partial \eta_s}{\partial x_l} n_l = \frac{\partial \varphi}{\partial \eta_s} n_s^* = 0 \tag{3.37}$$

on a streamline of the mean flow. The coefficients n_s^* may be interpreted as cartesian components of a vector in the deformed domain. Unfortunately, this vector is generally not normal to the deformed scatterer surface, which implies that the boundary condition on the scatterer surface cannot be expressed purely in terms of the potential flux across the deformed scatterer surface, but must also include the tangential derivatives with respect to the deformed surface.

Defining the unit vectors $\tilde{\mathbf{a}}$ and $\tilde{\mathbf{b}}$ as tangent vectors to the deformed surface $\tilde{S}$, then

$$\tilde{\mathbf{n}} = \tilde{\mathbf{a}} \times \tilde{\mathbf{b}} \tag{3.38}$$

is the unit normal to the deformed surface, and the the normal and tangential derivatives of potential in the deformed domain are given by

$$\frac{\partial \varphi}{\partial \tilde{n}} = \frac{\partial \varphi}{\partial \eta_s} \tilde{n}_s \tag{3.39}$$

$$\frac{\partial \varphi}{\partial \tilde{a}} = \frac{\partial \varphi}{\partial \eta_s} \tilde{a}_s \tag{3.40}$$

$$\frac{\partial \varphi}{\partial \tilde{b}} = \frac{\partial \varphi}{\partial \eta_s} \tilde{b}_s \tag{3.41}$$

Hence, the hard wall boundary condition in the deformed domain may be expressed

as

$$\frac{\partial \varphi}{\partial \tilde{n}} \tilde{n}_s n_s^* + \frac{\partial \varphi}{\partial \tilde{a}} \tilde{a}_s n_s^* + \frac{\partial \varphi}{\partial \tilde{b}} \tilde{b}_s n_s^* = 0 \tag{3.42}$$

Examining the coefficients of the derivatives in Eq. 3.42, it is apparent that the boundary condition is unchanged by the transformation whenever $\mathbf{n}^*$ is perpendicular to $\tilde{S}$. This only occurs at points on $\tilde{S}$ where the local surface normal is perpendicular or parallel to the uniform flow. At all other points, the boundary condition also contains surface derivatives of the potential.

3.2.2 Higher Order Transformation

Having established that a transformation exists that reduces the simplified convected Helmholtz equation (Eq. 3.21) to the ordinary Helmholtz equation (Eq. 3.34) under a small disturbance and low Mach number assumption, it is natural to ask whether the same methodology may be extended to the Eq. 3.11, without simplification, so that higher order terms in the Mach number expansion may be captured by the transformation. In order to investigate this idea, it is necessary to return to Eq. 3.11 and to consider a general transformation of the coordinates. Then by extracting the conditions that must be satisfied for the general transformation to reduce the CHE to the ordinary HE in the new coordinate system, specific transformations may be tested for this property.

Consider the following general transformation of the spatial coordinates combined with a general phase shift of the acoustic potential

$$\eta_s = \eta_s(x_m), \quad \tilde{k} = \beta k, \quad \phi'(x_m) = e^{j\tau(x_m)} \varphi(\eta_s) \tag{3.43}$$

with τ defined as in Eq. 3.24. Applying this general transformation to Eq. 3.11 equation and computing the coefficients of the derivatives via the transformation rules Eqs(3.25-3.28), gives the transformed equation

$$\widetilde{A}_{rs} \frac{\partial^2 \varphi}{\partial \eta_r \partial \eta_s} - 2j\tilde{k}\widetilde{B}_s \frac{\partial \varphi}{\partial \eta_s} + \tilde{k}^2 \widetilde{C} \varphi = 0 \tag{3.44}$$

where

$$\widetilde{A}_{rs} = A_{lm}\frac{\partial \eta_r}{\partial x_l}\frac{\partial \eta_s}{\partial x_m} \tag{3.45}$$

$$\widetilde{B}_s = \tfrac{1}{2}j\tilde{k}^{-1}A_{lm}\frac{\partial^2 \eta_s}{\partial x_l \partial x_m} + \left(\beta^{-1}M_m - \beta A_{lm}M_l\right)\frac{\partial \eta_s}{\partial x_m} \tag{3.46}$$

$$\widetilde{C} = \beta^{-2} + 2M^2 + A_{lm}\left(j\frac{\beta}{\tilde{k}c_\infty}\frac{\partial^2 \phi_0'}{\partial x_l \partial x_m} - \beta^2 M_l M_m\right). \tag{3.47}$$

Up to this point in the analysis, no additional approximations have been introduced by transforming the governing equations. Regardless of the transformation used, Eq. 3.44 and Eq. 3.11 describe exactly the same physical process. However, if a suitable transformation can be found that simplifies the coefficients $\widetilde{A}_{rs}$, $\widetilde{B}_s$ and $\widetilde{C}$ to constant values, then Eq. 3.44 becomes a more useful form of the equation for numerical analysis. For instance, if a transformation exists with the property that the coefficients above satisfy the conditions

$$\widetilde{A}_{rs} = \widetilde{C}\delta_{rs} \tag{3.48}$$

and

$$\widetilde{B}_s = 0 \tag{3.49}$$

then Eq. 3.44 reduces to the ordinary Helmholtz equation in the new coordinate system. The PGT transformation, presented in the previous section, is a specific example of a transformation that satisfies the above conditions in an approximate way when a low Mach number, small-disturbance expansion is applied.

An improvement to the PGT transformation may be obtained for a two-dimensional problem, by keeping all $O(M_\infty M')$ terms in the development of the transformation method. Depending on whether the steady flow potential satisfies the full potential equation or the incompressible approximation (ie. Laplace's equation), the term

$$\frac{\beta}{\tilde{k}c_\infty}A_{lm}\frac{\partial^2 \phi_0'}{\partial x_l \partial x_m} \tag{3.50}$$

in the coefficient $\widetilde{C}$, is either zero or of order $O(M^3 L_A/L_M)$ and may be neglected in

either case. Then by performing a small disturbance expansion and neglecting $O(M'^2)$ and $O(M^3)$ terms, the coefficients $\widetilde{B}_s$ and $\widetilde{C}$ reduce to

$$\widetilde{B}_s = \tfrac{1}{2} j \tilde{k}^{-1} A_{lm} \frac{\partial^2 \eta_s}{\partial x_l \partial x_m} \tag{3.51}$$

$$\widetilde{C} = 1 + 2M_\infty M_1' \tag{3.52}$$

Recalling that the conditions

$$\widetilde{A}_{rs} = \widetilde{C}\delta_{rs} + O(M'^2) + O(M^3) \tag{3.53}$$

and

$$\widetilde{B}_s = 0 + O(M'^2) + O(M^3) \tag{3.54}$$

must be satisfied so that the transformed convected Helmholtz equation is reduced to the ordinary Helmholtz equation to the correct order of approximation. Defining the matrices

$$\mathbf{J} = J_{rs} = \frac{\partial \eta_r}{\partial x_s} \tag{3.55}$$

$$\mathbf{A} = A_{rs} \tag{3.56}$$

where r is the row and s is the column, then the first set of constraints on the transformation Eq. 3.53, may be expressed as the matrix equation

$$\widetilde{\mathbf{A}} = \mathbf{J}\mathbf{A}\mathbf{J}^T = \widetilde{C}\,\mathbf{I} \tag{3.57}$$

so that the Jacobian matrix, $\mathbf{J}$ must satisfy

$$\mathbf{J}^T\mathbf{J} = \widetilde{C}\mathbf{A}^{-1} = \begin{bmatrix} \beta^2 + (\gamma+3)M_\infty M_1' & M_\infty M_2' \\ M_\infty M_2' & 1 + (\gamma+1)M_\infty M_1' \end{bmatrix} + O(M'^2) + O(M^3) \tag{3.58}$$

For a two-dimensional incompressible flow, we can introduce the steady flow stream function, defined so that

$$\Psi = U_\infty x_2 + \Psi' \tag{3.59}$$

and

$$U_1' = \frac{\partial \Psi'}{\partial x_2}, \quad U_2' = -\frac{\partial \Psi'}{\partial x_1} \tag{3.60}$$

Then the coordinate transformations

$$\eta_1 = \beta x_1 + \tfrac{1}{2}(\gamma+3) M_\infty \phi_0'/c_\infty, \quad \eta_2 = x_2 + \tfrac{1}{2}(\gamma+1) M_\infty \Psi'/c_\infty \tag{3.61}$$

give

$$\mathbf{J} = \begin{bmatrix} \beta + \frac{1}{2}(\gamma+3) M_\infty M_1' & \frac{1}{2}(\gamma+3) M_\infty M_2' \\ -\frac{1}{2}(\gamma+1) M_\infty M_2' & 1 + \frac{1}{2}(\gamma+1) M_\infty M_1' \end{bmatrix} \tag{3.62}$$

and

$$\mathbf{J}^T\mathbf{J} = \begin{bmatrix} \beta^2 + (\gamma+3) M_\infty M_1' & M_\infty M_2' \\ M_\infty M_2' & 1 + (\gamma+1) M_\infty M_1' \end{bmatrix} + O(M'^2) + O(M^3) \tag{3.63}$$

which satisfies Eq. 3.58.

The second constraint requires that

$$\tilde{k}^{-1} A_{lm} \frac{\partial^2 \eta_s}{\partial x_l \partial x_m} = 0 \tag{3.64}$$

For a two-dimensional incompressible potential flow we have,

$$\frac{\partial \phi_0'}{\partial x_m \partial x_m} = \frac{\partial \Psi'}{\partial x_m \partial x_m} = 0 \tag{3.65}$$

which implies that Eq. 3.64 is satisfied when order $O(M^3 L_A/L_M)$ terms are neglected. Therefore, the transformations described in Eq. 3.43 and Eq. 3.61 reduce the convected Helmholtz equation to the ordinary Helmholtz equation for a small disturbance about a low Mach number uniform flow with a modified source term

$$\frac{\partial^2 \varphi}{\partial \eta_s \partial \eta_s} + \tilde{k}^2 \varphi = \widetilde{C}^{-1} \tilde{\mathcal{F}}. \tag{3.66}$$

The transformed boundary conditions developed in the previous section also apply to this case and do not require any further analysis.

3.2.3 Comparison of Error Terms

The validity of the low Mach number small-disturbance approximation may be investigated by evaluating the the true value of the coefficients of the transformed propagation equation and comparing with the assumed values. The error in the coefficients as measured by the difference between the assumed values of the coefficients and the true values provides an estimate of the spatial regions where the low Mach number approximation performs well and the regions where it provides a poor approximation of the full equations.

For the second order derivative terms, the assumed values of the coefficients are: 1) zero for the coefficients of the cross-derivatives, 2) unity for the remaining coefficients, as evident in Eq. 3.66. Hence the error in the coefficients of second order derivates is given by

$$E_{A_{rs}} = \delta_{rs} - \widetilde{A}_{rs}/\widetilde{C} \tag{3.67}$$

Similarly, the magnitude of

$$E_{B_s} = \widetilde{B}_s/\widetilde{C} \tag{3.68}$$

provides a measure of the error in the coefficients of the first order derivatives.

The relative magnitudes of each of the error terms, for the various transformation methods, may explored with the example of incompressible potential flow around a Joukowski airfoil. This simple model problem simulates the main features of the outer flow surrounding an airfoil and is sufficient to illustrate the Mach number dependence of the discarded terms in the low Mach number approximation. Four transformations are considered:

1. Taylor's original transformation (Taylor), Eq. 2.26

2. Prandtl-Glauert 's original transformation (PG), Eq. 2.25

3. PGT transformation (PGT), Eq. 3.23

4. Two-dimensional, spatially nonuniform transformation (Nonuniform), Eq. 3.61

Given an offset unit circle in the complex plane $w = \exp(j\theta) + f + gj$, the Joukowski

transformation

$$\zeta = w + \frac{b^2}{w} \tag{3.69}$$

with

$$b = \sqrt{1 - g^2} - |f| \tag{3.70}$$

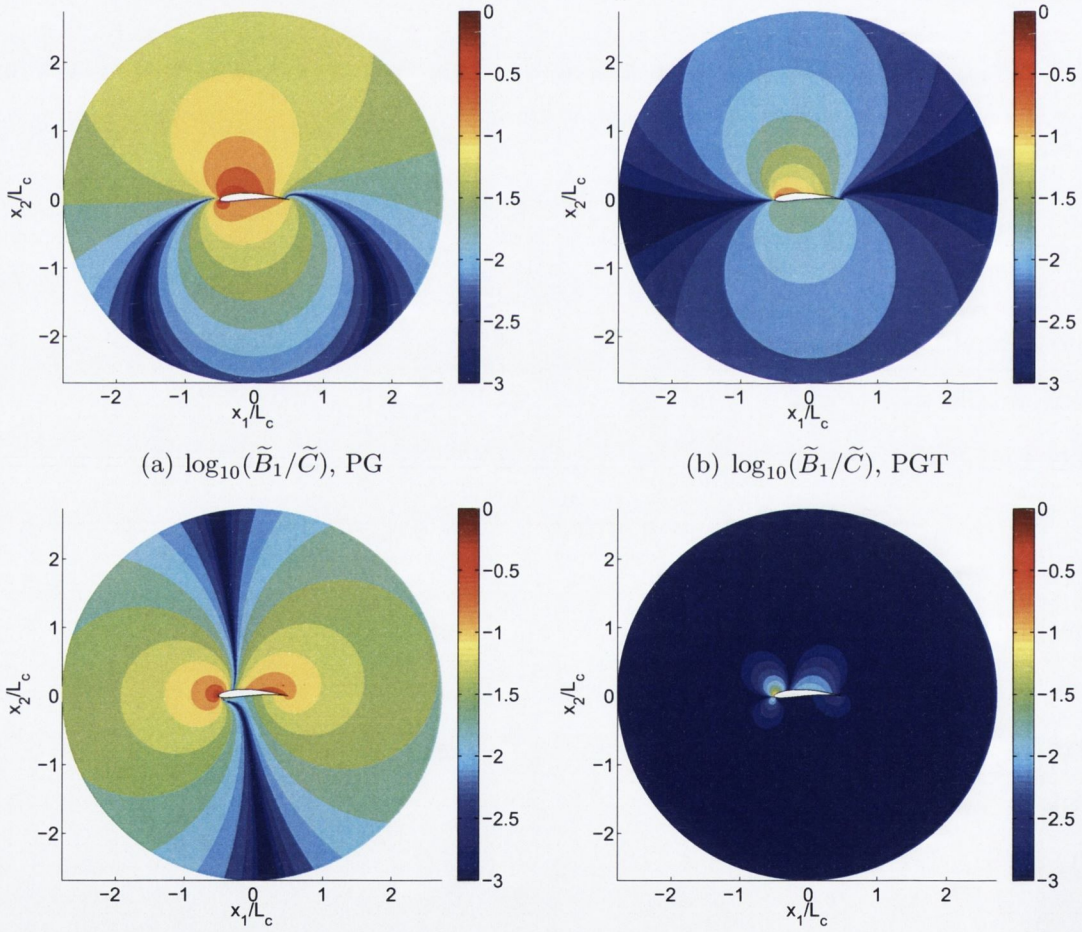
maps the circle to an airfoil shape in the ζ plane. Since an analytical solution for the complex-variable potential flow around a cylinder is available, the Joukowski mapping for the two-dimensional Laplace equation provides a convenient way to compute incompressible potential flow around an airfoil like shape (see Katz and Plotkin [83]).

As a test case, the flow around a Joukowski airfoil with parameters, $f = -0.08$ and $g = 0.1$ was computed by potential flow theory and the magnitudes of the error terms were extracted from the mean flow solution. The above parameters produce an airfoil with a thickness ratio of approximately 10% and a ratio of maximum camber to chord length of approximately 1.4%. The free stream Mach number is taken as $M_\infty = 0.3$ and the airfoil is rotated to the free stream flow with an angle of attack of 8°. In the contour plots presented, the η_1 and η_2 axes have been normalized with respect to the chord length C.

In Fig. 3.1, contours of the coefficients $\widetilde{B}_s/\widetilde{C}$ have been plotted on a log scale to show the spatial extent of the convective error terms. Comparing the PG transformation in plots 3.1(a) and 3.1(c), with the PGT method in plots 3.1(b) and 3.1(d), it is apparent that the use of a non-uniform phase function reduces the convective error term by approximately one order of magnitude over a large part of the domain. This is the principal advantage of using the PGT transformation over the ordinary PG approach.

In Fig. 3.2, the error in the coefficients $\widetilde{A}_{rs}/\widetilde{C}$ introduced by Taylor's approximation and the PGT approach, have been plotted on a log scale. At large distances from the flow disturbance, the error in the Taylor approximation reduces to a constant term as discussed in section 3.2. Although this constant term is removed by the PGT approach, the underlying error due to nonuniform flow can be quite large in the vicinity of the airfoil and in particular near the leading edge, where the flow is accelerated to high Mach number. The nonuniform coordinate stretching can considerably reduce the

spatial extent these terms. However the peak error, located at the leading edge, is of the same order of magnitude as the PGT method. The rapid decay of the error away from the source of flow disturbance suggests that the non-uniformity is more accurately captured by this approach. However, the fact that the maximum error does not change suggests that the Mach number dependence of the approximation is not necessarily improved.



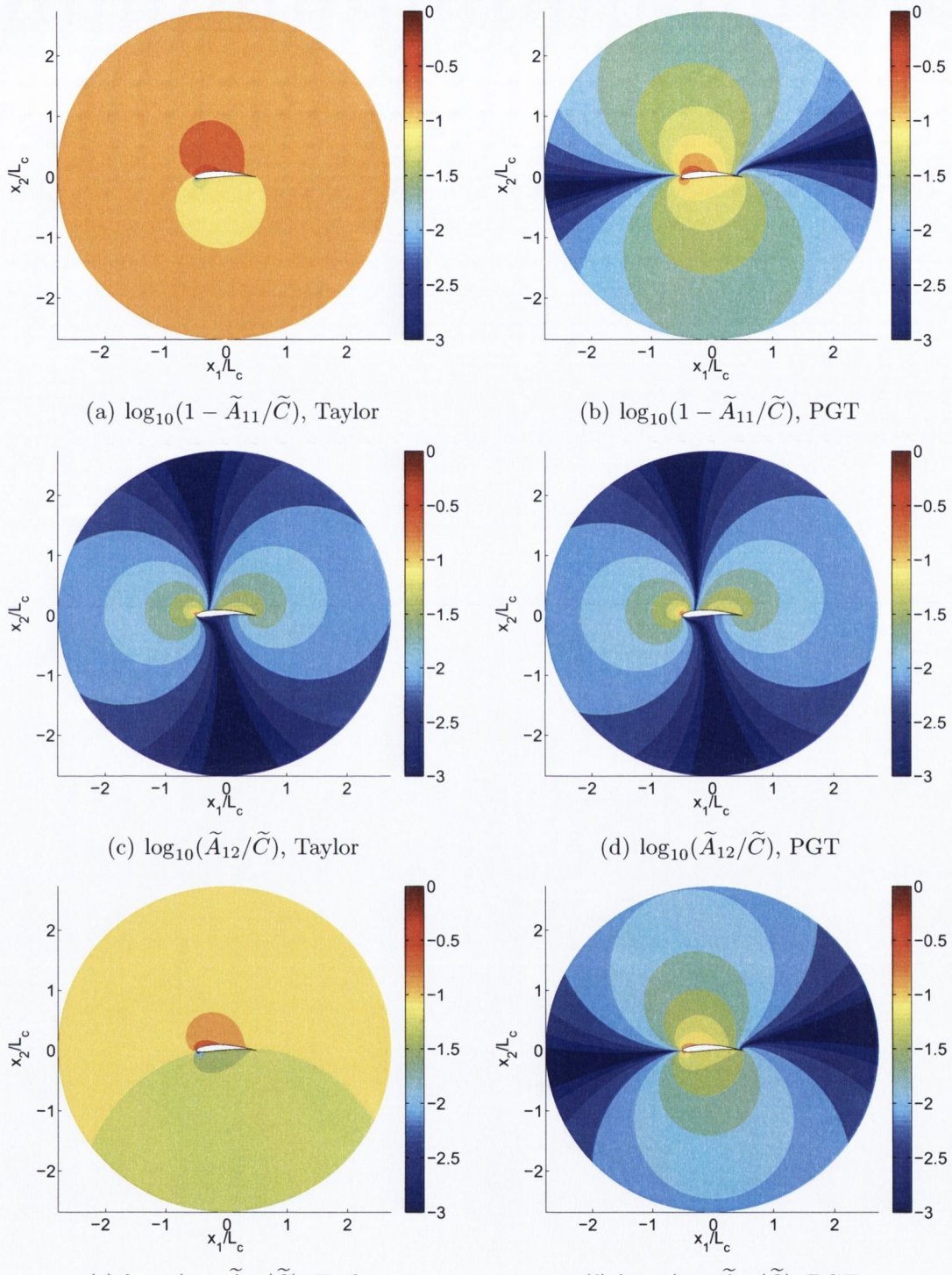
(a) $\log_{10}(\widetilde{B}_1/\widetilde{C})$, PG

(b) $\log_{10}(\widetilde{B}_1/\widetilde{C})$, PGT

(c) $\log_{10}(\widetilde{B}_2/\widetilde{C})$, PG

(d) $\log_{10}(\widetilde{B}_2/\widetilde{C})$, PGT

Figure 3.1: Contour plots of the convective error terms $(\widetilde{B}_s/\widetilde{C})$, in the transformation method, for a Joukowski airfoil with parameters $M_\infty = 0.3$, $\alpha = 8°$, $f = -0.08$, $g = 0.1$. (a) $\widetilde{B}_1/\widetilde{C}$ component of PG transformation, (b) $\widetilde{B}_1/\widetilde{C}$ component of PGT transformation, (c) $\widetilde{B}_2/\widetilde{C}$ component of PG transformation, (d) $\widetilde{B}_1/\widetilde{C}$ component of PGT transformation



(a) $\log_{10}(1 - \widetilde{A}_{11}/\widetilde{C})$, Taylor

(b) $\log_{10}(1 - \widetilde{A}_{11}/\widetilde{C})$, PGT

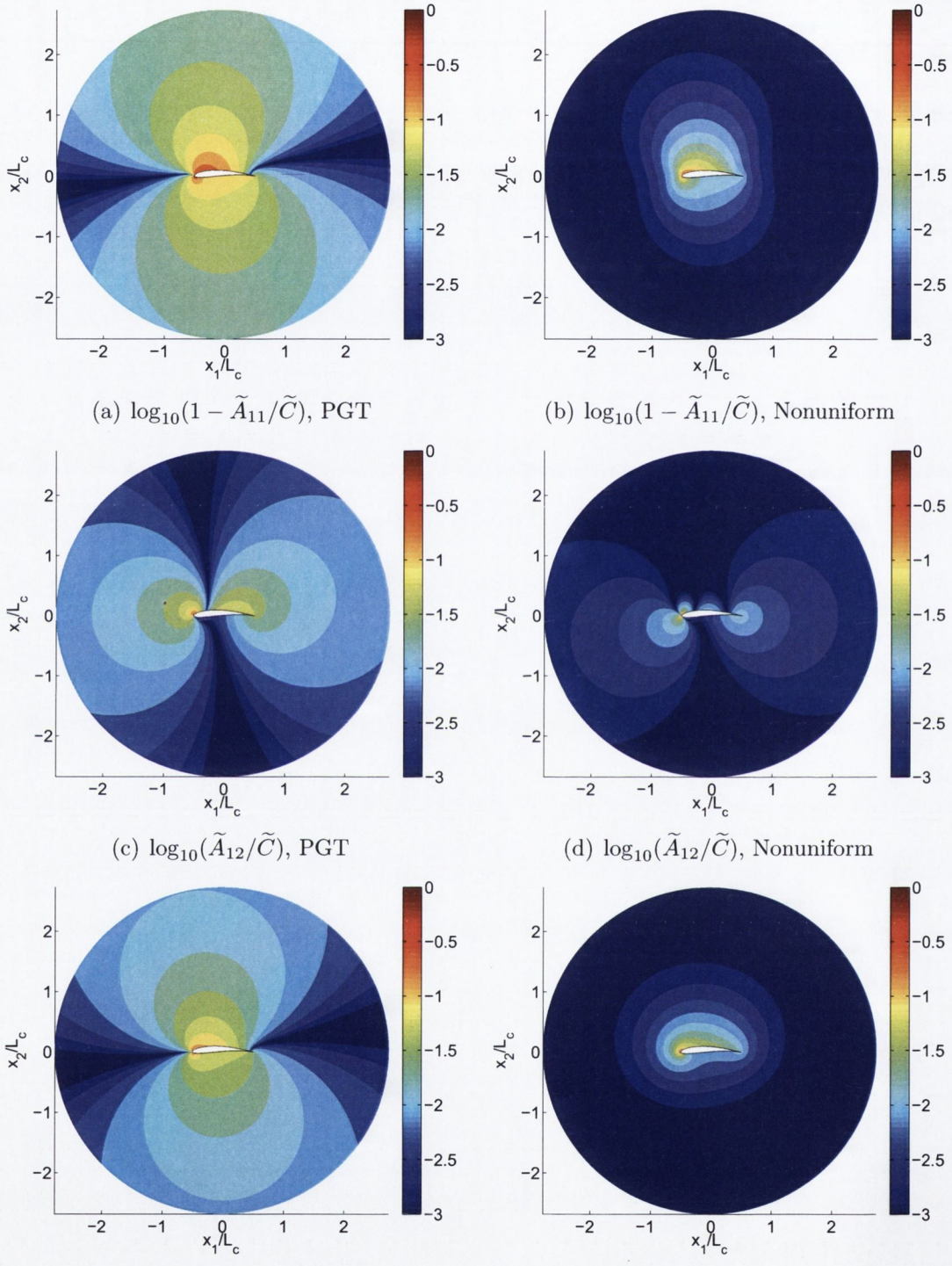
(c) $\log_{10}(\widetilde{A}_{12}/\widetilde{C})$, Taylor

(d) $\log_{10}(\widetilde{A}_{12}/\widetilde{C})$, PGT

(e) $\log_{10}(1 - \widetilde{A}_{22}/\widetilde{C})$, Taylor

(f) $\log_{10}(1 - \widetilde{A}_{22}/\widetilde{C})$, PGT

Figure 3.2: Contour plots of the error in the stiffness terms of the transformation method for a Joukowski airfoil with parameters $M_\infty = 0.3$, $\alpha = 8°$, $f = -0.08$, $g = 0.1$. (b) $1 - \widetilde{A}_{11}/\widetilde{C}$ error component for Taylor's transformation, (b) $1 - \widetilde{A}_{11}/\widetilde{C}$ error component for PGT transformation, (d) $\widetilde{A}_{12}/\widetilde{C}$ error component for Taylor's transformation, (d) $\widetilde{A}_{12}/\widetilde{C}$ error component for PGT transformation, (f) $1 - \widetilde{A}_{22}/\widetilde{C}$ error component for Taylor's transformation, (e) $1 - \widetilde{A}_{22}/\widetilde{C}$ error component for PGT transformation.



(a) $\log_{10}(1 - \widetilde{A}_{11}/\widetilde{C})$, PGT

(b) $\log_{10}(1 - \widetilde{A}_{11}/\widetilde{C})$, Nonuniform

(c) $\log_{10}(\widetilde{A}_{12}/\widetilde{C})$, PGT

(d) $\log_{10}(\widetilde{A}_{12}/\widetilde{C})$, Nonuniform

(e) $\log_{10}(1 - \widetilde{A}_{22}/\widetilde{C})$, PGT

(f) $\log_{10}(1 - \widetilde{A}_{22}/\widetilde{C})$, Nonuniform

Figure 3.3: Contour plots of the error in the stiffness terms of the transformation method for a Joukowski airfoil with parameters $M_\infty = 0.3$, $\alpha = 8°$, $f = -0.08$, $g = 0.1$. (a) $1 - \widetilde{A}_{11}/\widetilde{C}$ error component for PGT transformation, (b) $1 - \widetilde{A}_{11}/\widetilde{C}$ error component for nonuniform transformation, (c) $\widetilde{A}_{12}/\widetilde{C}$ error component for PGT transformation, (d) $\widetilde{A}_{12}/\widetilde{C}$ error component for nonuniform transformation , (f) $1 - \widetilde{A}_{22}/\widetilde{C}$ error component for PGT transformation, (e) $1 - \widetilde{A}_{22}/\widetilde{C}$ error component for nonuniform transformation.

3.2.4 Implications for Lifting Flows

A non-trivial complication arises in the transformation method when the acoustic medium is a lift producing steady potential flow. In two dimensions, the presence of bound circulation on an airfoil implies that the steady potential must have a branch cut, across which there is a fixed jump in potential. Now, considering the acoustic problem in a domain with a branch cut in the steady potential, the transformed quantity, $\varphi = e^{-j\tau(x_l)}\,\phi'$, is also discontinuous across the branch cut and Green's identities are no longer valid on the branch cut itself. Therefore, the wake must be included as part of the scattering surface when deriving a boundary integral equation for the domain and a suitable boundary condition is needed, if the two sides of the discontinuity are to be connected in a physically sensible way. If a nonuniform coordinate stretching is performed, the points either side of an infinitesimally thin wake are mapped to different coordinate points in the deformed domain so that the analogous acoustic problem is posed on a domain that is physically disconnected as well as having a phase discontinuity (see Fig. 3.4). Any numerical scheme that uses a nonuniform transformation would be required to reconnect the domain with an interface condition on the artificial boundaries. The question of the existence of the transformation must also be tackled for a nonuniform stretching. It appears from the example above, that the Jacobian determinant is always positive for the the case of a Joukowski airfoil, and hence the transformation is valid. However, this hypothesis was not tested in any detail.

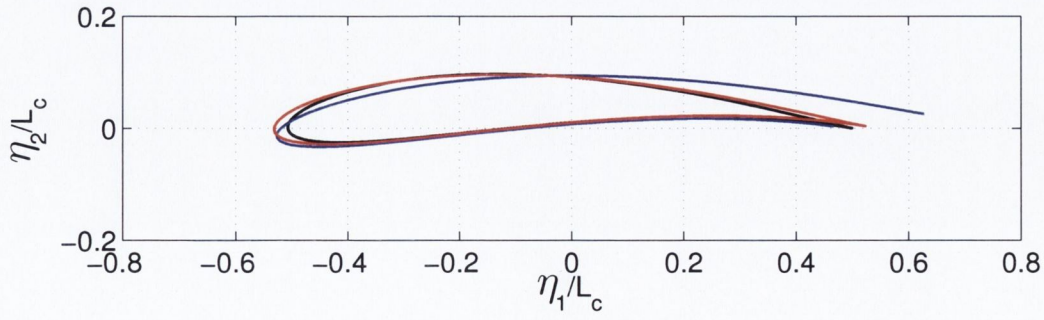


Figure 3.4: Profiles of deformed Joukowski airfoil. Non-deformed airfoil, Black; Prandtl-Glauert domain, Red; Nonuniform stretching, Blue.

In three-dimensional flow, the equivalent mechanism for introducing lift into a

potential flow formulation, is the vortex sheet wake that extends downstream of the trailing edge of a lift producing surface. Unlike the two dimensional case, in which the branch cut can be moved to a convenient location as desired, the vortex sheet is not a purely mathematical construction. Rather, it is a model of the shed vorticity produced when a Kutta condition is imposed on the trailing edge of a wing. The strength and location of the vortex sheet are governed by vortex dynamics. The equivalence of a surface distribution of potential jump and a vortex sheet can be established via the Biot-Savart law so that the vortex wake may also be viewed as a surface of discontinuity of the mean potential (see Katz and Plotkin [83]). As in the two-dimensional case, this surface must be considered as part of the scattering structure when simulating acoustic scattering by the transformation method.

3.3 Scattering of Sound by Steady Vorticity

Following from the arguments of the previous section, a three-dimensional lifting flow can never be regarded as a fully potential flow. At best it may be considered quasi-potential, in the sense that the vorticity is confined to a region that may be considered infinitesimally thin so that the wake can be treated as a surface of discontinuity of the mean potential. Accepting that any realistic shielding configuration will involve a mean flow containing at least some vorticity, a choice must be made to either abandon the velocity potential formulation for the acoustic field and revert to the LEEs or to introduce a model for the interaction of the sound field with the steady vorticity. As previously discussed, two distinct approaches to the modeling of acoustic-vorticity interactions by potential formulations are to be found in the literature. The vortex sheet model replaces the vorticity with an infinitely thin shear layer across which the mean velocity vector undergoes a sudden jump in its tangential component. A linearized form of the continuity of pressure and normal velocity is used to enforce the correct behavior of the acoustic field as it passes through the sheet. This particular model is well suited to the analysis of sound transmission through a jet shear layer or a splitter plate configuration and several examples of analytic and numerical methods incorporating the vortex sheet methodology may be found in the literature.

An alternative approach is to replace the distribution of vorticity with a set of discrete vortex filaments, and to treat the interaction of the sound field with the mean vorticity by adding a source term, from one of the acoustic analogies, to the propagation equation.

For the acoustic shielding problem under consideration, it would appear that the distribution of vorticity in the wake is not a perfect match to either a discrete vortex or a vortex sheet model. The typical distribution of trailing edge vortex strength for an attached flow over a tapered wing shows a region of concentrated vorticity in the wingtip which is best described as a discrete vortex, and a region of slowly varying vorticity over the main length of the wingspan that is best modeled as a weak vortex sheet. If the vortex sheet regime is analysed in isolation, it would appear that the steady shear velocity is too weak to have any impact on sound transmission. Campos and Kobayashi [68] derived transmission coefficients for sound propagation through a finite thickness shear layer with a hyperbolic tangent velocity profile. Even for the relatively high shear Mach number of $M = 0.3$, the characteristic variation of the transmission coefficients with angle of incidence shows a large region, centered on normal incidence, over which the transmission coefficient is very close to unity. This behavior appears to be characteristic of both finite thickness and infinitely thin shear layers, provided the shear Mach number is small. Given the shear velocity for attached flow over a wing is only a small fraction of the free stream Mach number at points on the trailing edge that are not close to the wing tip, it can safely be assumed that the the sound field will undergo total transmission through the weak shear in the wake. While a zone of silence was shown to exist for all shear layers, independent of the shear strength, the extent of this zone also depends on the shear Mach number and is limited to shallow grazing angles for low shear Mach number. Based on these arguments, it is proposed that the scattering of sound by steady vorticity is best approximated by the acoustic analogy method.

Consider a vortex filament with strength Γ. The direction of the vorticity vector and the direction of rotation of the induced velocity field is determined by the right hand rule and shown in Fig. 3.5. For the scattering of a plane wave by a rectilinear vortex, Howe describes three sources of of acoustic-flow interaction [78]. Two of these

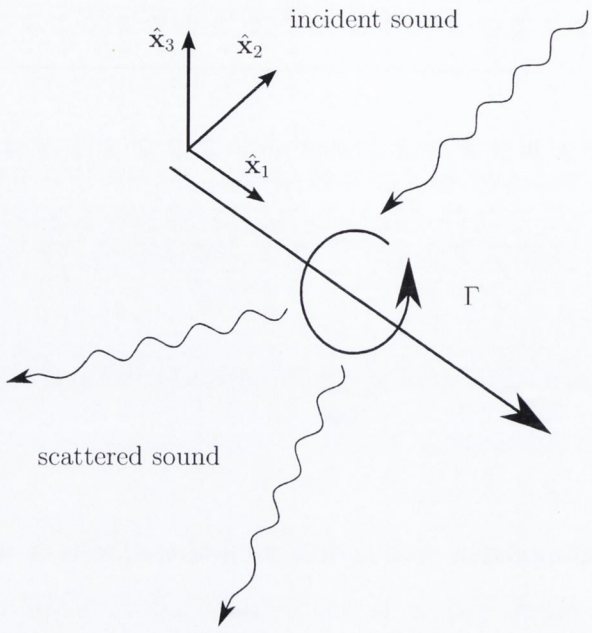


Figure 3.5: Scattering of sound by a vortex filament of strength Γ

effects are associated with the potential flow field induced by the vortex and the third is the acoustic dipole term associated with the oscillation of the vortex core by the incident sound field. The potential flow terms to which Howe refers are precisely the $O(M)$ velocity terms that have been discussed in the previous sections and may be treated by the transformation method with a correction for the phase jump across the wake. The dipole term is an additional source that is derived from the equations of vortex sound. Applying the low Mach number and small disturbance approximations to the linearized form of Howe's acoustic analogy Eq. 2.16, yields

$$\nabla^2 h' - M^2 \frac{\partial^2 h'}{\partial x_1^2} - 2j\frac{k}{c_\infty}\mathbf{M}\cdot\nabla h' + k^2 h' = -\nabla\cdot(\boldsymbol{\gamma}_0 \times \mathbf{u}' + \boldsymbol{\gamma}' \times \mathbf{u}_0) + \mathcal{F} \qquad (3.71)$$

for a time-harmonic incident field. The first term in the right hand side of the above account for the interaction of the acoustic field with steady vorticity, while the second term accounts for the production of sound by time unsteady vorticity. The final term on the right hand side is a classical volumetric source term that will be used to mimic the engine noise source in the calculations that are presented in Chapter 5. Eq. 3.71 is an inhomogeneous convected Helmholtz equation that may be solved by a Born series when the additional source terms are relatively weak. In the presence of a scatterer, the

zeroth order term in the Born series is the scattered field in the absence of the vortex term which may be obtained by solving the convected Helmholtz equation without the vortex interaction term,

$$\nabla^2 h'^0 - M^2 \frac{\partial^2 h'^0}{\partial x_1^2} - 2j\frac{k}{c_\infty}\mathbf{M}\cdot\nabla h'^0 + k^2 h'^0 = \mathcal{F}. \tag{3.72}$$

The first order term in the Born series, which is also called the Born approximation, is a correction to the zeroth field that satisfies the convected Helmholtz equation with a source term generated from the zeroth solution. Since there are no vortex sources present in the zeroth iteration of the Born series, the stagnation enthalpy may be expressed in terms of velocity potential by

$$h'^0 = -j\omega\phi'^0 \tag{3.73}$$

so that the Born approximation satisfies

$$\nabla^2 h'^1 - M^2 \frac{\partial^2 h'^1}{\partial x_1^2} - 2j\frac{k}{c_\infty}\mathbf{M}\cdot\nabla h'^1 + k^2 h'^1 = -\frac{j}{\omega}\nabla\cdot(\boldsymbol{\gamma}\times\nabla h'^0) \tag{3.74}$$

A further simplification may be made when the distributed vorticity $\boldsymbol{\gamma}$ is replaced by set of vortex filaments (see Fig. 3.5). The vorticity vector may then be expressed as

$$\boldsymbol{\gamma} = \Gamma\delta(x_2)\delta(x_3)\hat{\mathbf{x}}_1 \tag{3.75}$$

so that the source term becomes

$$-\frac{j}{\omega}\nabla\cdot(\boldsymbol{\gamma}\times\nabla h'^0) = -\frac{j}{\omega}\Gamma\left(\frac{\partial h'^0}{\partial x_2}\delta(x_2)\delta'(x_3) - \frac{\partial h'^0}{\partial x_3}\delta'(x_2)\delta(x_3)\right) \tag{3.76}$$

In this form, the dipole source may be easily convolved with a Green's function for the domain to give the vortex scattered field in the far-field. The vortex dipole source should also be allowed to scatter from the wing source by performing a second propagation step.

As discussed by Ford and Smith [77] [79], the validity of the Born approximation

solution to the vortex scattering problem cannot be demonstrated *a priori* but has been shown to yield the correct scattering behavior to the first order of approximation by the method of matched asymptotic expansion. While the validity of the Born approximation cannot be entirely justified for a configuration involving a scattering body with a trailing distribution of vorticity, it can be argued that the vorticity generated by a lifting surface is mostly concentrated at the wingtips, and that the vortexes are acoustically compact and well separated for many chord lengths downstream of the wingtips. Therefore, it seems likely that any unaccounted secondary scattering effects should be weak.

It has been assumed throughout this analysis that the zeroth order solution is available, in the following section a method is presented to obtain this solution via the Boundary Element Method.

3.4 BEM Formulation in a Steady Lifting Flow

In this section the limiting process to obtain the thin structure HIE is described, and a set of boundary integral equations with a unique solution, is derived on the vortex sheet wake surface. The resulting BIE system is discretized by the Boundary Element Method and solved by point collocation. The derivation of the integral equations closely follows the formulation described in Chapter 9 of von Estorff [34]. For clarity, the limiting process is indicated explicitly, following the work of Guiggiani et al. [35], [84], [44], [45]. Over several papers Guiggiani et al. have developed a general theory of so called hypersingular integral equations that may be applied to arbitrary scattering geometries with corner points. By performing a rigorous analysis of the limit to the boundary for the normal derivative BIE, they showed that all surface integrals are either finite or cancel with another diverging integral of opposite sign. In the development of the wake BIE, all discrete element surfaces will be assumed flat and only two types of surface potential discretization will be considered; (1) constant potential elements and (2) plane wave elements. It is worth noting however, that the extension of the theory presented in this section, to surface elements of non-zero curvature and higher order discretizations, is certainly within the scope of Guiggiani's general theory.

A schematic diagram of the thin structure scattering problem is shown in Fig. 3.6. For simplicity, the geometry is displayed as a two dimensional slice of what is actually a fully three dimensional problem. Also, the problem geometry is displayed in the PGT transformed domain, so that the spatial locations $\mathbf{x}$ and $\mathbf{y}$, in ordinary cartesian coordinates, have been transformed to $\boldsymbol{\eta}$ and $\boldsymbol{\xi}$. The scatterer shown is divided into two surfaces $\widetilde{S}^+$ and $\widetilde{S}^-$ that are separated by a small distance δ. Each subsurface has a well defined unit surface normal $\tilde{\mathbf{n}}^+$ and $\tilde{\mathbf{n}}^-$. In the limit as $\delta \to 0$, both surfaces collapse onto the median surface S and the points $\boldsymbol{\xi}^+$ and $\boldsymbol{\xi}^-$ collapse to the point $\boldsymbol{\xi}$. The external fluid domain $\widetilde{V}$, is punctured by two hemi-spherical half balls of radius ϵ, which are centered on the points $\boldsymbol{\xi}^+$ and $\boldsymbol{\xi}^-$ such that both points are always excluded from the fluid domain. Each of these half balls encloses a small surface area $\widetilde{S}_\epsilon^-$ and $\widetilde{S}_\epsilon^+$ on the upper and lower surfaces of the structure. Recalling that the transformed

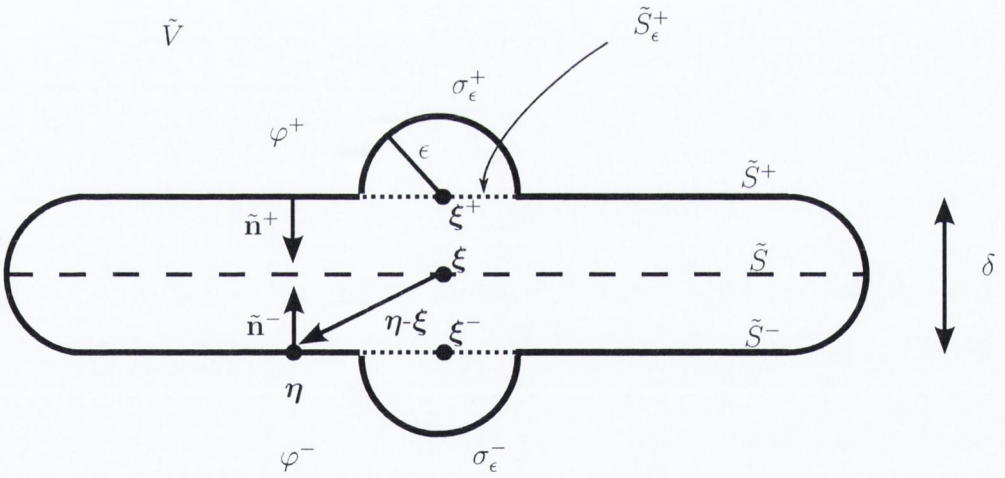


Figure 3.6: Schematic diagram for thin structure BEM formulation, showing a 2-D slice through the thin structure.

potential in the PGT deformed domain satisfies the ordinary Helmholtz equation (from Eq. 3.23), the well known Helmholtz integral equation may be derived for a point $\boldsymbol{\xi}$ on the surface $\widetilde{S}$. Defining the free space Green's function as the distribution satisfying the inhomogeneous Helmholtz equation,

$$\frac{\partial^2 G(\boldsymbol{\eta};\boldsymbol{\xi})}{\partial \eta_i \partial \eta_i} + \tilde{k}^2 G(\boldsymbol{\eta};\boldsymbol{\xi}) = -\delta(\boldsymbol{\eta} - \boldsymbol{\xi}) \tag{3.77}$$

Multiplying Eq. 3.34 with G and subtracting the product of φ with Eq. 3.77 and inte-

grating the results over the entire external fluid volume, a volume integral is obtained that may be converted to a surface integral via Green's identity so that

$$\int_{\widetilde{V}} \left(\frac{\partial^2 G(\boldsymbol{\eta};\boldsymbol{\xi})}{\partial \eta_i \partial \eta_i} \varphi(\boldsymbol{\eta}) - G(\boldsymbol{\eta};\boldsymbol{\xi}) \frac{\partial^2 \varphi(\boldsymbol{\eta})}{\partial \eta_i \partial \eta_i} \right) \mathrm{d}\widetilde{V} = - \int_{\widetilde{V}} G\tilde{\mathcal{F}} \, \mathrm{d}\widetilde{V} \tag{3.78}$$

becomes

$$\begin{aligned} &\int_{(\widetilde{S}^+ - \widetilde{S}_\epsilon^+ + \sigma_\epsilon^+)} \left(\frac{\partial G(\boldsymbol{\eta};\boldsymbol{\xi})}{\partial \tilde{n}_{\boldsymbol{\eta}}^+} \varphi(\boldsymbol{\eta}) - G(\boldsymbol{\eta};\boldsymbol{\xi}) \frac{\partial \varphi(\boldsymbol{\eta})}{\partial n_{\boldsymbol{\eta}}^+} \right) \mathrm{d}\widetilde{S}^+(\boldsymbol{\eta}) \\ &+ \int_{(\widetilde{S}^- - \widetilde{S}_\epsilon^- + \sigma_\epsilon^-)} \left(\frac{\partial G(\boldsymbol{\eta};\boldsymbol{\xi})}{\partial \tilde{n}_{\boldsymbol{\eta}}^-} \varphi(\boldsymbol{\eta}) - G(\boldsymbol{\eta};\boldsymbol{\xi}) \frac{\partial \varphi(\boldsymbol{\eta})}{\partial n_{\boldsymbol{\eta}}^-} \right) \mathrm{d}\widetilde{S}^-(\boldsymbol{\eta}) + \int_{\widetilde{V}} G\tilde{\mathcal{F}} \, \mathrm{d}\widetilde{V} = 0 \end{aligned} \tag{3.79}$$

The vanishing contribution from the surface integral at infinity has been discarded.

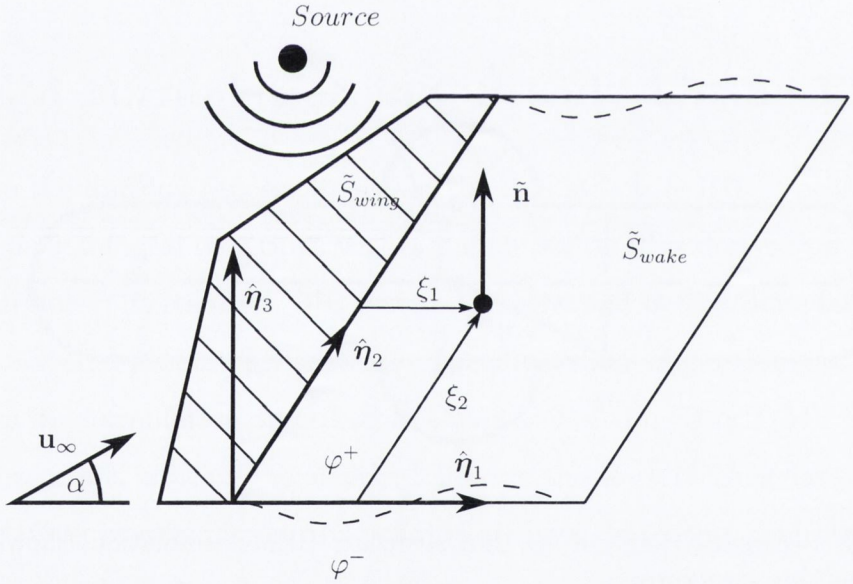


Figure 3.7: Schematic diagram of BEM formulation for a planar wing and wake. The wing surface $\tilde{S}_{wing}$ and the wake surface $\tilde{S}_{wake}$ are co-planar and have zero thickness.

It follows from (3.79), that a Boundary Integral Equation (BIE) may be derived at the point $\boldsymbol{\xi}$ on the median surface $\widetilde{S}$, but not lying on its boundary line, by taking the limit as $\delta \to 0$ followed by the limit as $\epsilon \to 0$. A schematic diagram of such a zero thickness surface is shown in Fig. 3.7. In the diagram, the general surface $\tilde{S}$ is shown as a union of two subsurfaces $\tilde{S}_{wing}$ and $\tilde{S}_{wake}$, both of which are included as part of the scattering surface. Two linearly independent BIEs will be derived below

that are valid for both the wing and the wake regions. The only difference between the two regions is the boundary condition that is applied to each subsurface. In the case of the wing, a sound hard boundary is applied. While for the wake region, a sound transparent boundary condition must be enforced. It should be noted that the assumption of a planar wake is an approximation of the true wake location, which is in general unknown and should be calculated as part of the mean flow solution. The planar wake assumption is consistent with lifting line theory for potential flow over finite wings, which is valid for high aspect ratio wings when the angle of attack, α is small and the flow mean flow in incompressible (see Katz and Plotkin [83]).

Making the following substitutions on the surface $(\widetilde{S} - \widetilde{S}_\epsilon)$,

$$\tilde{\mathbf{n}} = \tilde{\mathbf{n}}^- = -\tilde{\mathbf{n}}^+ \tag{3.80}$$

$$\begin{aligned} \Sigma\varphi &= \varphi^+ + \varphi^- & \delta\varphi &= \varphi^+ - \varphi^- \\ \frac{\partial \Sigma\varphi}{\partial \tilde{n}} &= \frac{\partial \varphi^-}{\partial \tilde{n}^-} - \frac{\partial \varphi^+}{\partial \tilde{n}^+} & \frac{\partial \delta\varphi}{\partial \tilde{n}} &= -\left(\frac{\partial \varphi^-}{\partial \tilde{n}^-} + \frac{\partial \varphi^+}{\partial \tilde{n}^+}\right) \end{aligned} \tag{3.81}$$

the following limit to the boundary is obtained,

$$\begin{aligned} \lim_{\epsilon \to 0} \Bigg[& \int_{(\widetilde{S} - \widetilde{S}_\epsilon)} \left(G(\boldsymbol{\eta}; \boldsymbol{\xi}) \frac{\partial \delta\varphi(\boldsymbol{\eta})}{\partial \tilde{n}_{\boldsymbol{\eta}}} - \frac{\partial G(\boldsymbol{\eta}; \boldsymbol{\xi})}{\partial n_{\boldsymbol{\eta}}} \delta\varphi(\boldsymbol{\eta}) \right) \mathrm{d}\widetilde{S}(\boldsymbol{\eta}) \\ & + \int_{\sigma_\epsilon^+} \left(\frac{\partial G(\boldsymbol{\eta}; \boldsymbol{\xi})}{\partial \tilde{n}_{\boldsymbol{\eta}}^+} \varphi(\boldsymbol{\eta}) - G(\boldsymbol{\eta}; \boldsymbol{\xi}) \frac{\partial \varphi(\boldsymbol{\eta})}{\partial n_{\boldsymbol{\eta}}^+} \right) \mathrm{d}\widetilde{S}^+(\boldsymbol{\eta}) \\ & + \int_{\sigma_\epsilon^-} \left(\frac{\partial G(\boldsymbol{\eta}; \boldsymbol{\xi})}{\partial \tilde{n}_{\boldsymbol{\eta}}^-} \varphi(\boldsymbol{\eta}) - G(\boldsymbol{\eta}; \boldsymbol{\xi}) \frac{\partial \varphi(\boldsymbol{\eta})}{\partial n_{\boldsymbol{\eta}}^-} \right) \mathrm{d}\widetilde{S}^-(\boldsymbol{\eta}) \Bigg] \\ & + \int_{\widetilde{V}} G\tilde{\mathcal{F}} \, \mathrm{d}\widetilde{V} = 0 \end{aligned} \tag{3.82}$$

Since all the integrals in Eq. 3.82 are regular, the derivative with respect to any coordinate at the point $\boldsymbol{\xi}$ may be taken. Hence, a second linearly independent equation may be obtained by taking the surface normal derivative of Eq. 3.82 with respect to

$\boldsymbol{\xi}$, yielding

$$\begin{aligned}\lim_{\epsilon\to 0}\Bigg[&\int_{(\widetilde{S}-\widetilde{S}_\epsilon)}\left(\frac{G(\boldsymbol{\eta};\boldsymbol{\xi})}{\partial\tilde{n}_{\boldsymbol{\xi}}}\frac{\partial\delta\varphi(\boldsymbol{\eta})}{\partial\tilde{n}_{\boldsymbol{\eta}}}-\frac{\partial^2 G(\boldsymbol{\eta};\boldsymbol{\xi})}{\partial\tilde{n}_{\boldsymbol{\xi}}\partial n_{\boldsymbol{\eta}}}\delta\varphi(\boldsymbol{\eta})\right)\,\mathrm{d}\widetilde{S}(\boldsymbol{\eta})\\&+\int_{\sigma_\epsilon^+}\left(\frac{\partial^2 G(\boldsymbol{\eta};\boldsymbol{\xi})}{\partial\tilde{n}_{\boldsymbol{\xi}}\partial\tilde{n}^+_{\boldsymbol{\eta}}}\varphi(\boldsymbol{\eta})-\frac{G(\boldsymbol{\eta};\boldsymbol{\xi})}{\partial\tilde{n}_{\boldsymbol{\xi}}}\frac{\partial\varphi(\boldsymbol{\eta})}{\partial\tilde{n}^+_{\boldsymbol{\eta}}}\right)\,\mathrm{d}\widetilde{S}^+(\boldsymbol{\eta})\\&+\int_{\sigma_\epsilon^-}\left(\frac{\partial^2 G(\boldsymbol{\eta};\boldsymbol{\xi})}{\partial\tilde{n}_{\boldsymbol{\xi}}\partial\tilde{n}^-_{\boldsymbol{\eta}}}\varphi(\boldsymbol{\eta})-\frac{G(\boldsymbol{\eta};\boldsymbol{\xi})}{\partial\tilde{n}_{\boldsymbol{\xi}}}\frac{\partial\varphi(\boldsymbol{\eta})}{\partial\tilde{n}^-_{\boldsymbol{\eta}}}\right)\,\mathrm{d}\widetilde{S}^-(\boldsymbol{\eta})\Bigg]\\&+\int_{\widetilde{V}}\frac{\partial G}{\partial\tilde{n}_{\boldsymbol{\xi}}}\tilde{\mathcal{F}}\,\mathrm{d}\widetilde{V}=0\end{aligned}\tag{3.83}$$

As discussed in [35], the correct procedure in deriving the hypersingular BIE is to take the surface normal derivative *before* the limit to the boundary is performed. Each of the integrals in Eq. 3.83 must then be expanded in powers of ϵ. The limiting process then produces a diverging component from the ϵ the half ball integrals that exactly cancels with a term of opposite sign in the surface integral over $\widetilde{S}-\widetilde{S}_\epsilon$. The remaining finite terms from the half ball integration are the usual free terms that depend on the local surface geometry in the vicinity of $\boldsymbol{\xi}$. If it is assumed that the surface $\widetilde{S}$ is flat in the vicinity of $\boldsymbol{\xi}$, the BIEs may be expressed as

$$\tfrac{1}{2}\Sigma\varphi(\boldsymbol{\xi})+\int_{\widetilde{S}}\left(G\,\frac{\partial\delta\varphi}{\partial\tilde{n}_{\boldsymbol{\eta}}}-\frac{\partial G}{\partial\tilde{n}_{\boldsymbol{\eta}}}\,\delta\varphi\right)\,\mathrm{d}\widetilde{S}=-\int_{\widetilde{V}}G\tilde{\mathcal{F}}\,\mathrm{d}\widetilde{V}\tag{3.84}$$

and

$$\begin{aligned}\frac{1}{2}\frac{\partial\Sigma\varphi(\boldsymbol{\xi})}{\partial\tilde{n}_{\boldsymbol{\xi}}}+\lim_{\epsilon\to 0}\Bigg[&\frac{\delta\varphi}{2\epsilon}+\int_{(\widetilde{S}-\widetilde{S}_\epsilon)}\left(\frac{\partial G}{\partial\tilde{n}_{\boldsymbol{\xi}}}\,\frac{\partial\delta\varphi}{\partial\tilde{n}_{\boldsymbol{\eta}}}-\frac{\partial^2 G}{\partial\tilde{n}_{\boldsymbol{\xi}}\partial n_{\boldsymbol{\eta}}}\,\delta\varphi\right)\,\mathrm{d}\widetilde{S}\Bigg]\\&=-\int_{\widetilde{V}}\frac{\partial G}{\partial\tilde{n}_{\boldsymbol{\xi}}}\tilde{\mathcal{F}}\,\mathrm{d}\widetilde{V}\end{aligned}\tag{3.85}$$

The details of the half ball integration may be found in Appendix. A. Equations (3.84)-(3.85) are two linearly independent boundary integral equations in four unknowns, for a perfectly thin structure. Two independent boundary conditions are required to close the system. This topic is discussed below in Section. 3.4.2

3.4.1 Planar Surface BEM Discretization

The system of BIEs Eq. 3.84 and Eq. 3.85 may be solved by the Boundary Element Method by splitting the surface $\widetilde{S}$ into discrete elements and expanding the surface potential within each element in terms of prescribed basis functions. The nodal values of the surface potential may then be obtained by solving a linear matrix equation in which the matrix coefficients are computed by numerical integration.

Consider the rectangular tiling of a planar surface shown in Fig. 3.8. Since the

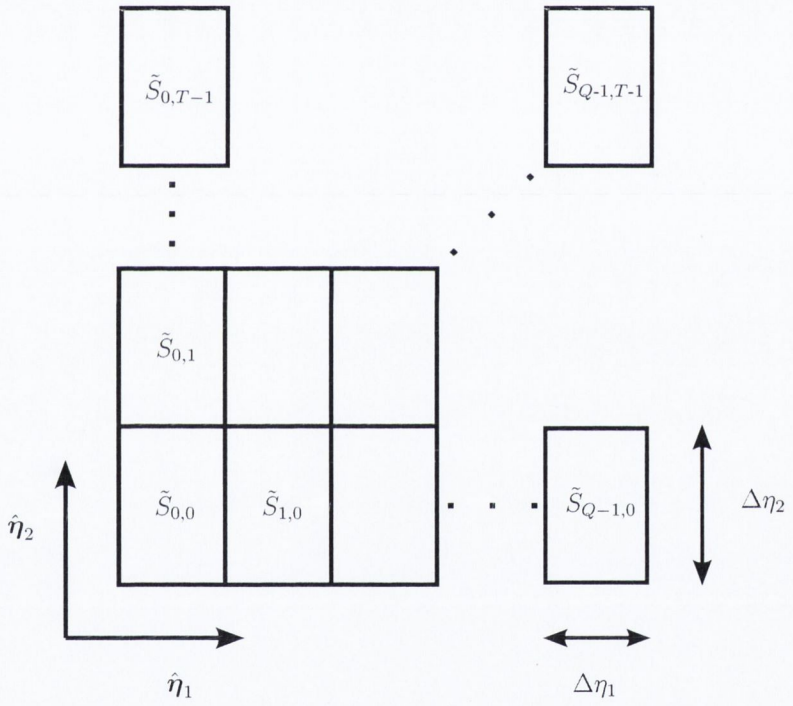


Figure 3.8: Rectangular tiled discretization of a planar surface

unit normal $\tilde{\mathbf{n}}$ is constant everywhere on a planar surface, the integral kernel $\frac{\partial G}{\partial \tilde{n}}$ is uniformly zero when both $\boldsymbol{\xi}$ and $\boldsymbol{\eta}$ are located on $\widetilde{S}$. Prescribing constant values of the unknown distributions

$$\begin{aligned} \delta\varphi &= \delta\varphi_{q,t}, & \Sigma\varphi &= \Sigma\varphi_{q,t} \\ \frac{\partial\delta\varphi}{\partial\tilde{n}} &= \delta f_{q,t}, & \frac{\partial\Sigma\varphi}{\partial\tilde{n}} &= \Sigma f_{q,t} \end{aligned} \qquad \text{on element } \widetilde{S}_{q,t} \tag{3.86}$$

on each element, then the BEM discretization of Eq. 3.84 and Eq. 3.85 can be written

as

$$\tfrac{1}{2}\Sigma\varphi_{a,b} + \sum_{q=0}^{Q-1}\sum_{t=0}^{T-1} G_{q,t;a,b}\ \delta f_{q,t} = \varphi^i_{a,b} \tag{3.87}$$

and

$$\tfrac{1}{2}\Sigma f_{a,b} - \sum_{q=0}^{Q-1}\sum_{t=0}^{T-1} H_{q,t;a,b}\ \delta\varphi_{q,t} = f^i_{a,b} \tag{3.88}$$

where the singular point is located at the centroid of element $\widetilde{S}_{a,b}$ so that

$$\boldsymbol{\xi} = \boldsymbol{\xi}_{a,b} = (a+\tfrac{1}{2})\Delta\eta_1\ \hat{\boldsymbol{\eta}}_1 + (b+\tfrac{1}{2})\Delta\eta_2\ \hat{\boldsymbol{\eta}}_2 \tag{3.89}$$

and the coefficients $G_{q,t;a,b}$, $\varphi^i_{a,b}$ and $f^i_{a,b}$ are given by

$$G_{q,t;a,b} = \int_{\widetilde{S}_{q,t}} G(\boldsymbol{\eta};\boldsymbol{\xi}_{a,b})\ \mathrm{d}\widetilde{S} \tag{3.90}$$

$$\varphi^i_{a,b} = -\int_{\widetilde{V}} G(\boldsymbol{\eta};\boldsymbol{\xi}_{a,b})\ \tilde{\mathcal{F}}\ \mathrm{d}\widetilde{V} \tag{3.91}$$

$$f^i_{a,b} = -\int_{\widetilde{V}} \frac{\partial G(\boldsymbol{\eta};\boldsymbol{\xi}_{a,b})}{\partial\tilde{n}}\ \tilde{\mathcal{F}}\ \mathrm{d}\widetilde{V} \tag{3.92}$$

The coefficients $H_{q,t;a,b}$, are given by

$$H_{a,b;a,b} = \lim_{\epsilon\to 0}\left[-\frac{1}{2\epsilon} + \int_{(\widetilde{S}_{a,b}-\widetilde{S}_\epsilon)} \frac{\partial^2 G(\boldsymbol{\eta};\boldsymbol{\xi}_{a,b})}{\partial\tilde{n}^2}\ \mathrm{d}\widetilde{S}\right] \tag{3.93}$$

when the collocation point is located within the element and

$$H_{q,t;a,b} = \int_{\widetilde{S}_{q,t}} \frac{\partial^2 G(\boldsymbol{\eta};\boldsymbol{\xi}_{a,b})}{\partial\tilde{n}^2}\ \mathrm{d}\widetilde{S} \tag{3.94}$$

when the collocation point is not contained within $\widetilde{S}_{q,t}$.

3.4.2 Boundary Conditions

Collocating at each element centroid yields two equations per element that interrelate the four degrees of freedom per element over the entire scatterer surface. Therefore,

two boundary conditions are required to close the system. For a scattering structure composed partially of a sound hard body (the wing), with the remaining portion made up of an acoustically transparent surface (the wake), the interface conditions will vary from element to element.

3.4.2.1 Sound Hard BC

On the sound hard portion of the scatterer, the condition given by Eq. 3.42 is applied. At low angles of attack, the free stream flow may be assumed approximately parallel to the wing surface, so that the the normal derivative of the transformed potential is zero on both sides of the wing, giving

$$\Sigma f_{a,b} = \delta f_{a,b} = 0 \tag{3.95}$$

everywhere on the wing surface. Hence, the hard wall boundary condition can be implemented simply by substituting Eq. 3.95 directly into the integral equations.

3.4.2.2 Wake Interface BC

In the proposed Born approximation for acoustic scattering, with a discrete vortex filament model of the wake, the zeroth order acoustic solution is computed without a vortex scattering forcing term. However, the refraction effect of the vorticity is still present through the interaction of sound with the potential velocity field induced by the vortex filaments. In the PGT transformation approach, the $O(M)$ terms describing the interaction between the nonuniform velocity field and the acoustic field are approximated through the nonuniform phase factor in the change of variables (Eq. 3.24). This phase factor may be discontinuous across the wake as a consequence of allowing the mean flow to develop lift, leading to a discontinuity in the phase of the acoustic solution, which is unacceptable physically. To correct for this behavior, the continuity of the physical potential and the acoustic particle velocity must be enforced explicitly at the collocation points on the wake surface. In typical implementations of potential flow solvers, the steady wake is relaxed to a zero normal flux condition so that the local streamlines are parallel to the vortex filaments. For the planar wing and wake

arrangement, this condition can only be approximately satisfied for small angles of attack for which the small flux through the wake may be neglected in the formulation.

Two different wake boundary conditions will be considered for the zeroth order solution of the Born series, the first of which is the interface condition specifying a fully continuous acoustic field. A second type of boundary condition is also considered, for which the wake may support a discontinuity due to a time-harmonic vorticity wave, shed from the trailing edge. The magnitude of the vorticity wave is determined by satisfying a form of the Kutta condition for acoustics and, once shed from the trailing edge, the vorticity wave is modeled as "frozen" vorticity that convects passively through the mean flow field. In physical terms, the jump in the acoustic potential on the wake satisfies the surface advection equation on the wake,

$$j\omega\delta\phi + \tfrac{1}{2}\Sigma\mathbf{u}_0 \cdot \nabla\delta\phi = 0 \tag{3.96}$$

where $\frac{1}{2}\Sigma\mathbf{u}_0 = \frac{1}{2}(\mathbf{u}_0^+ + \mathbf{u}_0^-)$ is the mean convection velocity on the wake surface. Eq. 3.96 can be integrated in the direction of $\Sigma\mathbf{u}_0$ to give

$$\delta\phi = \delta\phi^v \exp(-j\nu) \tag{3.97}$$

where $\delta\phi^v$ is the initial value of the vortex wave shed from the trailing edge and ν is the convection time for a vortex wave traveling from the trailing edge to a point on the wake. For a planar wing and wake, the sum in the steady velocity above and below the wake $\Sigma\mathbf{u}_0 = 2\mathbf{u}_\infty$ is a constant, which implies that ν is given by

$$\nu = \frac{k}{M_\infty}(x_1 - x_1^{TE}) \tag{3.98}$$

where $(x_1 - x_1^{TE})$ is the signed distance from the trailing edge to a point on the wake.

The Kutta condition is an empirical principle that is well established in steady aerodynamics and has been used extensively to calculate the lift coefficients of airfoils and wings by inviscid flow solvers. It is based on the observation that the effect of viscosity in the boundary layer near a sharp trailing edge can be replicated in a purely inviscid calculation by specifying that the inviscid velocity field remains bounded at

the trailing edge. Unfortunately, the range of flow condition for which the unsteady Kutta condition has been validated by experiment is much more limited than the steady flow case [85]. Although the validity of the Kutta condition for acoustics may be somewhat questionable, the sensitivity of the acoustic solution to the trailing edge flow condition can still be explored within the PGT scheme and some conclusions relating to when it may be necessary to consider vortex wave shedding may be drawn from parametric testing.

Morino and Bernardini [86] investigated the theoretical and numerical requirements that are sufficient to satisfy the Kutta condition in the steady flow case. They found that some of the continuity conditions that are theoretically imposed by the Kutta condition are not necessarily required in a numerical simulation by a potential flow solver. Specifically, the continuity requirement of the potential jump at the wing-wake junction and the local tangency of the wake were found to be necessary conditions for a unique solution while the continuity the surface derivatives of the potential at the wing-wake junction were found to be automatically satisfied whether explicitly enforced or otherwise. They argued that the solution by constant potential elements will still converge to the Kutta condition solution even though the surface derivatives of potential are discontinuous at the trailing edge. It will be shown in a later chapter, by comparison with an analytic solution, that the same result with constant potential elements is observed for the acoustic case.

For the planar wing and wake, the Kutta condition can be expressed simply by the relationship

$$\delta\phi^{v}(\eta_2) = \delta\phi^{TE}(\eta_2) \tag{3.99}$$

where the function $\delta\phi^{TE}(\eta_2)$ is the jump in potential across the wing at the cusped trailing edge. If the mean potential jump is assumed constant within each boundary element and the flux through the wake is neglected, the following relationships follow directly from the transformation of variables Eq. 3.24

$$\begin{bmatrix} \Sigma\varphi \\ \delta\varphi \end{bmatrix} = e^{-j\frac{1}{2}\Sigma\tau} \begin{bmatrix} \cos(\frac{1}{2}\delta\tau) & -j\sin(\frac{1}{2}\delta\tau) \\ -j\sin(\frac{1}{2}\delta\tau) & \cos(\frac{1}{2}\delta\tau) \end{bmatrix} \begin{bmatrix} \Sigma\phi \\ \delta\phi \end{bmatrix} \tag{3.100}$$

$$\begin{bmatrix} \frac{\partial \Sigma\varphi}{\partial \tilde{n}} \\ \frac{\partial \delta\varphi}{\partial \tilde{n}} \end{bmatrix} = e^{-j\frac{1}{2}\Sigma\tau} \begin{bmatrix} \cos(\frac{1}{2}\delta\tau) & -j\sin(\frac{1}{2}\delta\tau) \\ -j\sin(\frac{1}{2}\delta\tau) & \cos(\frac{1}{2}\delta\tau) \end{bmatrix} \begin{bmatrix} \frac{\partial \Sigma\phi}{\partial \tilde{n}} \\ \frac{\partial \delta\phi}{\partial \tilde{n}}. \end{bmatrix} \tag{3.101}$$

These relations allow the continuity of the acoustic variables in the physical domain to be expressed in terms of the transformed quantities and substituted directly into the BEM formulation. This leads to a modified BEM formulation on the wake for which the solution is sought in terms of the the auxiliary surface quantities

$$\delta\varphi^* = e^{-j\frac{1}{2}\Sigma\tau}\ \delta\phi \qquad \Sigma\varphi^* = e^{-j\frac{1}{2}\Sigma\tau}\ \Sigma\phi \tag{3.102}$$

$$\delta f^* = e^{-j\frac{1}{2}\Sigma\tau}\ \frac{\partial \delta\phi}{\partial \tilde{n}} \qquad \Sigma f^* = e^{-j\frac{1}{2}\Sigma\tau}\ \frac{\partial \Sigma\phi}{\partial \tilde{n}} \tag{3.103}$$

On the wing surface, the standard formulation in terms of φ is maintained.

3.4.3 BEM Equations

If the mean flow potential jump is assumed constant in each acoustic element, the direct substitution of Eq. 3.100 and Eq. 3.101 into the BEM formulation Eq. 3.87 and Eq. 3.88 with $\delta\phi^v = 0$ (ie. the no Kutta solution) gives

$$-\sum_{q=0}^{Q_{wing}-1}\sum_{t=0}^{T-1} H_{q,t;a,b}\ \delta\varphi_{q,t} + j\sum_{q=Q_{wing}}^{Q_{wake}-1}\sum_{t=0}^{T-1} H_{q,t;a,b}\ \sin(\tfrac{1}{2}\delta\tau_{q,t})\ \Sigma\varphi^*_{q,t} = f^i_{a,b} \tag{3.104}$$

when the singular point is on a wing element and

$$\begin{aligned} \tfrac{1}{2}\Sigma f^*_{a,b}\cos(\tfrac{1}{2}\delta\tau_{a,b}) - &\sum_{q=0}^{Q_{wing}-1}\sum_{t=0}^{T-1} H_{q,t;a,b}\ \delta\varphi_{q,t} \\ &+ j\sum_{q=Q_{wing}}^{Q_{wake}-1}\sum_{t=0}^{T-1} H_{q,t;a,b}\ \sin(\tfrac{1}{2}\delta\tau_{q,t})\ \Sigma\varphi^*_{q,t} = f^i_{a,b} \end{aligned} \tag{3.105}$$

and

$$\tfrac{1}{2}\Sigma\varphi^*_{a,b}\cos(\tfrac{1}{2}\delta\tau_{a,b}) - j\sum_{q=Q_{wing}}^{Q_{wake}-1}\sum_{t=0}^{T-1} G_{q,t;a,b}\ \sin(\tfrac{1}{2}\delta\tau_{q,t})\ \Sigma f^*_{q,t} = \varphi^i_{a,b} \tag{3.106}$$

when the singular point is on the wake. From the above equations, it is apparent that only a minor modification of the ordinary BEM formulation is required to capture the flow refraction effects. The main modification is the introduction of the trigonometric factors multiplying the auxiliary variables.

For non zero $\delta\phi^v$, the formulation is slightly more complicated and requires the introduction of plane wave basis functions if the solution on the wake is to be adequately resolved by the acoustic mesh. If the surface distribution of $\delta\varphi^*$ and Σf^* is assumed to vary locally within each element as

$$\delta\varphi^*(\boldsymbol{\eta}) = \delta\varphi^*_{q,t} \ \exp\left(-j\tilde{k}_v \left\{\eta_1 - (q+\tfrac{1}{2})\Delta\eta_1\right\}\right) \tag{3.107}$$

$$\Sigma f^*(\boldsymbol{\eta}) = \Sigma f^*_{q,t} \ \exp\left(-j\tilde{k}_v \left\{\eta_1 - (q+\tfrac{1}{2})\Delta\eta_1\right\}\right) \tag{3.108}$$

then modified influence coefficients $\overline{G}_{q,t;a,b}$ may be defined by

$$\overline{G}_{q,t;a,b} = \int_{\widetilde{S}_{q,t}} G(\boldsymbol{\eta};\boldsymbol{\xi}_{a,b}) \ \exp\left(-j\tilde{k}_v \left\{\eta_1 - (q+\tfrac{1}{2})\Delta\eta_1\right\}\right) \ \mathrm{d}\widetilde{S} \tag{3.109}$$

and the coefficients $\overline{H}_{q,t;a,b}$, by

$$\overline{H}_{a,b;a,b} = \lim_{\epsilon\to 0}\left[-\frac{1}{2\epsilon} + \int_{(\widetilde{S}_{a,b}-\widetilde{S}_\epsilon)} \frac{\partial^2 G(\boldsymbol{\eta};\boldsymbol{\xi}_{a,b})}{\partial\tilde{n}^2} \ \exp\left(-j\tilde{k}_v \left\{\eta_1 - (q+\tfrac{1}{2})\Delta\eta_1\right\}\right) \ \mathrm{d}\widetilde{S}\right] \tag{3.110}$$

when the collocation point is located within the element and

$$\overline{H}_{q,t;a,b} = \int_{\widetilde{S}_{q,t}} \frac{\partial^2 G(\boldsymbol{\eta};\boldsymbol{\xi}_{a,b})}{\partial\tilde{n}^2} \exp\left(-j\tilde{k}_v \left\{\eta_1 - (q+\tfrac{1}{2})\Delta\eta_1\right\}\right) \ \mathrm{d}\widetilde{S} \tag{3.111}$$

when the collocation point is not contained within $\widetilde{S}_{q,t}$. It should be noted that without the plane wave elements, the resolution requirements for the acoustic potential jump on the wake would be limited by the need to resolve the vortex wave which can be prohibitively costly for low mach numbers. The details of the numerical integration are outlined in Appendix. A.

The BEM formulation for vortex shedding solution may be expressed in terms of

the modified coefficients as

$$-\sum_{q=0}^{Q_{wing}-1}\sum_{t=0}^{T-1} H_{q,t;a,b}\ \delta\varphi_{q,t} + j\sum_{q=Q_{wing}}^{Q_{wake}-1}\sum_{t=0}^{T-1} H_{q,t;a,b}\ \sin(\tfrac{1}{2}\delta\tau_{q,t})\ \Sigma\varphi^*_{q,t}$$
$$-\sum_{q=Q_{wing}}^{Q_{wake}-1}\sum_{t=0}^{T-1} \overline{H}_{q,t;a,b}\ \delta\phi^v_t \cos(\tfrac{1}{2}\delta\tau_{q,t})\ \exp\left(-j\tilde{k}_v\left\{(q+\tfrac{1}{2})\Delta\eta_1 - \eta_1^{TE}\right\}\right) = f^i_{a,b} \quad (3.112)$$

on the wing and

$$\tfrac{1}{2}\Sigma f^*_{a,b}\cos(\tfrac{1}{2}\delta\tau_{a,b}) - \sum_{q=0}^{Q_{wing}}\sum_{t=0}^{T-1} H_{q,t;a,b}\ \delta\varphi_{q,t} + j\sum_{q=Q_{wing}}^{Q_{wake}-1}\sum_{t=0}^{T-1} H_{q,t;a,b}\ \sin(\tfrac{1}{2}\delta\tau_{q,t})\ \Sigma\varphi^*_{q,t}$$
$$-\sum_{q=Q_{wing}}^{Q_{wake}-1}\sum_{t=0}^{T-1} \overline{H}_{q,t;a,b}\ \delta\phi^v_t \cos(\tfrac{1}{2}\delta\tau_{q,t})\ \exp\left(-j\tilde{k}_v\left\{(q+\tfrac{1}{2})\Delta\eta_1 - \eta_1^{TE}\right\}\right) = f^i_{a,b} \quad (3.113)$$

and

$$\tfrac{1}{2}\left(\Sigma\varphi^*_{a,b}\cos(\tfrac{1}{2}\delta\tau_{a,b}) - j\delta\phi^v_b\ \sin(\tfrac{1}{2}\delta\tau_{a,b})e^{-j\tilde{k}_v\left\{(a+\frac{1}{2})\Delta\eta_1-\eta_1^{TE}\right\}}\right)$$
$$-j\sum_{q=Q_{wing}}^{Q_{wake}-1}\sum_{t=0}^{T-1}\overline{G}_{q,t;a,b}\ \sin(\tfrac{1}{2}\delta\tau_{q,t})\ \Sigma f^*_{q,t} = \varphi^i_{a,b} \quad (3.114)$$

on the wake. Since $\Sigma\mathbf{u}_0$ is a constant for the current configuration, the vortex wavenumber for the transformed problem $\tilde{k}_v$, is also constant and is given by

$$\tilde{k}_v = \frac{\tilde{k}}{M_\infty} \quad (3.115)$$

The system of equations(3.112-3.114), as it stands, is not completely closed. The Kutta condition has not yet been applied to the trailing edge function $\delta\phi^v$ and to do this within the BEM formulation, the function $\delta\phi^{TE}$ must be computed on the wing trailing edge via Equations(3.100). Augmenting the system with the additional set of trailing edge equations,

$$\tfrac{1}{2}\Sigma\varphi^{TE}_{a,b} - j\sum_{q=Q_{wing}}^{Q_{wake}-1}\sum_{t=0}^{T-1}\overline{G}_{q,t;a,b}\ \sin(\tfrac{1}{2}\delta\tau_{q,t})\ \Sigma f^*_{q,t} = \varphi^i_{a,b} \quad (3.116)$$

provides the additional terms $\Sigma\varphi^{TE}$ needed to compute $\delta\phi^v$ and close the system.

3.4.4 Vortex Scattering Correction

In this section the first order Born approximation for the vortex scattering term is incorporated into the BEM scheme. So far it has been assumed that the mean flow potential jump is constant on each acoustic element. For consistency with this approximation, the vortex filaments must be located along the boundaries of the acoustic elements. For the planar configuration, this implies that the vortex filaments are always located in the $\eta_1\eta_2$ plane with the vorticity vector pointing along $\hat{\boldsymbol{\eta}}_1$ (or $-\hat{\boldsymbol{\eta}}_1$). Recall that the Howe source term for an individual vortex filament is given by

$$-\frac{j}{\omega}\nabla\cdot(\boldsymbol{\gamma}\times\nabla B^0) = -\frac{j}{\omega}\Gamma\left(\frac{\partial B^0}{\partial x_2}\delta(x_2)\delta'(x_3) - \frac{\partial B^0}{\partial x_3}\delta'(x_2)\delta(x_3)\right) \tag{3.117}$$

and that the stagnation enthalpy B can always be expressed in terms of the acoustic potential in irrotational regions by $B = -j\omega\phi$ so that the source term for an equivalent formulation in terms of acoustic potential can be written as

$$\mathcal{F} = -\frac{j}{\omega}\Gamma\left(\frac{\partial \phi^0}{\partial x_2}\delta(x_2)\delta'(x_3) - \frac{\partial \phi^0}{\partial x_3}\delta'(x_2)\delta(x_3)\right) \tag{3.118}$$

A problem immediately arises when the PGT method is applied to Howe's vortex sound source. The PGT approach is formally valid for sources located in the irrotational regions of the flow. When the source resides inside the wake, the method breaks down because it is no longer possible to define a unique phase shift τ, at the source location. However, if the source is assumed to reside in a uniform flow, a phase shift is given simply by $\tau = \tilde{k}M_\infty\eta_1$. With this approximation the effects of vortex refraction on the sound scattered by the vortex core are neglected .

The PGT source term comprised of distributed discrete vortices on element bound-

aries is given by

$$\begin{aligned}\tilde{\mathcal{F}} = &-\frac{j}{\omega}H(\eta_1-\eta_1^{TE})\exp(-j\tilde{k}M_\infty\eta_1)\\ &\times\sum_{t=0}^{T}\Gamma_t\left(\frac{\partial\phi^0}{\partial\eta_2}\delta(\eta_2-t\Delta\eta_2)\delta'(\eta_3)-\frac{\partial\phi^0}{\partial\eta_3}\delta'(\eta_2-t\Delta\eta_2)\delta(\eta_3)\right)\end{aligned} \tag{3.119}$$

where

$$H(\eta_1)=\begin{cases}0 & \eta_1<0\\ \frac{1}{2} & \eta_1=0\\ 1 & \eta_1>0\end{cases} \tag{3.120}$$

is the Heaviside step function and η_1^{TE} is the η_1 coordinate of the trailing edge. The first order Born approximation is obtained by solving the scattering problem in the transformed domain with and incident field derived from the above source term. Convolving the source term with the free space Green's function $G(\boldsymbol{\eta};\boldsymbol{\xi})$, gives the incident field induced by the source

$$\begin{aligned}\varphi^i(\boldsymbol{\xi}) = \frac{j}{\omega}\int_{\widetilde{V}}\Bigg[&G(\boldsymbol{\eta};\boldsymbol{\xi})H(\eta_1-\eta_1^{TE})e^{-j(\tilde{k}M_\infty\eta_1)}\\ &\times\sum_{t=0}^{T}\Gamma_t\left(\frac{\partial\phi^0}{\partial\eta_2}\delta(\eta_2-t\Delta\eta_2)\delta'(\eta_3)-\frac{\partial\phi^0}{\partial\eta_3}\delta'(\eta_2-t\Delta\eta_2)\delta(\eta_3)\right)\Bigg]\,\mathrm{d}\widetilde{V}\end{aligned} \tag{3.121}$$

at the point $\boldsymbol{\xi}$, anywhere in the domain except on a vortex line. The above equation simplifies to

$$\varphi^i(\boldsymbol{\xi}) = \frac{j}{\omega}\sum_{t=0}^{T}\Gamma_t\int_{\eta_1^{TE}}^{L_w}\left(\frac{\partial G}{\partial\eta_3}\frac{\partial\Sigma\varphi^{*0}}{\partial\eta_2}\Big|_{\eta_2=t\Delta\eta_2}-\frac{\partial G}{\partial\eta_2}\frac{\partial\Sigma\varphi^{*0}}{\partial\eta_2}\Big|_{\eta_2=t\Delta\eta_2}\right)\mathrm{d}\eta_1 \tag{3.122}$$

when the wake is truncated to length L_w. Similarly, the normal velocity induced by the source is given by

$$f^i(\boldsymbol{\xi}) = \frac{j}{\omega}\sum_{t=0}^{T}\Gamma_t\int_{\eta_1^{TE}}^{L_w}\left(\frac{\partial^2 G}{\partial\tilde{n}\partial\eta_3}\frac{\partial\Sigma\varphi^{*0}}{\partial\eta_2}\Big|_{\eta_2=t\Delta\eta_2}-\frac{\partial^2 G}{\partial\tilde{n}\partial\eta_2}\frac{\partial\Sigma\varphi^{*0}}{\partial\eta_2}\Big|_{\eta_2=t\Delta\eta_2}\right)\mathrm{d}\eta_1 \tag{3.123}$$

For the discrete BEM problem with constant elements, the values of the potential

and normal derivative of the potential are only available at element centroids. The values of the derivatives on the edges of the elements, may be approximated by finite differences, for surface derivatives, and by linear interpolation for normal derivatives. The field induced by the vortex source may then be expressed as

$$\varphi^i(\boldsymbol{\xi}) = \frac{j}{\omega} \sum_{t=0}^{T} \Gamma_t \sum_{q=Q_{wing}}^{Q_{wake}-1} \left[D_{q,t} \left(\frac{\Sigma\varphi^{*0}_{q,t} - \Sigma\varphi^{*0}_{q,t-1}}{\Delta\eta_2} \right) - E_{q,t} \left(\frac{\Sigma f^{*0}_{q,t} + \Sigma f^{*0}_{q,t+1}}{2} \right) \right] \tag{3.124}$$

and the normal velocity induced by the source is given by

$$f^i(\boldsymbol{\xi}) = \frac{j}{\omega} \sum_{t=0}^{T} \Gamma_t \sum_{q=Q_{wing}}^{Q_{wake}-1} \left[I_{q,t} \left(\frac{\Sigma\varphi^{*0}_{q,t} - \Sigma\varphi^{*0}_{q,t-1}}{\Delta\eta_2} \right) - J_{q,t} \left(\frac{\Sigma f^{*0}_{q,t} + \Sigma f^{*0}_{q,t+1})}{2} \right) \right] \tag{3.125}$$

where the coefficients

$$D_{q,t} = \int_{q\Delta\eta_1}^{q+1\Delta\eta_1} \frac{\partial G(\boldsymbol{\eta};\boldsymbol{\xi})}{\partial\eta_3} \, \mathrm{d}\eta_1 \tag{3.126}$$

$$E_{q,t} = \int_{q\Delta\eta_1}^{q+1\Delta\eta_1} \frac{\partial G(\boldsymbol{\eta};\boldsymbol{\xi})}{\partial\eta_2} \, \mathrm{d}\eta_1 \tag{3.127}$$

$$I_{q,t} = \int_{q\Delta\eta_1}^{q+1\Delta\eta_1} \frac{\partial^2 G(\boldsymbol{\eta};\boldsymbol{\xi})}{\partial\tilde{n}\partial\eta_3} \, \mathrm{d}\eta_1 \tag{3.128}$$

$$J_{q,t} = \int_{q\Delta\eta_1}^{q+1\Delta\eta_1} \frac{\partial^2 G(\boldsymbol{\eta};\boldsymbol{\xi})}{\partial\tilde{n}\partial\eta_2} \, \mathrm{d}\eta_1 \tag{3.129}$$

may be computed by standard numerical quadrature rules. The above equations may be used to compute the vortex scattered sound field everywhere in the domain. Once the incident field has been computed on the surface of the scatterer, the PGT BEM formulation, with a uniform mean-flow field, may then be applied as normal to obtain the secondary scattered field. The full solution then contains three components (1) the zeroth order solution, (2) the vortex scattered field, (3) the interaction field of the vortex scattered field with the wing.

3.4.5 Artificial Truncation of the Wake

In order to minimize the scattering of sound by the artificial truncation of the wake, some care needs to be taken to smoothly taper the steady vorticity to zero over a

transition zone. Functions that are typically used to compute a partition of unity are useful for this task. In this work, the function

$$f_b(\eta_1) = \begin{cases} 1 & \eta_1' \leq 0 \\ \exp\left(\frac{2e^{-(1/\eta_1')}}{\eta_1'-1}\right) & 0 < \eta_1' < 1 \\ 0 & \eta_1' \geq 1 \end{cases} \tag{3.130}$$

where

$$\eta_1' = \frac{(\eta_1 - L_t)}{(L_w - L_t)} \tag{3.131}$$

is used to smoothly taper the vortex strength, and its derivatives, to zero over a transition region $L_t < \eta_1 < L_w$. The same treatment is applied to the vortex wave by replacing $\delta\phi_t^v$ with $f_b(q\Delta\eta_1)\delta\phi_t^v$ in the Kutta condition formulation. Similarly, Howe's vortex source term is tapered over the transition region to avoid edge scattering effects.

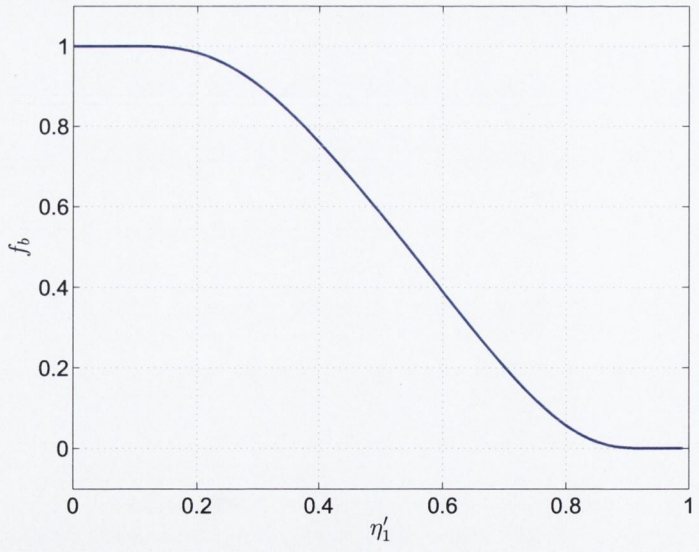


Figure 3.9: Blending function f_b over the transition region

3.4.6 Mean Flow BEM

The BEM methodology may also be applied to the solution of the mean flow problem. In the limit as $\tilde{k} \to 0$ the Helmholtz equation reduces to Laplace's equation. Given

a regular mesh of constant strength doublet elements on the thin wing surface, the BEM formulation for the Prandtl-Glauert transformed potential flow problem is given by Eq. 3.88 with $\tilde{k}$ set to zero. Since the wing is an impermeable surface, the boundary condition $\Sigma f_{a,b} = 0$ applies. The incident field is determined by the free stream flow conditions by

$$f^i = |\mathbf{u}_\infty| \sin(\alpha) \tag{3.132}$$

where α is the angle of attack of the thin wing. The treatment of the Kutta condition and the analytical integration of the Laplace kernels, over constant potential elements, is covered in detail in Katz and Plotkin [83].

3.5 Iterative Solution Strategies for Planar BEM Formulations

The most basic solution strategy for BEM problems is to arrange the unknown quantities into a single vector of length N, by assigning a unique number to each degree of freedom in the linear system, and to assemble a dense influence matrix from the coefficients G and H. A LU decomposition may then be used to solve for the unknowns with a right hand forcing vector assembled from φ^i and f^i. The complexity of the solution process is dominated by the LU decomposition stage, which has asymptotic complexity $O(N^3)$. Even with large scale computational resources, typical aircraft scattering problems rapidly become intractable as the frequency of excitation increases, typically well before the maximum source frequencies have been simulated.

The current state of the art solvers avoid the large asymptotic solution time of the LU decomposition by switching to iterative solution techniques and by accelerating the matrix vector multiplication steps with FMM type approximations. For certain problem types, such as the configuration considered in this work, the matrix multiplication can be accelerated by highly efficient structured matrix techniques that take advantage of the regular arrangement of the coefficients in the influence matrix. The $O(N \log N)$ complexity of the matrix multiplication step for structured matrix acceleration is equivalent to the current best performing FMM techniques, and

the performance characteristics of both approaches is directly comparable in terms of asymptotic growth of the solution time.

3.5.1 Fast Summation Algorithm

A closer examination of the coefficients $G_{q,t;a,b}$ and $H_{q,t;a,b}$ reveals that the values of these coefficients depend only on the quantities $a-q$ and $b-t$ when the surface is planar and regularly tiled. This implies that, of all the $(QT)^2$ entries in the influence matrix, only $(2Q-1)(2T-1)$ have unique values. The influence matrix storage requirement for the regularly tiled problem can therefore be reduced from $O(N^2)$ to $O(N)$. A further benefit of the structured grid can be gained by noting that the double summation operation in each of the BEM Equations.3.87-3.88 is actually a two-dimensional discrete convolution, which may be evaluated by fast algorithms based on the FFT. Two-dimensional fast convolution techniques are routinely applied in digital image processing and also in near-field acoustic holography. For completeness, the application of the fast convolution algorithm to the scattering kernels is outlined here.

3.5.2 One Dimensional Fast Convolution

Consider the evaluation of a one dimensional discrete convolution. Given an infinite sequence X_q and a finite sequence Y_q of length Q, a new sequence Z_a which is also of length Q, and is given by a summation of the form

$$Z_a = \sum_{q=0}^{Q-1} Y_q X_{a-q} \tag{3.133}$$

may be computed in a particularly efficient way by converting the sum into a circular convolution, and applying an FFT based fast convolution algorithm. Say the values of Z_a over the indices

$$a = \{0, 1, 2, 3, \ldots Q-1\} \tag{3.134}$$

are required. The first step in the fast convolution technique is to define the $\tilde{Q}$ long zero padded sequences

$$\tilde{X}_q = \begin{cases} X_q & 0 \leqslant q < Q \\ 0 & Q \leqslant q < \tilde{Q} - Q \\ X_{q-\tilde{Q}} & \tilde{Q} - Q \leqslant q < \tilde{Q} \end{cases} \tag{3.135}$$

$$\tilde{Y}_q = \begin{cases} Y_q & 0 \leqslant q < Q \\ 0 & Q \leqslant q < \tilde{Q} \end{cases} \tag{3.136}$$

The integer $\tilde{Q}$ may be adjusted to a highly composite number, usually a power of two, by padding with zeros. The sequence $\tilde{X}_q$ above may be periodically extended as follows

$$\tilde{X}^P_{q+d\tilde{Q}} = \tilde{X}_q \tag{3.137}$$

where d is an integer and $q = \{0, 1, 2, \ldots \tilde{Q} - 1\}$. The zero padded sequence $\tilde{Y}^P$ may be defined as

$$\tilde{Y}^P_{q+d\tilde{Q}} = \begin{cases} \tilde{Y}_q, & d = 1 \\ 0, & \text{otherwise} \end{cases} \tag{3.138}$$

With the following definitions of the discrete Fourier transform (DFT) and its inverse,

$$\mathcal{F}\{X_q\} = \sum_{q=0}^{Q-1} X_q \; e^{-2\pi jqa/Q} \tag{3.139}$$

$$\mathcal{F}^{-1}\{X_q\} = \frac{1}{Q} \sum_{q=0}^{Q-1} X_q \; e^{2\pi jqa/Q} \tag{3.140}$$

the circular convolution theorem gives

$$\tilde{Z}_a = \sum_{q=-\infty}^{\infty} \tilde{Y}^P_q \tilde{X}^P_{a-q} = \mathcal{F}^{-1}\{\mathcal{F}\{\tilde{X}_q\} \circ \mathcal{F}\{\tilde{Y}_q\}\} \tag{3.141}$$

where the operation $X_q \circ Y_q$ denotes elementwise multiplication of vectors. The convolution Z_a is contained in the first Q values of the $\tilde{Q}$ long sequence $\tilde{Z}_a$. The procedure

just outlined may also be interpreted as the multiplication of a vector by a Toeplitz matrix, which is computed in a fast way by embedding the Toeplitz matrix in a circulant matrix and then factorizing the circulant matrix into the product of an inverse DFT matrix, a diagonal matrix and a DFT matrix [55].

3.5.3 Two Dimensional Fast Convolution

The one-dimensional procedure is easily extended to discrete convolutions in two or more dimensions. Again, this may also be interpreted in terms of the multiplication of a vector by a block Toeplitz arrangement of Toeplitz matrices. Consider the two-dimensional convolution

$$Z_{a,b} = \sum_{t=0}^{T-1} \sum_{q=0}^{Q-1} Y_{q,t} X_{a-q,b-t}, \tag{3.142}$$

with $a = \{0, 1, 2, 3, \ldots Q-1\}$ and $b = \{0, 1, 2, 3, \ldots T-1\}$. The first step in the fast convolution algorithm is to form the matrices $\tilde{X}$ and $\tilde{Y}$,

$$\tilde{X}_{q,t} = \begin{cases} C_{q,t} & 0 \leqslant t < T \\ 0 & T \leqslant t < \tilde{T} - T \\ C_{q,t-\tilde{T}} & \tilde{T} - T \leqslant t < \tilde{T} \end{cases} \tag{3.143}$$

$$\tilde{Y}_{q,t} = \begin{cases} Y_{q,t} & 0 \leqslant q < Q \quad \text{and} \quad 0 \leqslant t < T \\ 0 & Q \leqslant q < \tilde{Q} \quad \text{or} \quad T \leqslant t < \tilde{T} \end{cases} \tag{3.144}$$

where

$$C_{q,t} = \begin{cases} X_{q,t} & 0 \leqslant q < Q \\ 0 & Q \leqslant q < \tilde{Q} - Q \\ X_{q-\tilde{Q},t} & \tilde{Q} - Q \leqslant q < \tilde{Q} \end{cases} \tag{3.145}$$

These matrix $\tilde{X}_{q,t}$ may be periodically extended in both dimensions such that

$$\tilde{X}^{P}_{q+d\tilde{Q},t+e\tilde{T}} = \tilde{X}_{q,t} \tag{3.146}$$

where d and e are integers and $\tilde{Y}_{q,t}$ may be zero padded in both directions to give

$$\tilde{Y}^P_{q+d\tilde{Q},t+e\tilde{T}} = \begin{cases} \tilde{Y}_{q,t}, & d=1 \quad \text{and} \quad e=1 \\ 0, & \text{otherwise} \end{cases} \tag{3.147}$$

Defining the two-dimensional DFT and its inverse as

$$\mathcal{F}_{2D}\{X_{q,t}\} = \sum_{t=0}^{T-1}\sum_{q=0}^{Q-1} X_{q,t}\ e^{-2\pi j(qa/Q+tb/T)} \tag{3.148}$$

$$\mathcal{F}^{-1}_{2D}\{X_{q,t}\} = \frac{1}{QT}\sum_{t=0}^{T-1}\sum_{q=0}^{Q-1} X_{q,t}\ e^{2\pi j(qa/Q+tb/T)} \tag{3.149}$$

then the two-dimensional circular convolution theorem gives

$$\tilde{Z}_{a,b} = \sum_{t=-\infty}^{\infty}\sum_{q=-\infty}^{\infty} \tilde{Y}^P_{q,t}\tilde{X}^P_{a-q,b-t} = \mathcal{F}^{-1}_{2D}\{\mathcal{F}_{2D}\{\tilde{X}_{q,t}\} \circ \mathcal{F}_{2D}\{\tilde{Y}_{q,t}\}\} \tag{3.150}$$

The matrix $Z_{a,b}$ is contained in the first Q rows and T columns of the matrix $\tilde{Z}_{a,b}$. The two-dimensional DFT in Eq. 3.148 can be implemented efficiently by applying the FFT algorithm along the columns of $X_{q,t}$, performing a matrix transpose, and then applying the FFT along the columns of the transposed matrix. It can be shown from the complexity analysis of the FFT that the operation count for the two-dimensional convolution grows asymptotically as $O(\tilde{Q}\tilde{T}\log_2(\tilde{Q}\tilde{T}))$ when $\tilde{Q}$ and $\tilde{T}$ are powers of 2.

3.5.4 Solution Procedure for Non-Rectangular Geometries

Non-rectangular wing planforms may also be accommodated within the acceleration scheme by masking off regions of the regular tiling. Take for example, the scattering of sound by a circular disc. This problem may be treated within the structured grid framework by overlaying the disc on a regular square grid. The disc geometry is discretized by selecting the list of elements within the regular grid whose centroids fall inside the disc, resulting in a staircased approximation of the boundary line of $\widetilde{S}$. For boundary lines with small curvature, the staircased approximation converges rapidly

to the solution with smooth boundary line as the element size is reduced. Given a list of elements selected from a regular grid, the fast convolution algorithm may always be applied to the BEM integrals by mapping the nodal values in the solution vector to elements in a regular *rectangular* grid and then performing fast convolution in the rectangular coordinates. The nodal values for elements in the regular grid that are not contained in the disc are set to zero before the convolution is applied. When the desired convolutions have been applied, the results may then be extracted from the regular grid and mapped back to the output vector containing the matrix-vector multiplication. Hence, the complexity of the matrix multiplication for non-rectangular scatterers can be reduced to $O(\tilde{Q}\tilde{T}\log_2(\tilde{Q}\tilde{T}))$, where the $\tilde{Q}$ and $\tilde{T}$ are the FFT sizes of the bounding rectangular grid that contains the scatterer.

3.5.5 Dimensionless Formulation

It is important to note that the solution vector may contain both potential and flux quantities. Scaling the independent variables by

$$\overline{\eta} = \tilde{k}\eta \tag{3.151}$$

$$\overline{k} = 1 \tag{3.152}$$

,and seeking a solution in terms of these scaled variables, ensures that the potential and flux quantities in the solution vector are of the same order of magnitude, which improves the conditioning of the system. The source term should also be scaled appropriately.

3.6 Propagation of the Solution to the Field Points

If the integral formulation and limiting process outlined in the previous section is repeated for a singular point $\boldsymbol{\xi}$, *not* located on the boundary of the fluid domain, the

field point integral,

$$\varphi(\boldsymbol{\xi}) = \int\limits_{\widetilde{S}} \left(\frac{\partial G}{\partial \tilde{n}_{\boldsymbol{\eta}}} \, \delta\varphi - G \, \frac{\partial \delta\varphi}{\partial \tilde{n}_{\boldsymbol{\eta}}} \right) \mathrm{d}\widetilde{S} - \int_{\widetilde{V}} G\tilde{\mathcal{F}} \, \mathrm{d}\widetilde{V} \tag{3.153}$$

is obtained for the potential, and

$$\frac{\partial \varphi(\boldsymbol{\xi})}{\partial \xi_i} = \int\limits_{\widetilde{S}} \left(\frac{\partial^2 G}{\partial \xi_i \partial \tilde{n}_{\boldsymbol{\eta}}} \, \delta\varphi - \frac{\partial G}{\partial \xi_i} \, \frac{\partial \delta\varphi}{\partial \tilde{n}_{\boldsymbol{\eta}}} \right) \mathrm{d}\widetilde{S} - \int_{\widetilde{V}} \frac{\partial G}{\partial \xi_i} \tilde{\mathcal{F}} \, \mathrm{d}\widetilde{V} \tag{3.154}$$

is obtained for the derivatives. For the discrete problem with a known distribution of $\delta\varphi_{a,b}$ and $\delta f_{a,b}$, the above equations yield the explicit formulae

$$\varphi(\boldsymbol{\xi}) = \sum_{q=0}^{Q-1} \sum_{t=0}^{T-1} \left[\delta\varphi_{q,t} \int\limits_{\widetilde{S}_{q,t}} \frac{\partial G(\boldsymbol{\eta};\boldsymbol{\xi})}{\partial \tilde{n}_{\boldsymbol{\eta}}} \, \mathrm{d}\widetilde{S} - \delta f_{q,t} \int\limits_{\widetilde{S}_{q,t}} G(\boldsymbol{\eta};\boldsymbol{\xi}) \, \mathrm{d}\widetilde{S} \right] - \int_{\widetilde{V}} G\tilde{\mathcal{F}} \, \mathrm{d}\widetilde{V} \tag{3.155}$$

and

$$\frac{\partial \varphi(\boldsymbol{\xi})}{\partial \xi_i} = \sum_{q=0}^{Q-1} \sum_{t=0}^{T-1} \left[\delta\varphi_{q,t} \int\limits_{\widetilde{S}_{q,t}} \frac{\partial^2 G(\boldsymbol{\eta};\boldsymbol{\xi})}{\partial \xi_i \partial \tilde{n}_{\boldsymbol{\eta}}} \, \mathrm{d}\widetilde{S} - \delta f_{q,t} \int\limits_{\widetilde{S}_{q,t}} \frac{\partial G(\boldsymbol{\eta};\boldsymbol{\xi})}{\partial \xi_i} \, \mathrm{d}\widetilde{S} \right] - \int_{\widetilde{V}} \frac{\partial G}{\partial \xi_i} \tilde{\mathcal{F}} \, \mathrm{d}\widetilde{V} \tag{3.156}$$

for the potential and its derivatives everywhere in the fluid.

Equation (3.155) is also valid for the mean flow solution, provided that $\tilde{k}$ is set to zero in the Green's function. Once, the mean flow solution has been obtained, the acoustic pressure in the far-field is calculated by applying the inverse transformation at the field points and then applying Bernoulli's equation

$$p' = \rho_0 \left(j\omega\phi' + \nabla\phi_0 \cdot \nabla\phi' \right) \tag{3.157}$$

to extract the acoustic pressure from the acoustic potential and its derivatives. The gradient of ϕ' in Bernoulli's equation may be calculated by applying a chain rule and

a product rule to the derivative so that

$$\frac{\partial \phi'(\mathbf{y})}{\partial y_i} = \frac{\partial \phi'}{\partial \xi_i}\frac{\partial \xi_i}{\partial y_i} = e^{j\tau}\left(\frac{\partial \varphi(\boldsymbol{\xi})}{\partial \xi_i}\frac{\partial \xi_i}{\partial y_i} + j\varphi(\boldsymbol{\xi})\frac{\partial \tau}{\partial \xi_i}\frac{\partial \xi_i}{\partial y_i}\right) \tag{3.158}$$

The derivatives of φ in the above equation may be calculated by Eq. 3.156 and the derivatives of $\tau = \tau(\phi_0)$ may be calculated similarly, using the gradient of the mean flow potential.

The fast convolution techniques outlined in the previous section may also be extended to the field integrals. Provided the field grid is a simple translation of the surface grid or a subset of the surface grid, the fast convolution methods may be applied. Even if the field grid only matches the spacing and orientation of the surface grid in one direction, one-dimensional fast convolutions may provide a significant speed up in the evaluation of field integrals.

Chapter 4

Scattering of Monopole Sources by a Half-Plane in Flow

In this chapter an idealized solution to the problem of sound diffraction at a tailing edge is described. This analytical solution is used to benchmark the BEM formulation of Chapter. 3.

The scattering of acoustic waves by a semi-infinite half-plane has been treated in detail by Carslaw, Macdonald and Clemmow who extended Sommerfield's seminal work on the scattering of waves by a semi-infinte plate. This canonical scattering problem is one of the few geometries for which convective solutions can be found. Jones [81] studied the effect of applying a Kutta-Joukowski condition at the edge of a semi-infinite plate acting as a trailing edge in a uniform mean flow. Balasubramanyam [87] attempted to extend Jones' analysis to the case of a point source incident on a half-plane by evaluating an appropriate convolution of Jones' two dimensional solution. It will be shown later in the chapter that the Green's function derived by Balasubramanyam is incorrect due to an error in the calculation of the inverse Fourier transform. In the following sections, formulae for half-plane Green's functions are presented in a form that is convenient for computation. Also, the analysis of Balasubramanyam is corrected and the formulae for computing the Kutta condition solution for a point source are developed.

4.1 Problem Description

Consider a half-plane $x_3 = 0$, $x_1 \leqslant 0$ with the edge along the x_2 axis (see Fig. 4.1). Depending on the problem under consideration, either a line source at (y_1, y_3) or a

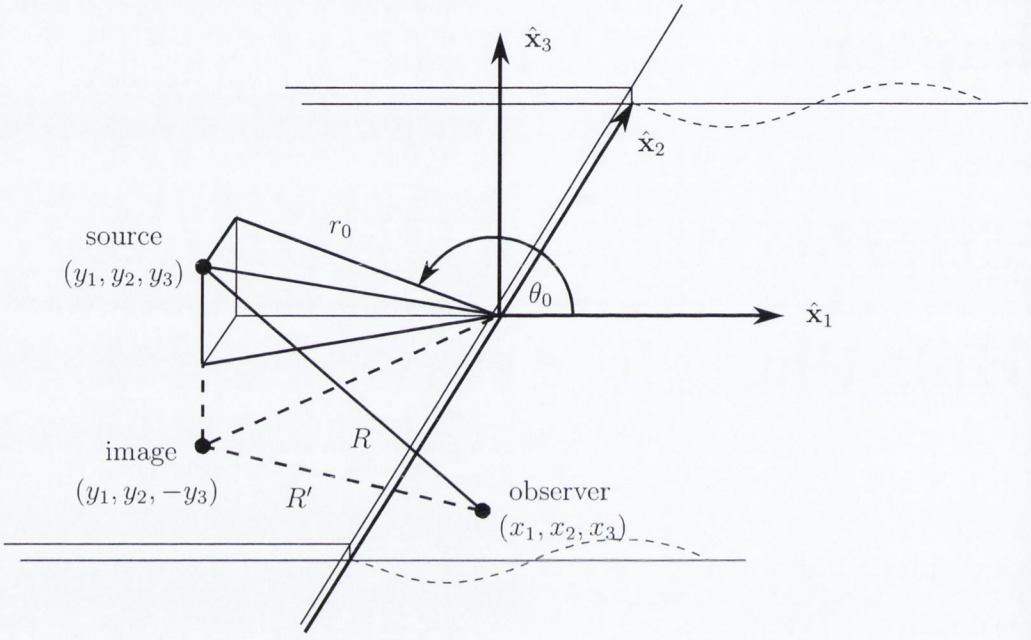


Figure 4.1: Geometric definitions for the half-plane geometry.

point source at (y_1, y_2, y_3), radiates acoustic waves into the domain. The acoustic field is sought at the observer point (x_1, x_2, x_3). It is also useful to define an image source at $(y_1, y_2, -y_3)$, which is a reflection of the real source in the plane $x_3 = 0$. This virtual source can be thought of as a device to generate the reflected field in the zone of specular reflection. The distances R and R', measured from the point of observation to the real source and from the observation point to the virtual source, are defined as

$$R = \sqrt{(x_1 - y_1)^2 + (x_2 - y_2)^2 + (x_3 - y_3)^2} \tag{4.1}$$

$$R' = \sqrt{(x_1 - y_1)^2 + (x_2 - y_2)^2 + (x_3 + y_3)^2} \tag{4.2}$$

where the term $(x_2 - y_2)^2$ can be ignored for the line source problem. It is convenient to introduce a set of cylindrical polar coordinates , defined so that

$$x_1 = r\cos\theta, \quad x_2 = x_2, \quad x_3 = r\sin\theta \tag{4.3}$$

$$y_1 = r_0 \cos\theta_0, \quad y_2 = y_2, \quad y_3 = r_0 \cos\theta_0 \tag{4.4}$$

With these coordinates, a new distance may be defined by

$$R_1 = \sqrt{(r + r_0)^2 + (x_2 - y_2)^2}. \tag{4.5}$$

It will be shown later in this chapter that R_1 may be interpreted as the total length of the diffracted ray path, in the high frequency approximation of the problem.

When a uniform flow field is introduced, the Mach number, M, is positive when the flow vector points in the positive x_1 direction. With the usual acoustic assumption of small amplitude disturbances about a steady mean flow, the equation governing the linearized acoustic potential is

$$\left(1 - M^2\right) \frac{\partial^2 \phi'}{\partial x_1^2} - 2jkM \frac{\partial \phi'}{\partial x_1} + \frac{\partial^2 \phi'}{\partial x_3^2} + k^2 \phi' = -\delta\left(x_1 - y_1\right) \delta\left(x_3 - y_3\right) \tag{4.6}$$

for the line source case, and

$$\left(1 - M^2\right) \frac{\partial^2 \phi'}{\partial x_1^2} - 2jkM \frac{\partial \phi'}{\partial x_1} + \frac{\partial^2 \phi'}{\partial x_2^2} + \frac{\partial^2 \phi'}{\partial x_3^2} + k^2 \phi' = -\delta\left(x_1 - y_1\right) \delta\left(x_2 - y_2\right) \delta\left(x_3 - y_3\right) \tag{4.7}$$

for the point source case.

The boundary conditions on the half-plane $x_3 = 0$, $x_1 \leqslant 0$ are

$$\frac{\partial \phi'}{\partial x_3} = 0 \tag{4.8}$$

The solution to the problem must also satisfy the radiation condition which specifies that the solution contains only outgoing waves.

Applying the Prandtl-Glauert transformation to the above equations reduces the problem to the solution of an analogous problem in a stationary medium. Substituting

$$\beta = (1 - M^2)^{-1/2}, \qquad \eta_1 = \beta x_1, \qquad \eta_2 = x_2, \qquad \eta_3 = x_3, \qquad \tilde{k} = \beta k, \tag{4.9}$$

$$\phi'(\mathbf{x}, k) = \varphi(\boldsymbol{\eta}, \tilde{k})\, e^{j\tilde{k}M\eta_1}$$

into (4.6-4.7) and similarly transforming the coordinates of the source, so that $\mathbf{y}$ is transformed to $\boldsymbol{\xi}$ gives

$$\frac{\partial^2 \varphi}{\partial \eta_1^2} + \frac{\partial^2 \varphi}{\partial \eta_3^2} + \tilde{k}^2 \varphi = -\delta(\eta_1 - \xi_1)\,\delta(\eta_3 - \xi_3) \tag{4.10}$$

and

$$\frac{\partial^2 \varphi}{\partial \eta_1^2} + \frac{\partial^2 \varphi}{\partial \eta_2^2} + \frac{\partial^2 \varphi}{\partial \eta_3^2} + \tilde{k}^2 \varphi = -\delta(\eta_1 - \xi_1)\,\delta(\eta_2 - \xi_2)\,\delta(\eta_3 - \xi_3) \tag{4.11}$$

for the line source and point source problems. The boundary conditions in the transformed coordinates are given by

$$\frac{\partial \phi'}{\partial \eta_3} = 0, \qquad \text{on } \eta_3 = 0, \eta_1 \leqslant 0 \tag{4.12}$$

and are unchanged from the boundary conditions expressed in physical coordinates.

As shown by Jones', in the presence of a uniform mean flow the solution may have a discontinuity in the potential, extending into the flow from the edge, in order to satisfy the Kutta Joukowski condition at the trailing edge. This discontinuity is of the form

$$\varphi(\eta_1, \eta_2, +0) - \varphi(\eta_1, \eta_2, -0) = A(\eta_2)\, e^{-j\mu\eta_1} \tag{4.13}$$

where μ is a positive constant and A is an amplitude factor that controls the release of vorticity and must be matched to the incident field in order to satisfy the Kutta condition. Since the pressure due to the acoutic potential is given by

$$p' = -\rho_\infty \left(\frac{\partial \phi'}{\partial t} + c_\infty M \frac{\partial \phi'}{\partial x_1} \right) \tag{4.14}$$

where ρ_∞ is the mean density, continuity of pressure across the wake requires that

$$\mu = \tilde{k}/M \tag{4.15}$$

4.2 Solutions

The solution to the half-plane problem in the Prandtl-Glauert domain (Eqs.(4.10-4.13)) can be expressed as the sum of two components,

$$\varphi = \varphi_G + \varphi_{KJ} \tag{4.16}$$

The first component, φ_G, is simply the half-plane Green's function, which is calculated in Prandtl-Glauert coordinates rather than with physical coordinates. The second component is a vortex shedding eigensolution, which has been described by Jones[81] for the line source problem and by Balasubramanyam [87] for the point source problem.

4.2.1 No Kutta Condition Solutions

Consider the zero mean flow and no Kutta condition problem. Since both $A = M = 0$ in the problem formulation, the solution is given by the well known Green's function for the half-plane (see the reference [88])

$$\phi' = G(x_1, x_3, k) = \frac{e^{-jkR}}{2\pi} \int_{-m_1}^{\infty} \frac{e^{-ju^2}}{\sqrt{u^2 + 2kR}}\, \mathrm{d}u + \frac{e^{-jkR'}}{2\pi} \int_{-m_2}^{\infty} \frac{e^{-ju^2}}{\sqrt{u^2 + 2kR'}}\, \mathrm{d}u \tag{4.17}$$

for a line source at (y_1, y_3). The corresponding solution for a point source is given by

$$\phi' = G(x_1, x_2, x_3, k) = -\frac{jk}{4\pi} \left[\int_{-m_1}^{\infty} \frac{H_1^{(2)}(u^2 + kR)}{\sqrt{u^2 + 2kR}}\, \mathrm{d}u + \int_{-m_2}^{\infty} \frac{H_1^{(2)}(u^2 + kR')}{\sqrt{u^2 + 2kR'}}\, \mathrm{d}u \right] \tag{4.18}$$

for a source located at (y_1, y_2, y_3). The limits of integration in the formulae above are determined by

$$m_1 = 2\sqrt{\frac{krr_0}{R_1 + R}} \cos\left(\tfrac{(\theta - \theta_0)}{2}\right) = \operatorname{sgn}\left\{\cos\left(\tfrac{(\theta - \theta_0)}{2}\right)\right\} \sqrt{k(R_1 - R)} \tag{4.19}$$

$$m_2 = -2\sqrt{\frac{krr_0}{R_1 + R'}} \cos\left(\tfrac{(\theta + \theta_0)}{2}\right) = -\operatorname{sgn}\left\{\cos\left(\tfrac{(\theta + \theta_0)}{2}\right)\right\} \sqrt{k(R_1 - R')} \tag{4.20}$$

The no Kutta condition solution, $(A = 0)$, to the convective problem is then obtained by the Prandtl-Glauert transformation as

$$\begin{aligned}\phi'(x_1, x_2, x_3, k, M) &= \varphi_G(\eta_1, \eta_2, \eta_3, \tilde{k})\ \beta e^{j\tilde{k}M(\eta_1 - \xi_1)} \\ &= G\left(\beta x_1, x_2, x_3, \beta k\right)\ \beta e^{jk\beta^2 M(x_1 - y_1)}\end{aligned} \tag{4.21}$$

4.2.2 Jones' Two Dimensional Vortex Shedding Solution

When A is non-zero, an additional field is generated by the presence of a time-harmonic wake and its interaction with the plate. By introducting polar coordinates in the Prandtl-Glauert domain, defined so that

$$\eta_1 = \tilde{r}\cos\tilde{\theta}, \quad \eta_2 = \eta_2, \quad \eta_3 = \tilde{r}\sin\tilde{\theta} \tag{4.22}$$

$$\xi_1 = \tilde{r}_0\cos\tilde{\theta}_0, \quad \xi_2 = \xi_2, \quad \xi_3 = \tilde{r}_0\cos\tilde{\theta}_0 \tag{4.23}$$

the field due to the wake can be expressed as[81]

$$\varphi_A = \frac{A}{8\pi^{3/2}}\, e^{j\left(\frac{\pi}{4} - \tilde{k}\tilde{r}\right)} \times \begin{cases} \left[F(\nu_1) + F(\nu_2)\right], & \tilde{\theta} > 0 \\ -\left[F(-\nu_1) + F(-\nu_2)\right], & \tilde{\theta} < 0 \end{cases} \tag{4.24}$$

where

$$\cos(\tilde{\theta}_1) = \frac{\mu}{\tilde{k}}, \qquad 0 \leqslant \mathrm{Re}(\tilde{\theta}_1) < \pi \tag{4.25}$$

$$\nu_1 = \sin\left(\frac{(\tilde{\theta} - \tilde{\theta}_1)}{2}\right)\sqrt{2\tilde{k}\tilde{r}} \tag{4.26}$$

$$\nu_2 = \sin\left(\frac{(\tilde{\theta} + \tilde{\theta}_1)}{2}\right)\sqrt{2\tilde{k}\tilde{r}} \tag{4.27}$$

and the complex Fresnel integral, $F(t)$, is defined by

$$F(t) = e^{jt^2}\int_t^\infty e^{-j\tau^2}\,\mathrm{d}\tau \tag{4.28}$$

with the condition that $-\pi/2 < \arg(\tau) < 0 \quad \text{as} \quad \tau \to \infty$.

When the Kutta Joukowski condition is applied, A is determined by the following

expression

$$A = 2\left(\frac{2\pi}{\tilde{k}\tilde{r}_0}\right)^{1/2} \frac{\sin\left(\frac{1}{2}\tilde{\theta}_0\right)}{\cos\left(\frac{1}{2}\tilde{\theta}_1\right)} e^{-j\tilde{k}\tilde{r}_0 - j\pi/4} \tag{4.29}$$

where the line source is located at $(\tilde{r}_0, \tilde{\theta}_0)$ in the Prandtl-Glauert domain. Therefore, the solution to the original problem that satisfies the Kutta Joukowski condition is given by

$$\begin{aligned}\phi' &= \beta e^{j\tilde{k}M(\eta_1-\xi_1)} \left[\varphi_G(\eta_1,\eta_2,\eta_3,\tilde{k}) + \varphi_{KJ}(\eta_1,\eta_2,\eta_3,\tilde{k},M)\right] \\ &= \beta e^{jkM\beta^2(x_1-y_1)} \left[G\left(\beta x_1, x_2, x_3, \beta k\right) + \varphi_{KJ}\left(\beta x_1, x_2, x_3\beta k, M\right)\right]\end{aligned} \tag{4.30}$$

where φ_{KJ} is the vortex shedding solution (Eq. 4.24), with A determined by Eq. 4.29.

4.2.3 Point Source Extension to Jones' Solution

A correction of Balasubramanyam's work gives the Kutta condition solution for the half-plane problem with a point source. Following the procedure outlined in [87], the z direction spatial Fourier transform of the potential is defined as

$$\chi(\eta_1, s, \eta_3) = \int_{-\infty}^{\infty} \varphi(\eta_1, \eta_2, \eta_3)\, e^{js(\eta_2-\xi_2)}\, \mathrm{d}\eta_2 \tag{4.31}$$

Applying the Fourier transform to the governing equations in the Prandtl-Glauert domain then gives

$$\frac{\partial^2\chi}{\partial\eta_1^2} + \frac{\partial^2\chi}{\partial\eta_3^2} + (\tilde{k}^2 - s^2)\chi = -\delta\left(\eta_1 - \xi_1\right)\delta\left(y - y_0\right) \tag{4.32}$$

$$\chi(\eta_1, s, +0) - \chi(\eta_1, s, -0) = A(\{\tilde{k}^2 - s^2\}^{\frac{1}{2}})\, e^{-j\mu\eta_1} \qquad \eta_1 > 0 \tag{4.33}$$

$$\frac{\partial\chi}{\partial\eta_3}(\eta_1, s, 0) = 0 \qquad \eta_1 \leqslant 0 \tag{4.34}$$

which is essentially the same as the two dimensional problem. It follows that the Fourier transform of the Kutta Joukowski field, χ_{KJ}, is given by Eqs.(4.25-4.29) with $\tilde{k}$ replaced by $(\tilde{k}^2 - s^2)^{\frac{1}{2}}$ throughout. Hence, the additional field generated by imposing the Kutta condition is given by the inverse Fourier transform of χ_{KJ}, which can be

expressed as the contour integral

$$\varphi_{KJ} = \int_{-\infty}^{\infty} \frac{\sin\frac{1}{2}\tilde{\theta}_0 \; e^{-j\left((\eta_2-\xi_2)s+(\tilde{r}+\tilde{r}_0)(\tilde{k}^2-s^2)^{\frac{1}{2}}\right)}}{4\pi^2\cos\frac{1}{2}\tilde{\theta}_1\sqrt{2\tilde{r}_0(\tilde{k}^2-s^2)^{\frac{1}{2}}}}\left[F\left\{\nu_1(s)\right\}+F\left\{\nu_2(s)\right\}\right]\,\mathrm{d}s \qquad (4.35)$$

Considering the case where $\tilde{k}$ has a positive real part and a vanishing negative imaginary component, then the integrand has two poles on the real axis and the contour of integration is deflected below the pole at $s=-\tilde{k}$ and above the pole at $s=\tilde{k}$. It is also necessary to adjust the branch cut of the function $(\tilde{k}^2-s^2)^{\frac{1}{2}}$ so that it does not cross the s contour. A suitable branch cut is shown in Fig. 4.2 along with some sample "steepest descents" paths for the exponential factor in the integrand. The complex

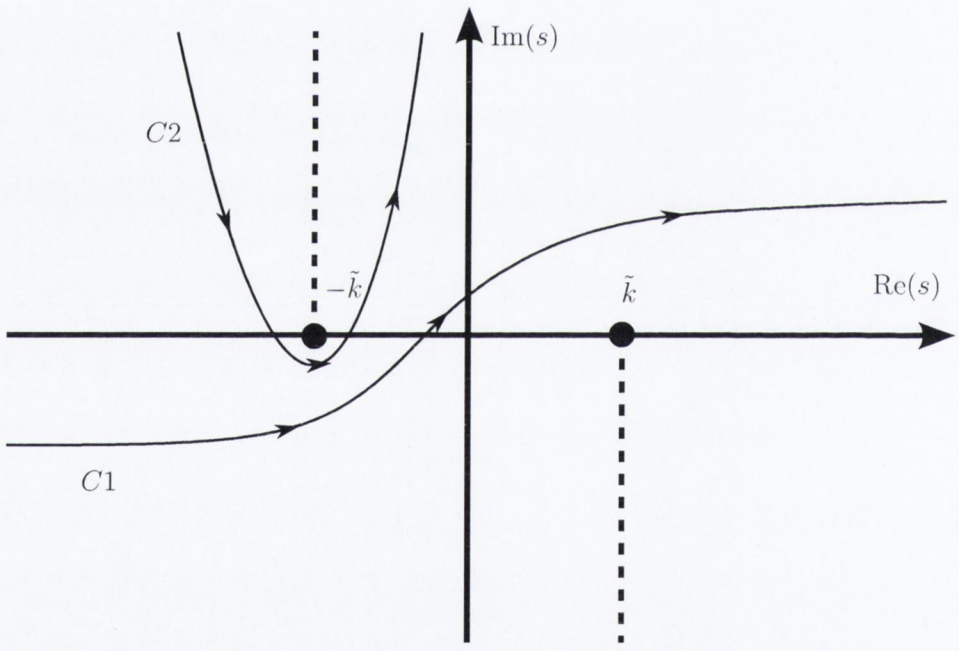


Figure 4.2: The branch cut of the complex square root in the s plane is shown by the dashed line. The thin solid lines show representative steepest descents contours (C_1 for large $(\eta_2-\xi_2)$, C_2 for small $(\eta_2-\xi_2)$).

square root function with this particular branch cut can be defined in terms of the principal square root function by

$$(\tilde{k}^2-s^2)^{\frac{1}{2}} = \begin{cases} -\sqrt{\tilde{k}^2-s^2}, & \pi/2-\arg\tilde{k} < \arg(1-s\tilde{k}^{-1}\mathrm{sgn}\{\mathrm{Re}(s)\}) \leqslant \pi \\ \sqrt{\tilde{k}^2-s^2}, & \text{otherwise} \end{cases} \qquad (4.36)$$

When evaluating the integral above, Balasubramanyam treated the factors containing $\tilde{\theta}_1$ as constants. However, noting that the condition for continuity of pressure on the wake still requires, $\mu = \tilde{k}/M$, and replacing $\tilde{k}$ with $(\tilde{k}^2 - s^2)^{\frac{1}{2}}$ in Eq. 4.25 gives

$$\cos(\tilde{\theta}_1) = \frac{\mu}{(\tilde{k}^2 - s^2)^{\frac{1}{2}}} = \frac{\tilde{k}}{M(\tilde{k}^2 - s^2)^{\frac{1}{2}}} \tag{4.37}$$

which shows the implicit dependence of $\tilde{\theta}_1$ on s. To make this dependence explicit, the expressions

$$\cos(\tfrac{1}{2}\tilde{\theta}_1) = \sqrt{\tfrac{1}{2}\left(1 + \cos\tilde{\theta}_1\right)} = \sqrt{\tfrac{1}{2}\left(1 + \frac{\tilde{k}}{M(\tilde{k}^2 - s^2)^{\frac{1}{2}}}\right)} \tag{4.38}$$

$$\sin(\tfrac{1}{2}\tilde{\theta}_1) = \sqrt{\tfrac{1}{2}\left(1 - \cos\tilde{\theta}_1\right)} = \sqrt{\tfrac{1}{2}\left(1 - \frac{\tilde{k}}{M(\tilde{k}^2 - s^2)^{\frac{1}{2}}}\right)} \tag{4.39}$$

$$\tag{4.40}$$

may be used to replace $\tilde{\theta}_1$ in the denominator of the integrand in Eq. 4.35 and in the sine functions in Eqs.(4.26-4.27) giving

$$\varphi_{KJ} = \frac{\sin\frac{1}{2}\tilde{\theta}_0}{4\pi^2\sqrt{\tilde{r}_0}} \int_{-\infty}^{\infty} \frac{e^{-j\left((\eta_2 - \xi_2)s + (\tilde{r} + \tilde{r}_0)(\tilde{k}^2 - s^2)^{\frac{1}{2}}\right)}}{\sqrt{\tilde{k}M^{-1} + (\tilde{k}^2 - s^2)^{\frac{1}{2}}}} \left[F\left\{\nu_1(s)\right\} + F\left\{\nu_2(s)\right\}\right] \, \mathrm{d}s \tag{4.41}$$

for $\tilde{\theta} > 0$, with

$$\nu_1(s) = \tilde{r}^{\frac{1}{2}} \left(\sin\left(\tfrac{1}{2}\tilde{\theta}\right)\sqrt{\tilde{k}M^{-1} + (\tilde{k}^2 - s^2)^{\frac{1}{2}}} + \cos\left(\tfrac{1}{2}\tilde{\theta}\right)\sqrt{(\tilde{k}^2 - s^2)^{\frac{1}{2}} - \tilde{k}M^{-1}}\right) \tag{4.42}$$

$$\nu_2(s) = \tilde{r}^{\frac{1}{2}} \left(\sin\left(\tfrac{1}{2}\tilde{\theta}\right)\sqrt{\tilde{k}M^{-1} + (\tilde{k}^2 - s^2)^{\frac{1}{2}}} - \cos\left(\tfrac{1}{2}\tilde{\theta}\right)\sqrt{(\tilde{k}^2 - s^2)^{\frac{1}{2}} - \tilde{k}M^{-1}}\right) \tag{4.43}$$

When $\tilde{\theta} > 0$, the expression

$$\left[F\left\{\nu_1(s)\right\} + F\left\{\nu_2(s)\right\}\right]$$

should be replaced with

$$-\left[F\left\{-\nu_1(s)\right\}+F\left\{-\nu_2(s)\right\}\right]$$

in integral (4.41), as shown in (4.35).

4.3 Computation of Solutions

The integrals in the zero mean flow formulae (Eqs.(4.17,4.18)) are regular for $R \neq 0$, $R' \neq 0$ and can be evaluated directly by gaussian quadrature rules. However, the rate of convergence can be improved by first performing some manipulations. When the limits of integration are small, the integrals can be rearranged as

$$\frac{1}{2\pi}\int_{-m_1}^{\infty}\frac{e^{-j(u^2+kR)}}{\sqrt{u^2+2kR}}\,\mathrm{d}u=-\frac{j}{8}H_0^{(2)}(kR)+\mathrm{sgn}(m_1)\frac{1}{2\pi}\int_0^{|m_1|}\frac{e^{-j(u^2+kR)}}{\sqrt{u^2+2kR}}\,\mathrm{d}u \quad (4.44)$$

and

$$-\frac{jk}{4\pi}\int_{-m_1}^{\infty}\frac{H_1^{(2)}(u^2+kR)}{\sqrt{u^2+2kR}}\,\mathrm{d}u=\frac{e^{-jkR}}{8\pi R}-\mathrm{sgn}(m_1)\frac{jk}{4\pi}\int_0^{|m_1|}\frac{H_1^{(2)}(u^2+kR)}{\sqrt{u^2+2kR}}\,\mathrm{d}u \quad (4.45)$$

so that the limits of integration are finite, and for small values of m_1 or m_2, the formulae above can be accurately integrated by gaussian quadrature rules. The same manipulation can be performed for the integrals involving R'.

When the magnitude of m_1 or m_2 is large, the numerical integrals can be computed more efficiently by applying a "steepest descents" substitution to the exponential factor in the integrand. For negative m_1, the substitution

$$u=-j\sqrt{j\mu^2+k(R-R_1)} \quad (4.46)$$

gives

$$\begin{aligned}\frac{e^{-jkR}}{2\pi}\int_{|m_1|}^{\infty}\frac{e^{-ju^2}}{\sqrt{u^2+2kR}}\,\mathrm{d}u &= \frac{e^{-jkR_1}}{2\pi}\int_0^{\infty}\frac{\mu\, e^{-\mu^2}}{\sqrt{\mu^4+2jkR_1\mu^2+k^2(R^2-R_1^2)}}\,\mathrm{d}\mu \\ &\approx \frac{e^{-jkR_1}}{2\pi}\int_0^{\mu_1}\frac{\mu\, e^{-\mu^2}}{\sqrt{\mu^4+2jkR_1\mu^2+k^2(R^2-R_1^2)}}\,\mathrm{d}\mu\end{aligned} \tag{4.47}$$

where the infinite upper limit of integration has been replaced by the finite value, μ_1, so that standard Gauss-Legendre quadrature rules can be applied. When m_1 is positive, the integral can be computed by noting that

$$\frac{e^{-jkR}}{2\pi}\int_{-m_1}^{\infty}\frac{e^{-ju^2}}{\sqrt{u^2+2kR}}\,\mathrm{d}u = -\frac{j}{4}H_0^{(2)}(kR) - \frac{e^{-jkR}}{2\pi}\int_{m_1}^{\infty}\frac{e^{-ju^2}}{\sqrt{u^2+2kR}}\,\mathrm{d}u \tag{4.48}$$

Similarly for the point source solution, the substitution Eq. 4.46 acts as an approximate "steepest descent" approach because the asymptotic behavior of the Hankel function,

$$H_1^{(2)}(u^2+kR) \sim \sqrt{\frac{2}{\pi(u^2+kR)}}\, e^{-j(u^2+kR-3\pi/4)}, \qquad \text{as} \quad u\to\infty \tag{4.49}$$

has the same exponential factor as in the line source case. Therefore, the formula

$$-\frac{jk}{4\pi}\int_{|m_1|}^{\infty}\frac{H_1^{(2)}(u^2+kR)}{\sqrt{u^2+2kR}}\,\mathrm{d}u \approx -\frac{jk}{4\pi}\int_0^{\mu_1}\frac{\mu\, H_1^{(2)}(kR_1-j\mu^2)}{\sqrt{\mu^4+2jkR_1\mu^2+k^2(R^2-R_1^2)}}\,\mathrm{d}\mu \tag{4.50}$$

can be used to compute the integrals in the point source solution when m_1 is negative. For m_1 positive, the expression

$$-\frac{jk}{4\pi}\int_{-m_1}^{\infty}\frac{H_1^{(2)}(u^2+kR)}{\sqrt{u^2+2kR}}\,\mathrm{d}u = \frac{e^{-jkR}}{4\pi R} + \frac{jk}{4\pi}\int_{m_1}^{\infty}\frac{H_1^{(2)}(u^2+kR)}{\sqrt{u^2+2kR}}\,\mathrm{d}u \tag{4.51}$$

may be used to compute the integrals efficiently.

In practice, the Green's functions can be calculated to arbitrary precision by increasing the order of the quadrature rule and the value of μ_1. An approximate rule for selecting μ_1, given a prescribed error tolerance, can be obtained by examining where the gaussian envelope of the integrand becomes smaller than the prescribed tolerance.

Based on this criterion μ_1 can be chosen as

$$\mu_1 = \sqrt{N \ln(10)} \tag{4.52}$$

where N is the number of decimal places of accuracy. The gaussian quadrature rule should then be chosen so that the numerical integration error is also on the order of 10^{-N}. For engineering accuracy, values of $\mu_1 = 3.5$ with a quadrature rule of order 8 are more than sufficient.

For optimal efficiency, a rule should be specified for when to use Eq. 4.44/Eq. 4.45 in preference to Eq. 4.47/Eq. 4.47. Based on numerical testing, the small m_1 formula requires fewer integration points to achieve engineering accuracy when $m_1 \lessapprox 6$. The exception to this rule is when the integrals are evaluated in the vicinity of the image source. For this case, the evaluation of the virtual source integral with the small argument formula may lose accuracy due to truncation error, when the numerical component of the integral is subtracted from the near-singular analytical part. In this region the large argument formula should be used regardless of the magnitude of m_2.

4.3.1 Computation of Jones' Kutta Condition Solution

Jones' vortex shedding eigensolution is given in a closed form and does not pose any difficulties for computation. The only numerical issue concerns the evaluation of the complex Fresnel integral, which could be considered a non-standard special function. However, the Fresnel integral is easily expressed in terms of the complementary error function, $\mathrm{erfc}(t)$, or the Fadeeva function, $w(t)$. Both of these functions are found in numerical libraries. By definition

$$\mathrm{erfc}(t) = \frac{2}{\sqrt{\pi}} \int_t^\infty e^{-\tau^2} \, \mathrm{d}\tau \tag{4.53}$$

and

$$w(t) = e^{-t^2} \mathrm{erfc}(-jt) \tag{4.54}$$

A simple change of variables then gives the Fresnel integral in terms of the other two functions

$$\begin{aligned} F(t) &= e^{jt^2} \int_t^\infty e^{-j\tau^2} \, \mathrm{d}\tau \\ &= \tfrac{\sqrt{\pi}}{2} \, e^{j(t^2-\pi/4)} \, \mathrm{erfc}(e^{j\pi/4} \, t) \qquad (4.55) \\ &= \tfrac{\sqrt{\pi}}{2} \, e^{-j\pi/4} \, w(-e^{-j\pi/4} \, t) \qquad (4.56) \end{aligned}$$

4.3.2 Point Source Extension to Jones' Solution

The vortex shedding solution for the point source may be evaluated by a steepest descents approach. An appropriate deflection of the s contour may be found by considering the behavior of the Fresnel integral in the complex plane. An asymptotic expansion of $F(t)$ is given by

$$F(t) \sim \begin{cases} -\frac{j}{2t}, & -\pi < \arg t < \frac{1}{2}\pi \\ \sqrt{\pi} e^{jt^2 - j\pi/4} \; - \frac{j}{2t}, & \frac{1}{2}\pi < \arg t < \pi \end{cases} \qquad (4.57)$$

as $|t| \to \infty$. Since the the Fresnel integral has an exponential term for arguments $\frac{1}{2}\pi < \arg t < \pi$, the steepest descent path should be chosen with the behavior of the Fresnel integral in mind. For observer locations far from the wake, the argument of the Fresnel integrals, ν_1 and ν_2, satisfy the condition $-\pi < \arg t < \frac{1}{2}\pi$ over the portion of the path of integration that provides the dominant contribution to the integral. Therefore the Fresnel integral behaves as $F(t) \sim -\frac{j}{2t}$, and the approximate steepest descent path is given by

$$s(\mu) = \frac{-j(\eta_2 - \xi_2)}{\tilde{R}_1^2} \left(\mu^2 + j\tilde{k}\tilde{R}_1 \right) + \frac{(\tilde{r} + \tilde{r}_0)}{\tilde{R}_1^2} \, \mu \sqrt{\mu^2 + 2j\tilde{k}\tilde{R}_1} \qquad (4.58)$$

where

$$\tilde{R}_1 = \sqrt{(\tilde{r} + \tilde{r}_0)^2 + (\eta_2 - \xi_2)^2} \qquad (4.59)$$

is the length of the diffracted ray path in the Prandtl-Glauert domain. With this substitution the contour integral Eq. 4.41 becomes

$$\varphi_{KJ} = \frac{\sin\frac{1}{2}\tilde{\theta}_0}{4\pi^2\sqrt{\tilde{r}_0}} \int_{-\infty}^{\infty} \frac{e^{-(\mu^2+j\tilde{k}\tilde{R}_1)}}{\sqrt{\tilde{k}M^{-1}+\sqrt{\tilde{k}^2-s(\mu)^2}}} \left[F(\nu_1\{s(\mu)\}) + F(\nu_2\{s(\mu)\})\right] \frac{\mathrm{d}s}{\mathrm{d}\mu}\,\mathrm{d}\mu \tag{4.60}$$

where

$$\frac{\mathrm{d}s}{\mathrm{d}\mu} = \frac{-2j\mu(\eta_2-\xi_2)}{\tilde{R}_1^2} + \frac{2(\tilde{r}+\tilde{r}_0)(\mu^2+j\tilde{k}\tilde{R}_1)}{\tilde{R}_1^2\sqrt{\mu^2+2j\tilde{k}\tilde{R}_1}} \tag{4.61}$$

When the observer point is away from the wake, Eq. 4.60 may be evaluated by gaussian quadrature rules over a truncated interval. Since the integrand contains the same gaussian envelope as found in the zero flow Green's functions, the value of the integral limits can be selected by Eq. 4.52.

For observation points on or very near the wake, as $|\tilde{\theta}| \to 0$, the Fresnel integral behaves as $F(t) \sim \sqrt{\pi}e^{jt^2-j\pi/4} - \frac{j}{2t}$, and the steepest descent path is better approximated by

$$s(\mu) = \frac{-j(\eta_2-\xi_2)}{\tilde{R}_2^2}\left(\mu^2+j\tilde{k}\tilde{R}_2\right) + \frac{\tilde{r}_0}{\tilde{R}_2^2}\,\mu\sqrt{\mu^2+2j\tilde{k}\tilde{R}_2} \tag{4.62}$$

where $\tilde{R}_2 = \sqrt{\tilde{r}_0^2+(\eta_2-\xi_2)^2}$. Hence, the solution should be computed from the integral

$$\varphi_{KJ} = \frac{\sin\frac{1}{2}\tilde{\theta}_0}{4\pi^2\sqrt{\tilde{r}_0}} \int_{-\infty}^{\infty} \frac{e^{-j\left((\eta_2-\xi_2)s(\mu)+(\tilde{r}+\tilde{r}_0)\sqrt{\tilde{k}^2-s(\mu)^2}\right)}}{\sqrt{\tilde{k}M^{-1}+\sqrt{\tilde{k}^2-s(\mu)^2}}} \left[F(\nu_1\{s(\mu)\}) + F(\nu_2\{s(\mu)\})\right] \frac{\mathrm{d}s}{\mathrm{d}\mu}\,\mathrm{d}\mu \tag{4.63}$$

In practice some rule must be applied in deciding which form of integral to use for computing the vortex shedding solution. An empirical estimate of the zone in which the near wake formulation should be used is given by $|\eta_3| > 2\pi aM/\tilde{k}$, for $\eta_1 > 0$, where a is a parameter close to 1.

4.4 Far-field Asymptotic Solution

When $\tilde{k}\tilde{R}_1$ is large and the observer point is away from the wake, the integrand of Eq. 4.60 can be expressed as the product of a gaussian function and a slowly varying function. In general, integrals of this type can be approximated by Laplace's method as follows

$$\int_{-\infty}^{\infty} g(N^{-\frac{1}{2}}\mu)e^{-\mu^2}\,\mathrm{d}\mu = \sqrt{N}\int_{-\infty}^{\infty} g(\tau)e^{-N\tau^2}\,\mathrm{d}\tau \tag{4.64}$$

$$\sim \sqrt{N}\,g(0)\int_{-\infty}^{\infty} e^{-N\tau^2}\,\mathrm{d}\tau \qquad \text{as } N\to\infty \tag{4.65}$$

$$= g(0)\sqrt{\pi} \tag{4.66}$$

By this approach, an asymptotic expansion of Eq. 4.60 is given by

$$\varphi_{KJ} \sim \frac{\sin\theta_D\ \sin\frac{1}{2}\tilde{\theta}_0}{2\pi^{\frac{3}{2}}(2\tilde{r}_0\tilde{R}_1)^{\frac{1}{2}}(M^{-1}+\sin\theta_D)^{\frac{1}{2}}}\left[F(\nu_1|_{\mu=0})+F(\nu_2|_{\mu=0})\right]\ e^{-j\tilde{k}\tilde{R}_1+j\pi/4} \tag{4.67}$$

as $\tilde{k}\tilde{R}_1\to\infty$ with $\tilde{\theta}>0$, where

$$\sin\theta_D = \frac{\tilde{r}+\tilde{r}_0}{\tilde{R}_1} \tag{4.68}$$

$$\nu_1|_{\mu=0} = (\tilde{k}\tilde{r})^{\frac{1}{2}}\left(\sin\left(\tfrac{1}{2}\tilde{\theta}\right)\sqrt{M^{-1}+\sin\theta_D}+\cos\left(\tfrac{1}{2}\tilde{\theta}\right)\sqrt{\sin\theta_D-M^{-1}}\right) \tag{4.69}$$

$$\nu_2|_{\mu=0} = (\tilde{k}\tilde{r})^{\frac{1}{2}}\left(\sin\left(\tfrac{1}{2}\tilde{\theta}\right)\sqrt{M^{-1}+\sin\theta_D}-\cos\left(\tfrac{1}{2}\tilde{\theta}\right)\sqrt{\sin\theta_D-M^{-1}}\right) \tag{4.70}$$

A further simplification can be made if the observation point is in the far field. As $\tilde{k}\tilde{r}\to\infty$, the Fresnel integral may be replaced by its asymptotic formula giving

$$\varphi_{KJ} \sim \frac{M\sin\theta_D\ \sin\frac{1}{2}\tilde{\theta}_0\ \sin\frac{1}{2}\tilde{\theta}}{2\pi^{\frac{3}{2}}(2\tilde{k}\tilde{r}\tilde{r}_0\tilde{R}_1)^{\frac{1}{2}}(1-M\sin\theta_D\cos\tilde{\theta})}\ e^{-j\tilde{k}\tilde{R}_1-j\pi/4} \tag{4.71}$$

The Kutta condition field may be recombined with the asymptotic expansion of the no Kutta solution to give the total field in the far-field. The no Kutta solution is conveniently expanded in terms of a geometric acoustics field and a diffracted field as (see [88]),

$$\varphi_G = \varphi_{GA}+\varphi_D \tag{4.72}$$

where,

$$\varphi_{GA} = \begin{cases} \frac{e^{-j\tilde{k}\tilde{R}}}{4\pi\tilde{R}} + \frac{e^{-j\tilde{k}\tilde{R}'}}{4\pi\tilde{R}'} & \text{for} \quad \pi - \tilde{\theta}_0 < \tilde{\theta} < \pi \\ \frac{e^{-j\tilde{k}\tilde{R}}}{4\pi\tilde{R}} & \text{for} \quad \tilde{\theta}_0 - \pi < \tilde{\theta} < \pi - \tilde{\theta}_0 \\ 0 & \text{for} \quad -\pi < \tilde{\theta} < \tilde{\theta}_0 - \pi \end{cases} \tag{4.73}$$

and

$$\begin{aligned} \varphi_D = \operatorname{sgn}(\tilde{\theta}_0 - \tilde{\theta} - \pi) \frac{e^{-j\tilde{k}\tilde{R}_1 + j\pi/4}}{4\pi\sqrt{\pi}} \sqrt{\frac{2}{\tilde{R}_1(\tilde{R}_1 + \tilde{R})}} F\left(\sqrt{\tilde{k}(\tilde{R}_1 - \tilde{R})}\right) \\ + \operatorname{sgn}(\pi - \tilde{\theta}_0 - \tilde{\theta}) \frac{e^{-j\tilde{k}\tilde{R}_1 + j\pi/4}}{4\pi\sqrt{\pi}} \sqrt{\frac{2}{\tilde{R}_1(\tilde{R}_1 + \tilde{R}')}} F\left(\sqrt{\tilde{k}(\tilde{R}_1 - \tilde{R}')}\right) \end{aligned} \tag{4.74}$$

When the different components of the scattered field are expanded in this form, it is clear that the Kutta condition field is actually an edge diffracted wave with the same phase dependence as φ_D and that the asymptotic expansion of the Kutta condition solution is compatible with ray theory. Hence, the diffraction coefficient associated with the vortex shedding field may be extracted directly from Eq. 4.67.

4.4.1 Comparison with Balasubramanyam's Solution

In Balasubramanyam's study of the half-plane scattering problem in uniform flow [87], an asymptotic solution for point source scattering is given in terms of several non-standard complex valued functions such as the complex Fresnel integral and a complex signum function. The lack of precise definitions for the complex signum function and of the branch cuts in the complex square root functions introduces some ambiguity into the evaluation of the solution, which causes difficulty when attempting to compare (4.67) with Balasubramanyam's original solution. However, a ratio of the Kutta condition eigensolution to the ordinary no Kutta condition Green's function is given in [87], that is expressed in terms of standard functions. This ratio may be used to investigate the relative change in the far-field solution after the correction (4.37) is introduced. Taking the ratio of φ_G to φ_{KJ} and then expanding about $\tilde{r}_0 = 0$ gives,

$$\frac{\varphi_G}{\varphi_{KJ}} = 2j\tilde{k}\tilde{r}_0((M\sin\theta_D)^{-1} - \cos\tilde{\theta})\frac{\tilde{r}}{\tilde{R}_1} \tag{4.75}$$

Balasubramanyam's derivation of this ratio yields

$$\frac{\varphi_G}{\varphi_{KJ}} = 2j\tilde{k}\tilde{r}_0(M^{-1} - \cos\tilde{\theta})\frac{\tilde{r}}{\tilde{R}_1} \tag{4.76}$$

and so the impact of the correction to the solution is apparent in the factor $\sin\theta_D$ that multiplies the Mach number in (4.75).

4.5 Ray Tracing Solution for a Planar Acoustic Shield

The analysis of sound diffraction at a halfplane may be extended to arbitrary planar polygonal geometries in an approximate way through ray theory and in particular by application of the Geometrical Theory of Diffraction (GTD) [58]. Propagation effects due to a uniform base flow may be accounted for by solving the ray tracing equations in the Prandtl-Glauert domain. Hence, the problem of finding ray paths is reduced to a purely geometrical problem in the transformed domain, in which all rays travel in straight lines. Reflected rays may be computed from the law of specular reflection, ie. the incident ray angle is equal to the reflected ray angle, where angles are measured relative to the surface normal of the scatterer. Diffracted rays may be computed from Keller's law of edge diffraction, which states that the angle of diffraction and the angle of incidence are equal. In this case, the incident angle and diffracted angle are measured relative to the local tangent to the edge at the diffraction point, so that the set of diffracted rays form a cone centered on the diffraction point and with an axis aligned to the local edge tangent [58].

The main steps in obtaining the ray-tracing solution are as follows:

1. Apply the Prandtl-Glauert transformation to the planar geometry.

2. Define an infinite plane that contains the finite planar geometry. A point and a surface normal is sufficient to uniquely determine the plane.

3. Given a monopole source of known magnitude, define an image source as the reflection of the real source in the infinite plane.

4. In the Prandtl-Glauert domain, find the intersection of the line connecting the real source and the receiver with the infinite plane. Perform a point in polygon test on the intersection point and the polygon that describes the boundary line of the planar geometry. If the point lies inside the polygon, then the direct line of sight is obscured and no direct ray exists. If the point lies outside the polygon, the direct ray exists and the acoustic field may be calculated with (4.73).

5. The reflected ray is obtained by applying the law of reflection. In the Prandtl-Glauert domain, find the intersection of the line connecting the image source and receiver with the infinite plane. Repeat the point in polygon test as in the case for the direct line of sight ray. If the point lies inside the polygon, a reflected ray path exists and the reflected field may be calculated by (4.73).

6. Find all diffracted ray paths and amplitudes by applying the law of edge diffraction as described in the algorithm below.

7. Sum the contributions due to all ray paths for each acoustic source in the transformed domain and subsequently apply an inverse transformation to return to the physical domain.

To obtain the diffracted ray paths with a planar polygon, the following algorithm may be applied:

1. Choose one the finite length edge segments on the boundary of the polygonal scatterer and extend the edge artificially as a half-plane.

2. Establish local coordinates on the edge and compute the quantities $\tilde{r}$, $\tilde{r}_0$ and $d_0 + d$ as shown in Fig. 4.3.

3. Use the law of diffraction, which states that the angle of incidence on the edge must be equal to the angle of diffraction θ_D, to obtain the point of diffraction. This implies that $d = \tilde{r}(d_0 + d)/(\tilde{r} + \tilde{r}_0)$.

4. Test that the diffraction point lies on the finite section of edge length that forms part of the boundary of the scatterer. If the point is on the boundary, the diffracted ray exists and its amplitude may be computed with (4.74).

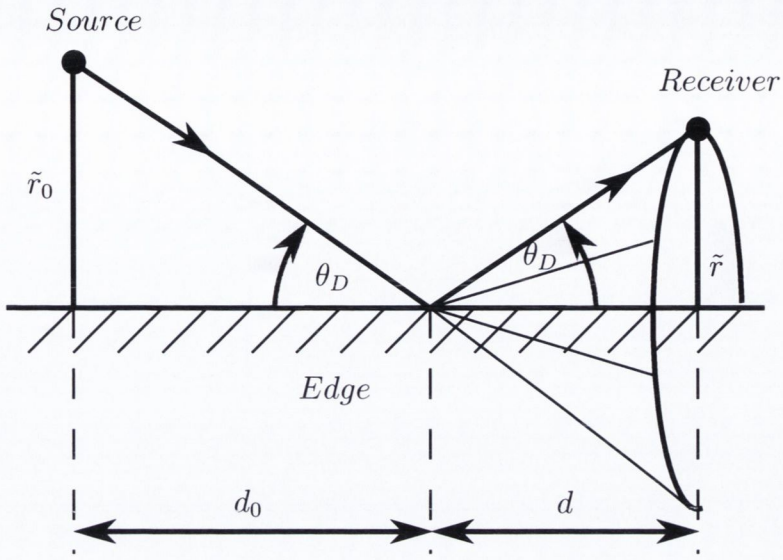


Figure 4.3: Schematic diagram of edge diffracted ray problem showing the Keller cone for edge diffraction.

5. If the diffracting edge is acting as a trailing edge in the flow, use (4.71) to add the contribution of the vortex shedding field to the ray amplitude.

6. Repeat the process for all edges and sources.

The ray paths for a sample calculation with a tapered wing insonified by a single monopole source are shown in Fig. 4.4. The red sphere shown above the wing is a monopole source in a location representative of a high acoustical shielding configuration for an aircraft engine. The blue spheres shown are two sample observer locations within the shadow zone of the wing. For these locations, the direct rays and the reflected rays are absent from the solution and only the edge diffracted rays exist.

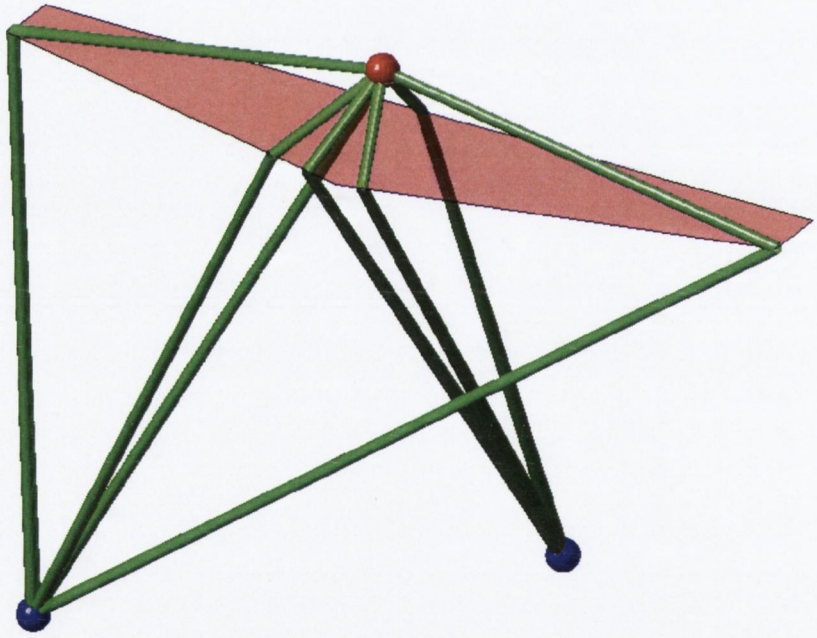


Figure 4.4: Edge diffracted ray paths for sample source and receiver points.

Chapter 5

Assessment of the BEM formulations

Acoustic scattering predictions for an isolated wing, insonofied by monopole sources, have been made with the BEM formulations detailed in the previous chapter and compared with reference solutions obtained by a ray tracing approach and by a commercial Linearized Euler solver (ACTRAN DGM). Ultimately, scattering predictions performed with any solver type must be validated against experiment data in order to assess the potential usefulness of computational tools for the design of low noise aircraft configurations. For the problem under consideration, reliable experimental results are difficult to obtain. Since this work deals primarily with the effects of flight on acoustic propagation, useful experimental data requires a well defined source that is modified by the flight effect in a predictable way. Although shielding measurements for jet noise and fan noise have been performed in programs such as NACRE, attempting to isolate the effects of convection on pure sound propagation from the modification of the sound source by the flow would introduce a major uncertainty into any interpretation of the cause of discrepancies between observed and predicted results. In the absence of directly applicable experimental data for the effects of flight on acoustic shielding, the BEM approach has been compared against two reference solutions. One of these is a high fidelity numerical method and the other is of semi-analytic type. This comparison may be considered as a weak form of validation for the BEM ap-

proach since the Linearized Euler solver has itself been validated for several similar propagation problems such as the radiation of aft fan noise through the bypass shear layer (carried out under TURNEX).

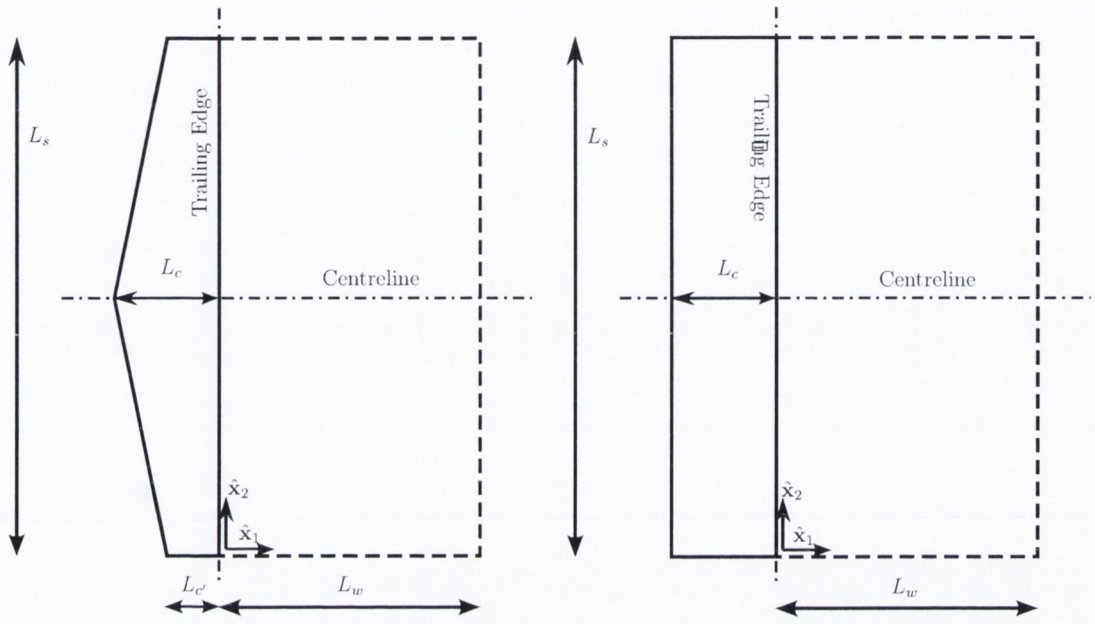
In pure acoustic modeling terms, the direct comparison of the LEE and BEM predictions also tests the assumptions provided in the reduction of the LEEs to the BEM formulation. The comparison of the BEM approach with the ray-traced solution tests several numerical aspects of the BEM model such as the artificial truncation of the wake and the validity of the vortex shedding model. The diffraction coefficients derived for the ray-tracing solution are based on the same assumptions as the BEM and therefore, give a good reference for numerical error in the BEM approach. Both methods should agree in the high frequency limit.

5.1 Description of Model Problem

A test geometry for the assessment of the BEM approach applied to aeroacoustic shielding is shown in Fig. 5.1. An isolated symmetric wing immersed in a low Mach number flow and insonified by a monopole, or multiple monopole sources, was chosen as a representative shielding problem since it includes most of the features of a general scattering problem with a full airframe. Specifically, the model problem involves sound propagation and scattering in a nonuniform lift-producing flow and is further complicated by the shedding of time-varying vorticity along the length of the trailing edge and the possible interaction of the sound field with the steady vorticity contained in the wake. Monopole sources are useful test sources for measuring flow refraction effects since the directional radiation pattern of the source is weakly affected by the presence of flow, which allows the effect of flow on pure propagation to be isolated from the modification of the source by a mean flow.

5.1.1 Wing Geometry

The dimensions of the wing and the free stream flow conditions used for flow simulations have been summarized in table Table. 5.1. The airfoil thickness profile has not



(a) Case A: Tapered Planform (b) Case B: Rectangular Planform

Figure 5.1: Wing Planform

Root Chord Length (L_c),	$[m]$	2
Span (L_s),	$[m]$	10
Tip Chord Length ($L_{c'}$),	$[m]$	0.8
Static Pressure at Infinity (P_∞),	$[Pa]$	101325
Density at Infinity (ρ_∞),	$[kg\ m^{-3}]$	1.176

Table 5.1: Wing geometry and free stream flow parameters

been specified in Table. 5.1 because two different profiles are used for the BEM and the LEE calculations. In order to apply the acceleration strategy described in Section. 3.5, the wing must be modeled as a zero thickness structure so that the thin structure BEM formulation applies. Since the mean flow is also modeled by a thin wing approximation, this simplification causes no difficulties in the BEM approach. However, an LEE simulation requires that the flow field is physically realistic everywhere in the domain and this criterion is not met by the flow field around an infinitely thin wing in the vicinity of the leading edge. Results from two dimensional potential flow theory show that a square root singularity appears in the potential when the leading edge has zero thickness and the airfoil produces lift (see [83]) . For this reason, a NACA 0009 (see Fig. 5.2) profile was selected as the wing profile for RANS flow calculations and for the LEE simulations running on top of the RANS flow. A thin symmetric NACA airfoil provides a very similar lift distribution to a flat plate airfoil under inviscid and incompressible flow conditions.

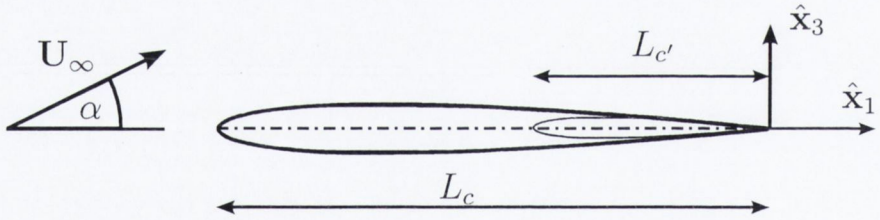


Figure 5.2: NACA 0009 thickness profile

5.1.2 Symmetry Planes and Source Position

A major computational saving can be made, for both RANS and LEE calculations, by taking advantage of the symmetry of the geometry. By introducing a symmetry plane passing through the centreline of the wing and with a surface normal pointing along the trailing edge (the x_2 direction), the domain size is effectively halved. An equivalent BEM problem consists of the full geometry with an image source placed at the reflection of the real source in the symmetry plane.

5.1.3 Far-Field Coordinates

For the purpose of assessing the performance of the BEM calculations in the far-field, the acoustic pressure distribution was computed on a sphere of radius 1km, centered on the source distribution. In the absence of a scattering obstacle, the acoustic pressure due to a monopole source in a quiescent medium is constant on the source sphere. Hence, the angular redistribution of acoustic energy caused by the presence of a scatterer is easily visualized in spherical coordinates centered on the source. For cases in which multiple sources or symmetry planes are present, the sphere is centered on the mean position of the distribution of sources. The coordinate system on this sphere is defined with respect to the source and the wing (see Fig. 5.3). The polar

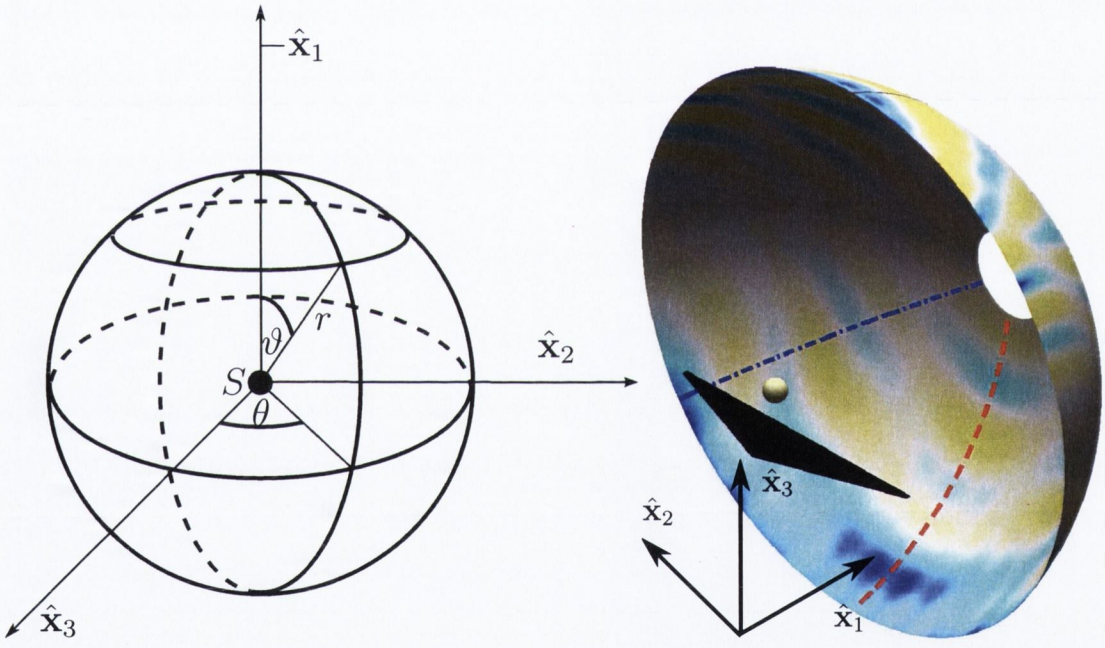


Figure 5.3: Left: spherical coordinates in the far field. Right: Diagram showing flyover plane (red line) and sideline plane (blue line). The wing is not to scale.

angle ϑ, is measured with respect to the vector pointing along the wing centreline, from the trailing edge to the leading edge ($-\hat{\mathbf{x}}_1$). This slightly unusual definition is chosen so that the far-field pressure plots presented in following sections can be interpreted in the same "direction" as the near-field plots, i.e. upstream points are located on the left hand side of a plot and downstream points are located on the right. The azimuthal angle θ, is measured from the $\hat{\mathbf{x}}_3$ axis in the x_3 x_2 plane. A flyover arc and a nominal sideline arc are defined on the sphere as the circular arcs with constant azimuthal

angle of 0° and 56° respectively. These curves are visible on the right hand plot of Fig. 5.3 by the red and blue lines.

5.2 Steady Flow Simulations

The steady flow solutions for the flow field surrounding the wing were obtained by two methods. The commercial finite volume RANS solver FLUENT, was used to obtain the steady flow field around the finite thickness airfoil while the potential flow solver described in Section. 3.4.6 was used to compute the mean flow potential for the BEM calculations. Three angles of attack $\alpha = 0°, 4°, 8°$, were considered and the free stream Mach number was set to $M_\infty = 0.3$, which is close to the highest Mach number at which the assumptions behind the BEM formulation may be applied and is representative of the flight speed of a jetliner at take-off and landing.

5.2.1 RANS Simulations

The volumetric mesh around the NACA 0009 wing was developed from a two dimensional C-grid, shown in Fig. 5.4(a) and Fig. 5.4(b). This planar grid was swept along the wingspan from the wing root to the wingtip. The remaining portion of the fluid volume was meshed with unstructured tetrahedral cells. The outer boundary of the C-grid was constructed from a parabolic arc that passes through the points $(20L_c, \frac{1}{2}L_s, 25L_c)$, $(-20L_c, \frac{1}{2}L_s, 0)$, $(20L_c, \frac{1}{2}L_s, -25L_c)$ that was meshed with 560 cells, and an outflow line from $(20L_c, \frac{1}{2}L_s, -25L_c)$ to $(20L_c, \frac{1}{2}L_s, 25L_c)$ that was meshed with 160 cells. The grid spacing in the surface normal direction of the first layer of boundary cells on the airfoil was adjusted so that the cell spacing near the leading edge is approximately $10^{-4}m$ and the spacing near the trailing edge is $10^{-3}m$. For the flow conditions under consideration, the quality of the C-grid was shown to be sufficient to achieve mesh independence of the surface pressure distribution for two-dimensional simulations and the boundary layer spacing satisfies the y^+ constraints for the FLUENT standard wall treatment, as detailed in the FLUENT user guide.

In the spanwise direction, the structured mesh contains 101 elements which gives a

total of 4524800 cells in the structured portion of the volumetric mesh. The spanwise element spacing was clustered near the wingtip so that the spacing was reduced to $3 \times 10^{-3} m$, where the flow is fully three dimensional.

The outer boundary of the unstructured portion of the mesh was constructed from the surface of revolution obtained by revolving the outer boundary of the C-grid about the $\hat{\mathbf{x}}_1$ axis (see Fig. 5.5). The unstructured mesh was developed using the GAMBIT meshing tool and the spacing of the mesh was adjusted so as to match, as closely as possible, the cell spacing of the structured mesh across the interface between the two zones. The growth in cell spacing with distance from the wing was controlled by attaching size functions to the wingtip faces.

All simulations were performed with the parallel version of FLUENT (version 6.3.26) using the pressure based implicit solver with default settings. The physical properties of the fluid were determined by the default values of air as specified in the FLUENT database, summarized in Table. 5.2. The variation in density was determined by the ideal gas law. Turbulence was modeled with a standard $k - \epsilon$ model with standard wall functions and default parameters, as shown in Table. 5.3. Pressure far-field boundary conditions were applied at the outer boundaries of the domain with the turbulent intensity set to 0.5% and the turbulent viscosity ratio set to 10. These parameters reflect normal atmospheric flight conditions. A symmetry boundary condition was applied to the translated x_1 x_3 plane containing the wing centerline.

Cp (Specific Heat) ,	$[j/kg - K]$	1006.43
Thermal Conductivity ,	$[w/m - K]$	0.0242
Viscosity,	$[kg/m - s]$	1.7894e-05
Molecular Weight ,	$[kg/kgmol]$	28.966

Table 5.2: Properties of air from FLUENT material database

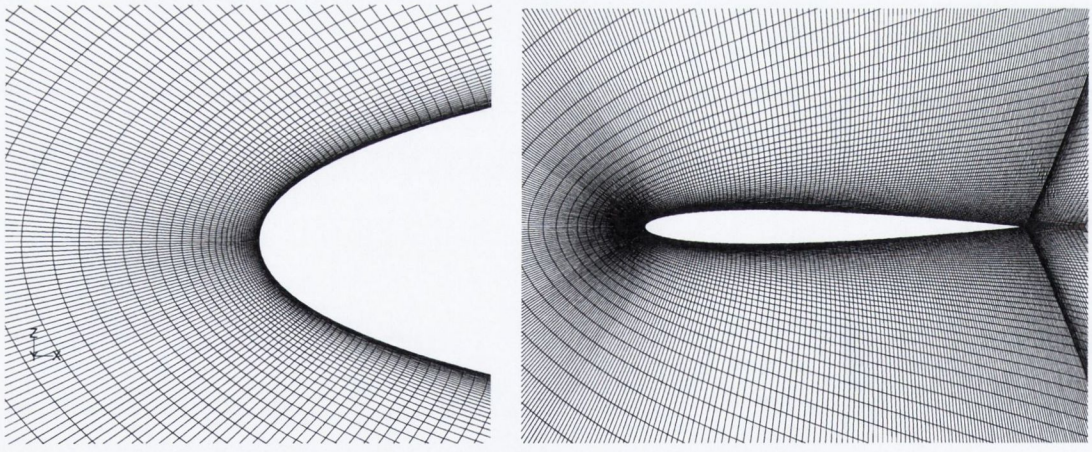
Cmu	0.09
C1-Epsilon	1.44
C2-Epsilon	1.92
TKE Prandtl Number	1

Table 5.3: k-epsilon model constants from FLUENT database

For reasons relating to the interpolation of RANS results onto LEE meshes, a zero

wall shear stress boundary condition was applied to the wing surface. This removes the need for a projection of the outer inviscid flow onto the surface of the wing as an intermediate step in the interpolation procedure. The accuracy of the flow interpolation procedure is critical to the stability of the LEE simulations as will be discussed in later sections. However, to demonstrate that the presence of attached boundary layers has a minimal effect on the outer inviscid flow, for the given Reynold's number of the model problem, the FLUENT simulations were repeated for the $\alpha = 8°$ with a no slip wall condition on the wing.

From inspection of figures (5.6-5.9) it is clear that the production of lift adds considerably to the nonuniformity of the steady flow Mach number. In addition, the peak Mach number in the symmetry plane increases from 0.35 to 0.49 when the angle of attack is increased from 0° to 8°. However, these high velocities occur in a relatively small area of the symmetry plane and over the majority of the domain, the Mach number may be considered small.



(a) RANS grid near the leading edge (b) RANS grid near the wing

Figure 5.4: FLUENT RANS grid on the symmetry plane

5.2.2 BEM Flow Simulations

The steady flow data, used as input to the acoustic BEM code, were calculated with a steady potential flow BEM solver on a planar wing geometry. The Toeplitz acceleration strategy for the planar BEM allows for very fast mean flow calculations, which makes it

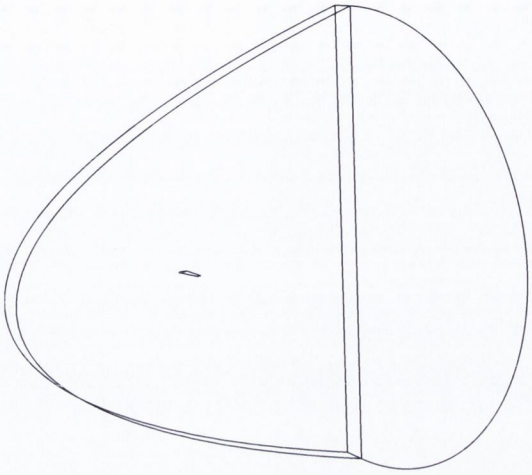


Figure 5.5: Outer boundary of the RANS mesh showing the boundary between structured and unstructured portions of the mesh

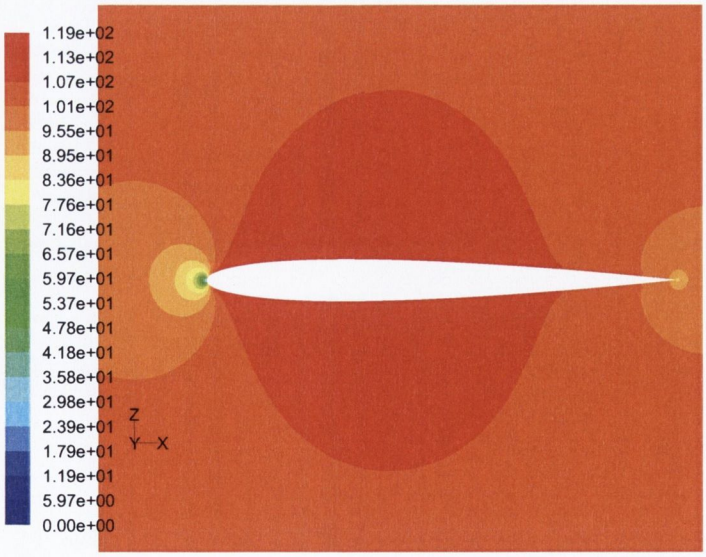


Figure 5.6: Contours of velocity magnitude on the symmetry plane, $\alpha = 0°$

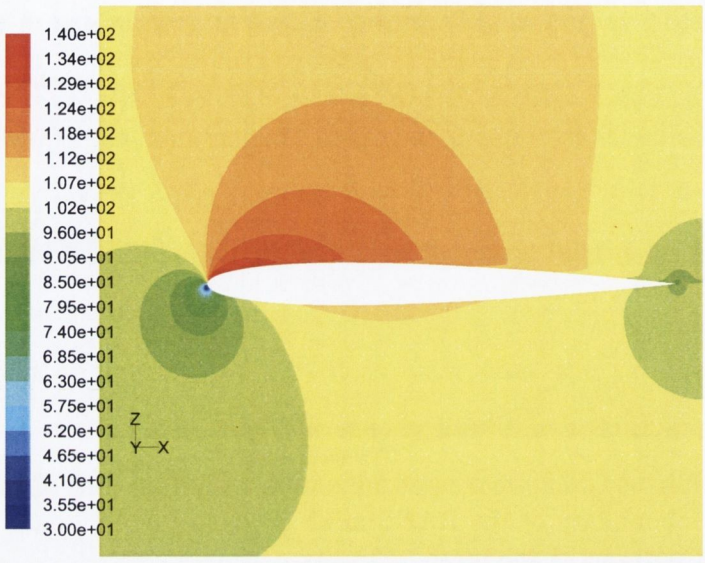


Figure 5.7: Contours of velocity magnitude on the symmetry plane, $\alpha = 4°$

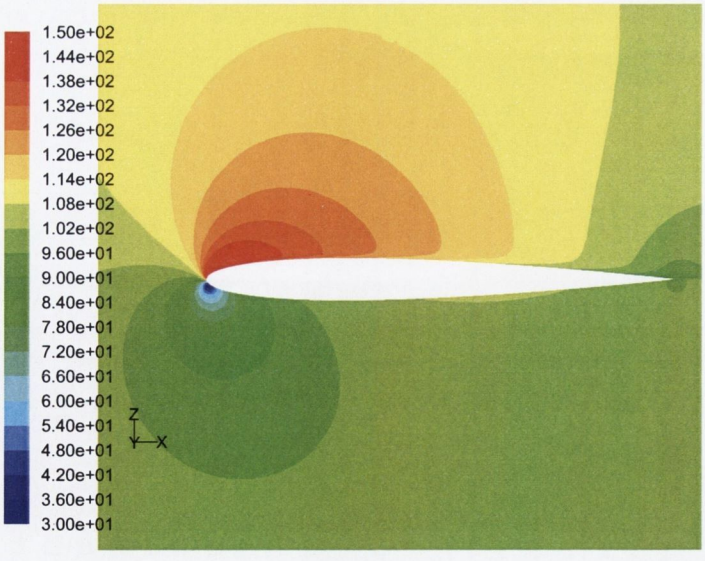


Figure 5.8: Contours of velocity magnitude on the symmetry plane, $\alpha = 8°$

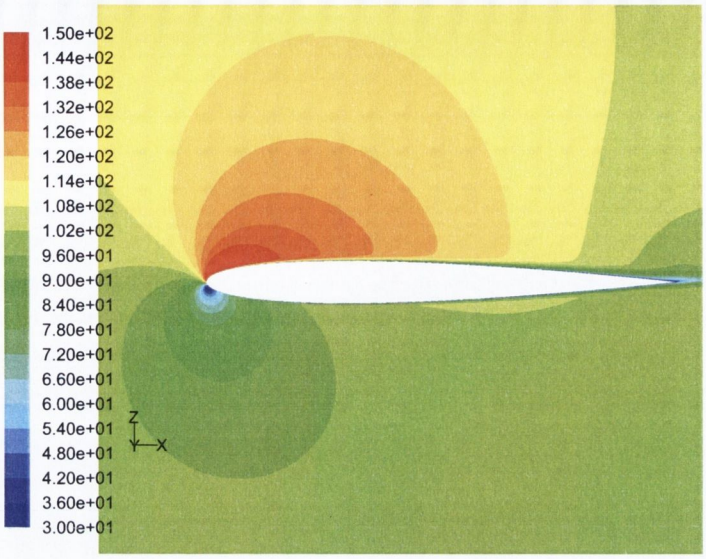
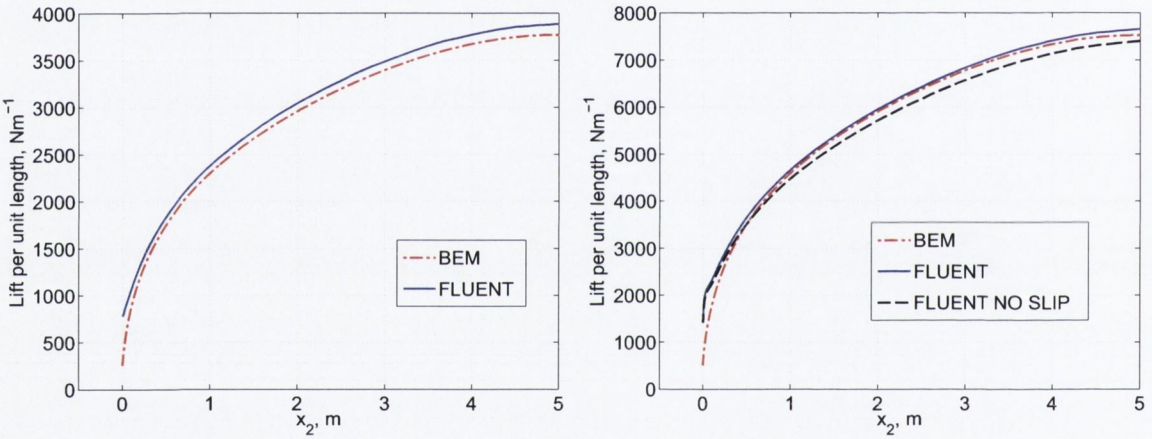


Figure 5.9: Velocity magnitude on the symmetry plane (No Slip Condition), $\alpha = 8°$

practical to compute the steady potential on the same mesh as the acoustic calculation, as a preprocessing step for each case.

Since the nonuniform refraction effects in the BEM approach are primarily controlled by the trailing edge distribution of circulation, through the phase shift τ, the fine details of the potential flow over the full acoustic domain are not relevant to the acoustic calculation stage. The distribution of trailing edge circulation is intrinsically linked to the spanwise lift distribution under thin airfoil theory, this implies that the spanwise lift distribution is a good measure of the correspondence of the BEM and FLUENT simulations, when treated as inputs to an acoustic BEM calculation. Examining Fig. 5.10(a) and Fig. 5.10(b), the lift distribution predicted by the potential flow solver agrees closely with the FLUENT simulations except near the wingtips ($x_2 = 0$) where a strong vortex forms in the RANS solution. This suggests that the potential flow solution and RANS solution are well matched and provide a fair comparison for the purposes of comparing the acoustic simulations that run on top of the computed base flows.



(a) Lift distribution, $\alpha = 4°$

(b) Lift distribution, $\alpha = 8°$

Figure 5.10: Comparison of predicted spanwise lift distribution for BEM and FLUENT solutions

5.3 Solution Procedures

5.3.1 BEM Solution

The solution procedure for the BEM solver in a nonuniform flow is relatively straightforward and only adds one additional stage to the procedure in the absence of flow. As a preprocessing step, the steady potential flow is calculated and the distribution of circulation along the span is extracted. The circulation distribution and the mean velocity field on the wake are input to the acoustic BEM solver, which computes the transformed acoustic potential distribution on the scatterer surface. An additional propagation step is required to obtain the potential, and the derivatives of potential, in the far-field. The pressure in the far-field is then obtained via Bernoulli's equation.

The MATLAB implementation of the iterative Krylov solver BICGstab was used at the linear solver stage for all BEM calculations. A tolerance of 10^{-3} on the relative residual was found to be sufficient for convergence of the solution when engineering accuracy is required. For high accuracy solutions, the grid spacing and relative residual tolerance should be lowered in tandem. Although the mesh spacing for the mean flow solver has different requirements to the acoustic mesh, it was found that using the same meshes for both calculations had little effect on quality of mean flow results for the frequencies tested.

5.3.2 LEE Solution

The solution procedure for the LEE solver is slightly more involved than for the BEM solver. As with the BEM approach, the first stage is to calculate the steady flow solution with some form of CFD solver such as a RANS solver. This base flow is then interpolated onto the acoustic mesh with a preprocessing module supplied with ACTRAN DGM. The LEE solver that runs on top of the base flow is implemented as a time-stepping method which is driven by a time-harmonic source (in the continuity equation), and the solution is marched in time from a zero field initial solution until a time harmonic solution is achieved on the outer boundaries of the domain.

The pressure in the far field is obtained with a post-processing module that cal-

culates a Fast Fourier Transform (FFT) of the time signal on the outer boundary and then implements a Ffowcs-Williams Hawkings (FW-H) surface integration, which propagates the near-field solution to the far-field.

5.3.2.1 Meshing Requirements

The size of the LEE problem at hand constitutes a significant computational challenge even with medium scale parallel processing. In fact for the given geometry, a frequency of 500Hz was close to the upper limit of the capabilities of the available computational resources. Achieving a good compromise between a practical solution time and physical accuracy and also stability of solution was therefore critical to the success of the solution process.

It was found that the minimum element size was the most sensitive mesh parameter with regard to solution time and the stability of the solution. A wide variation in element size may be tolerated by the DGM scheme because each individual element is permitted to have a different order of internal polynomial interpolation. However, the time-step for the marching process is determined by the minimum element size and therefore, it is critical that the elements are made as large as possible without under-resolving the mean flow.

The LEE domain consists of a box of size $(4L_c \times 3.5L_c \times 2.5L_c)$ surrounding the wing surface, which in turn is surrounded by a buffer zone of thickness L_c. The purpose of the buffer zone is to absorb outgoing waves and thus minimize the reflections from the outer artificial boundary. The ideal mesh size for the DGM scheme is determined from the free stream Mach number, the free stream sonic speed and the frequency of the source by the relation

$$\Delta s = 1.5 \left[2\pi\omega^{-1} c_\infty (1 - M_\infty) \right] . \tag{5.1}$$

For the 500Hz source, this criterion produces a mesh spacing of $\Delta s \approx 0.7m$ which is significantly larger than the thickness of the wing. In the vicinity of the wing and particularly near the leading edge, the mesh was refined, in order to resolve the mean flow and the geometry of the wing. The spacing was reduced by a factor of 20 in the

leading edge zone and smoothly blended into the coarse mesh with the size function tool in GAMBIT. This local refinement is visible in Fig. 5.11.

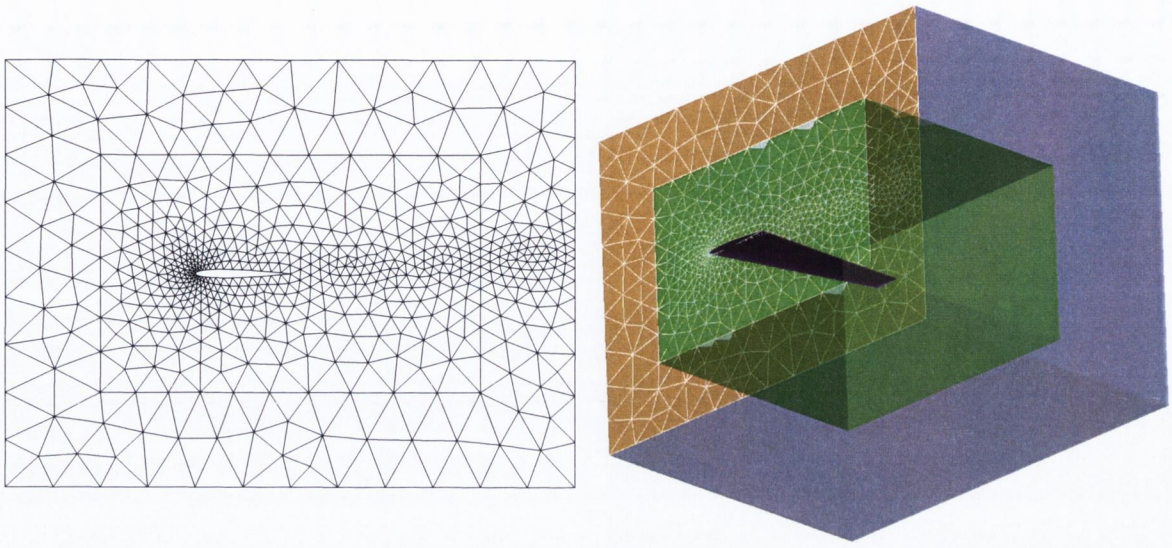


Figure 5.11: Left: Acoustic mesh (LEE) on the symmetry plane. Right: LEE domain showing buffer zone (blue)

5.3.2.2 Mean Flow Interpolation

It is important to note that a good interpolation of the CFD solution onto the acoustic grid proved to be of critical importance in obtaining a stable time-stepping of the LEE solution. The key stage in this process is the regularization of the flow field on the surface of the wing. Since a viscous RANS solution satisfies a no slip boundary condition on a wall, the flow from just outside the boundary layer must be projected onto the surface of the wall and the normal components of velocity must be set to zero, which ensures that the mean flow does not penetrate the surface of the scatterer. ACTRAN DGM provides a built in pre-processing routine to perform this type of regularization. For better control over the process of regularization, the flow data was imported into MATLAB and regularized by a different procedure , which is described in the following paragraph.

The LEE mesh is comprised entirely of tetrahedral elements. This means that for any given boundary node on a curved portion of the acoustic surface mesh, the surface normal is non-unique and must be approximated by a weighted sum of the surface normals from the neighbouring elements. Stable results were obtained by selecting

the normal direction from the list of neighbouring element normals with reference to the flow velocity vector. A particular element was selected from the list of connecting elements so that the flow velocity points into that element. Although crude, this process was found to produce the smoothest interpolation of the flow field in the leading edge region of the LEE mesh. It was also found from numerical tests that the most stable results were obtained by foregoing the projection step and replacing the viscous RANS solution with the flow field obtained with a slip wall boundary condition.

5.4 Scattering Predictions in Non-Lifting Flow

Results of shielding prediction by the ray-tracing and BEM methods for a non-lifting mean flow are now presented. Two shielding configurations were considered. Firstly, a thin planar wing with the dimensions given in Table. 5.1 was insonified by a unit strength monopole at position $(-0.5L_c, 0.5L_s, 0.5L_c)$. This configuration is referred to as case A. The ray-tracing approach was found to perform poorly for this configuration due to the strong influence of the vertex scattering on far-field pressure. The second configuration, referred to as case B, consists of an untapered rectangular wing with the same chord length and aspect ratio as the tapered wing and which was also insonified by a monopole at $(-0.5L_c, 0.5L_s, 0.5L_c)$. Case B is considered a better geometry for the comparison of the ray tracing method with the BEM approach because the corner diffracted fields are significantly reduced for this configuration. For both configurations, the frequency has been set to $500Hz$, which corresponds to a kL_c value of 18.1. It should be noted that the absolute value of the far field pressure has no physical significance in the plots that follow. The sound pressure level (SPL) values are plotted and compared with shielding factor values purely to illustrate the effect of convection on a unit strength monopole source, relative to no flow conditions. The shielding factor is defined as the ratio of the shielded acoustic pressure to unshielded acoustic pressure.

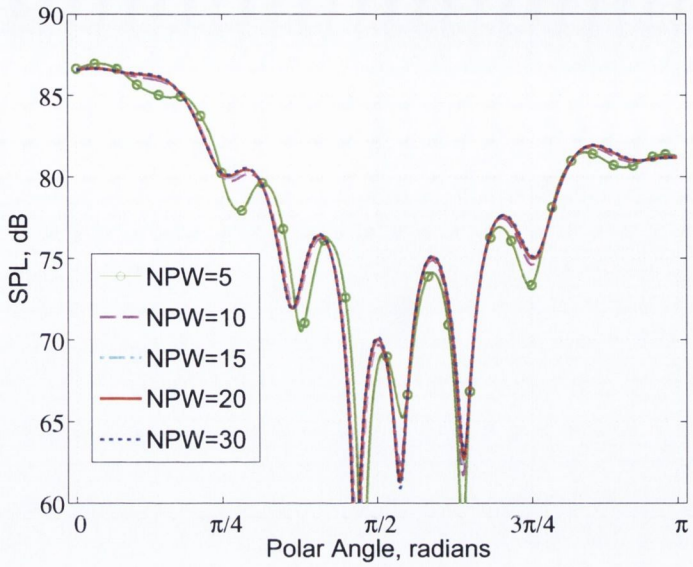
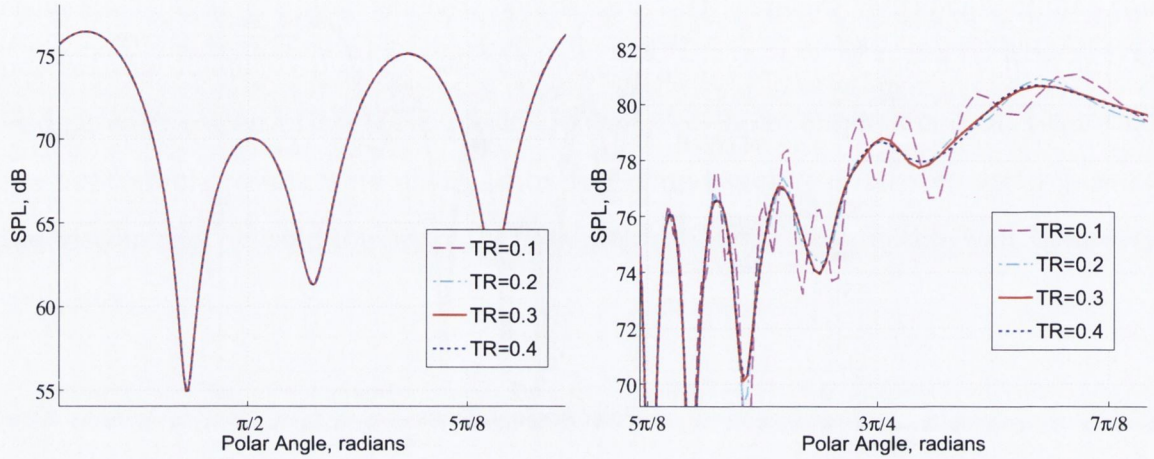


Figure 5.12: Convergence of far-field BEM solution with grid resolution, 500Hz, WR=3, TR = 0.3

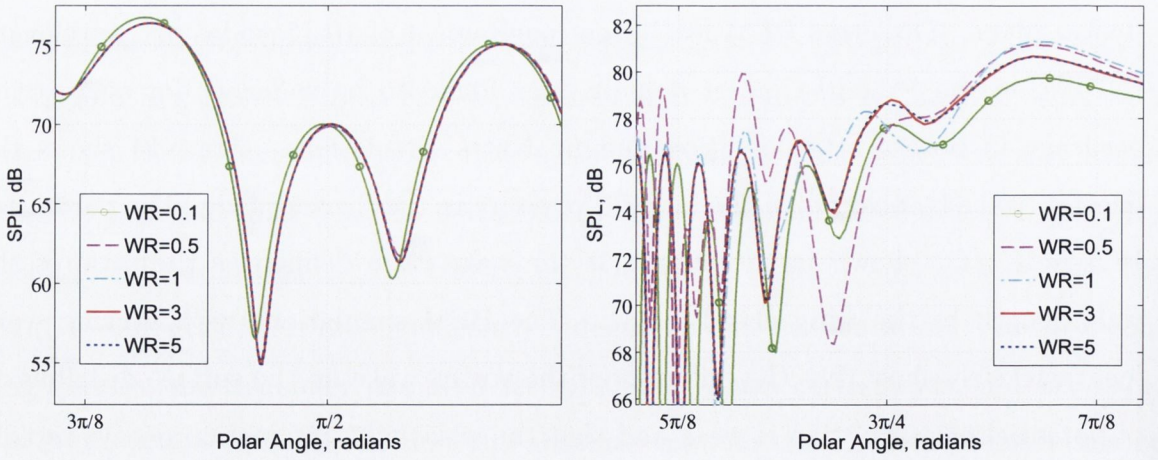
5.4.1 Convergence Studies

An initial study of the wake truncation length and resolution requirements of the PG BEM scheme was performed with the Case A geometry, to determine appropriate values for the wake length, the extent of the wake damping region and the grid spacing. Fig. 5.12 shows the effect of varying the grid resolution on the far-field pressure in the flyover plane. The usual BEM resolution requirement of 10-15 nodes per wavelength (NPW), in the Prandtl-Glauert domain, was found to be sufficient for engineering accuracy in both Kutta condition and no Kutta simulations. Fig. 5.14 shows the effect of wake truncation on the far-field pressure in the flyover plane. The parameter $WR = L_w/L_c$, shown in the legend, is the wake ratio defined as the ratio of the wake length to the wing chord length. The BEM simulations with varying wake lengths clearly show that the influence of the vortex wake on the surface distribution of potential over the wing is weak and that the wake-wing interaction decays rapidly beyond a few convective wavelengths downstream of trailing edge. For the lower Mach number case, the solution converges rapidly over the entire far-field source sphere. The high Mach number case is slower to converge in a zone around the polar angle $\frac{3}{4}\pi$ radians, in the flyover plane. This behavior is caused by the larger convective wavelength of the vortex wake for high Mach numbers.



(a) Flyover shielding, $M = 0.3$ (b) Flyover shielding, $M = 0.9$

Figure 5.13: Convergence of far-field BEM solution with taper ratio, Case A, 500Hz, WR=3, NPW=20



(a) Flyover shielding, $M = 0.3$ (b) Flyover shielding, $M = 0.9$

Figure 5.14: Convergence of far-field BEM solution with wake ratio, Case A, 500Hz, TR=0.3, NPW=20

The length of the wake damping zone also has an impact on the convergence of the solution in the far-field. Although the strategy for wake truncation was found to have a weak influence on the BEM solution in general for non-lifting flow cases, the far-field propagation step showed greater sensitivity to the details of wake truncation. Shielding curves for a fixed wake length of $L_w = 3L_c$ and with varying wake transition ratios are plotted in Fig. 5.13. The transition ratio $TR = L_t/L_w$ is defined as the ratio of the transition zone on the wake to the total wake length. For low Mach numbers the solution converges rapidly with TR and as a rule of thumb, the solution was found to converge once the the vortex damping region contained a few convective wavelengths. Arguments from the stationary phase method may be applied here to explain the requirement for a smooth transition of the wake vorticity from finite values down to zero. During the propagation step, the distribution of surface potential jump is convolved with the derivative of the Green's function to obtain the radiated potential in the far-field. The dominant contribution to this integral occurs at points where the phase of the integrand is a local extremum point. Consider the case of a constant potential jump on the wake. The phase of the integrand then varies purely with the distance between the source point and the receiver point, which implies that a local stationary phase point exists where the distance between the wake and the receiver point is a local minimum (not located at the wake boundary). For a planar wake, this point is located at the projection of the receiver point on the wake surface along the surface normal direction. If the constant potential jump on the wake is replaced by a function of the form

$$\delta\varphi = \exp\left(-jK_v\eta_1\right) \tag{5.2}$$

then the stationary phase point is located at the projection of the receiver point along a vector with angle α to the wake surface normal, where

$$\alpha = \sin^{-1}(K_v/K). \tag{5.3}$$

Since the convective wavenumber in the Prandtl-Glauert domain, K_v, is always larger than the acoustic wavelength of the Green's function kernel, K, the integrand never has a stationary point when the observer is located in the far-field. However, the endpoint

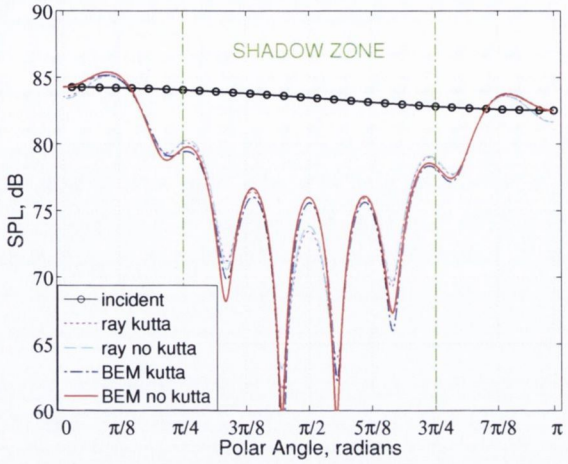
contribution to the integral can be significant if the wake is truncated artificially with a discontinuous jump in wake vorticity at the wake truncation line. A smooth tapering of the wake vorticity over a few convective wavelengths will remove the endpoint contribution from the integral leaving only the contribution from the integral over the wing surface.

From numerical testing it was found that optimal values of WR and TR depends on the Mach number of the mean flow and on the frequency of the source. However, for convenience the values of $WR = 3$, $TR = 0.3$ and $NPW = 15$ were used in all tests unless otherwise noted. These values were sufficient for convergence of the solution in the far-field.

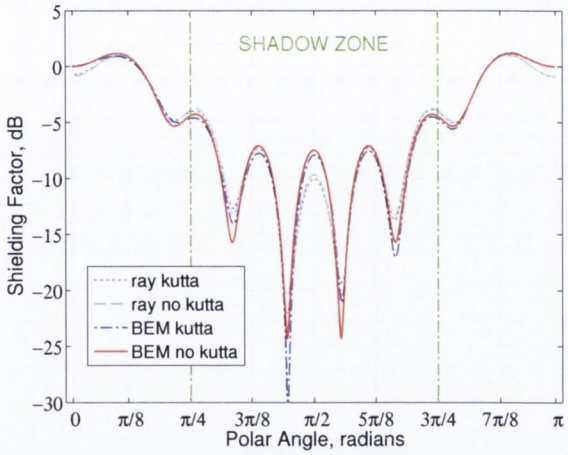
5.4.2 Effect of Kutta Condition in non-lifting Flow

To study the effects of vortex shedding on the far-field solution, a comparison of the solutions with and without the Kutta condition, was made for three Mach numbers $M = 0.1$, $M = 0.3$ and $M = 0.9$. While the first two Mach numbers are characteristic of low Mach number flight speeds, the third case was chosen to deliberately exaggerate the vortex shedding effects, which were found to be almost negligible at low Mach number.

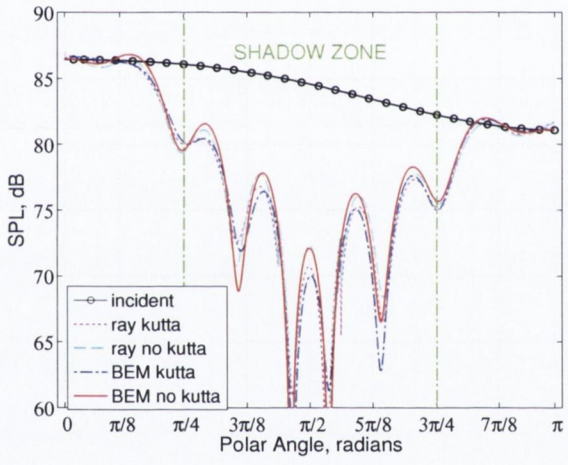
A comparison of far-field pressure and shielding factor in the flyover plane is shown in Fig. 5.15. One feature of the SPL plots that is immediately apparent for all solutions, is the Doppler amplification of the incident pressure field due to convection, visible in Fig. 5.15 While the modification of the pressure field is dominated by this phenomenon, the Doppler amplification is noticeably absent from the shielding factor plots due to cancellation of this factor by taking a ratio of the scattered and incident fields. The modest effect of convection on the shielding factor at low Mach number is visible when comparing Fig. 5.15(b) and Fig. 5.15(d). A maximum change of 5dB in the flyover shielding factor is noticeable at a polar angle of $\pi/2$ radians when the Mach number is increased from $M = 0.1$ to $M = 0.3$, however this feature is mostly an artifact of the local change in the interference pattern rather than a global redistribution of acoustic energy. At the highest Mach number, the effect of convection has a significant impact



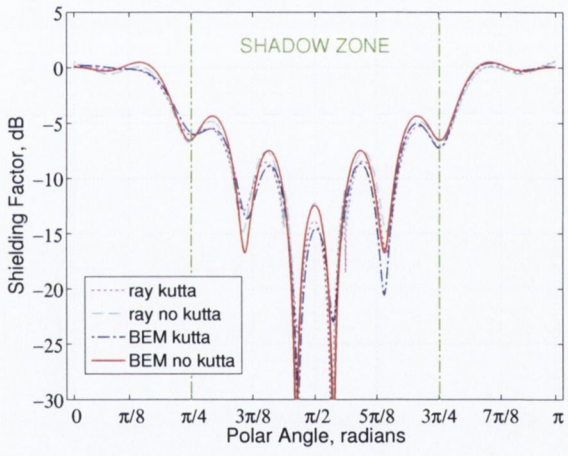
(a) SPL, $M = 0.1$, flyover



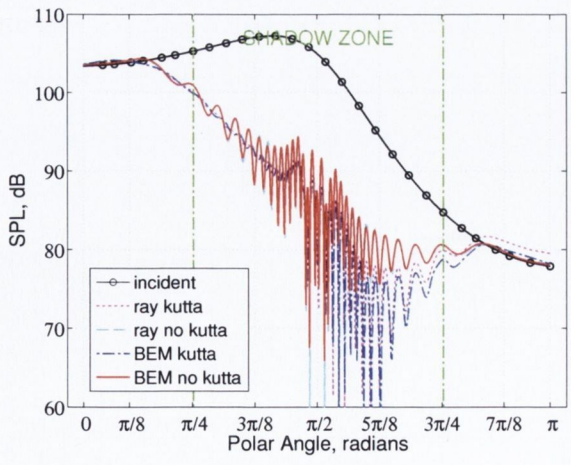
(b) Shielding Factor, $M = 0.1$, flyover



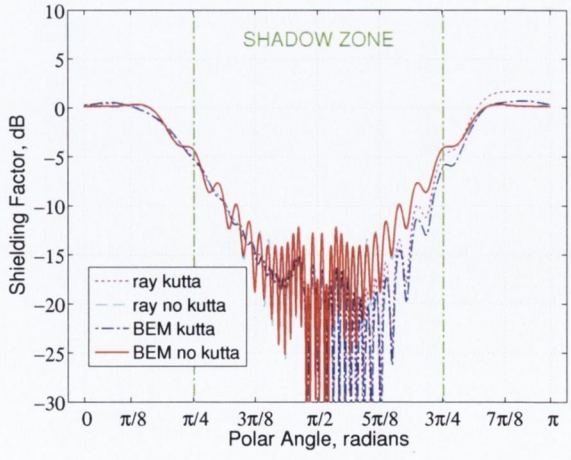
(c) SPL, $M = 0.3$, flyover



(d) Shielding Factor, $M = 0.3$, flyover



(e) SPL, $M = 0.9$, flyover



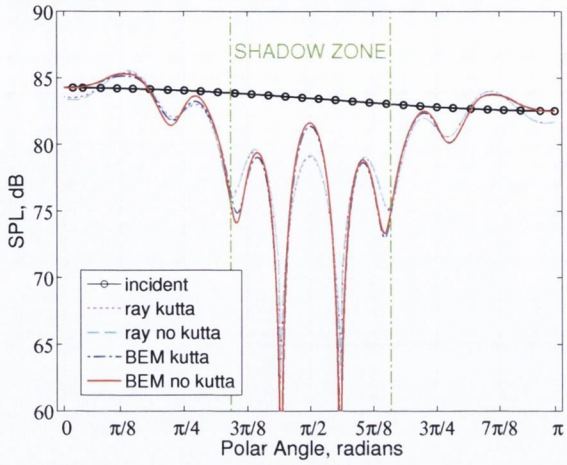
(f) Shielding Factor, $M = 0.9$, flyover

Figure 5.15: Case B: Variation of far-field pressure with Mach number and Kutta condition in the flyover. Left: Pressure in the flyover. Right: Shielding factor in the flyover.

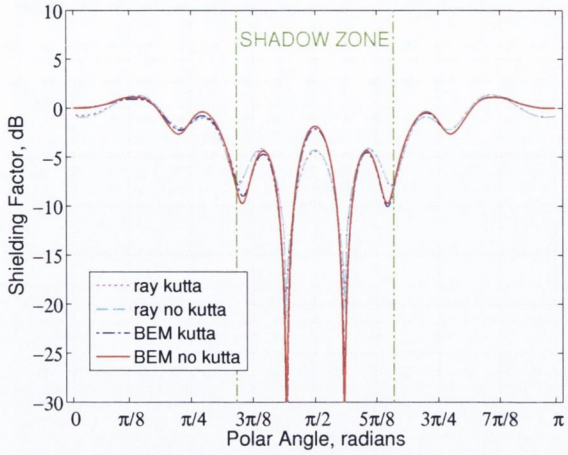
on the scattered field. For $M = 0.9$, the apparent chord length in the Prandtl-Glauert domain is 5 times larger than the true chord length, which explains both the high shielding factors and the highly oscillatory interference pattern in the far-field, visible in Fig. 5.15(f).

The effect of applying a Kutta condition can be estimated by comparison of the No Kutta solutions (magenta and red) with the full Kutta condition solutions (cyan and blue) in Fig. 5.15 and Fig. 5.16. At the lower Mach numbers, the application of a Kutta condition at the trailing edge provides a near negligible modification of the far-field pressure. For the high Mach number case, the overall trend is masked by the highly oscillatory interference pattern. In Fig. 5.17, this interference pattern has been removed, by two different methods, to expose the smoothly varying trend that is characteristic of real shielding experiments with aeroacoustic sources. The left hand plot shows the shielding factor after post-processing by a zero phase implementation of a Butterworth filter in MATLAB. As an alternative to filtering the far-field data of a single frequency solution, a frequency averaged shielding factor may be derived from a simulated source spectral density. For the results shown, the acoustic power was assumed to be constant over a third octave band, which was centered on the target frequency. Both procedures give a smoother shielding curve that shows a clear increase in shielding for the Kutta solution in the flyover for polar angle between $\pi/2$ and $3\pi/4$, with the largest increase of approximately -8dB occurring at $3\pi/5$ radians. By contrast, even at high Mach number the shielding factor in the sideline is relatively unaffected by vortex shedding at the trailing edge. This behavior is to be expected since the asymptotic solution for the half-plane problem clearly shows a decay in the Kutta condition induced field as the the sideline angle in increased, through the factor β in Eq. 4.71. The maximum influence of vortex shedding on the far-field behavior is correctly predicted to occur in the flyover.

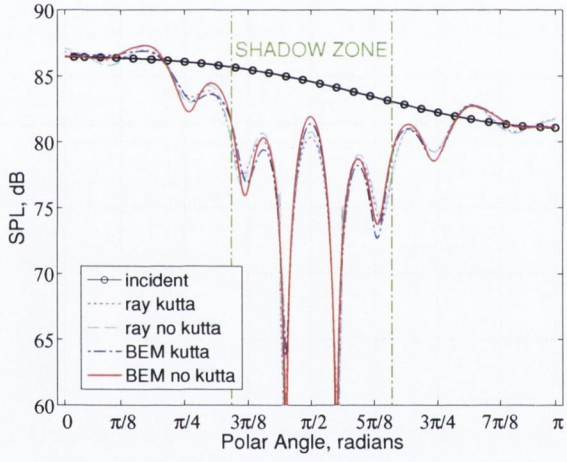
Overall, the shielding results for case B show reasonable agreement between BEM and ray-traced solutions. The tendency for closer agreement at higher frequencies and at larger Mach numbers is to be expected since the interaction of the edge diffracted fields, which is a secondary diffraction process that is neglected in the ray-traced solution, decays relative to the primary field with increasing Prandtl-Glauert wavenumber



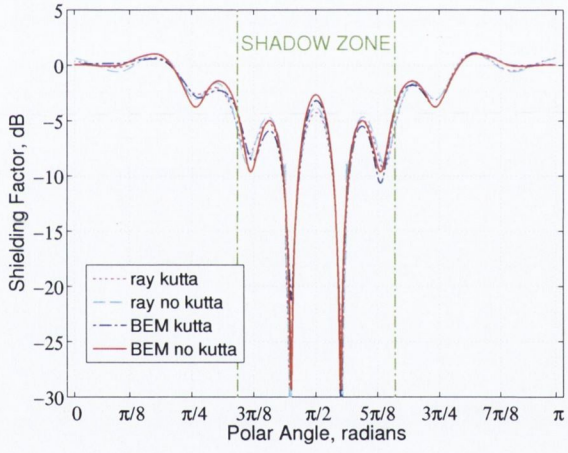
(a) SPL, $M = 0.1$, sideline



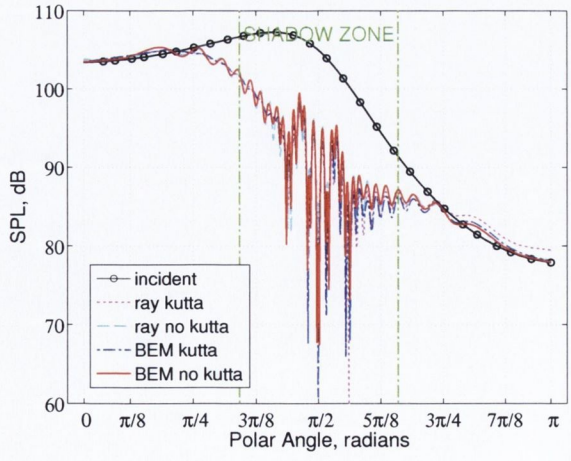
(b) Shielding Factor, $M = 0.1$, sideline



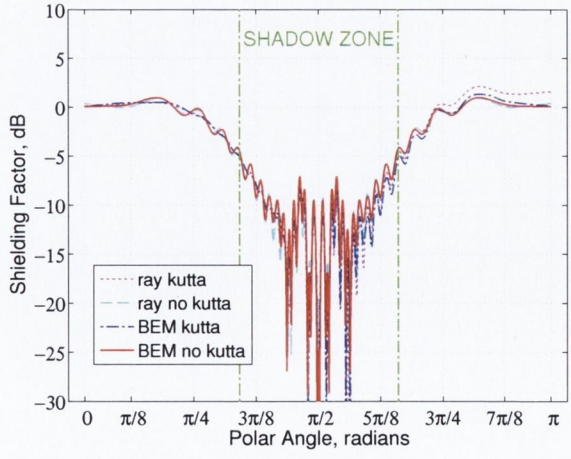
(c) SPL, $M = 0.3$, sideline



(d) Shielding Factor, $M = 0.3$, sideline

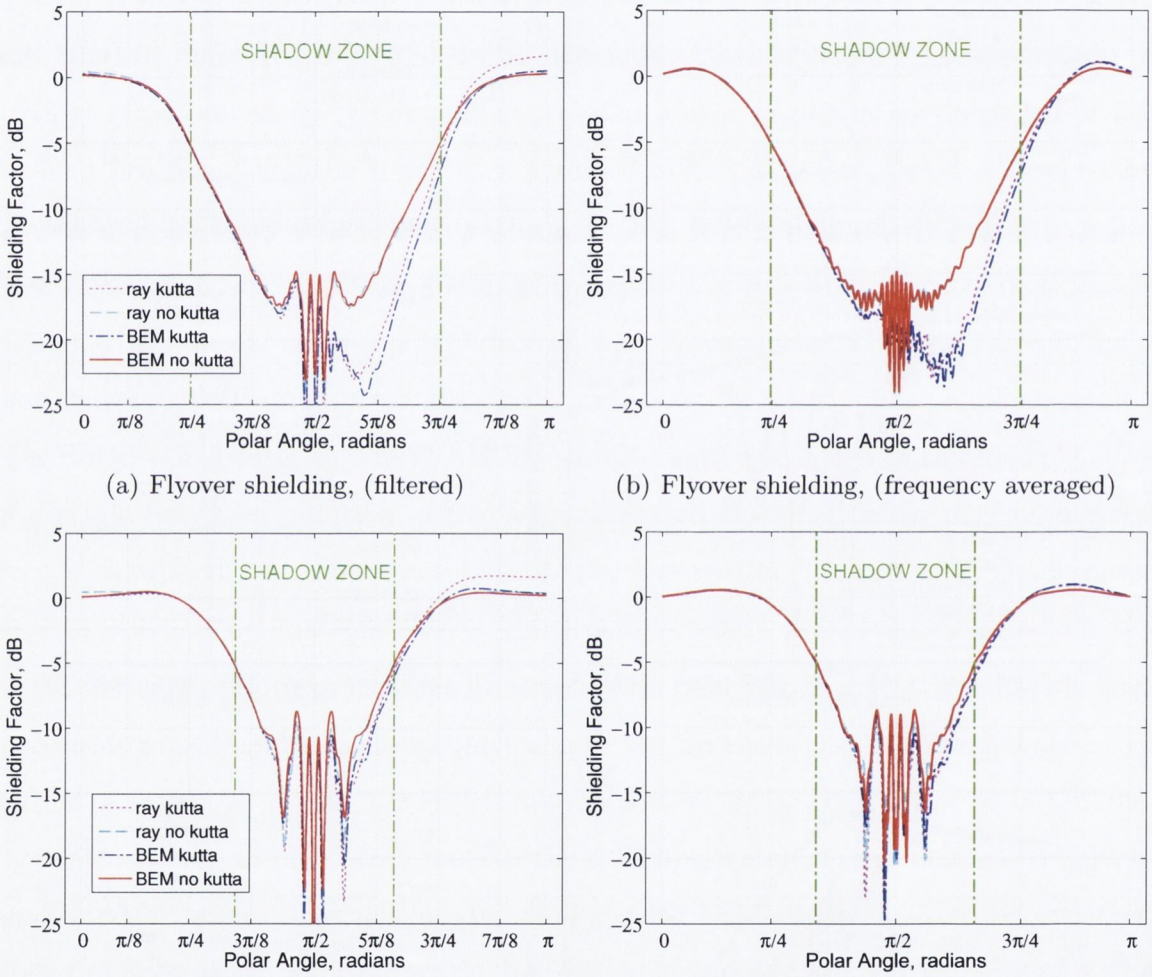


(e) SPL, $M = 0.9$, sideline



(f) Shielding Factor, $M = 0.9$, sideline

Figure 5.16: Case B: Variation of far-field pressure with Mach number and Kutta condition in the sideline. Left: Pressure in the sideline. Right: Shielding factor in the sideline.



(a) Flyover shielding, (filtered)

(b) Flyover shielding, (frequency averaged)

(c) Sideline shielding, (filtered)

(d) Sideline shielding, (frequency averaged)

Figure 5.17: Smoothed shielding factor, Case B $M = 0.9$. Ray-traced (Kutta); Magenta :, Ray-traced (No Kutta); Cyan –, BEM (Kutta); Blue –·, BEM (No Kutta), Red -

K, and with increasing separation of the edges in the Prandtl-Glauert domain. At lower Mach numbers, the difference between the ray-tracing and BEM solutions is more significant than the effect of the Kutta condition, but the relative change produced by vortex shedding is similar for both formulations. For $M = 0.9$, the impact of vortex shedding is much more pronounced and is easily distinguished from the error in the ray-tracing method. The smoothed shielding curves for BEM and ray-traced solutions match well for this case and suggest that the BEM solution does converge to the correct solution despite the artificial truncation of the wake and the use of discontinuous boundary elements at the wing-wake junction. This is further validated by examination of the vortex shedding amplitude of the BEM solution, which closely resembles the amplitude predicted by the half-plane solution as shown in Fig. 5.18 and Fig. 5.19.

Conversely, the scattering predictions for case A shows poor agreement between BEM and ray-traced solutions as expected (see Fig. 5.20). The discrepancy in this case is due to a strong contribution of the vertex diffracted wave, emanating from the vertex on the symmetry plane, that is present in the BEM solution but is unaccounted for in the ray-traced solution. This highlights one of the weaknesses of a simplified ray-tracing approach for shielding calculations, in that higher order diffraction mechanisms can become important contributors to the scattered field in the shielded region when the complexity of the geometry increases. The accuracy of a ray prediction is, therefore, sensitive to the existence and inclusion of ray models for high-order scattering modes. Sophisticated methods are usually required on realistic geometries where multiple diffraction-reflection mechanisms become possible and where vertex diffraction and "whispering gallery" type modes can occur.

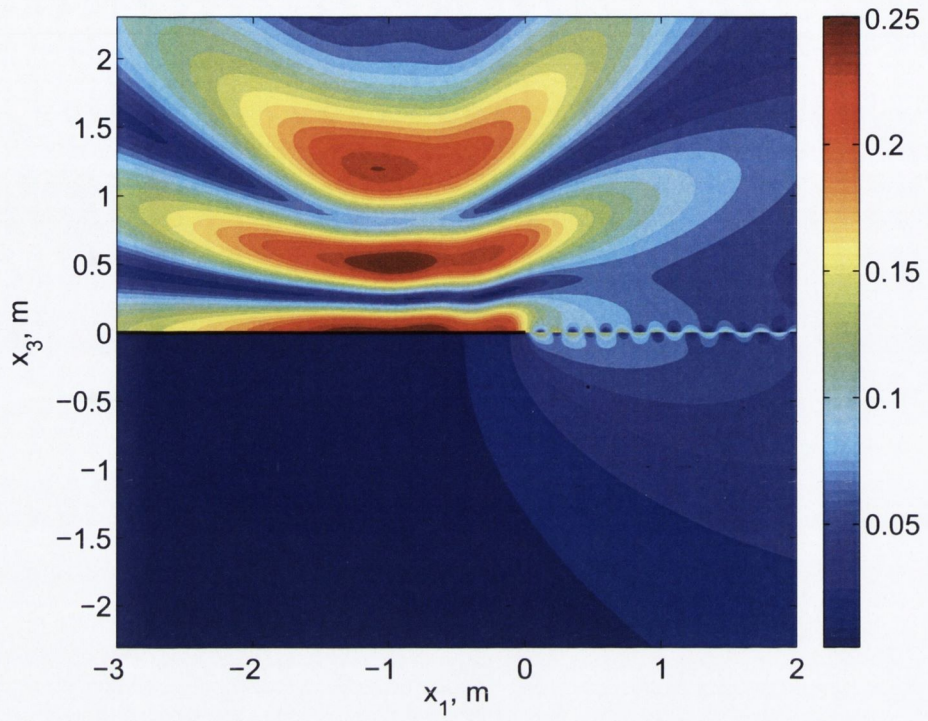


Figure 5.18: Near field contours of the magnitude of the acoustic potential, $|\phi|$. Half plane solution, $x_2 = 2L_c$

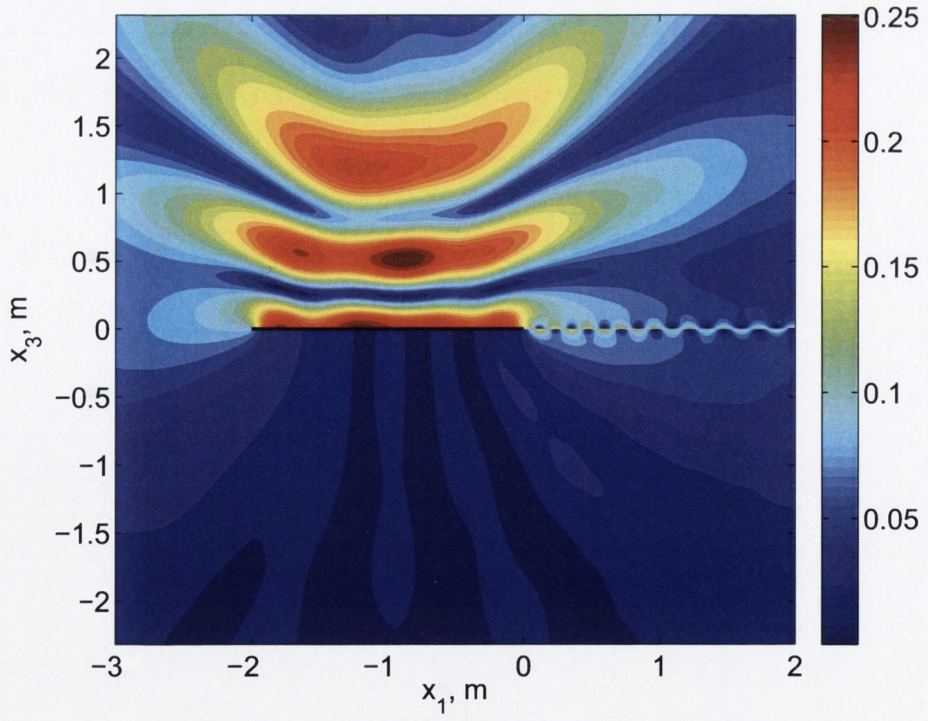
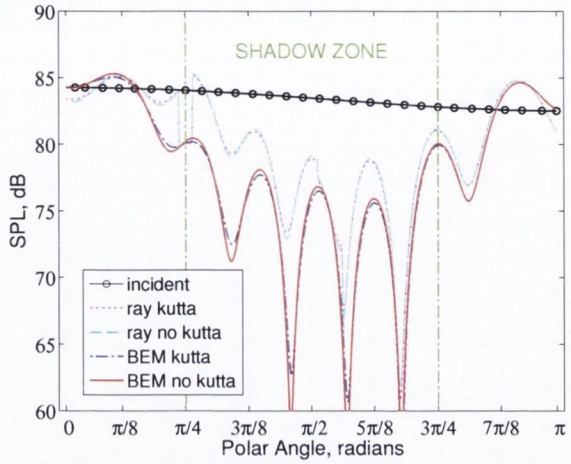
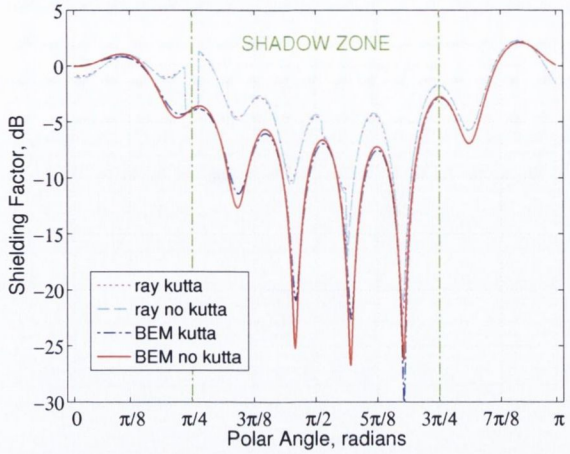


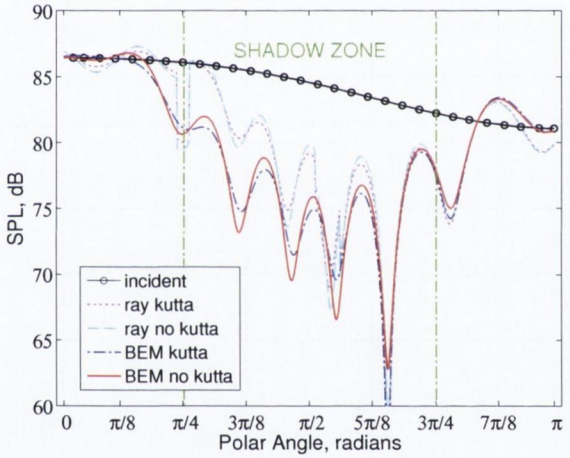
Figure 5.19: Near field contours of the magnitude of the acoustic potential, $|\phi|$. BEM solution, $x_2 = 2L_c$



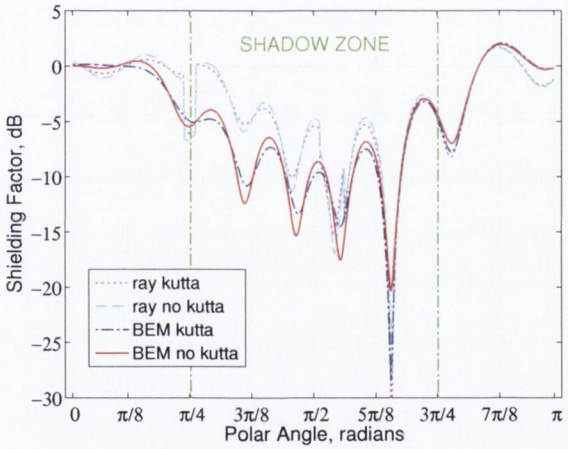
(a) SPL, $M = 0.1$, flyover



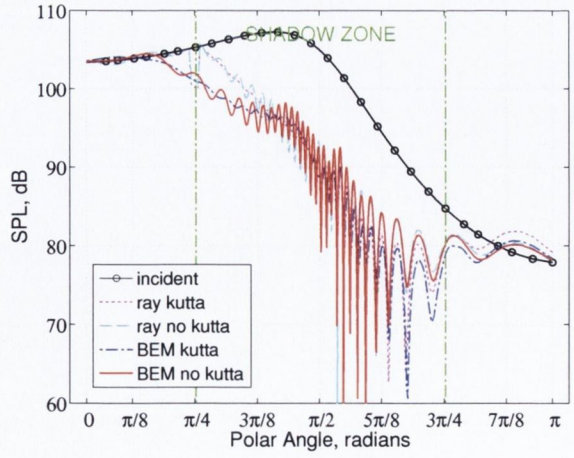
(b) Shielding Factor, $M = 0.1$, flyover



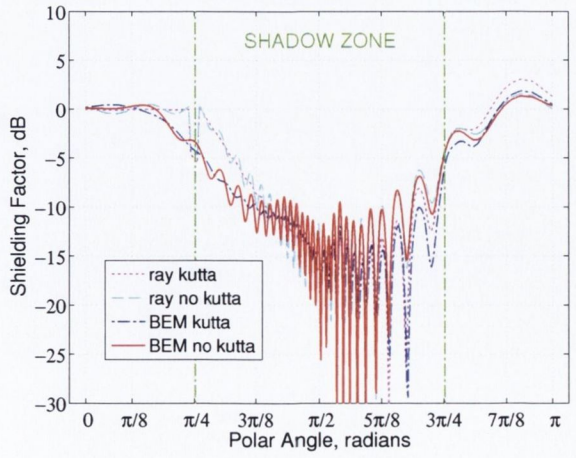
(c) SPL, $M = 0.3$, flyover



(d) Shielding Factor, $M = 0.3$, flyover

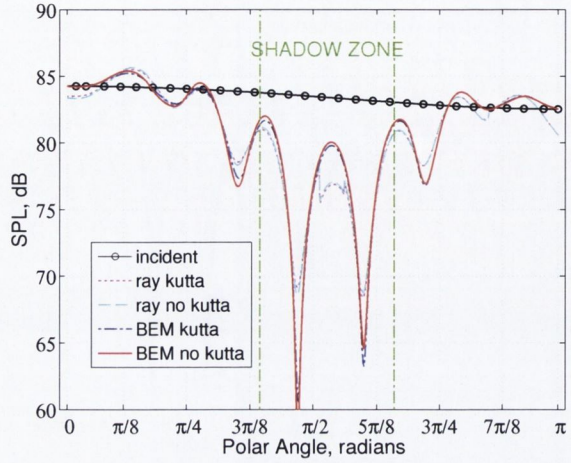


(e) SPL, $M = 0.9$, flyover

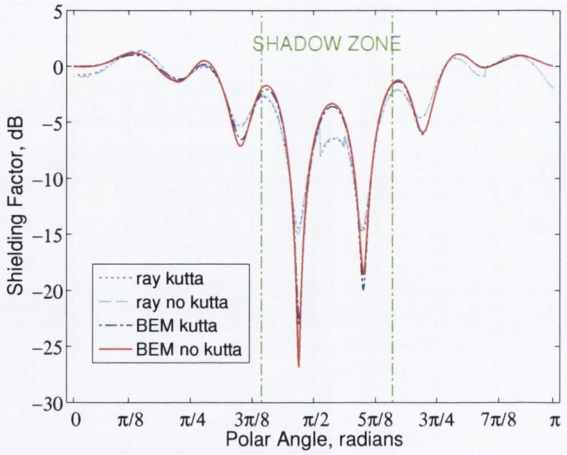


(f) Shielding Factor, $M = 0.9$, flyover

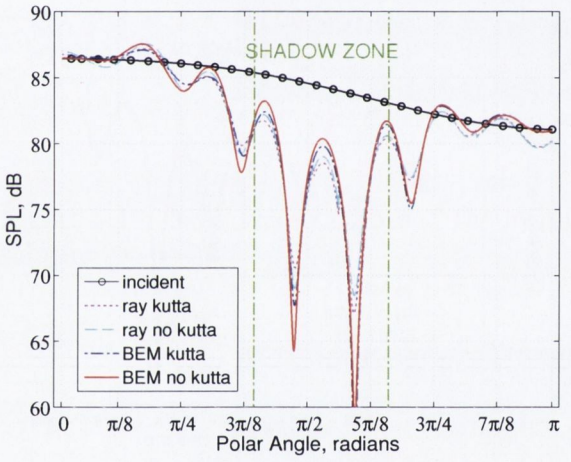
Figure 5.20: Case A: Variation of far-field pressure with Mach number and Kutta condition in the flyover. Left: Pressure in the flyover. Right: Shielding factor in the flyover.



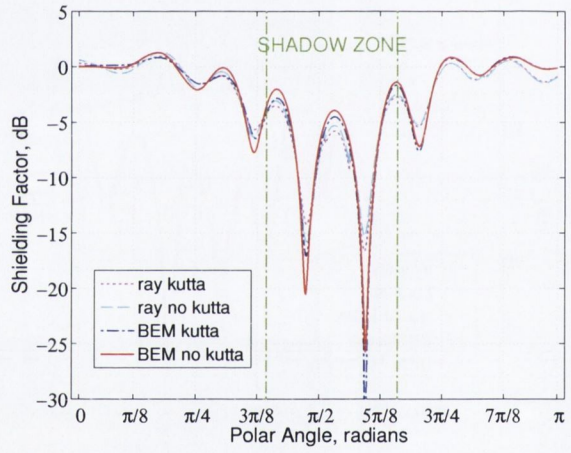
(a) SPL, $M = 0.1$, sideline



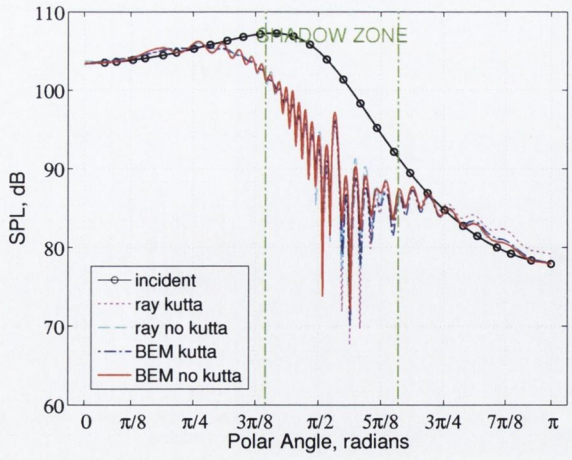
(b) Shielding Factor, $M = 0.1$, sideline



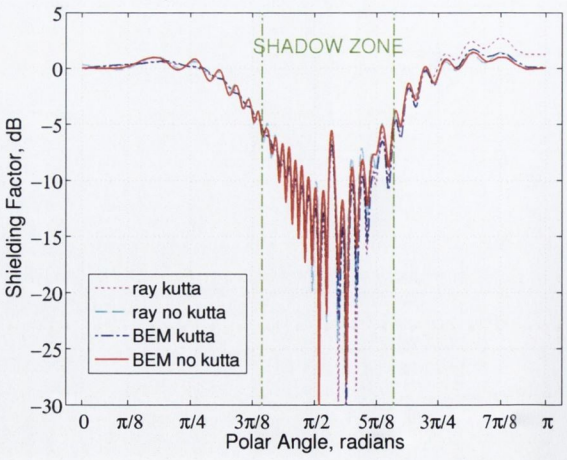
(c) SPL, $M = 0.3$, sideline



(d) Shielding Factor, $M = 0.3$, sideline



(e) SPL, $M = 0.9$, sideline



(f) Shielding Factor, $M = 0.9$, sideline

Figure 5.21: Case A: Variation of far-field pressure with Mach number and Kutta condition in the sideline. Left: Pressure in the sideline. Right: Shielding factor in the sideline.

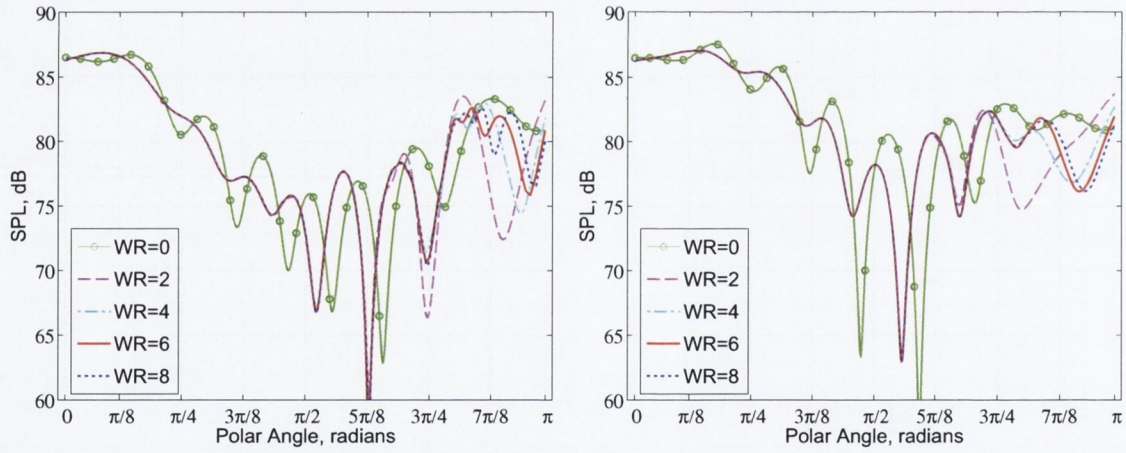
5.5 Scattering Predictions in Lifting Flows

Results for sound scattering in the presence of a lifting flow are now presented. Similar to the results of the previous section, two configurations were considered. Case A is a tapered wing while case B is the untapered rectangular geometry. To reduce the computational load for LEE simulations, a symmetry plane was introduced in the LEE simulations, as described previously. To mimic the behavior of the symmetry plane in the BEM solution, a virtual source was placed at the reflection of the true source in the symmetry plane. For the comparison of the BEM method with the LEE presented here, the true source was positioned at $(-0.5L_c, 0.4L_s, 0.5L_c)$, and the virtual source is located at $(-0.5L_c, 0.6L_s, 0.5L_c)$, and the source magnitudes were scaled to give unit acoustic power. For all the other results presented here, a single monopole of unit volume velocity was placed at the location $(-0.5L_c, 0.5L_s, 0.5L_c)$, unless it is noted otherwise.

5.5.1 Convergence Studies

A parametric study was carried out to determine the correct wake truncation length, transition length and grid resolution for the BEM solution with the Case A geometry. In Fig. 5.22, the SPL in the flyover and sideline has been plotted for several wake truncation lengths, while holding all other parameters constant. Examining the convergence of the solution with increasing wake length, it is clear that the solution in the rear arc, from polar angles of $3\pi/4$ to π, is more sensitive to the wake length than the forward arc. As in the case with non-lifting flow, it was found that this feature is a result of errors introduced at the propagation step, rather than during the BEM surface solution step. Generally, the solution over the wing surface converges rapidly with wake length once the truncation line of the wake is located a few wavelengths downstream of the wing trailing edge. In the previous section, arguments from the stationary phase method were used to explain the behavior of the Kutta condition field for different wake truncation conditions. By the same reasoning, the BEM solution in a lifting flow also requires a gradual transition of the wake scattering terms to reduce edge scattering effects. Examining the surface solution in the PGT transformed do-

main, shown in Fig. 5.23, it is apparent that the phase of the induced potential jump on the wake, due to the presence of steady circulation in the flow, is well matched to the phase of the incident field. Hence, the stationary phase approximation predicts that the asymptotic contribution of the wake surface potential to the far-field integral occurs where the direct path of propagation intersects the wake. The SPL curves plotted in Fig. 5.24 illustrate how the truncation line contribution of the far-field integral can be removed by smoothly fading out the discontinuities in the transformed potential over the wake surface. As a rule of thumb, this transition zone needs to capture at least two wavelengths to function well. The highly oscillatory component in the $TR = 0$ solution is the effect of the vortex wave at the truncation line, which is damped more rapidly with increasing TR than the potential jump induced by lifting flow. For the results presented in rest of this section, the numerical parameters were set to the values $WR = 6$, $TR = 0.3$ and $NPW = 15$.



(a) Flyover (b) Sideline

Figure 5.22: Variation in far-field acoustic pressure with WR, $\alpha = 8°$, frequency = 500Hz, M=0.3, TR=0.3

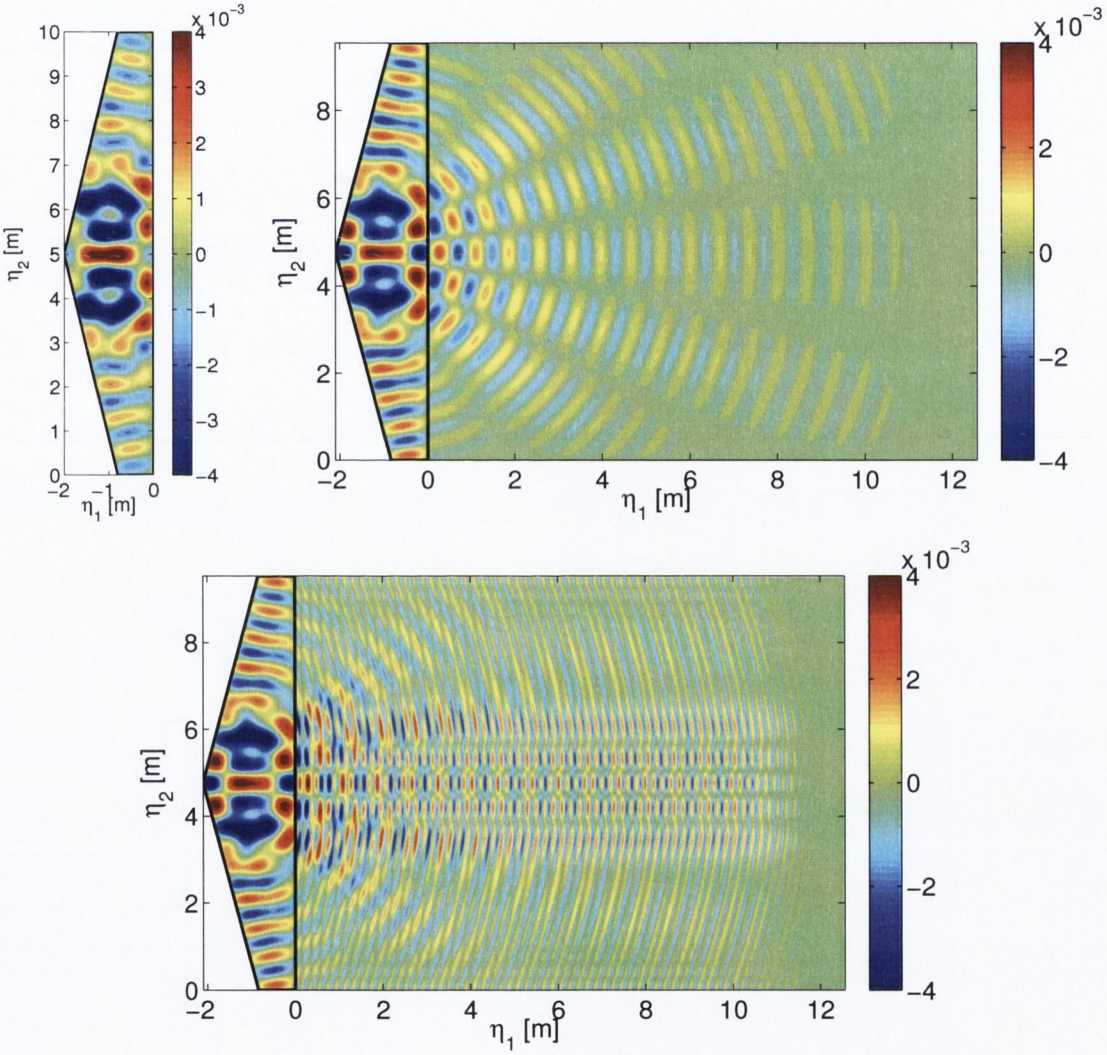
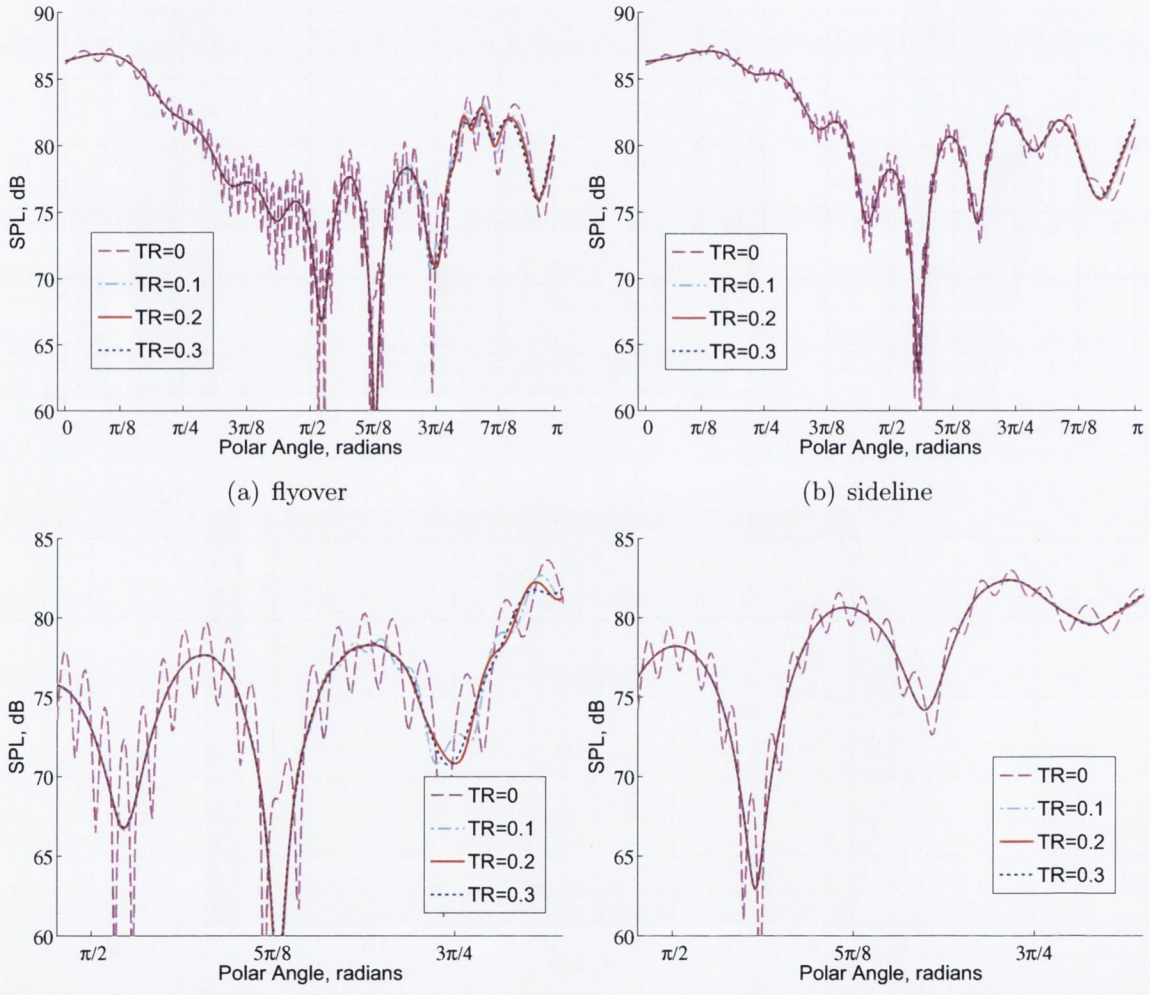


Figure 5.23: Contours of $\delta\varphi$, the jump in transformed potential, on the wing and wake surface in the PGT domain (real part), 500Hz, symmetric solution, M=0.3, TR=0.3, WR=6. Top Left: no flow. Top Right: M=0.3, $\alpha = 8°$, no Kutta condition. Bottom: M=0.3, $\alpha = 8°$, Kutta condition solution.



(a) flyover

(b) sideline

(c) flyover, detailed view

(d) sideline, detailed view

Figure 5.24: Variation in SPL with increasing TR, 500Hz, WR=6, M=0.3

5.5.2 Near-field BEM solution

The influence of steady lift on the BEM solution is illustrated clearly, by plotting the real part of the acoustic potential on a cutplane perpendicular to the wing. In Fig. 5.25, the incident acoustic potential is plotted on the symmetry plane, which is perpendicular to the wing and parallel to the free stream flow. The phase jump in the incident field is visible along the line $x_3 = 0$, where the steady flow potential is discontinuous. This physically unacceptable behavior is removed in the BEM solution step by forcing the scattered field to have an equal and opposite phase discontinuity that cancel when the two fields are summed. The convected vortex wave may also be seen in the scattered and total field plots, as a short wave component along the wake line.

The scattered field resulting from the Born approximation of Howe's analogy is plotted in Figures 5.26-5.29. One striking feature of these plots is the scale of acoustic potential relative to the zeroth solution in the Born series, shown in Fig. 5.25. For the particular frequency and flow conditions simulated here, the first order Born approximation of the vortex scattered field is two orders of magnitude lower than the incident field. Although the dimensionless wavenumber, kL_c, is somewhat on the small side relative to typical values of engine noise components on a full scale airliner, it is possible to extrapolate the current shielding results to higher frequency cases. From Eq. 3.122, the potential field induced by Howe's vortex scattering term scales with $\Gamma k\ \varphi^0/c_\infty$, where Γ is the circulation of the vortex filament and φ^0 is the local value of the zeroth order field on the filament. Extrapolating from the current results, it seems unlikely that Howe's vortex scattering term will impact on the predicted value of acoustic shielding unless the frequency of sound is at least an order of magnitude larger and the scattering vorticity is located very close to the source region, where the local potential field is of higher magnitude. Also, the interaction between the vortex scattered field and the wing is almost negligible, as shown in Figures. 5.28-5.29, which suggests that the source can be treated in isolation as a correction to the forward scattered field, without the need for a further BEM solution step. The other noticeable feature of the Howe scattered field is the obvious concentration of the Howe source

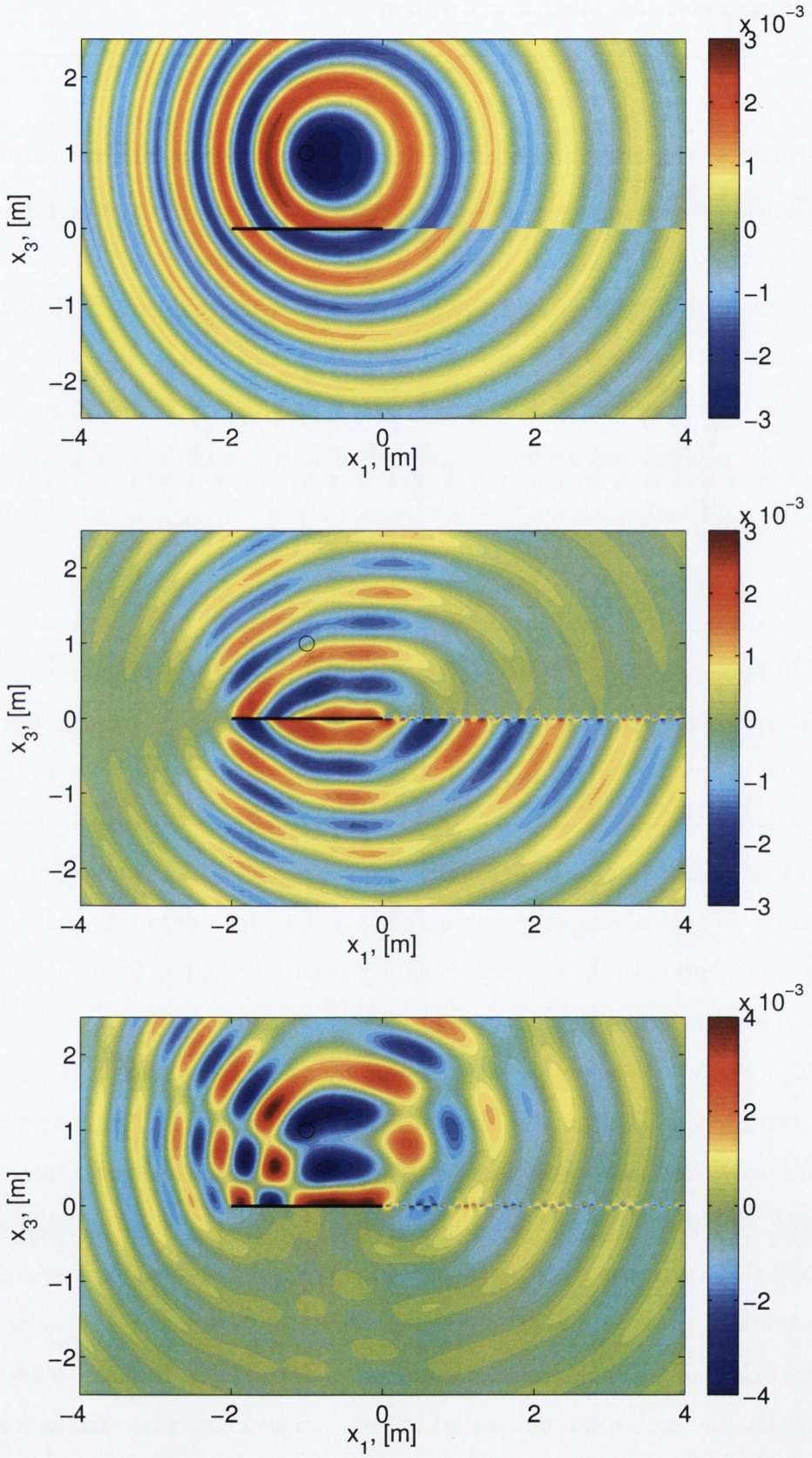


Figure 5.25: Countours of near-field acoustic potential on the symmetry plane, linear scale (real part), BEM, $\alpha = 8°$, M=0.3, frequency=500Hz. Top: Incident field, Middle: Scattered field, Bottom: Total field. The source position is marked with a black circle.

term in the wingtip region. This feature tends to support the argument for modeling the streamwise steady vorticity as a set of discrete vortex filaments rather than as a vortex sheet approximation.

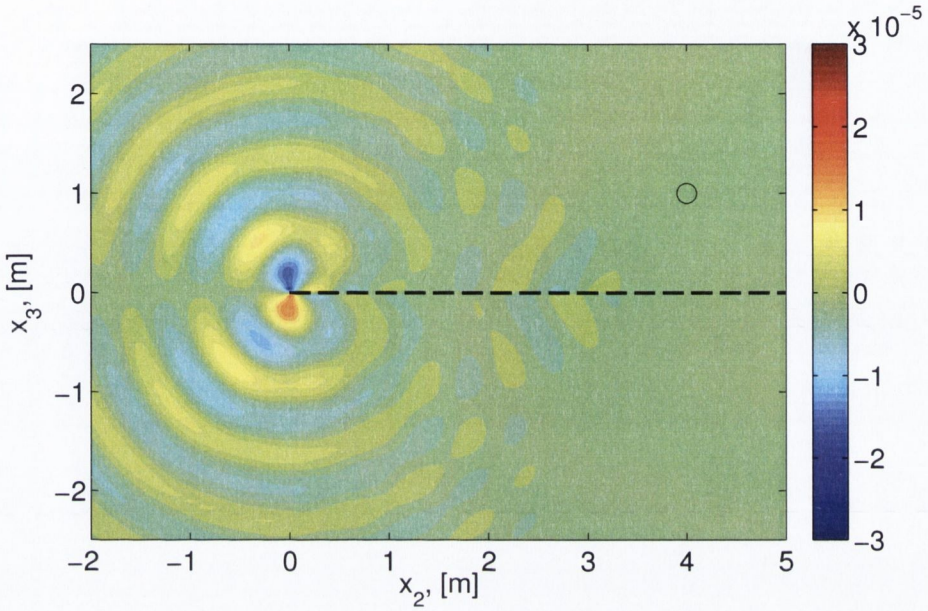


Figure 5.26: Countours of near-field acoustic potential on the plane $x_1 = 0$, Born approximation vortex scattered field, linear scale (real part), $\alpha = 4°$, M=0.3, frequency=500Hz. The source position is marked with a black circle.

5.5.3 Near-field Comparison of BEM and LEE solutions

5.5.3.1 Pressure Comparions

A comparison of the acoustic pressure in the near-field, as predicted by the BEM and LEE solvers, is shown in Figures 5.30-5.34. For the no flow case in Fig. 5.30, the agreement is excellent. Despite the differences in geometry between the two simulations, a close match is to be expected at the frequencies under consideration. For higher frequencies when the wavelength of sound becomes comparable with the radius of curvature of the leading edge, the mechanism of diffraction at the leading edge switches from edge diffraction to a creeping wave mode and the results may differ. However, these frequency ranges were not considered in this analysis. The other noticeable feature of the no flow solutions is the smoothness of the contours and the close match of the solutions at the boundary of the domain. This suggests that the boundary con-

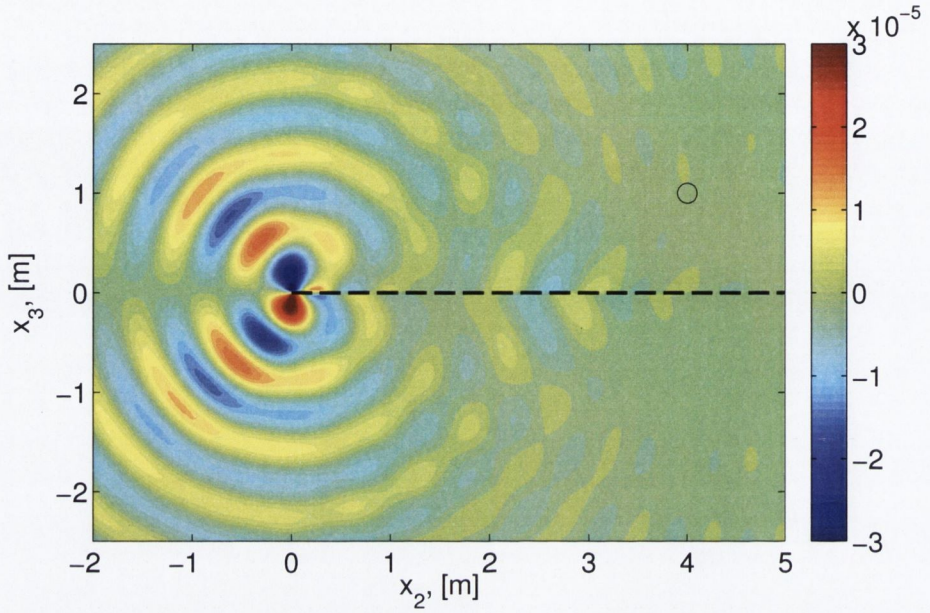


Figure 5.27: Countours of near-field acoustic potential on the plane $x_1 = 0$, Born approximation vortex scattered field, linear scale (real part), BEM, $\alpha = 8°$, M=0.3, frequency=500Hz. The source position is marked with a black circle.

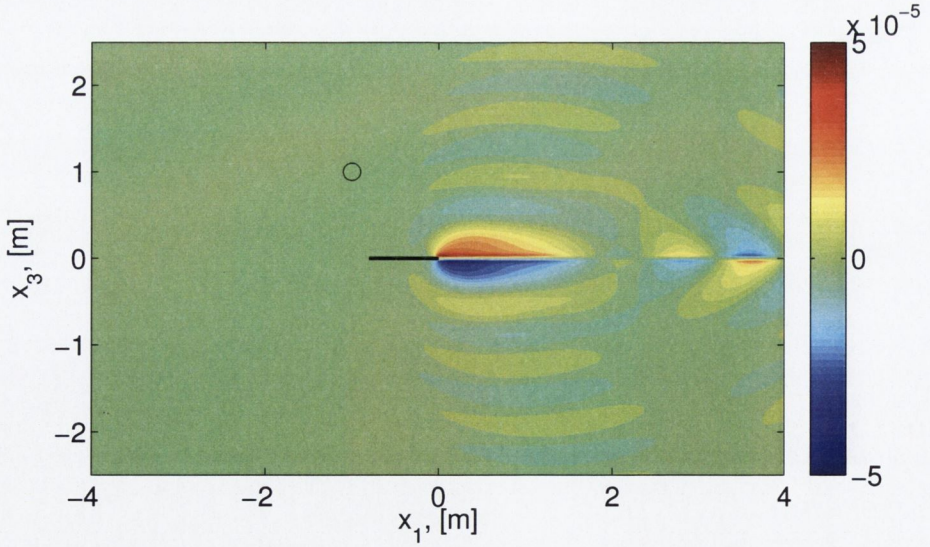


Figure 5.28: Countours of near-field acoustic potential on the plane $x_2 = 0$, Born approximation vortex scattered field, linear scale (real part), BEM, $\alpha = 4°$, M=0.3, frequency=500Hz. The source position is marked with a black circle.

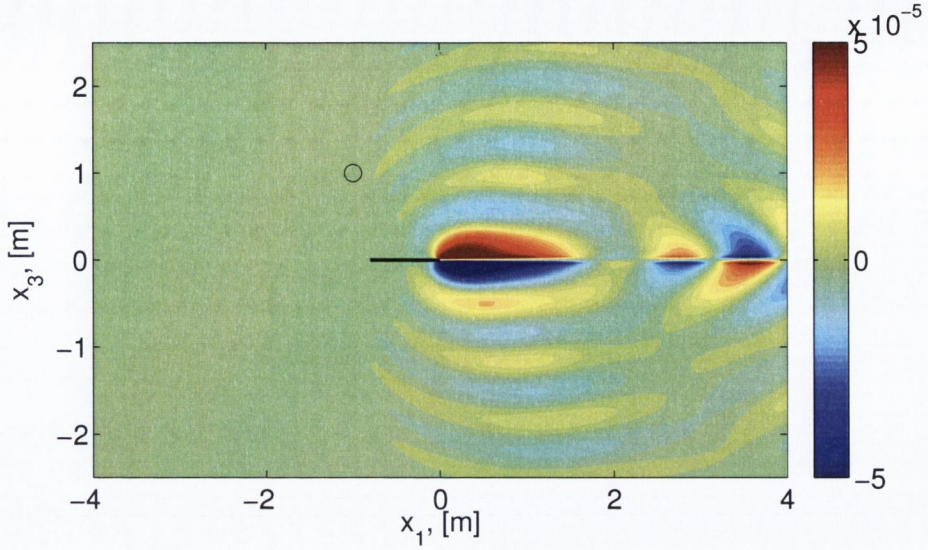


Figure 5.29: Countours of near-field acoustic potential on the plane $x_2 = 0$, Born approximation vortex scattered field, linear scale (real part), BEM, $\alpha = 8°$, M=0.3, frequency=500Hz. The source position is marked with a black circle.

ditions are well captured by the buffer zone treatment in the LEE simulation. Some small ripples in pressure contours are present in the corners of the LEE domain, which indicate that a low level of reflection occurs at the corner points.

For lifting flow conditions, the boundary conditions do not perform quite as well as in the non-lifting conditions. In particular, the pressure field in the top left hand corner of Fig. 5.33 and Fig. 5.34 show some distortion due to reflections at the boundaries. The level of scattering at the artificial boundaries increases with angle of attack but still remains relatively small at the $\alpha = 8°$ case. This may be attributed to the non-uniform flow conditions at the artificial boundaries.

Examining the non-lifting flow results in Fig. 5.32, the doppler amplification of the pressure is visible in the forward propagating direction when compared with the no flow solutions. This feature is also well captured by the BEM solution. Of the two BEM solutions, the no Kutta solution appears to show marginally better agreement with the LEE simulation in the near-field. However, the relatively small magnitude of the field induced by the Kutta condition makes it difficult to draw any firm conclusions and the far-field results show that the Kutta condition solution is actually a closer match to the LEE result.

In the Kutta condition BEM solution, at the high angle of attack, there is a subtle

short wave disturbance in the pressure contours near the wake region. This feature is caused by the approximation of the wake geometry by a planar surface and the error in the acoustic boundary conditions that results from a net flux in steady flow through the wake. The error associated with the planar wake approximation could be eliminated by adding a wake relaxation scheme to the mean flow potential solver. The basic idea behind wake relaxation is to to approximate the dynamics of the wake in an iterative process so that the wake takes up a force free shape, with minimal flux through the vortex sheet surface. Examples of such schemes are described in Katz and Plotkin [83].

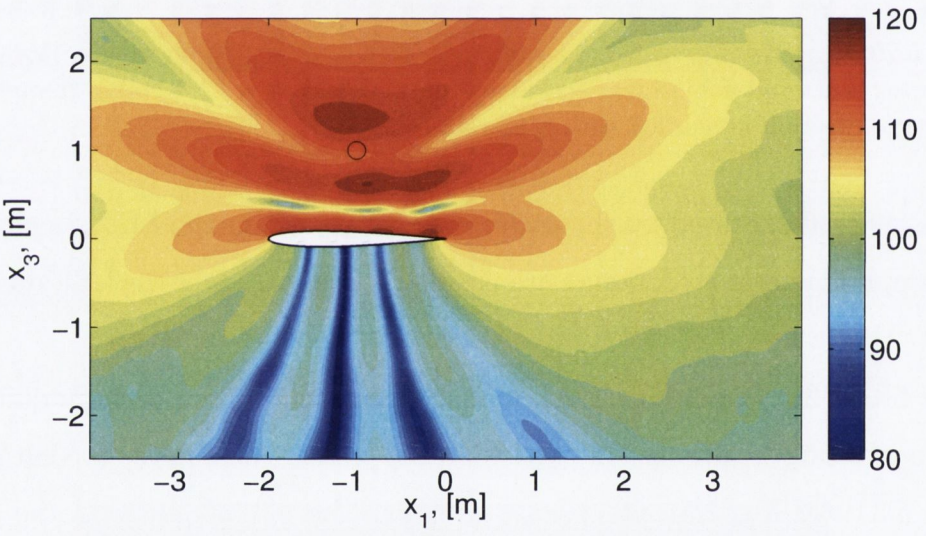


Figure 5.30: Countours of near-field acoustic pressure, dB scale, LEE, No Flow. The source position is marked with a black circle.

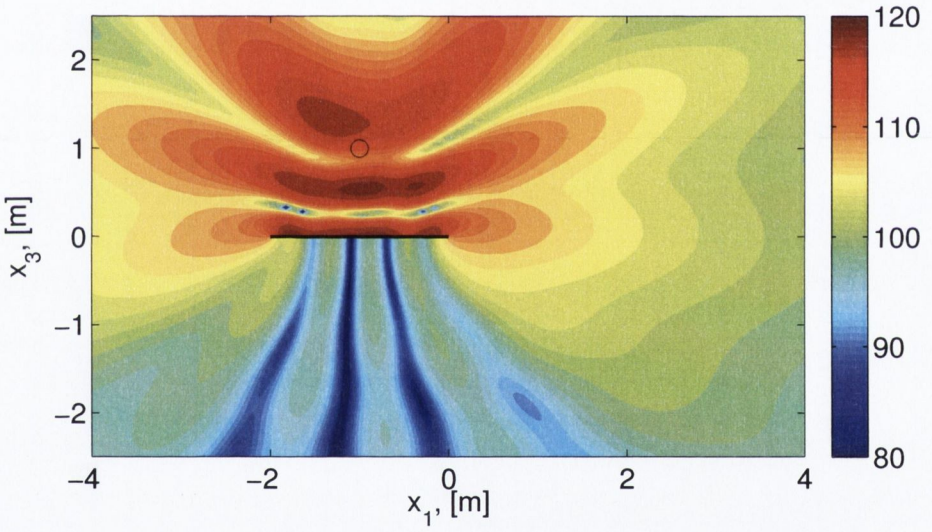


Figure 5.31: Countours of near-field acoustic pressure, dB scale, BEM, No Flow. The source position is marked with a black circle.

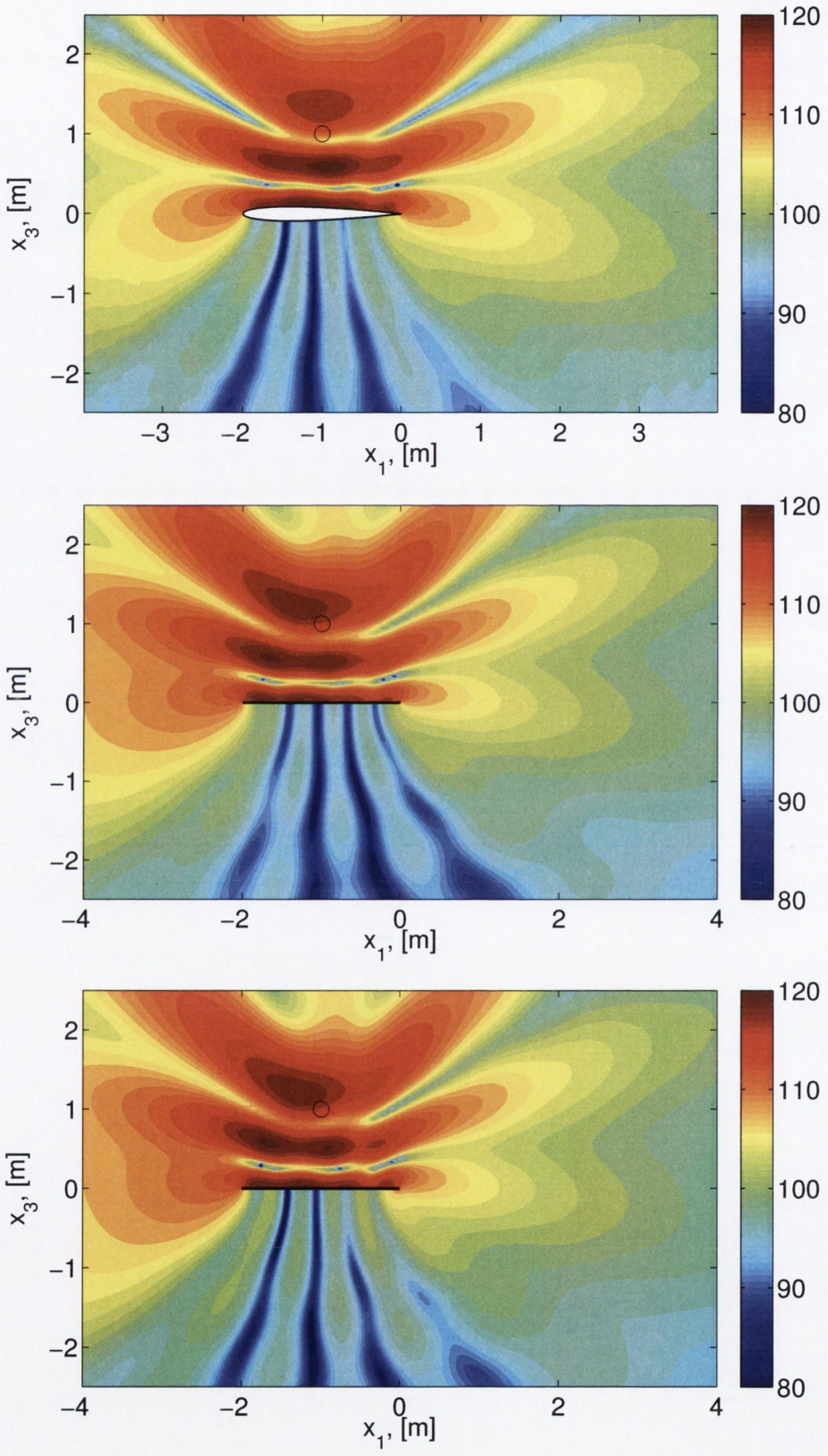


Figure 5.32: Contours of near-field acoustic pressure, dB scale, $\alpha = 0°$, 500Hz. Top: LEE, Middle: BEM Kutta condition, Bottom: BEM no Kutta. The source position is marked with a black circle.

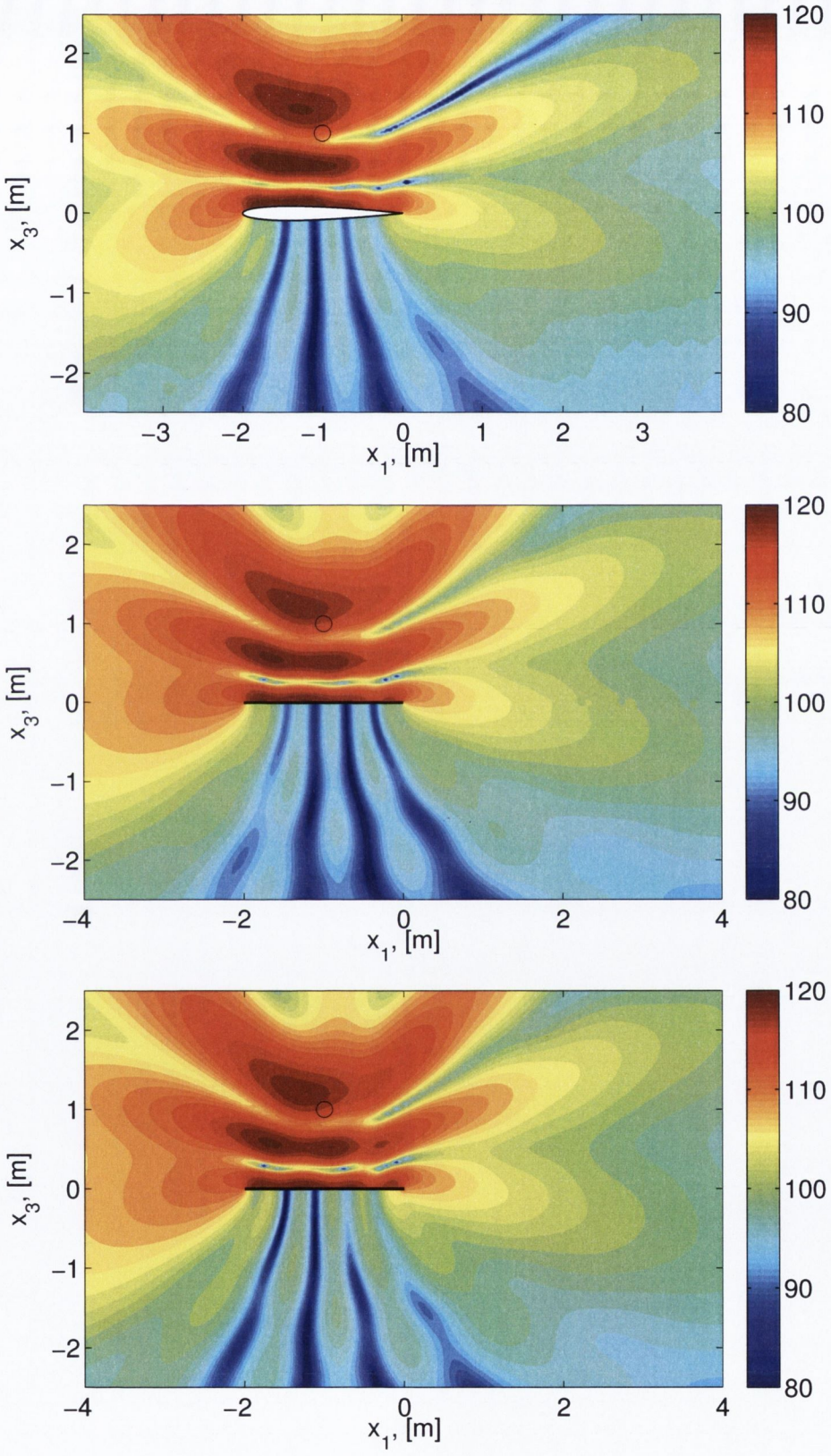


Figure 5.33: Contours of near-field acoustic pressure, dB scale, $\alpha = 4°$, 500Hz. Top: LEE, Middle: BEM Kutta condition, Bottom: BEM no Kutta. The source position is marked with a black circle.

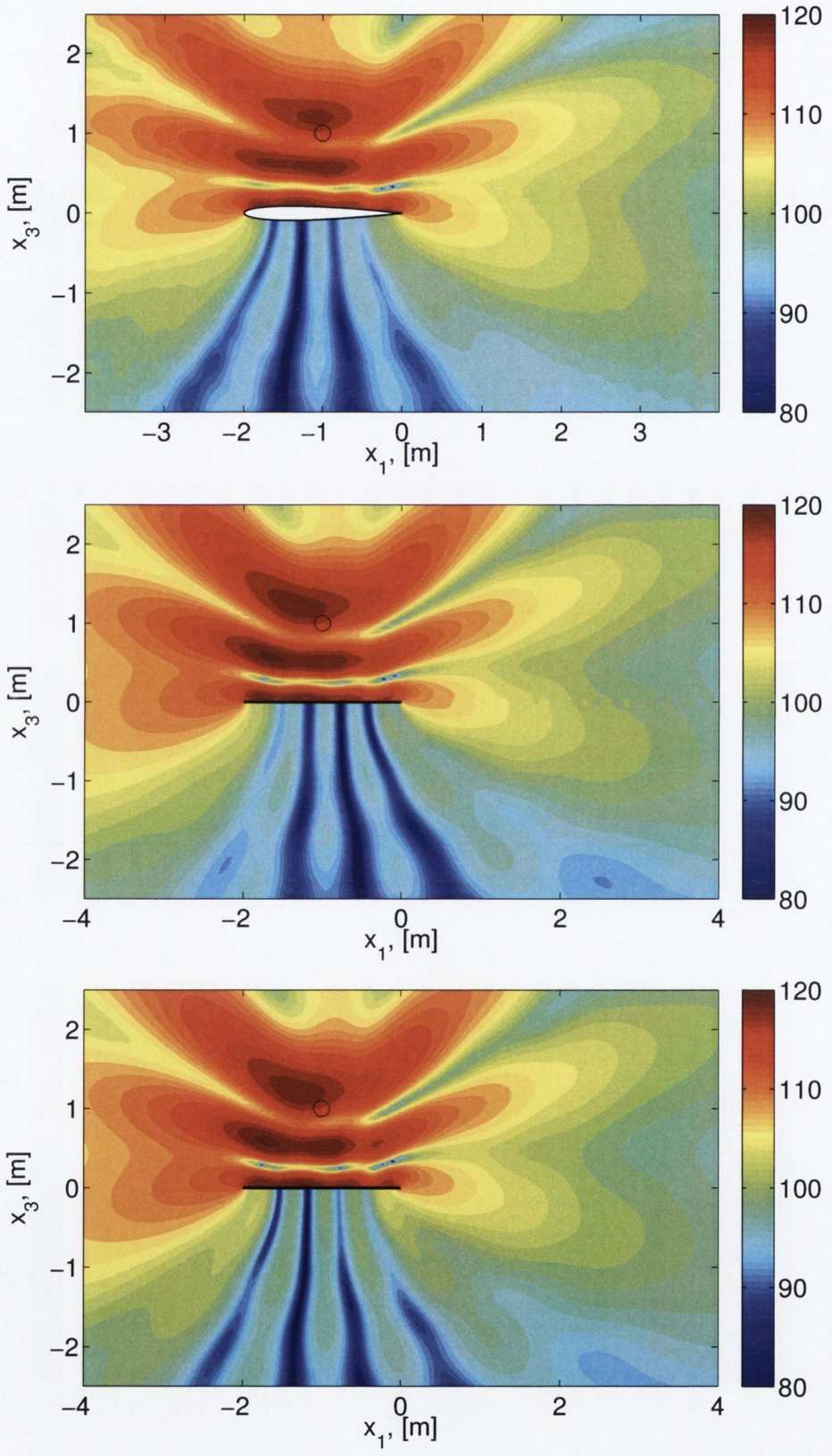


Figure 5.34: Contours of near-field acoustic pressure, dB scale, $\alpha = 8°$, 500Hz. Top: LEE, Middle: BEM Kutta condition, Bottom: BEM no Kutta. The source position is marked with a black circle.

5.5.3.2 Acoustic Velocity Comparison

While the contour plots of the perturbation pressure field provide a good measure of the magnitude of the acoustic mode of the perturbation field, the vortex wave modes are more clearly highlighted by plotting the unsteady perturbation velocity field. Near field contour plots of the magnitude of the acoustic velocity field, at a fixed phase point, are shown in Figures. 5.35-5.39. In the no flow case, vortex modes are not supported by the linearized flow equations and both the BEM and LEE solutions behave as expected. It appears that a small short wave error is present near the trailing edge of the wing in the LEE solution. This component resembles a vortex mode but its magnitude is very weak and the disturbance is not convected due to the absence of a steady flow. As a baseline case for comparison of the two solution approaches, the no flow case shows excellent agreement of the magnitude and of the phase pattern of the predicted velocity field. The subtle rearrangement of the interference pattern in the zone of reflection can be explained by the small but non-negligible curvature of the upper surface of the wing for the LEE wing profiles.

For the non-lifting steady flow conditions, shown in Fig. 5.37, the BEM and LEE simulations are also well matched. The phase patterns are very similar with the exception of the pronounced low magnitude nodal line extending to the top left corner of the domain in the LEE solution. The other noticeable feature of the simulations is the prediction of a strongly damped vortex wave, shed from the trailing edge of the wing in the LEE simulation. By comparison, the BEM formulation does not include any mechanism for artificial damping of the vortex wave and the magnitude of this mode is constant as it is convected downstream. Based on the shielding predictions of the previous section, it is clear that the damping of the vortex wave far downstream of the trailing edge has no effect on the far-field solution whatsoever. The vortex wave convects passively in the steady flow and does not interact with the wing once it has convected a few wavelengths downstream of the trailing edge. What is more important is that the amplitude of the vortex sheet shed from the trailing edge is correctly predicted and the velocity plots show that the LEE and BEM predictions are of a similar magnitude in the trailing edge region. In any case, when the Kutta

condition solution is compared with the no Kutta solution, it is clear that the influence of the vortex mode is very weak for the flow conditions simulated.

Under lifting flow conditions, the agreement between the LEE and BEM solutions diverges slightly in the region of strong flow non-uniformity, particularly in the region close to the leading edge. A slight mismatch in the phase of the velocity field near the leading edge is visible in Fig. 5.38 and is even more pronounced in Fig. 5.39. The BEM solution predicts that a local peak in velocity occurs at the leading edge, while the LEE predicts that the peak shifts slightly towards the trailing edge on the suction surface side, when the angle of attack is increased. When the far-field results are examined, it appears that the phase error in the BEM solution is mostly a local feature that does not have a strong influence on the predicted far-field pressure. This result is to be expected since the error analysis of the transformation method shows that the BEM solution is the least accurate in the leading edge region where flow non-uniformity and highly accelerated flow locally violate the assumptions of the small disturbance theory. However, the accuracy of the LEE prediction in the leading edge region may also be questionable since there is clearly some small level of leading edge vortex shedding occurring in both the $\alpha = 4°$ and the $\alpha = 8°$ simulations. These vortex waves are visible as a short wave ripple in the velocity field on the entire suction side of the wing, which then combine with the trailing edge vortex wave. This unphysical behavior is most likely caused by under-resolving the leading curvature with the LEE mesh. The NACA 0009 profile was deliberately chosen as a suitable test case for comparison with the thin structure BEM code because it has low curvature over the bulk of the airfoil surface and has very low thickness. Consequently, the airfoil surface must also have very large curvature at the leading edge, which can be problematic for meshing with planar elements. A careful compromise was made between the maximum number of elements in the mesh and the resolution of the flow and geometric details. This required a moderately coarsened mesh in the leading edge region.

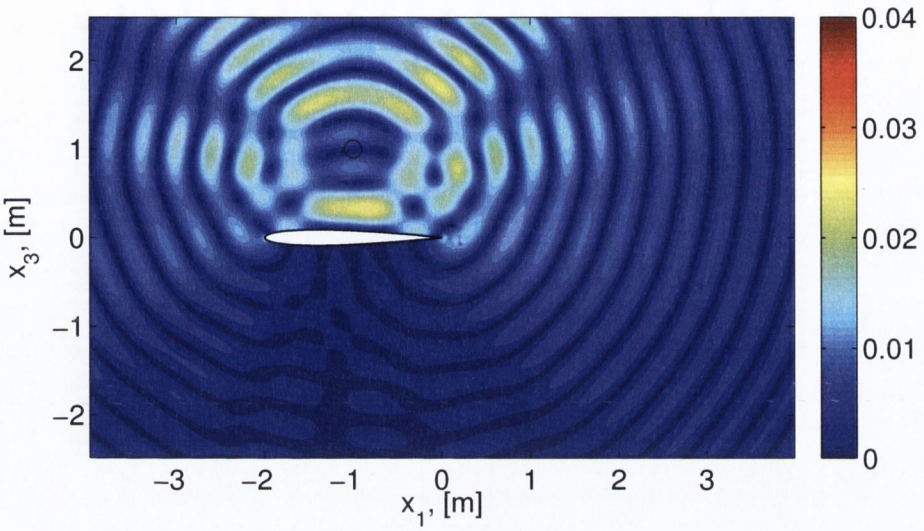


Figure 5.35: Countours of near-field acoustic velocity, linear scale, LEE simulation, no flow. The source position is marked with a black circle.

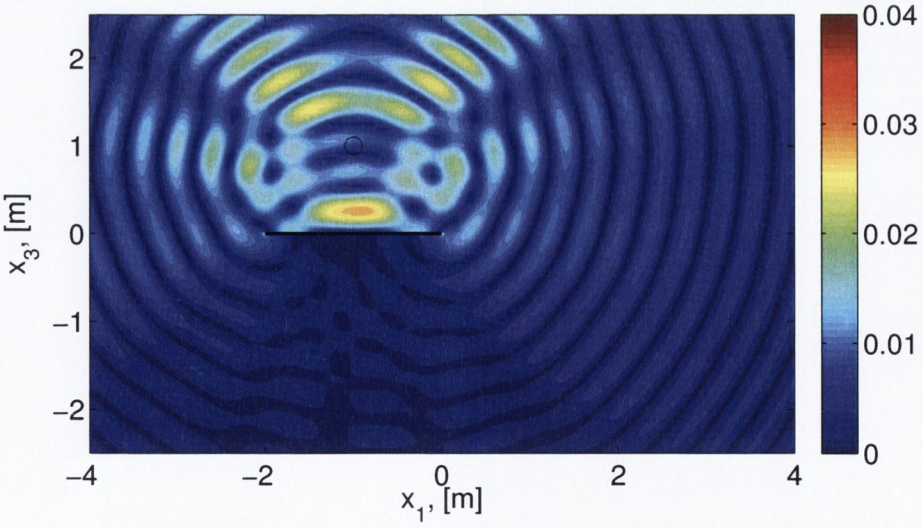


Figure 5.36: Countours of near-field acoustic velocity, linear scale, BEM simulation, no flow. The source position is marked with a black circle.

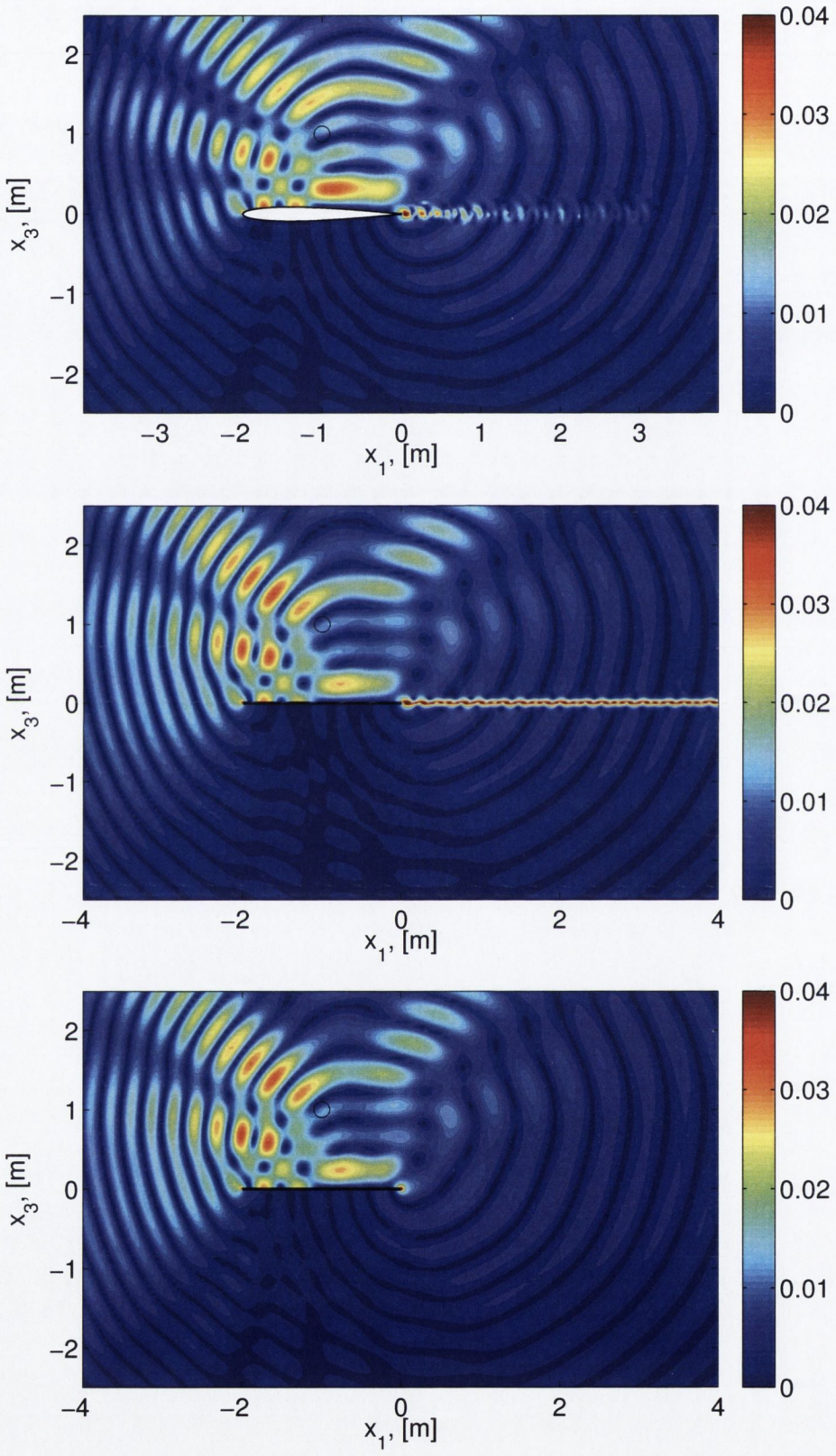


Figure 5.37: Countours of near-field acoustic velocity, linear scale, $\alpha = 0°$, 500Hz. Top: LEE, Middle: BEM Kutta condition, Bottom: BEM no Kutta. The source position is marked with a black circle.

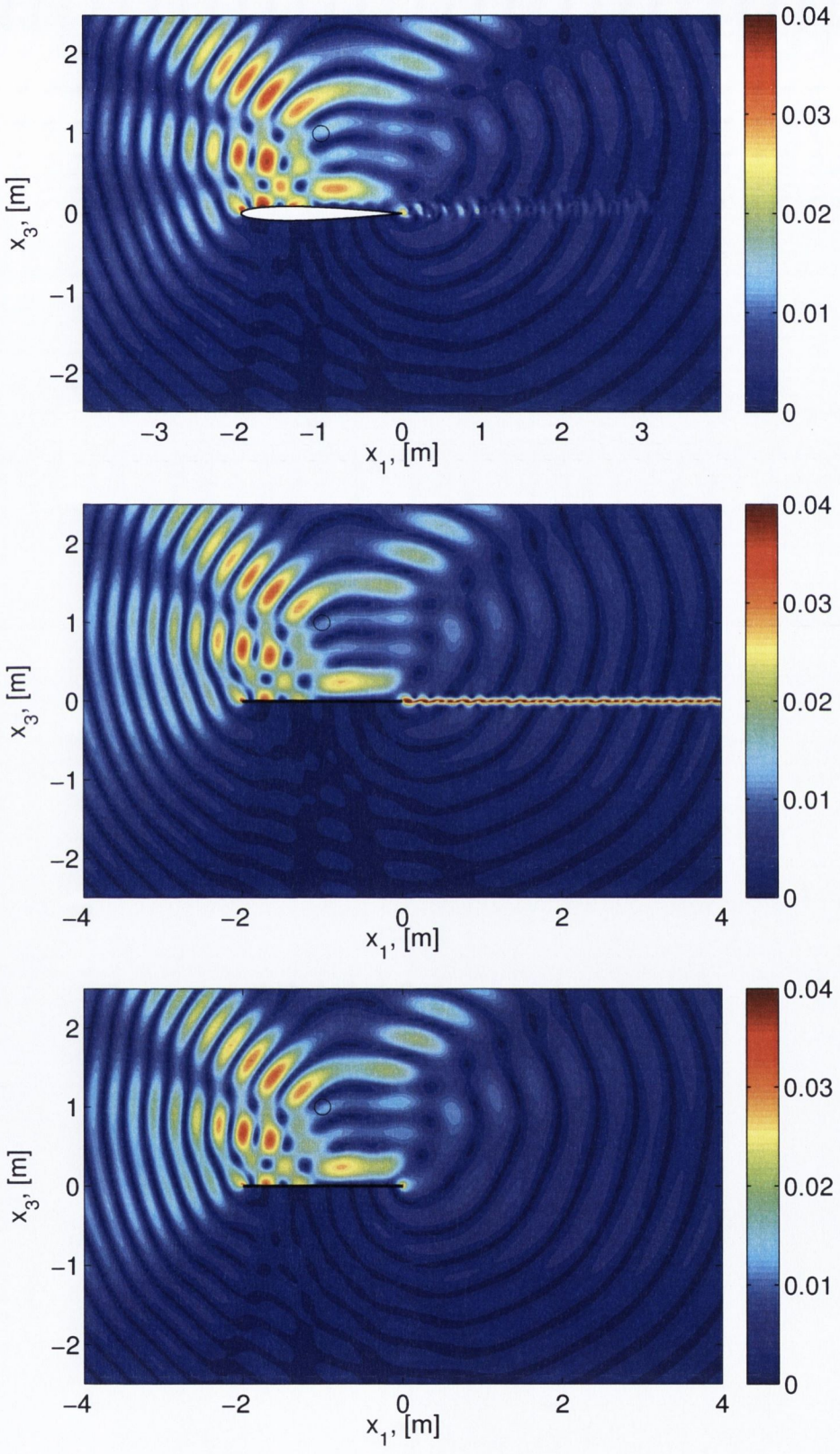


Figure 5.38: Countours of near-field acoustic velocity, linear scale, $\alpha = 4°$, 500Hz. Top: LEE, Middle: BEM Kutta condition, Bottom: BEM no Kutta. The source position is marked with a black circle.

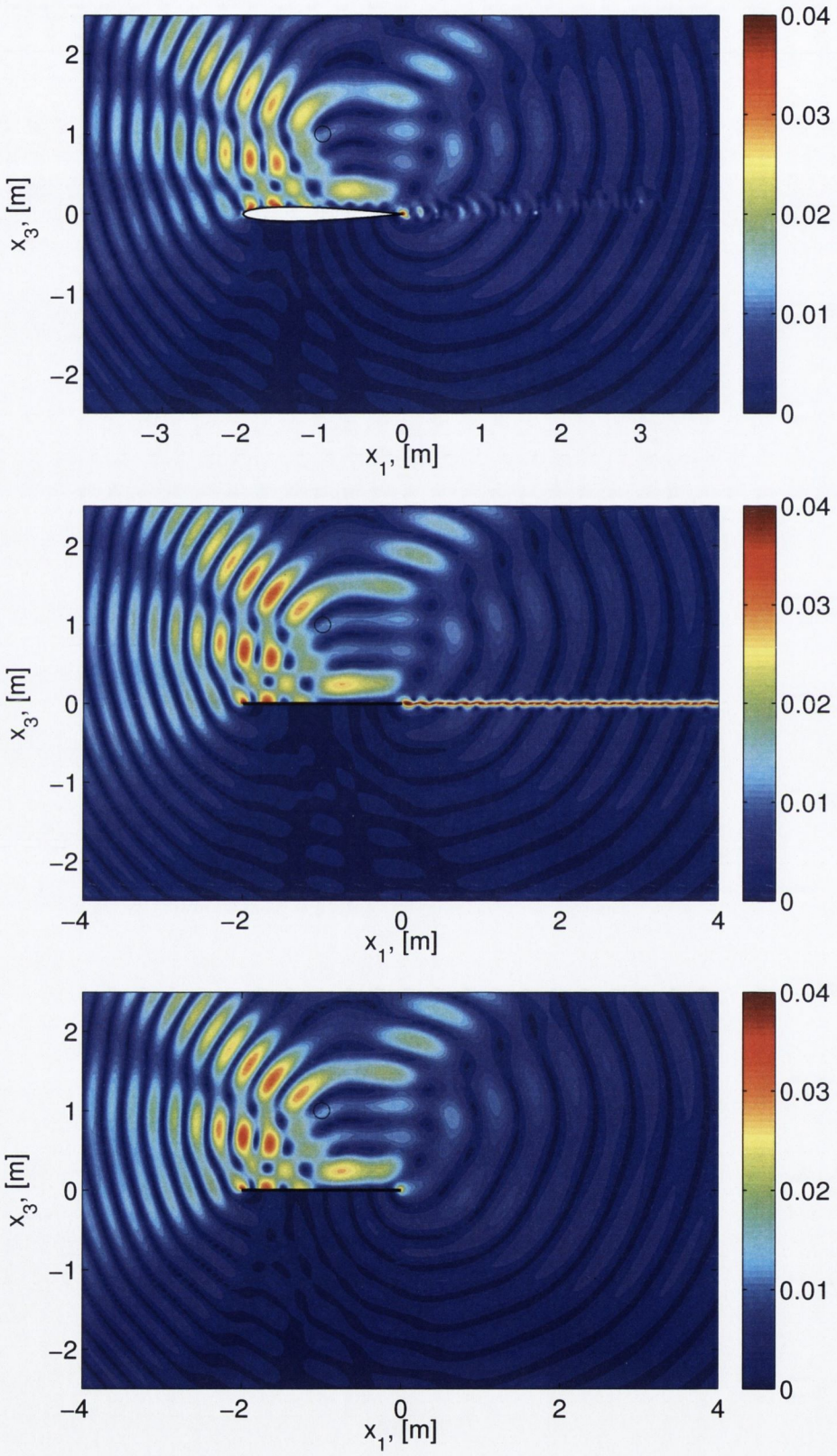
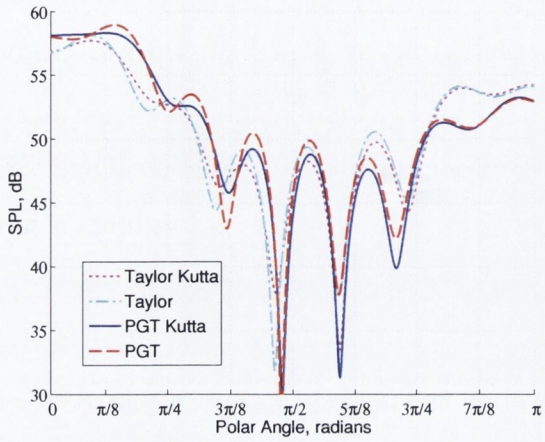


Figure 5.39: Countours of near-field acoustic velocity, linear scale, $\alpha = 8°$, 500Hz. Top: LEE, Middle: BEM Kutta condition, Bottom: BEM no Kutta. The source position is marked with a black circle.

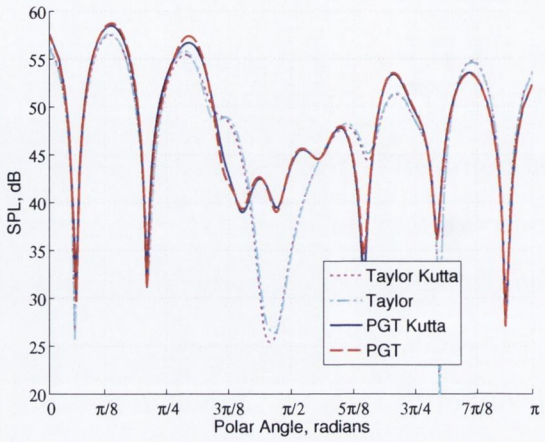
5.5.4 Far-field Comparison of BEM and LEE Solutions

Figures.5.40-5.43 present a comparison of the far-field scattering patterns as predicted by the LEE and BEM solutions on the tapered wing configuration with a symmetry plane. The shielding factor has not been plotted for this configuration because the interference pattern established by a pair of isolated monopole sources (real and virtual sources), introduces nodal lines into the incidence field, which then produces a zero in the denominator of the shielding factor.

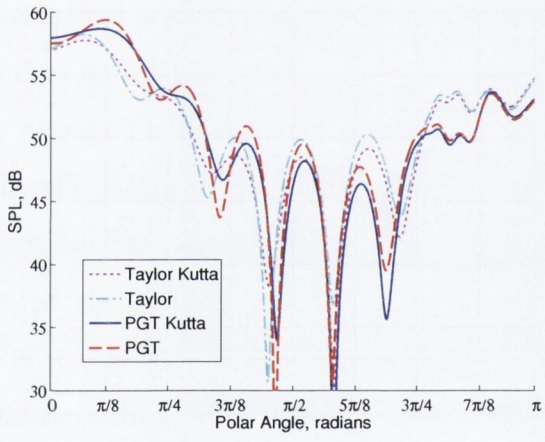
In order to compare the effects of neglecting different terms in the small disturbance theory of Chapter. 3, the sound pressure level on the far-field has been plotted for four different BEM formulations. In Fig. 5.40, the far-field pressure is plotted for the PGT formulation and the Taylor transformation BEM formulation, with a Kutta and a no Kutta condition for each case. The scattering pattern predicted by an ordinary Prandtl-Glauert transformation approach may be inferred from the PGT results with $\alpha = 0°$, since the two methods are equivalent under these conditions. The most noticeable differences between the formulations occur in the flyover arc, where the locations and magnitudes of the peaks in the SPL curves change significantly between the BEM formulations. For the $\alpha = 8°$ case, the peak located between $5\pi/8$ and $3\pi/4$ decreases by a maximum of 5 dB in the flyover arc, when the Kutta condition is switched on and the PGT formulation is used in place of the Taylor transformation BEM. This change in the SPL is a result of several mechanisms. Firstly, the Kutta condition effect contributes in the region of a 2 dB decrease in SPL over the no Kutta condition. The other effect is the correct treatment of the free stream component of the steady flow that is accounted for by the Prandtl-Glauert stretching of the x_1 coordinate when a PGT formulation is used. This stretching tends to shift the peaks towards the angle $\pi/2$, in the forward and rear arc of the SPL curve and also decreases the magnitudes of the peaks due to the increase in the "acoustic length" of the wing chord. For a Mach number of $M = 0.3$, the product of the wavenumber and wing chord in the Prandtl-Glauert domain, is 10% larger than in the physical domain, due to the factor $\sqrt{1 - M^2}$ that multiplies the wavenumber k, and the x_1 coordinate in transformation Eq. 3.23. This produces an overall increase in the shielding effect of the wing when compared with no flow conditions.



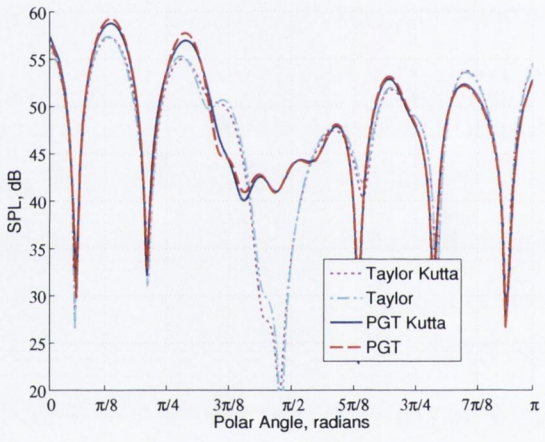
(a) Far-field SPL, $\alpha = 0°$, flyover



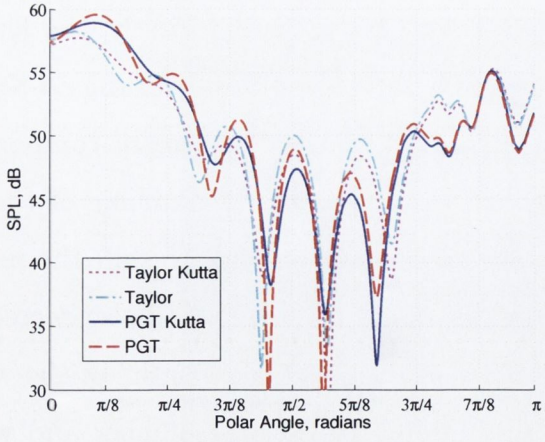
(b) Far-field SPL, $\alpha = 0°$, sideline



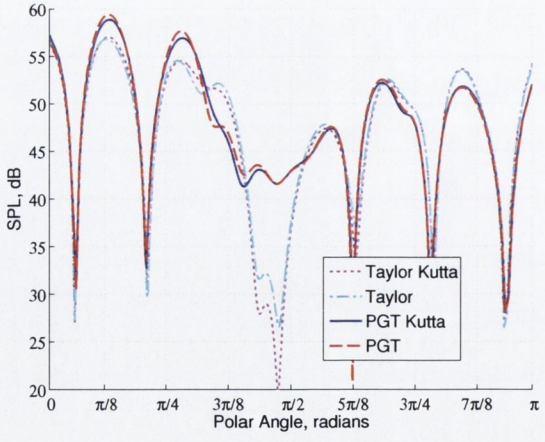
(c) Far-field SPL, $\alpha = 4°$, flyover



(d) Far-field SPL, $\alpha = 4°$, sideline



(e) Far-field SPL, $\alpha = 8°$, flyover



(f) Far-field SPL, $\alpha = 8°$, sideline

Figure 5.40: SPL on the far-field sphere for the flyover and sideline arcs. freq=500Hz, TR=0.3, WR=6

The other distinct scattering mechanism that is captured by both the PGT and Taylor transformation is the scattering of sound by lift producing flow conditions. An intuitive explanation for the shift in the far-field interference pattern, caused by an increase in steady lift produced by the wing, may be developed by considering a ray tracing approach to sound transmission through a wake. When the standard ray tracing method is applied in the PGT domain, the phase along a ray varies only with the distance from the source. This implies that the actual acoustic phase in the physical domain will have a discontinuity across the wake when the inverse transformation is applied. By adding an equal but opposite phase jump at the ray-wake junction in the PGT domain, the discontinuity in the physical domain can be removed.

This method of correcting the phase of a ray-traced solution in the PGT domain was implemented for the rectangular wing (caseB), in a flow of Mach number $M = 0.3$ at an angle of attack $\alpha = 4°$. The result of this computation is compared with the BEM prediction for the same conditions. The SPL curves for a single monopole of frequency $1500Hz$, of unit volume velocity and located at $(-0.5L_c, 0.5L_s, 0.5L_c)$ are plotted in Fig. 5.41. The chosen high frequency and simplified wing planform reduce the error between the BEM and ray-tracing methods so that the net effect of the lifting flow can be seen clearly in the plots. The simple treatment of the wake in the ray-tracing method accurately predicts the shift in the interference pattern in the flyover arc. This demonstrates that the main effect of net circulation in the steady flow is to shift the arrival time of the sound waves at the receiver points so that the relative phase of the sound arriving from the leading edge and the trailing edge is shifted slightly. Consequently, the locations of the peaks and troughs in the interference pattern are shifted in space. However, this approach is not entirely physical as no attempt has been made to match the wake surface normal velocity on the upper and lower sides of the wake in the physical domain. A more rigorous approach would be to develop transmission coefficients by considering a canonical problem of sound transmission through a wake and to implement these coefficients in a ray-tracing formulation.

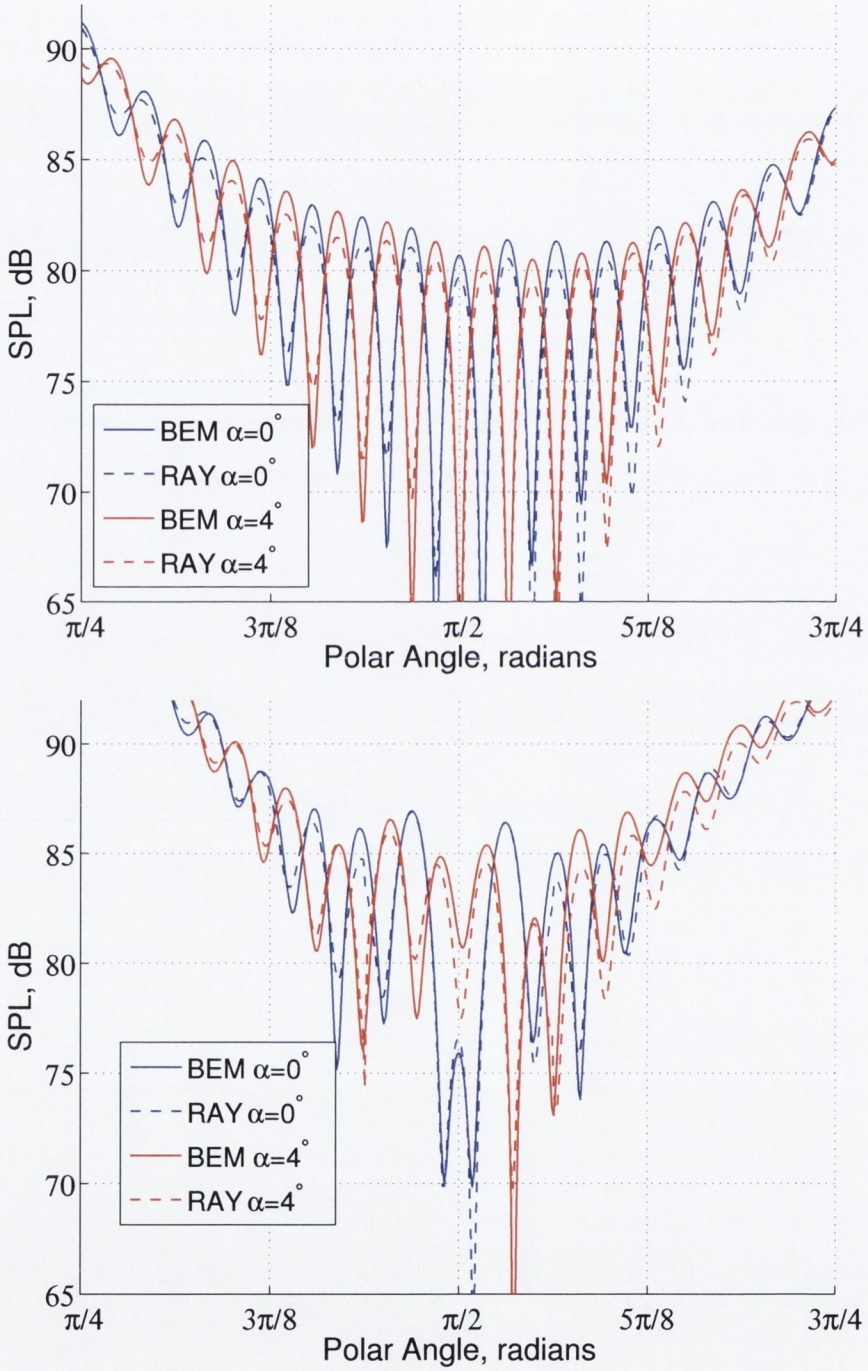
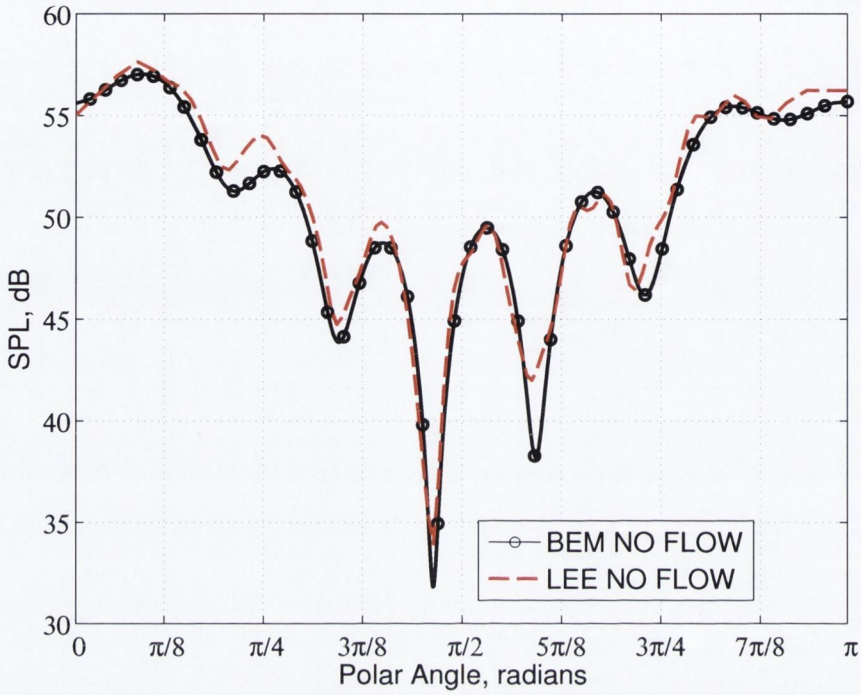


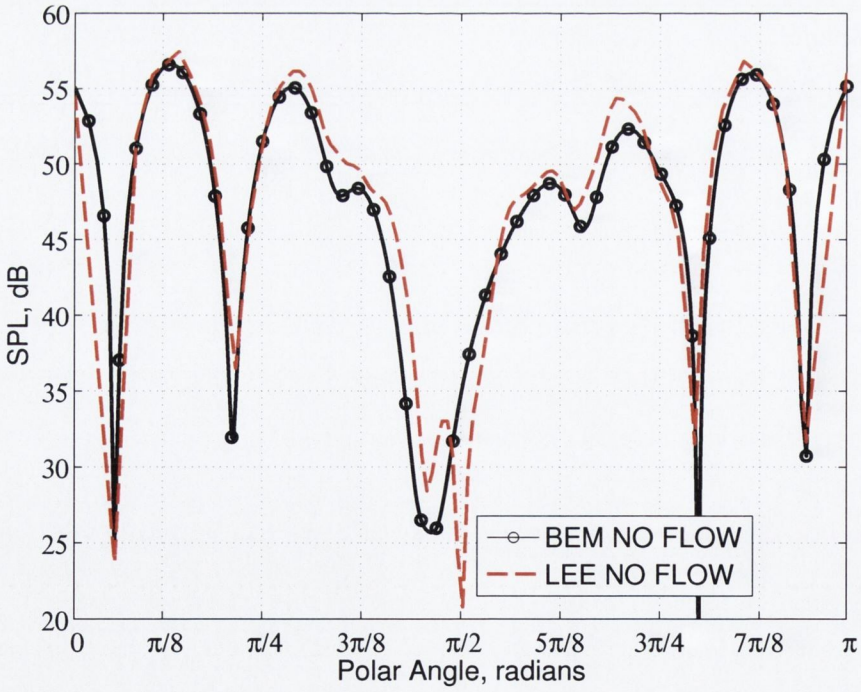
Figure 5.41: Comparison of predicted SPL in the flyover and sideline, Top: flyover. Bottom: sideline. 1500Hz, M=0.3, WR=6, TR=0.3

A comparison of the BEM and LEE solutions in the far-field is shown in Fig. 5.43. A reference BEM solution with no flow conditions, has been included to show the relative effect of increasing steady lift on far-field SPL. The no flow solutions of the BEM and LEE have also been compared separately in Fig. 5.42 and show close agreement for this baseline case. It was found that the best agreement in predicted SPL between BEM and LEE simulation was obtained for the PGT BEM scheme with the Kutta condition. The magnitudes and locations of the peaks are closely matched across the three different steady flow angles, although the LEE simulations tend to show several additional minor peaks that are most likely caused by artificial reflections at the boundaries. The $\alpha = 4°$ case for the LEE simulation also shows an unusual dip in SPL to the forward arc. This feature does not appear to be caused by any particular artificial contamination based on the near-field plots shown previously. Although the dip in SPL also appears in the sideline, it must be noted that the receiver points are positioned along a circular arc and that the polar angle $\vartheta = 0$ is a single point on the far-field sphere. Given that the surface area represented by the range of angles close to $\vartheta = 0$ is small, the error in this zone should not be given too much emphasis.

A second LEE calculation was performed for the $\alpha = 8°$ case, in order to examine the impact of variations in the density and sound speed of the acoustic medium on the far-field scattering pattern. The mean flow for this run was computed with the incompressible FLUENT solver and with the density and sound speed fixed at the free stream values listed in Table. 5.1. The shielding results for this case are visible in Fig. 5.43(e) and Fig. 5.43(e) as the green dashed line. The close agreement between the incompressible case and the compressible case suggests that the compressibility of the steady flow has a minimal influence on far-field pressure values for a Mach number of 0.3.

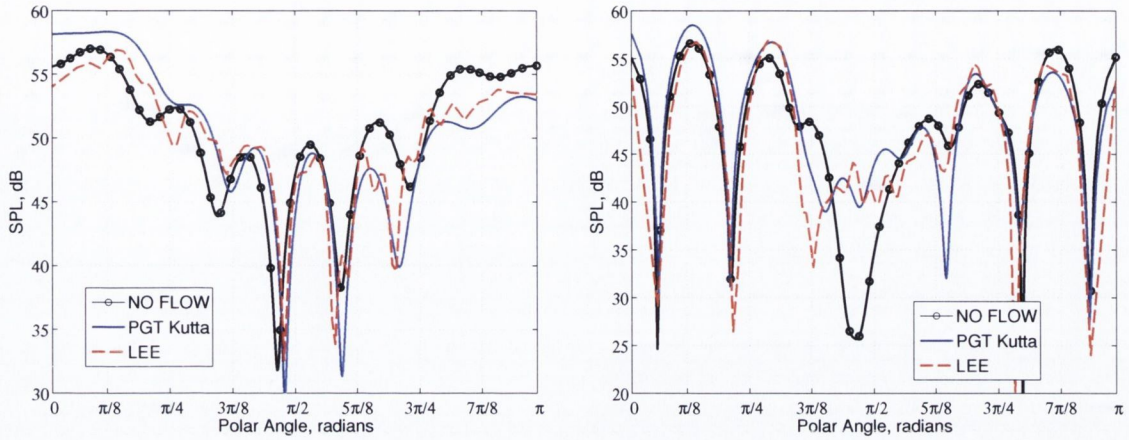


(a) Static conditions, flyover



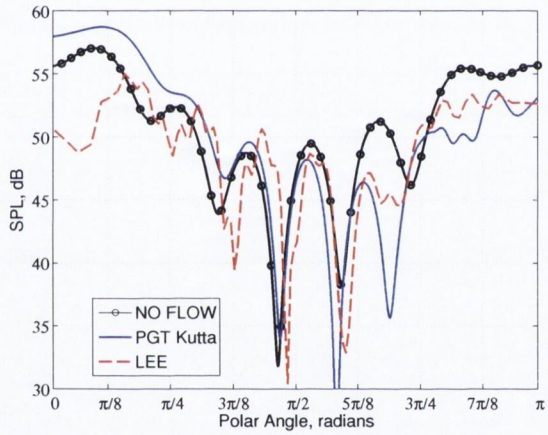
(b) Static conditions, sideline

Figure 5.42: SPL plots comparing LEE simulation with BEM in flyover and sideline, $M = 0$, $500Hz$, symmetry plane solution.

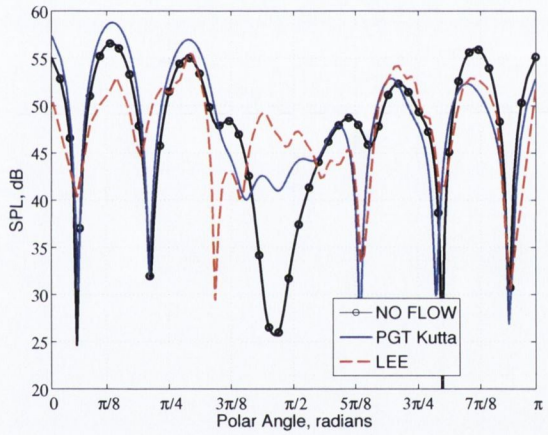


(a) $\alpha = 0°$, flyover

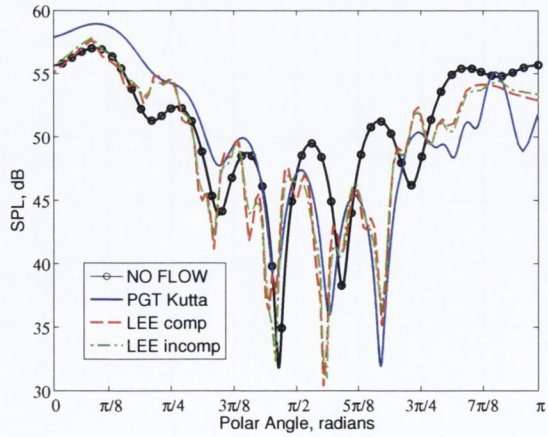
(b) $\alpha = 0°$, sideline



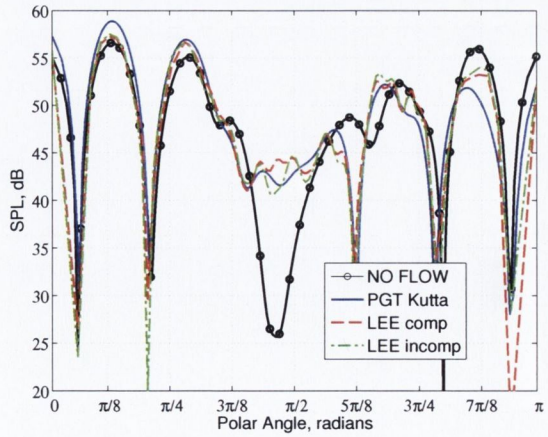
(c) $\alpha = 4°$, flyover



(d) $\alpha = 4°$, sideline



(e) $\alpha = 8°$, flyover



(f) $\alpha = 8°$, sideline

Figure 5.43: SPL plots comparing LEE simulation with BEM (PGT Kutta) in flyover and sideline, $M = 0.3$, $500Hz$, symmetry plane solution.

5.5.5 Frequency Averaged Shielding Factor

Due to the oscillatory nature of the scattered field, the overall impact of the flow conditions on the shielding effectiveness of a particular wing is difficult to appreciate when single frequency results are plotted. The tendency of a non-lifting flow to increase the shielding effect of a wing is intuitively understood in terms of the stretching of the wing chord in the Prandtl-Glauert domain, which then increases the angle subtended by the source on the wing relative to the non-transformed geometry. However, the effect of a lift producing flow on sound propagation to the far-field is less obvious. Howe's theory of vortex scattering predicts that refraction of sound should occur as waves pass through a potential vortex. This suggests that a change in the magnitude of the sound field should be observed on the far-field sphere in the region where the direct path of propagation passes through the wingtip vortices. The presence of a strong interference pattern tends to obscure small to moderate changes in the magnitude of the sound field. In order to reduce the oscillatory pattern in the shadow region, a process of averaging the shielding factor over a frequency band was performed for several test cases.

Given an acoustic source with a known spectral density, the root mean squared pressure field can be calculated indirectly by, by uniformly sampling the spectral density of the source, performing discrete frequency calculations of the scattered pressure field, and then summing the pressures incoherently in the the far-field. This method of calculation follows directly from Parseval's theorem. Since the root mean squared pressure is defined as,

$$p_{rms} = \sqrt{\frac{1}{T}\int_{-T/2}^{T/2} [p(t)]^2 \, \mathrm{d}t} \tag{5.4}$$

and the time domain pressure field may be replaced by its Fourier series when it is composed of a set of uniformly sampled frequencies,

$$p(t) = \sum_{n=-\infty}^{\infty} p(\omega) e^{2\pi j n t/T} \tag{5.5}$$

Then by Parseval's theorem,

$$p_{rms} = \sqrt{\sum_{n=-\infty}^{\infty} |p(\omega)|^2} \tag{5.6}$$

and the infinite sum may be truncated to some finite interval when the source spectral density is band limited. A frequency averaged shielding ratio may then be computed by taking the ratio of the root mean squared values of the shielded and unshielded pressures. This process tends to remove the interference pattern and expose the overall trend in the scattered pressure magnitudes as the bandwidth of the spectral density is widened.

The frequency averaged shielding factor was computed for several test cases with monopole sources. In each case the shielding factor has been plotted over the far-field sphere. The horizontal and vertical axes of the plots are the polar angle and azimuthal angle of the spherical coordinate system defined in Fig. 5.3. The sideline and flyover arc have been plotted as dashed lines as a reference to the previous plots.

In Fig. 5.44, shielding results in a non-lifting and lifting flow are compared for a single monopole source positioned at the reference location of $(-0.5L_c, 0.5L_s, 0.5L_c)$. The source has constant acoustic power density over a one third octave band, and the centre frequency of the one third octave band is $500Hz$. The shielding factor was calculated with a set of ten uniformly spaced samples over the frequency band. For this frequency range, the scattering of sound by the potential flow at the wingtip vortices is relatively weak but is still visible in the contour plots as a yellow colored fringe of higher shielding, next to the sideline arc. This fringe initially runs along a line of constant azimuthal angle and is visible from a polar angle of $\pi/2$, extending into the rear arc. As it extends further into the rear arc, it joins another line of increased shielding that approximates a line of constant polar angle. These regions correspond to the line of sight that passes through the wingtip vortex and the starting vortex respectively. The increase in shielding factor appears to match Howe's theory, at least qualitatively, since the region of increased shielding is on the inside of the vortex lines, where sound waves propagate in the same direction as the induced velocity produced

by the vortices. It is somewhat surprising that an apparent interaction with a starting vortex appears in the shielding results at all. The steady flow calculation itself, does not include any starting vortex because the vortex filaments are extended to infinity by approximating the wake as a set of horseshoe vortices. The explanation for this feature is the artificial truncation of the wake in the acoustic BEM solution. By reducing the circulation in the wake to a zero value over a transition region with an artificial blending function, the transition zone behaves just like a starting vortex that has been smoothed out over a finite region, despite the fact that the steady flow was computed with no artificial truncation.

In Fig. 5.45, the frequency has been increased to $1000Hz$ and once again the source is assumed to have constant acoustic power density over a one third octave band. The vortex scattering effect is clearly enhanced by increasing the frequency. This effect is to be expected since Howe's theory predicts that the magnitude of the scattered field scales with, $\Gamma k\ \varphi^0/c_\infty$, as discussed previously. The distribution of vorticity also plays a role in the strength of the scattering effect. This can be seen in Fig. 5.46, where the tapered wing has been replaced by a rectangular wing of the same wingspan as the tapered wing but with a constant wing chord, equal to the root chord of the tapered wing. The switch from the tapered to rectangular planform increases the lift on the wing by a small amount and also redistributes the streamwise vorticity towards the wingtips so that the wingtip vortices are increased in strength. As a result of the increased vortex strength, the shielding factor in the sideline fringes is enhanced. This is clearly noticeable when compared against the symmetric shielding pattern of the no flow conditions.

To demonstrate that the scattering effect is genuinely an artifact of scattering by wingtip vortices, the source position was moved incrementally along the wingspan to vary the angle subtended by the source on the wingtip vortices. In Fig. 5.47, the monopole source has been moved to the locations $x_2 = 0.3L_s$ and $x_2 = 0.1L_s$ while keeping the other source coordinates constant. It is clear that the fringe pattern follows the line of sight that connects the source to the vortex lines as the source is moved.

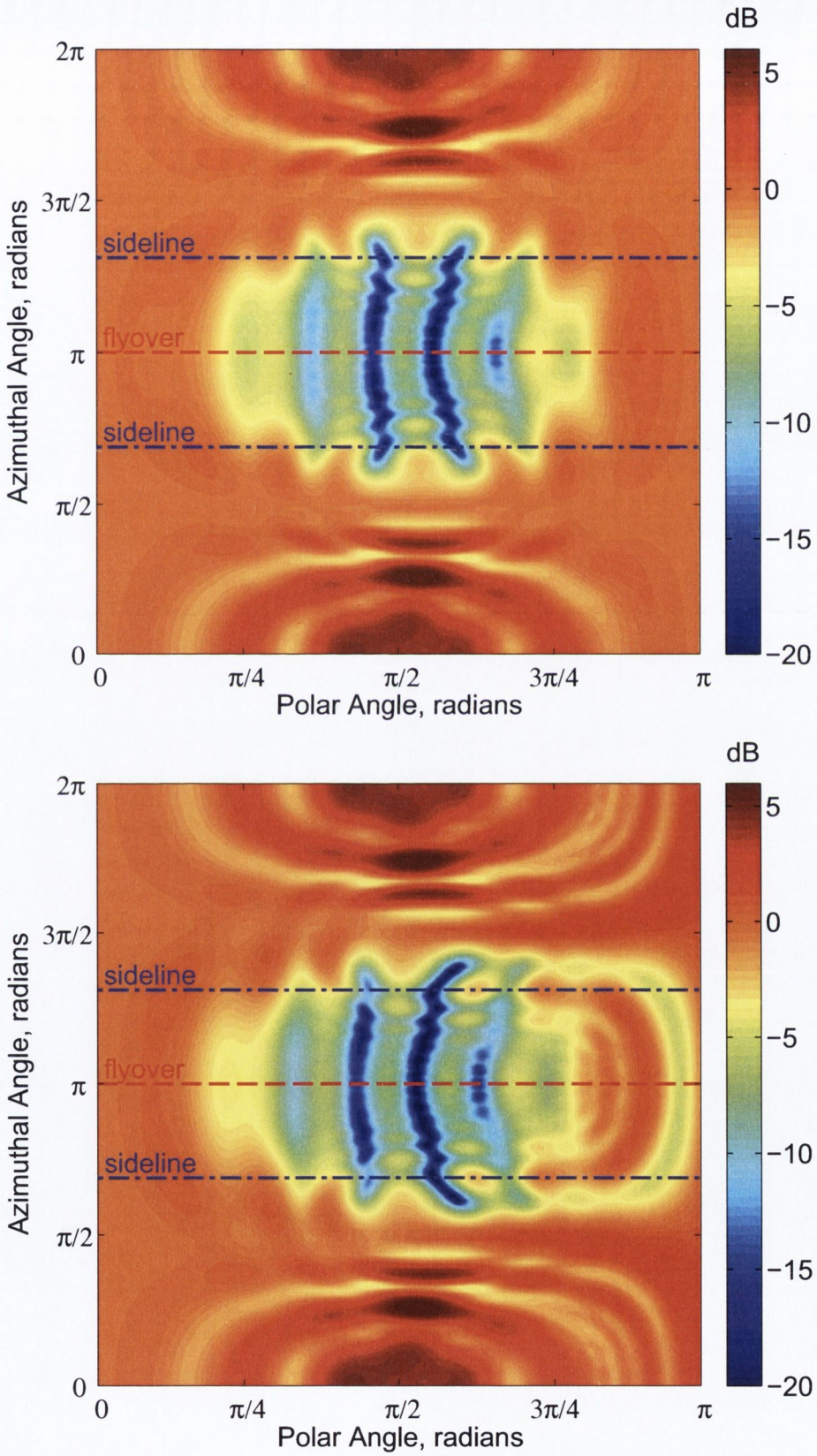


Figure 5.44: Contours of frequency averaged shielding factor (decibel scale), tapered wing, $500Hz$, $M = 0.3$, $TR = 0.3$, $WR = 6$. Top: $\alpha = 0°$. Bottom: $\alpha = 8°$

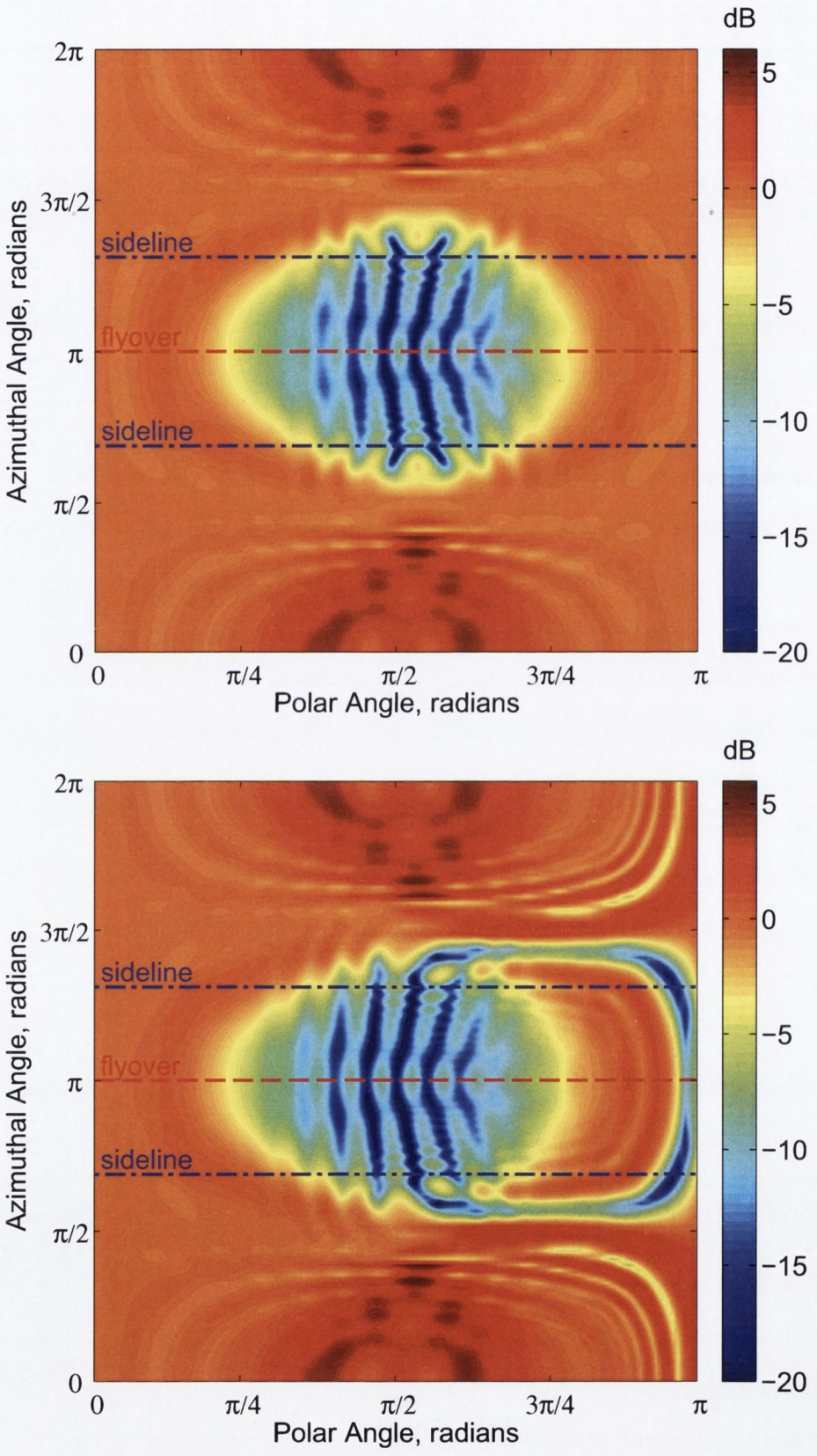


Figure 5.45: Contours of frequency averaged shielding factor (decibel scale), tapered wing, $1000Hz$, $M = 0.3$, $TR = 0.3$, $WR = 6$. Top: $\alpha = 0°$. Bottom: $\alpha = 8°$

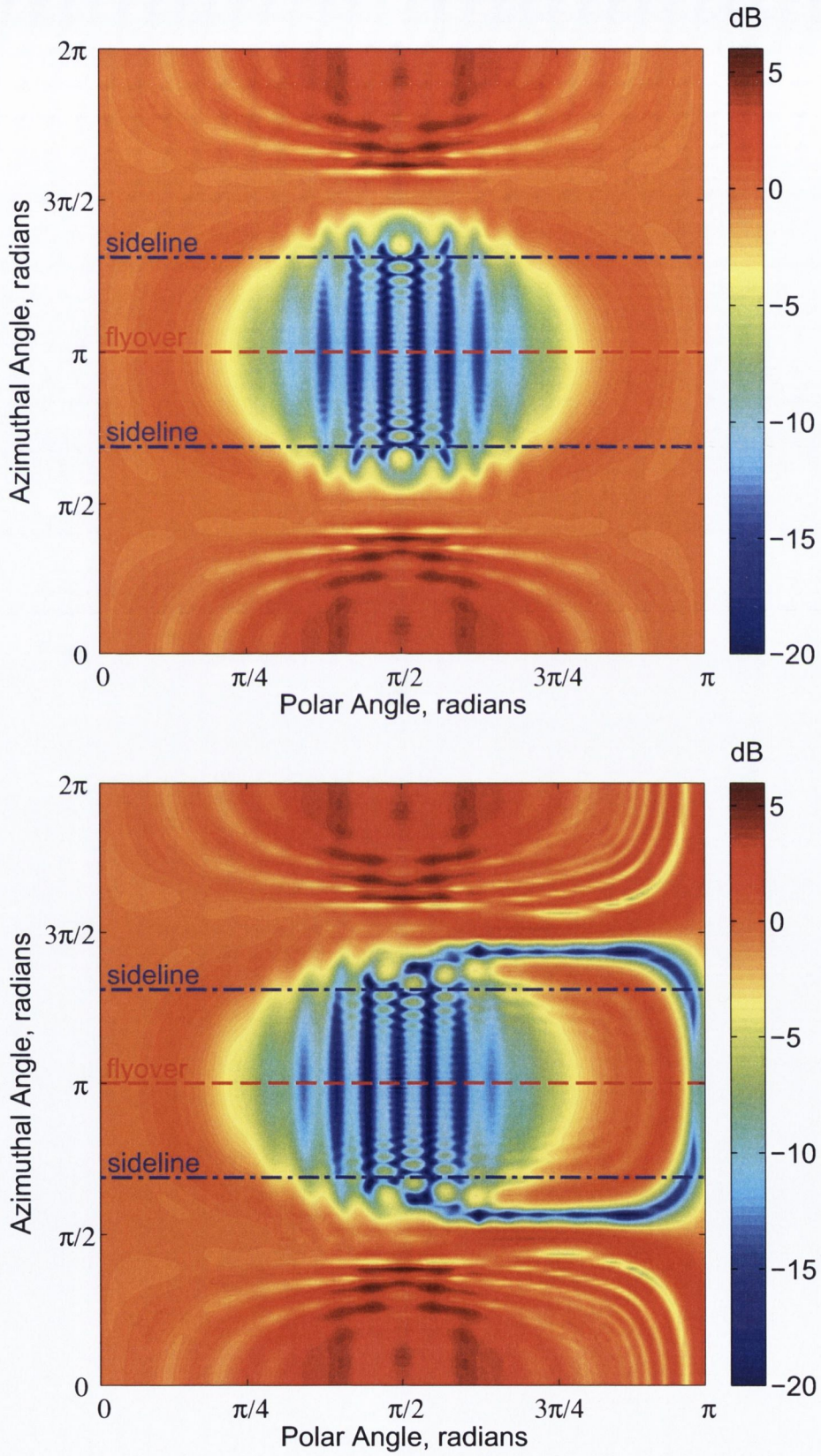


Figure 5.46: Contours of frequency averaged shielding factor (decibel scale), rectangular wing, $1000Hz$, $M = 0.3$, $TR = 0.3$, $WR = 6$. Top: $\alpha = 0°$. Bottom: $\alpha = 8°$

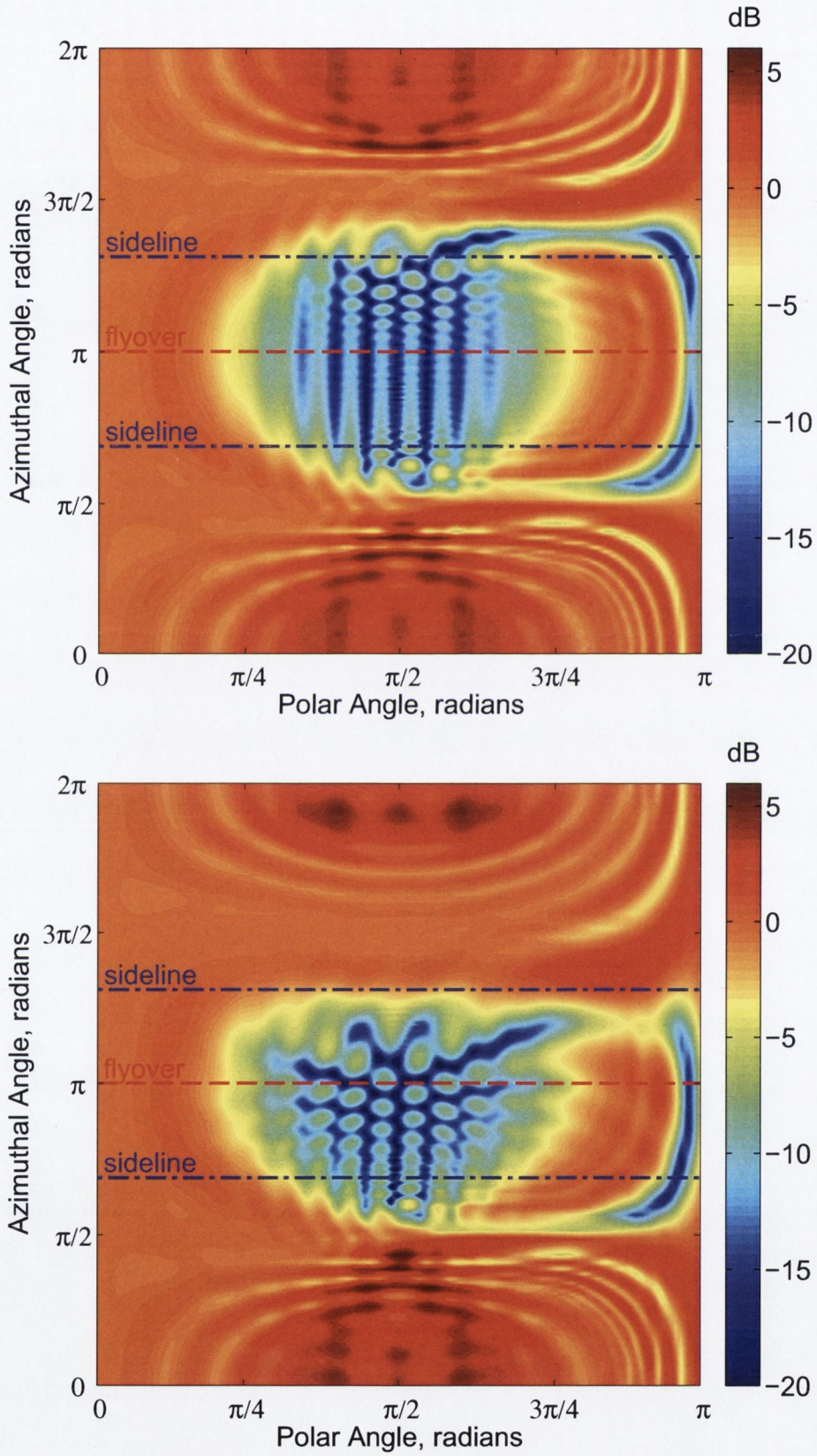


Figure 5.47: Contours of frequency averaged shielding factor (decibel scale), rectangular wing, $1000Hz$, $M = 0.3$, $TR = 0.3$, $WR = 6$, $\alpha = 8°$ Top: source x_2 position, $0.3L_s$. Bottom: source x_2 position, $0.1L_s$

5.6 Performance of BEM solver

The MATLAB implementation of the biconjugate gradient stabilized (BCGSTAB) method was used to solve the matrix equation system in the BEM discretization. Each iteration of the BCGSTAB method requires two matrix vector products. This step was accelerated with the fast block Toeplitz matrix multiplication algorithm described in Section. 3.5.1. As an illustration of the effectiveness of this acceleration, the cpu time for one iteration of the linear solver is typically less than 10 seconds for the largest problems considered in this work. While a detailed comparison of the performance of the LEE and BEM methods is not particularly useful because the two methods have been optimized for different applications, an order of magnitude comparison can be performed to give an appreciation for the computational demands of the two methods.

For the LEE problem, the acoustic meshes typically consisted of 100,000 to 500,000 elements. Under no flow conditions, a coarse mesh of 100,000 elements was found to be more than sufficient for accuracy and stability. Under lifting flow conditions, a higher mesh density was required near the leading edge to ensure the stability of the solver. Since the LEE method uses a high order discretization in each element, the actual number of degrees of freedom is much higher than the element count. The number of degrees of freedom per element varies with element order according to

$$NDOF = \tfrac{1}{6}(p+1)(p+2)(p+3) \tag{5.7}$$

where p is the order of the element. The value of p is selected automatically by the code to an optimal value based on the wavelength of sound, the local flow velocity and the element size. For the flows and frequencies considered in this work, the average element order was close to 6 for the 100,000 element meshes and approximately 4 for the 500,000 element mesh. This corresponds to a solution vector of between 50 and 100 million degrees of freedom. By comparison, the BEM surface discretization requires only a small fraction of the total number of degrees of freedom. Table. 5.4 shows the typical variation in the number of degrees of freedom required to resolve the solution at $500Hz$ when various wake truncation lengths are used.

Comparing the run times of the two codes, the LEE simulations were run for 4 to 6 hours on 32 cpus (AMD Opteron 2300-series "Barcelona", 16GB RAM), when running with no flow conditions. For lifting flow conditions, the each run was carried out on 64 cores and taking approximately 16 hours to complete. The run time was found to increase rapidly as the resolution of the leading edge was increased due to the small time-step required to satisfy the CFL condition. For the BEM solver, the solution time is on the order of at most tens of minutes on a single desktop processor (Intel pentium 4, 1GB RAM). It should be noted that the LEE computational time is not a fair reflection of the full potential of the DGM method because the calculations were performed in the time domain for single frequency sources. With a broadband source, all frequencies up to the maximum frequency permitted by mesh density may be simulated in one computation. By contrast, the frequency domain BEM solver requires multiple solver iterations to cover a wide frequency range. The values mentioned above are included purely to give an order of magnitude comparison in performance between the two solution strategies.

WR	Degrees of Freedom
0	5049
2	24633
4	44217
8	83385

Table 5.4: Growth in BEM linear system size for various wake ratios. Frequency $500Hz$, $M = 0.3$

The impact on performance due to the addition of the mean flow effects in the BEM formulation has been assessed for various flow conditions and frequency ranges. The most obvious performance impact of adding the wake to the BEM discretization is the increase in the discrete system size because of an increase in the length of the scatterer. For the accelerated BEM scheme used in this work, the growth in the solution time with the scatterer size is slow because of the $O(NlogN)$ time complexity of the matrix multiplication step. A more critical issue for the iterative solution approach is the conditioning of the linear system, which determines the number of iterations required for convergence. In Fig. 5.48, the convergence behavior of the BCGSTAB solver is plotted for various flow incidence angles. Examining the slopes of the convergence

curves it is clear that the inclusion of the wake in the BEM formulation tends to have a negative impact on the conditioning of the system. This trend is also visible when the angle of attack is fixed and the frequency of the source is increased, as shown in Fig. 5.49. These results suggest that some preconditioning may be required at higher frequencies to improve the rate of convergence of the iterative solver.

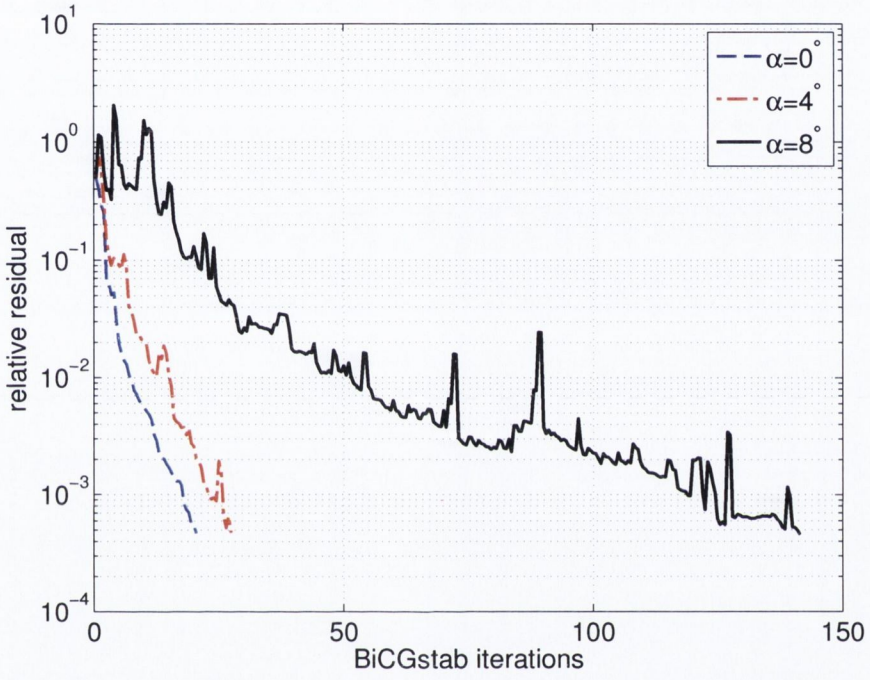


Figure 5.48: Convergence of BCGSTAB for the PGT BEM formulation, $M = 0.3$, Frequency= $500Hz$

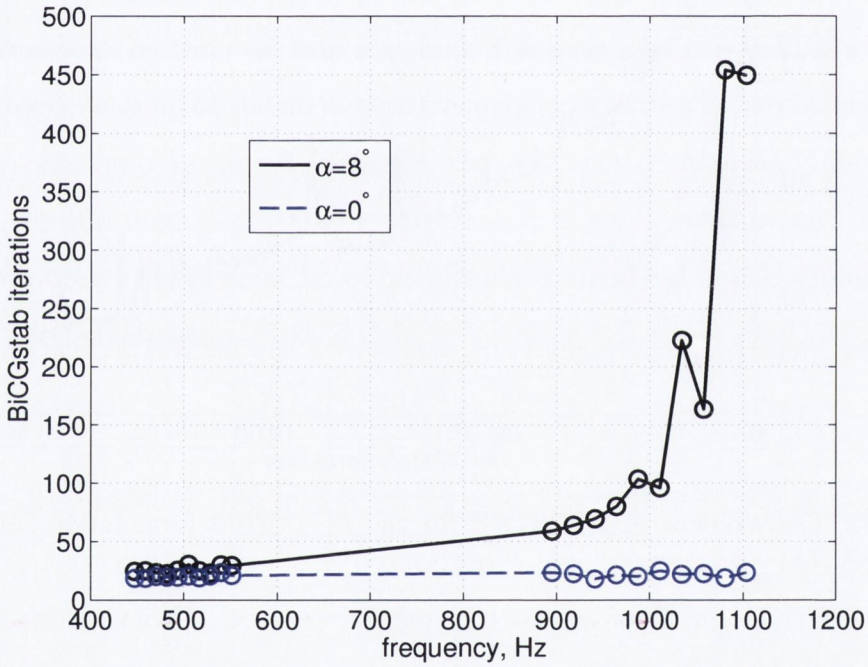


Figure 5.49: Variation in iteration count with frequency for the BCGSTAB solver with PGT BEM. $M = 0.3$

5.7 Discussion

5.7.1 Scattering Mechanisms in Low Mach Number Flow

In Chapter. 3, it was argued that the uniform flow BEM formulation neglects several scattering mechanisms that may have a significant impact on the accuracy of in-flight acoustic shielding predictions. In particular, the measurements of vortex refraction effects by Jeffrey et. al. [12] show an increase in shielding of 8 dB in the sideline. These effects are fully three dimensional in nature and cannot be captured by simulations that only consider a section of the wing and fuselage. Scattering simulations on full aircraft geometries that only account for a uniform flow also fail to capture these phenomena. The novel BEM approach described in this work, has been developed to extend the capability of the standard formulation to include the scattering effects of lifting potential mean flows at low Mach number. These additional mechanisms are comprised of:

1. Refraction of sound by the potential flow field surrounding a vortex filament.

2. Conversion of acoustic waves to vortex modes at a sharp trailing edge.

3. The Interaction of sound with compact vorticity in a vortex filament.

The relative importance of these three mechanisms has been explored through a model problem of shielding by a symmetric wing. For low Mach number conditions the results show a number of clear trends. Firstly, the magnitudes of the scattering effects are moderate to weak, relative to the strength of the incident field. Secondly, only the first mechanism, of the three scattering effects listed, has a significant impact on the shielding factor when frequency averaging is performed. Based on the results in Figures 5.44-5.47, the most significant change to the far-field shielding occurs on the region of the far-field sphere where sound passes close to the wingtip vortices. There are two lobes associated with the vortex scattered field, one of which tends to increase the shielding factor and the other decreases it. The region of increased shielding effectiveness occurs on the side of the vortex where sound propagates past the vortex in the same direction as the steady velocity field induced by the vortex. The shielding

factor increases in magnitude by approximately 6-8 dB for a $1000Hz$ monopole in the far-field zone where the vortex scattering effect is strong. The shielding results in uniform flow show that the shedding of vorticity may be of significance at higher Mach number but the low speed conditions encountered during take-off and landing are in the Mach number range in which the Kutta condition effect is small. The final mechanism in the list above was shown to be at least an order of magnitude smaller than the incident field and can be neglected from the analysis with no loss in the accuracy of the prediction. Another noticeable feature is the lack of interaction between the Kutta condition and vortex refraction mechanism. When both are included in a single calculation, the combined effect appears to be a superposition of the scattered fields produced by each mechanism in isolation, with little or no interaction between the two.

At higher Mach number, these trends will change. The transformation method may not be used to explore this parameter range because it is based on a small Mach number expansion of the steady flow. However, it is still worth considering how the various scattering terms scale during different flight conditions. At take off and landing conditions, the lifting-flow refraction mechanism has the largest impact on the far-field shielding factor relative to the other flow scattering mechanisms. This trend is clear from the shielding plots at low Mach number. As the flight speed increases, the effect of vortex shedding will become more significant and may account for an increase in shielding of up to 5dB, as the shielding results with the Kutta condition at high Mach number demonstrate (see Fig. 5.17). In contrast, the scattering effect of the lifting flow will decrease with flight speed. Considering that the lift on the aircraft remains almost constant during flight, the bound circulation on the wing must drop as the flight speed increases. This is a direct consequence of the Kutta-Joukowski theorem. According to Helmholtz's theorems of vortex filaments, the wingtip vortices will decrease in strength by the same amount as the bound circulation. Hence, the lifting-flow scattering term will decrease in strength as flight speed increases and lift remains constant. This suggests that scattering by the wingtip vortices will only dominate at low flight speed conditions.

One feature of the perturbation field that emerges from analysis of the near-field results, is the complex manner in which the pressure and velocity fields are modified by a nonuniform flow field. By comparison, the magnitude of the acoustic potential field is constant to order $O(M^2)$. This is the quantity that should be examined for near-field refraction effects. Both Howe[13] and Doak [89] have argued that the perturbation stagnation enthalpy is the appropriate fundamental dependent variable for aeroacoustic analyses. In an irrotational and homentropic flow, this quantity is closely linked to the perturbation potential through the relation

$$B' = -\frac{\partial \phi}{\partial t} = -j\omega\phi \tag{5.8}$$

and the two quantities are effectively interchangeable for time-harmonic analysis in potential mean flow. The fact that the acoustic potential is weakly modified by low Mach number flow highlights the importance of distinguishing the convection effects that may be regarded as refractive from the non-refractive effects. The term refraction itself is often used loosely to describe any modification of the perturbation field due to inhomogeneity of the acoustic medium. In this work, the term refraction is used only to describe changes in the direction of energy propagation as a result of inhomogeneity of the medium. This distinction is made because the usefulness of a shielding prediction hinges on the accurate calculation of the angular redistribution of acoustic energy. The arrival time of the sound and the subtle details of the scattering pattern are arguably of no relevance when assessing shielding effectiveness. Consider the expression for the acoustic energy flux in a homentropic irrotational flow [13],

$$\mathbf{I}_a = -\frac{\partial \phi}{\partial t}\left(\rho_0 \mathbf{v}' + p'/c^2 \mathbf{U}\right) \tag{5.9}$$

Taylor's transformation and Bernoulli's equation (Eq. 2.26 and Eq. 2.27), may be used to write the energy flux entirely in terms of the transformed potential giving

$$\mathbf{I}_a = -j\omega\varphi e^{j\tau}\left(\rho_0 \nabla(\varphi e^{j\tau}) - \frac{\rho_0}{c^2}\left(j\omega\varphi e^{j\tau} + \mathbf{U}\cdot\nabla(\varphi e^{j\tau})\right)\mathbf{U}\right) \tag{5.10}$$

$$= -j\omega\rho_0 e^{2j\tau}\varphi\nabla\varphi \quad + O(M^2) \tag{5.11}$$

in the low Mach number approximation. This clearly shows that the magnitude of the energy flux in a low Mach number potential flow is independent of the mean flow to $O(M^2)$. The complex variation in the magnitudes of the pressure field and the velocity field are actually explained by a transfer of energy from potential to kinetic states and vice versa and not by refraction due to a non-uniform mean velocity. From this perspective, the pressure or velocity fields are not reliable indicators of the refractive effects of a mean-flow. Instead, the acoustic potential or stagnation enthalpy should be examined for evidence of true refractive effects. However, this does not diminish the fact that the observer actually hears the acoustic pressure disturbance and not a derived quantity.

5.7.2 Limitations of the PGT Transformation Method

The novel BEM approach described in this work is based on a simplified form of the convected wave equation. The development of this approximate model of sound propagation relies on a number of key assumptions:

- The mean flow can be assumed homentropic and irrotational.
- The mean flow may be expanded as a low Mach number disturbance to a uniform flow, which is also of low Mach number.

Considering the first of these assumptions, the boundary layers on the wing surfaces and the vorticity shed from the boundary layers into the wake are assumed to have a negligible impact on sound scattering. This approximation is common to most aeroacoustic propagation models for both potential and LEE solvers. In industrial applications, the boundary layers are usually removed from the mean flow field, even when a viscous RANS solver is used to calculate the steady flow field. There is still a difference between a RANS solution in which boundary layers have been removed and a fully inviscid flow. This difference primarily occurs in the wake region, where a RANS solution has a large drop in the total pressure and the velocity magnitude in the wake itself. The vorticity associated with the shed boundary layers is distinct from the streamwise vorticity that is shed due to the production of lift. Only the

latter component of vorticity introduces a net circulation into the steady flow. In the long wavelength limit, it is the net circulation of the vorticity that impacts on sound propagation. In this sense, the PGT approach is limited to wavelengths that are larger than the typical thickness of the boundary layers.

The other implication of assuming potential mean flow is that a potential flow solver must be introduced into the calculation loop. Panel solvers for Laplace's equation have been used in industry for decades and the numerical methods are well developed. There are still a few disadvantages to this approach. Firstly, the treatment of the wake is awkward in a panel method. While there are no theoretical barriers to treating complex aircraft configurations and multi-element wings with a potential solver, the implementation details become far more complicated when multiple wakes are present and the possibility of wakes intersecting with solid bodies becomes problematic. Secondly, RANS solvers are now standard for aerodynamic simulations, which implies the potential step is redundant as far as aerodynamic analysis is concerned. In this respect, the mean flow potential solution really constitutes an additional step in the acoustic scattering solution.

The last assumption in the list above is the most limiting in practice. In Chapter. 3, it was shown that the largest error term in the Mach number expansion of the mean flow is the $O(M_\infty M_1')$ term. For the two dimensional case, a non-uniform transformation was proposed to account for this term. It is possible that a generalization of this approach to the fully three dimensional case could capture the $O(M_\infty M_1')$ effects for general geometries but this seems unlikely for two reasons. Firstly, the two dimensional transformation utilizes the stream function in the transformation approach. In three dimensions, this would presumably require a knowledge of the dual stream functions that describe sets of intersecting stream surfaces. These functions are difficult to compute for realistic flows and are rarely if ever computed in practice. Secondly, the treatment of the steady potential jump across a wake is non trivial and would require some special treatment to reconnect points on either side of the wake that are split by a non-uniform coordinate stretching. However, the results presented in this chapter demonstrate that a close agreement in the far-field pressure can be obtained between an LEE simulation and the BEM model when the simplified transformation is used.

It appears that the modifications to the far-field pressure, induced by a lifting potential flow, can be captured to within a tolerance of +/- 2 dB by the relatively crude approximations of the PGT approach with no need to model higher order terms.

Chapter 6

Conclusions

In this work a boundary element formulation was developed for the prediction of acoustic shielding of aircraft noise in low Mach number flight. The acoustic field is modeled by the convected wave equation for the acoustic velocity potential under the assumption that the mean flow is irrotational and homentropic everywhere except for a thin wake extending from the trailing edge. The propagation model has been further simplified by applying a small disturbance and low Mach number expansion to the convected wave equation and neglecting the higher order terms. A novel transformation method was proposed to reduce the convected propagation equation to an analogous problem in static conditions. An analysis of the modeling errors in the transformation approach, for a Joukowski airfoil in a lifting flow, showed that the novel method captures the convective effects of a nonuniform flow more accurately than either the Prandtl-Glauert or Taylor transformation methods.

The baseline BEM model was modified to account for two additional scattering mechanisms. Unsteady vortex shedding is captured by adding a convected vortex wave to the acoustic solution. This vortex mode satisfies an unsteady Kutta condition at the trailing edge. A Born approximation to the scattering of sound by the rotational core of a vortex filament was also included in simulations. It was found that this scattering mechanism was several orders of magnitude smaller than the incident field and could be neglected from shielding calculations without loss of accuracy.

An analytical model was developed for the diffraction of monopole sources by a half

plane in uniform flow. A far-field expansion of this reference solution shows that the Kutta condition field for a monopole is strongest in the flyover plane and diminishes in magnitude as the angle of edge diffraction is increased. This reference solution has also been used to explore the impact of the unsteady Kutta condition on the noise shielding effectiveness of a wing by extracting diffraction coefficients from the analytical solution for use in a ray-tracing prediction method.

Acoustic shielding predictions have been presented for a planar wing immersed in a low Mach number flow. The far-field shielding factor predicted by the novel BEM approach agrees with a reference LEE solution to a tolerance of 2 dB for various angles of flow incidence, with the exception of a few isolated points. The most significant additional scattering mechanism caused by the introduction of lift has been identified as the refraction of sound by the potential flow field induced by the wingtip vortices. The magnitude of this effect is approximately 6-8 dB in the sideline, for a $1000Hz$ source at the highest lift setting considered. This was shown to be significantly larger than the effect of the Kutta condition, which increased the shielding factor by a maximum of 2dB in the flyover plane, for the same flow conditions.

Analysis of the near-field results highlights the importance of distinguishing the convection effects that are refractive from the non-refractive effects. The modification of the near-field pressure and velocity fields by a low Mach number flow were shown to be caused by a transfer of acoustic energy between potential and kinetic states rather than by an angular redistribution of energy. This type of convection effect is of minor importance when assessing shielding effectiveness because it does not produce a net change in the far-field shielding factor.

The novel BEM formulation developed in this work shows considerable potential for use as a design tool in shielding calculations on novel aircraft configurations. It has been demonstrated that the relatively weak scattering effects of a lifting flow may be captured by the PGT transformation strategy with a straightforward modification to the standard BEM formulation. This lifting flow correction could be added to existing fast BEM solvers with minor modifications to the source code. The compatibility of the novel formulation with accelerated iterative solvers has been demonstrated by application of a fast Toeplitz matrix multiplication strategy with the BCGSTAB solver.

However, the performance of the solver degrades with increasing magnitude of the flow nonuniformity. Future work on simulating the shielding pattern of a full aircraft configuration should be directed at investigating the use of preconditioning strategies for improving the rate of convergence of the accelerated BEM scheme.

Bibliography

[1] B. Berglund, T. Lindvall, and D.H. Schwela. Who guidelines for community noise. *http://www.who.int/docstore/peh/noise/guidelines2.html*, 1999.

[2] *Noise standards: Aircraft Type Certification*, volume 34. Fed. Regist., Nov 1969.

[3] *Annex 16 - Environmental Protection.* International Civil Aviation Organisation, 1971.

[4] R.J. Astley, A. Agarwal, K.R. Holland, P.F. Joseph, R. Sugimoto, R.H. Self, M.G. Smith, and B.J. Tester. Predicting and reducing aircraft noise. In *14th International Congress on Sound and Vibration*, July 2007.

[5] H. Batard and A. France. the zero splice engine intake liner: an efficient way of reducing aircraft noise without any weight or aerodynamic penalty. In *2004 24 th ICAS Congress, Tokyo Japan.*

[6] R.W. Jeffery and T.A. Holbeche. Experimental studies of noise shielding effects for a delta-winged aircraft. *AIAA Paper 75-513*, 1975.

[7] E. Maury. Rosas final meeting: Overview of achievements. *http://www.who.int/docstore/peh/noise/guidelines2.html*, 2005.

[8] J. FROTA. Nacre novel aircraft concepts. *Aeronautical Journal*, 114(1156):399–404, 2010.

[9] A. Dowling and E. Greitzer. The silent aircraft initiative-overview. In *45 th AIAA Aerospace Sciences Meeting and Exhibit*, pages 8–11, 2007.

[10] AP Dowling and T. Hynes. Towards a silent aircraft. *Aeronautical Journal*, 110(1110):487–494, 2006.

[11] J.M. Song and W.C. Chew. Large scale computations using fisc. In *Antennas and Propagation Society International Symposium*, volume 4, pages 1856–1859, Salt Lake City, UT, USA, 2000. IEEE.

[12] R.W. Jeffery and E.G. Broadbent. Wind-tunnel investigation of vortex refraction effects on aircraft noise propagation. In *3rd AIAA Aeroacoustics Conference*, August 1977.

[13] M.S. Howe. *Acoustics of Fluid-Structure Interactions*. Cambridge University Press, 1998.

[14] A. Agarwal and P.J. Morris. Calculation of sound propagation in nonuniform flows: Suppression of instability waves. *AIAA Journal*, 42(1):80–88, 2004.

[15] C. Bogey, C. Bailly, and D. Juve. Computation of flow noise using source terms in linearized eulers equations. *AIAA Journal*, 40(2):235–243, 2002.

[16] R. Ewert and W. Schroder. Acoustic perturbation equations based on flow decomposition via source filtering. *Journal of Computational Physics*, 188(2):365–398, July 2003.

[17] K.C. Hall and E.F. Crawley. Calculation of unsteady flows in turbomachinery using the linearized euler equations. *AIAA journal*, 27(6):777–787, JUN 1989.

[18] M. Khan, W.H. Brown, and K.K. Ahuja. Computational aeroacoustics as applied to the diffraction of sound by cylindrical bodies. *AIAA Paper 86-1879*.

[19] K.S. Huh and R.K. Agarwal. Numerical simulation of acoustic diffraction of two-dimensional rigid bodies in arbitrary flows. *AIAA Paper 90-3920*.

[20] C.K.W. Tam and J.C. Webb. Dispersion-relation-preserving finite-difference schemes for computational acoustics. *Journal of Computational Physics*, 107(2):262–281, AUG 1993.

[21] H. Dechipre, M. Hartmann, J.W. Delfs, and R. Ewert. Aeroacoustic simulation based on linearized euler equations and stochastic sound source modelling. In *Acoustic '08, Paris.*

[22] S. Redonnet, E. Manoha, and P. Sagaut. Numerical simulation of propagation of small perturbations interacting with flows and solid bodies. In *7th AIAA/CEAS Aeroacoustics Conference*, 2001.

[23] Graham Ashcroft and Xin Zhang. Optimized prefactored compact schemes. *Journal of Computational Physics*, 190(2):459 – 477, 2003.

[24] F.Q. Hu. Development of PML absorbing boundary conditions for computational aeroacoustics: A progress review. *Computers & Fluids*, 37(4):336–348, May 2008.

[25] R. Hixon. Radiation and wall boundary conditions for computational aeroacoustics: A review. *International Journal of Computational Fluid Dynamics*, 18(6):523–531, Aug 2004.

[26] T. Sumi, T. Kurotaki, and J. Hiyama. Generalized characteristic interface conditions for high-order multi-block computation. *International Journal of Computational Fluid Dynamics*, 21(9-10):335–350, OCT-DEC 2007.

[27] S. Redonnet, G. Desquesnes, E. Manoha, and C. Parzani. Numerical Study of Acoustic Installation Effects with a Computational Aeroacoustics Method. *AIAA Journal*, 48(5):929–937, May 2010.

[28] F.Q. Hu, M.Y. Hussaini, and P. Rasetarinera. An analysis of the discontinuous galerkin method for wave propagation problems* 1. *Journal of Computational Physics*, 151(2):921–946, 1999.

[29] D. Stanescu, D.A. Kopriva, and M.Y. Hussaini. Dispersion analysis for discontinuous spectral element methods. *Journal of Scientific Computing*, 15(2):149–171, 2000.

[30] D. Stanescu, M.Y. Hussaini, and F. Farassat. Aircraft engine noise scattering - a discontinuous spectral element approach. *AIAA Paper 2002-0800*, 2002.

[31] J. Xu, D. Stanescu, M.Y. Hussaini, and F. Farassat. Computation of engine noise propagation and scattering off an aircraft. *AIAA Paper 2003-0542*, 2003.

[32] D. Stanescu, M.Y. Hussaini, and F. Farassat. Aircraft engine noise scattering by fuselage and wings: a computational approach. *Journal of Sound and Vibration*, 263(2):319–333, 2003.

[33] A.D. Pierce. Wave equation for sound in fluids with unsteady inhomogeneous flow. *Journal of the Acoustical Society of America*, 87(6):2292–2299, 1990.

[34] O. von Estorff, editor. *Boundary Elements in Acoustics Advances and Applications*. WIT Press, 2000.

[35] M. Guiggiani, G. Krishnasamy, T.J. Rudolphi, and F.J. Rizzo. A general algorithm for the numerical solution of hypersingular boundary integral equations. *ASME J. Appl. Mech*, 59(3):604–614, 1992.

[36] S. Marburgh and T.W. Wu. *Computational Acoustics of Noise Propagation in Fluids - Finite and Boundary Element Methods*, chapter 15. Springer, 2008.

[37] H.A. Schenk. Improved integral formulation for acoustic radiation problems. *Journal of the Acoustical Society of America*, pages 41–58, 1967.

[38] G.F. Miller and A.J. Burton. The application of integral equation method to the numerical solution of some exterior boundary value problems. *Proceedings of the Royal Society of London. A.*, 323, 1971.

[39] R. Kress. Minimizing the Condition Number of Boundary Integral-Operators in Acoustic and Electromagnetic Scattering. *Quarterly Journal of Mechanics and Applied Mathematics*, 38(2):323–341, 1985.

[40] Y. Liu and S. Chen. A new form of the hypersingular boundary integral equation for 3-D acoustics and its implementation with C^0 boundary elements. *Computer Methods in Applied Mechanics and Engineering*, 173(3-4):375–386, 1999.

[41] Y. Liu and F.J. Rizzo. A weakly singular form of the hypersingular boundary integral equation applied to 3-D acoustic wave problems. *Computer Methods in Applied Mechanics and Engineering*, 96(2):271–287, 1992.

[42] C.C. Chien, H. Rajiyah, and S.N. Atluri. An effective method for solving the hyper-singular integral equations in 3-D acoustics. *The Journal of the Acoustical Society of America*, 88:918, 1990.

[43] M. Tanaka, V. Sladek, and J. Sladek. Regularization techniques applied to boundary element methods. *Applied Mechanics Reviews*, 47:457, 1994.

[44] M. Guiggiani. Hypersingular boundary integral equations have an additional free term. *Computational Mechanics*, 16(4):245–248, 1995.

[45] A. Frangi and M. Guiggiani. Free terms and compatibility conditions for 3d hypersingular boundary integral equations. *ZAMM*, 81(10):651, 2001.

[46] T. Terai. On calculation of sound fields around three dimensional objects by integral equation methods. *Journal of Sound and Vibration*, 69(1):71–100, 1980.

[47] K. Taylor. A transformation of the acoustic equation with implications for wind-tunnel and low-speed flight tests. *Proceedings of the Royal Society of London. A.*, 363(1713):271–281, 1978.

[48] R.J. Astley and J.G. Bain. A three-dimensional boundary element scheme for acoustic radiation in low mach number flows. *Journal of Sound and Vibration*, 109(3):445–465, 1986.

[49] A. Agarwal and A. Dowling. Low-frequency acoustic shielding by the silent aircraft airframe. *AIAA Journal*, 45(2):358–365, 2007.

[50] C.C. Lu and W.C. Chew. Fast far field approximation for calculating the RCS of large objects. In *Antennas and Propagation Society International Symposium*, volume 1, pages 22–25, Newport Beach, CA, USA, 1995.

[51] W.C. Chew, H.Y. Chaoa, T.J. Cuib, C.C. Luc, S. Ohnukia, Y.C. Pand, J.M. Songe, S. Velamparambilf, and J.S. Zhaog. Fast integral equation solvers in computational electromagnetics of complex structures. *Engineering Analysis with Boundary Elements*, 27:803–823, 2003.

[52] D. Huybrechs and S. Vandewalle. A two-dimensional wavelet-packet transform for matrix compression of integral equations with highly oscillatory kernel. *J. Comput. Appl. Math.*, 197(1):218–232, 2006.

[53] O.P. Bruno and L.A. Kunyansky. Surface scattering in 3-D: an accelerated high order solver. *Proceedings of the Royal Society of London. A.*, 457:2921–2934, 2001.

[54] M.C. Recchioni and F. Zirilli. The use of wavelets in the operator expansion method for time-dependent acoustic obstacle scattering. *SIAM J. Sci. Comput.*, 25(4):1158–1186, 2003.

[55] E. Sjöström. Singular value computations for toeplitz matrices. Master's thesis, Linköping University, 1996.

[56] P.J. Flatau. *Scattering by irregular particles in anomalous diffraction and discrete dipole approximations.* PhD thesis, Colorado State University, 1992.

[57] A. Xavier, C. Chniti, and K. Ramdani. On the numerical approximation of high-frequency acoustic multiple scattering problems of circular cylinders. *Journal of Computational Physics*, 227:1754–1771, 2008.

[58] J.B. Keller and R.M. Lewis. Asymptotic methods for partial differential equations: The reduced wave equation and maxwell's equations. In D. McLaughlin J.B. Keller, G. Papanicolau, editor, *Surveys in Applied Mathematics.* New York, NY: Plenum Press, 1995.

[59] P.E. Hussar, V. Oliker, H.L. Riggins, E.M. Smith-Rowlan, W.R. Klocko, and L. Prussner. An implementation of the UTD on facetized CAD platform models. *IEEE Antennas and Propagation Magazine*, 42:100–106, April 2000.

[60] S. Sefi. *Ray Tracing Tools for High Frequency Electromagnetics Simulations.* PhD thesis, KTH Stockholm, 2003.

[61] A. Agarwal, A. Dowling, H.C. Shin, W. Graham, and S. Sandy. Ray tracing approach to calculate acoustic shielding by a flying wing airframe. *AIAA Journal*, 45(5):1080–1090, 2007.

[62] O.P. Bruno, C.A. Geuzaine, J.A. Monroe, and F. Reitich. Prescribed error tolerances within fixed computational times for scattering problems of arbitrarily high frequency: the convex case. *Philosophical Transactions of the Royal Society of London. A.*, 362(1816):629 – 645, March 2004.

[63] J. Edlund. A parallel, iterative method of moments and physical optics hybrid solver for arbitrary surfaces. Master's thesis, Uppsala University, 2001.

[64] R.J. Burkholder. Forward-backward iterative physical optics algorithm for computing the RCS of open-ended cavities. *IEEE transaction on antennas and propagation*, 53(2):793–799, 2005.

[65] Ufimstev P.A. *Fundamentals of the Physical Theory of Diffraction.* Wiley-IEEE Press, 2007.

[66] D.S. Jones. The scattering of sound by a vortex sheet. *IMA Journal of Applied Mathematics*, 15(1):33, 1975.

[67] D.S. Jones. The scattering of sound by a simple shear layer. *Philosophical Transactions for the Royal Society of London. Series A, Mathematical and Physical Sciences*, 284(1323):287–328, 1977.

[68] L.M.B.C. Campos and M.H. Kobayashi. On the reflection and transmission of sound in a thick shear layer. *Journal of Fluid Mechanics*, 424:303–326, 2000.

[69] J.D. Morgan. The interaction of sound with a semi-infinite vortex sheet. *Journal of the Institute of Mathematics and Its Applications*, 27(4):465–487, 1974.

[70] R.M. Munt. The interaction of sound with a subsonic jet issuing from a semi-infinite cylindrical pipe. *Journal of Fluid Mechanics*, 83(04):609–640, 1977.

[71] G. Gabard and R.J. Astley. Theoretical model for sound radiation from annular jet pipes: far-and near-field solutions. *Journal of Fluid Mechanics*, 549:315–341, 2006.

[72] A. Demir and S. Rienstra. Sound radiation from a lined exhaust duct with lined afterbody. In *16th AIAA/CEAS Aeroacoustics Conference*, 2010.

[73] W. Eversman and D. Okunbor. Aft fan duct acoustic radiation. *Journal of Sound and Vibration*, 213(2):235–257, 1998.

[74] J. Manera, R. Leneveu, and S. Caro. Broadband turbomachinery noise: Exhaust noise computations with Actran/TM and Actran/DGM. In *15th AIAA/CEAS Aeroacoustics Conference*, Miami, FL, USA, 2009.

[75] P.V. Sakov. Sound scattering by a vortex filament. *Acoustical Physics*, 39(3):280–282, 1993.

[76] S. O'shea. Sound scattering by a potential vortex. *Journal of Sound and Vibration*, 43(1):109–116, 1975.

[77] R. Ford and S.G.L. Smith. Scattering of acoustic waves by a vortex. *Journal of Fluid Mechanics*, 386:305–328, 1999.

[78] M.S. Howe. On the scattering of sound by a rectilinear vortex. *Journal of Sound and Vibration*, 227(5):1003–1017, 1999.

[79] S.G.L. Smith and R. Ford. Three-dimensional acoustic scattering by vortical flows. I. general theory. *Physics of Fluids*, 13:2876, 2001.

[80] T. Colonius, S.K. Lele, and P. Moin. The scattering of sound waves by a vortex: numerical simulations and analytical solutions. *Journal of Fluid Mechanics*, 260:271–298, 2006.

[81] D.S. Jones. Aerodynamic sound due to a source near a half-plane. *Journal of the Institute of Mathematics and Its Applications*, 9:114–122, 1972.

[82] L. Lee, T.W. Wu, and P. Zhang. A dual-reciprocity method for acoustic radiation in a subsonic non-uniform flow. *Engineering Analysis with Boundary Elements*, 13:365–370, 1994.

[83] J. Katz and A. Plotkin. *Low-speed aerodynamics.* Cambridge University Press, Cambridge, 2001.

[84] M. Guiggiani. Formulation and numerical treatment of boundary integral equations with hypersingular kernels. *Singular integrals in boundary element methods*, pages 85–124, 1998.

[85] D.G. Crighton. The kutta condition in unsteady flow. *Annual Review of Fluid Mechanics*, 17(1):411–445, 1985.

[86] L. Morino and G. Bernardini. Singularities in BIEs for the Laplace equation; Joukowski trailing-edge conjecture revisited. *Engineering analysis with boundary elements*, 25(9):805–818, 2001.

[87] R. Balasubramanyam. Aerodynamic sound due to a point source near a half-plane. *IMA Journal of Applied Mathematics*, 33(1):71, 1984.

[88] J.J. Bowman, editor. *Electromagnetic and acoustic scattering by simple shapes.* Taylor & Francis, 1988.

[89] PE Doak. Fluctuating total enthalpy as the basic generalized acoustic field. *Theoretical and Computational Fluid Dynamics*, 10(1):115–133, 1998.

Appendix A

Singular Integrals

In this section the limit to the boundary for the hypersingular BIE on a smooth surface is developed, with reference to Guiggiani's theory for hypersingular BIEs. The integration of the hypersingular kernel over a planar constant potential element is then evaluated in polar coordinates and reduced to a contour integral of a regular function over the boundary of an element, similar to Terai's method of integration for a planar geometry [46]. Finally, the semi-analytical approach to singular integration is extended to the case in which the potential distribution over the element surface is a plane wave.

A.1 Derivation of Integral Kernels

The free space Green's function for the Helmholtz equation is given by

$$G(\boldsymbol{\eta};\mathbf{y}) = \frac{e^{-jk|\boldsymbol{\eta}-\mathbf{y}|}}{4\pi|\boldsymbol{\eta}-\mathbf{y}|} = \frac{e^{-jkr}}{4\pi r} \tag{A.1}$$

with $\mathbf{r} = \boldsymbol{\eta} - \mathbf{y}$ and $r = |\mathbf{r}|$. Taking the derivative with respect to $\boldsymbol{\eta}$ yields

$$\nabla_\eta G(\boldsymbol{\eta};\mathbf{y}) = \frac{\partial G}{\partial r}\nabla_\eta r = \frac{\partial G}{\partial r}\frac{\mathbf{r}}{r} \tag{A.2}$$

and so we have

$$\frac{\partial G}{\partial n_\eta} = \nabla_\eta G(\boldsymbol{\eta}; \mathbf{y}) \cdot \hat{\mathbf{n}}_\eta \tag{A.3}$$

$$= \frac{\partial G}{\partial r} \frac{(\mathbf{r} \cdot \hat{\mathbf{n}}_\eta)}{r} \tag{A.4}$$

for the singular integral kernel in the Helmholtz integral equation. Noting that taking derivative with respect to $\mathbf{y}$ can be related to taking derivatives with respect to $\boldsymbol{\eta}$ by changing a sign we also have that

$$\frac{\partial G}{\partial n_y} = -\nabla_\eta G(\boldsymbol{\eta}; \mathbf{y}) \cdot \hat{\mathbf{n}}_y \tag{A.5}$$

$$= -\frac{\partial G}{\partial r} \frac{(\mathbf{r} \cdot \hat{\mathbf{n}}_y)}{r} \tag{A.6}$$

for the normal derivative kernel in the hypersingular Helmholtz integral equation. Noting that the Hessian matrix of partial derivatives of G is given by

$$\frac{\partial^2 G}{\partial \eta_i \partial \eta_j} = \frac{\partial^2 G}{\partial r^2} \frac{\partial r}{\partial \eta_i} \frac{\partial r}{\partial \eta_j} + \frac{\partial G}{\partial r} \frac{\partial^2 r}{\partial \eta_i \partial \eta_j} \tag{A.7}$$

$$= \frac{\partial^2 G}{\partial r^2} \frac{1}{r^2} r_i r_j + \frac{\partial G}{\partial r} \left(\frac{1}{r} \delta_{ij} - \frac{1}{r^3} r_i r_j \right) \tag{A.8}$$

$$= \frac{1}{r} \frac{\partial G}{\partial r} \delta_{ij} + \frac{1}{r^2} \left(\frac{\partial^2 G}{\partial r^2} - \frac{1}{r} \frac{\partial G}{\partial r} \right) r_i r_j \tag{A.9}$$

where δ_{ij} is the Kronecker delta, the hypersingular integral kernel may be expressed as

$$\frac{\partial^2 G}{\partial n_y \partial n_\eta} = -\frac{1}{r} \frac{\partial G}{\partial r} (\hat{\mathbf{n}}_\eta \cdot \hat{\mathbf{n}}_y) - \left(\frac{\partial^2 G}{\partial r^2} - \frac{1}{r} \frac{\partial G}{\partial r} \right) \frac{(\mathbf{r} \cdot \hat{\mathbf{n}}_\eta)(\mathbf{r} \cdot \hat{\mathbf{n}}_y)}{r^2} \tag{A.10}$$

Finally noting that the radial derivatives of G are

$$\frac{\partial G}{\partial r} = -\left(jk + \frac{1}{r} \right) G \tag{A.11}$$

$$\frac{\partial^2 G}{\partial r^2} = \left(-k^2 + \frac{2jk}{r} + \frac{2}{r^2} \right) G \tag{A.12}$$

the various Helmholtz integral kernels can be written as

$$G(\boldsymbol{\eta};\mathbf{y}) = \frac{e^{-jkr}}{4\pi r} \tag{A.13}$$

$$\frac{\partial G}{\partial n_\eta} = -\frac{e^{-jkr}}{4\pi r}\left(jk+\frac{1}{r}\right)\frac{(\mathbf{r}\cdot\hat{\mathbf{n}}_\eta)}{r} \tag{A.14}$$

$$\frac{\partial G}{\partial n_y} = \frac{e^{-jkr}}{4\pi r}\left(jk+\frac{1}{r}\right)\frac{(\mathbf{r}\cdot\hat{\mathbf{n}}_y)}{r} \tag{A.15}$$

$$\frac{\partial^2 G}{\partial n_y \partial n_\eta} = \frac{e^{-jkr}}{4\pi r}\left[\left(\frac{jk}{r}+\frac{1}{r^2}\right)(\hat{\mathbf{n}}_y\cdot\hat{\mathbf{n}}_\eta)+\left(k^2-\frac{3jk}{r}-\frac{3}{r^2}\right)\frac{(\mathbf{r}\cdot\hat{\mathbf{n}}_y)(\mathbf{r}\cdot\hat{\mathbf{n}}_\eta)}{r^2}\right] \tag{A.16}$$

A.2 Extraction of Free Terms

The free terms in the BEM formulation described in Section. 3.4 may be evaluated explicitly at a point on a smooth surface with a smooth surface potential distribution. On the planar element S, the surface normal is constant so that

$$\hat{\mathbf{n}}_y = \hat{\mathbf{n}} \tag{A.17}$$

at the loading point $\mathbf{y}$ (see Fig. A.1). Following the procedure outlined in Section. 3.4 , a half ball region centered on $\mathbf{y}$ is excluded from the BEM domain on the upper and lower surfaces. On the upper surface half ball $\sigma^+(\epsilon)$, the inward pointing surface normal is given by

$$\hat{\mathbf{n}}_\eta^+ = -\cos(\vartheta) \tag{A.18}$$

so that

$$\hat{\mathbf{n}}_\eta^+\cdot\hat{\mathbf{n}}_y = -\cos(\vartheta) \tag{A.19}$$

$$r = \epsilon \tag{A.20}$$

$$\mathbf{r}\cdot\hat{\mathbf{n}}_\eta^+ = -\epsilon \tag{A.21}$$

$$\mathbf{r}\cdot\hat{\mathbf{n}}_y = \epsilon\,\cos(\vartheta) \tag{A.22}$$

Hence on $\sigma^+(\epsilon)$,

$$\frac{\partial^2 G}{\partial n_y \partial n_\eta^+} = G(\epsilon)\left(\frac{2}{\epsilon^2}+\frac{2jk}{\epsilon}-k^2\right)\cos(\vartheta) \tag{A.23}$$

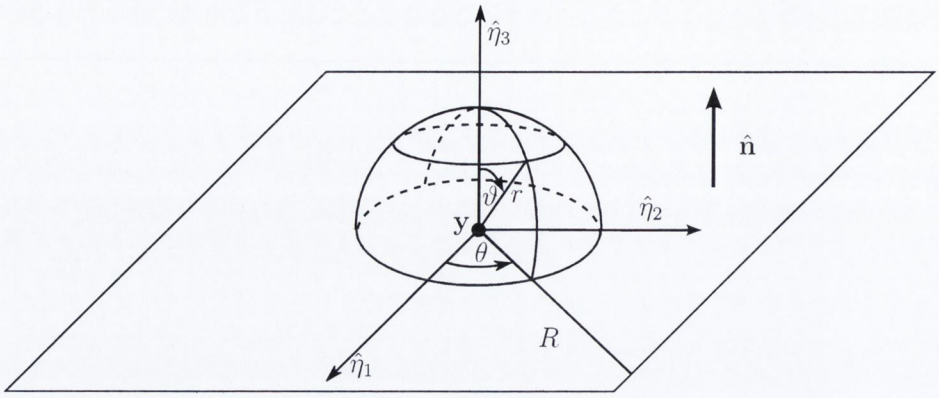


Figure A.1: Coordinates on the boundary element S and on the half-ball σ_ϵ^+, excluded from the BEM domain

so that the integral of the hypersingular kernel over the half ball can be written as

$$\int_{\sigma_\epsilon^+} \frac{\partial^2 G(\boldsymbol{\eta};\mathbf{y})}{\partial n_y \partial n_\eta^+} \varphi^+(\boldsymbol{\eta}) \mathrm{d}S^+ = G(\epsilon) \left(\frac{2}{\epsilon^2} + \frac{2jk}{\epsilon} - k^2 \right) \int_{\sigma_\epsilon^+} \cos(\vartheta) \varphi^+(\boldsymbol{\eta}) \mathrm{d}S^+ \tag{A.24}$$

$$= G(\epsilon)(1 + jk\epsilon - \tfrac{1}{2}k^2\epsilon^2) \int_0^{2\pi} \int_0^{\frac{\pi}{2}} \varphi^+(\epsilon,\theta,\vartheta) \sin(2\vartheta) \mathrm{d}\vartheta \mathrm{d}\theta \tag{A.25}$$

Taylor expanding $\varphi^+(\epsilon,\theta,\vartheta)$ as a function of ϵ we get

$$\varphi(\epsilon,\theta,\vartheta) = \varphi^+(\mathbf{y}^+) - \epsilon \nabla \varphi^+(\mathbf{y}^+) \cdot \hat{\mathbf{n}}_\eta^+ + O(\epsilon^2). \tag{A.26}$$

Using

$$\int_0^{2\pi} \int_0^{\frac{\pi}{2}} \sin(2\vartheta) \, \mathrm{d}\vartheta \, \mathrm{d}\theta = 2\pi \tag{A.27}$$

$$\int_0^{2\pi} \int_0^{\frac{\pi}{2}} \hat{\mathbf{n}}_\eta^+ \sin(2\vartheta) \, \mathrm{d}\vartheta \, \mathrm{d}\theta = -\frac{4\pi}{3} \hat{\mathbf{n}}_y \tag{A.28}$$

we get

$$\int_0^{2\pi} \int_0^{\frac{\pi}{2}} \varphi^+(\epsilon,\theta,\vartheta) \sin(2\vartheta) \, \mathrm{d}\vartheta \, \mathrm{d}\theta = 2\pi \varphi^+(\mathbf{y}^+) + \epsilon \, \frac{4\pi}{3} \frac{\partial \varphi^+}{\partial n_y}(\mathbf{y}^+) + O(\epsilon^2) \tag{A.29}$$

and hence

$$\int_{\sigma_\epsilon^+} \frac{\partial^2 G(\boldsymbol{\eta};\mathbf{y})}{\partial n_y \partial n_\eta^+} \varphi^+(\boldsymbol{\eta})\, \mathrm{d}S^+(\boldsymbol{\eta}) = \frac{1}{2\epsilon}\varphi^+(\mathbf{y}^+) + \frac{1}{3}\frac{\partial \varphi^+}{\partial n_y}(\mathbf{y}^+) + O(\epsilon) \tag{A.30}$$

Now for the second integral on σ_ϵ^+ we have

$$\frac{\partial G}{\partial n_y} = G(\epsilon)\left(jk + \frac{1}{\epsilon}\right)\cos(\vartheta) \tag{A.31}$$

and

$$\frac{\partial \varphi^+}{\partial n_\eta^+}(\epsilon,\theta,\vartheta) = \nabla\varphi^+(\mathbf{y}^+)\cdot\hat{\mathbf{n}}_\eta^+ + O(\epsilon) \tag{A.32}$$

and again using Eq. A.28 we get

$$\int_{\sigma_\epsilon^+} \frac{\partial G(\boldsymbol{\eta};\mathbf{y})}{\partial n_y}\frac{\partial \varphi^+(\boldsymbol{\eta})}{\partial n_\eta^+}\, \mathrm{d}S^+(\boldsymbol{\eta}) = \frac{1}{8\pi}\nabla\varphi^+(\mathbf{y}^+)\cdot\int_0^{2\pi}\int_0^{\frac{\pi}{2}} \hat{\mathbf{n}}_\eta^+ \sin 2\vartheta\, \mathrm{d}\vartheta\, \mathrm{d}\theta + O(\epsilon) \tag{A.33}$$

$$= -\frac{1}{6}\frac{\partial \varphi^+}{\partial n_y}(\mathbf{y}^+) + O(\epsilon) \tag{A.34}$$

and so we have

$$\int_{\sigma_\epsilon^+}\left(\frac{\partial^2 G(\boldsymbol{\eta};\mathbf{y})}{\partial n_y \partial n_\eta^+}\varphi^+(\boldsymbol{\eta}) - \frac{\partial G(\boldsymbol{\eta};\mathbf{y})}{\partial n_y}\frac{\partial \varphi^+(\boldsymbol{\eta})}{\partial n_\eta^+}\right)\mathrm{d}S^+(\boldsymbol{\eta}) = \frac{1}{2\epsilon}\varphi^+(\mathbf{y}^+) + \frac{1}{2}\frac{\partial \varphi^+}{\partial n_y}(\mathbf{y}^+) + O(\epsilon) \tag{A.35}$$

Similarly it can be shown that

$$\int_{\sigma_\epsilon^-}\left(\frac{\partial^2 G(\boldsymbol{\eta};\mathbf{y})}{\partial n_y \partial n_\eta^-}\varphi^-(\boldsymbol{\eta}) - \frac{\partial G(\boldsymbol{\eta};\mathbf{y})}{\partial n_y}\frac{\partial \varphi^-(\boldsymbol{\eta})}{\partial n_\eta^-}\right)\mathrm{d}S^-(\boldsymbol{\eta}) = -\frac{1}{2\epsilon}\varphi^-(\mathbf{y}^-) + \frac{1}{2}\frac{\partial \varphi^-}{\partial n_y}(\mathbf{y}^-) + O(\epsilon) \tag{A.36}$$

Formally, the limit of the half-ball integrals as $\epsilon \to 0$ do not exist because of the diverging $O(\epsilon^{-1})$ terms on the right hand side of the expansions Eqs.(A.35,A.36). However, when these integrals are considered together with the contribution from the surface $S - S_\epsilon$ it is found that the diverging components cancel between the two integrals and the remaining terms are finite.

A.3 Hypersingular Integration for Constant Elements

Consider the evaluation of the hypersingular integral over a planar rectangular element with upper and lower half ball exclusions around the singularity as shown in Fig. A.1. For a smooth surface, the finite free terms from the half ball integration may be extracted and treated separately. The remaining terms in the integral must be kept inside the ϵ limit. For a planar surface scattering problem with an unknown surface potential, the following integral must be evaluated numerically in the BEM

$$H = \lim_{\epsilon \to 0} \left(-\frac{\delta\varphi(\mathbf{y})}{2\epsilon} + \int_{S-S_\epsilon} \frac{\partial^2 G(\boldsymbol{\eta}; \mathbf{y})}{\partial n^2} \delta\varphi(\boldsymbol{\eta}) \, \mathrm{d}S \right) \tag{A.37}$$

Since

$$\mathbf{r} \cdot \hat{\mathbf{n}} = 0 \tag{A.38}$$

$$\hat{\mathbf{n}} \cdot \hat{\mathbf{n}} = 1 \tag{A.39}$$

the hypersingular kernel simplifies to

$$\frac{\partial^2 G}{\partial n^2} = \frac{e^{-jkr}}{4\pi r^3} (1 + jkr) \tag{A.40}$$

over the integration region $S - S_\epsilon$ that excludes the singularity. Setting the potential to a constant value,

$$\delta\varphi(\boldsymbol{\eta}) = \delta\varphi(\mathbf{y}) \tag{A.41}$$

over an element, allows the integral to be evaluated as follows. Taking the constant factors outside the integral and changing to polar coordinates gives

$$H = \delta\varphi(\mathbf{y}) \lim_{\epsilon \to 0} \left(-\frac{1}{2\epsilon} + \int_0^{2\pi} \int_\epsilon^{R(\theta)} \frac{e^{-jkr}}{4\pi r^3} (1 + jkr) r \, \mathrm{d}r \, \mathrm{d}\theta \right) \tag{A.42}$$

The radial integral may be carried out analytically giving

$$H = \delta\varphi(\mathbf{y}) \lim_{\epsilon \to 0} \left(-\frac{1}{2\epsilon} + \int_0^{2\pi} - \left[\frac{e^{-jkr}}{4\pi r} \right]_\epsilon^{R(\theta)} \, \mathrm{d}\theta \right) \tag{A.43}$$

$$= \delta\varphi(\mathbf{y}) \lim_{\epsilon \to 0} \left(-\frac{1}{2\epsilon} + \frac{e^{-jk\epsilon}}{2\epsilon} - \frac{1}{4\pi} \int_0^{2\pi} \frac{e^{-jkR(\theta)}}{R(\theta)} \, \mathrm{d}\theta \right) \tag{A.44}$$

$$= \delta\varphi(\mathbf{y}) \left(-\frac{jk}{2} - \frac{1}{4\pi} \int_0^{2\pi} \frac{e^{-jkR(\theta)}}{R(\theta)} \, \mathrm{d}\theta \right) \tag{A.45}$$

Provided the singular point is not on the element boundary, the remaining angular integral is finite and can be efficiently evaluated with standard gaussian quadrature rules. By the same procedure, the integral of $G(\boldsymbol{\eta}; \mathbf{y})$ over the element S may be evaluated as

$$\begin{aligned} \int_S \frac{e^{-jkr}}{4\pi r} \, \mathrm{d}S &= \frac{1}{4\pi} \int_0^{2\pi} \int_0^{R(\theta)} \frac{e^{-jkr}}{r} r \, \mathrm{d}r \, \mathrm{d}\theta \\ &= \frac{1}{4\pi jk} \left(2\pi - \int_0^{2\pi} e^{-jkR(\theta)} \, \mathrm{d}\theta \right) \end{aligned} \tag{A.46}$$

A.4 Hypersingular Integration for Plane Wave Elements

The computation of the hypersingular integral over a plane wave distribution of potential may also be reduced to a sequence of one dimensional integrals around the boundary contour of the element. Given a surface distribution

$$\delta\varphi(\boldsymbol{\eta}) = \delta\varphi(\mathbf{y}) \, e^{-jk_v r \cos\theta} \tag{A.47}$$

the hypersingular integral over the element S may be reduced to

$$\tilde{H} = \lim_{\epsilon \to 0} \left(-\frac{\delta\varphi(\mathbf{y})}{2\epsilon} + \int_{S - S_\epsilon} \frac{\partial^2 G(\boldsymbol{\eta}; \mathbf{y})}{\partial n^2} \delta\varphi(\mathbf{y}) \, e^{-jk_v r \cos\theta} \, \mathrm{d}S \right) \tag{A.48}$$

$$= \delta\varphi(\mathbf{y}) \lim_{\epsilon \to 0} \left(-\frac{1}{2\epsilon} + \frac{1}{4\pi} \int_0^{2\pi} \int_\epsilon^{R(\theta)} \frac{e^{-j(k_v \cos\theta + k) \, r}}{r^3} (1 + jkr) r \, \mathrm{d}r \, \mathrm{d}\theta \right) \tag{A.49}$$

For real k and k_v, the above integral can be split easily into real and imaginary parts and evaluated separately as

$$\tilde{H} = \delta\varphi(\mathbf{y}) \lim_{\epsilon \to 0} \left[-\frac{1}{2\epsilon} + \frac{1}{4\pi} \int_0^{2\pi} \int_\epsilon^{R(\theta)} \left(\frac{\cos(ar)}{r^2} + \frac{k \sin(ar)}{r} \right) \mathrm{d}r \, \mathrm{d}\theta \right.$$
$$\left. + \frac{j}{4\pi} \int_0^{2\pi} \int_\epsilon^{R(\theta)} \left(-\frac{\sin(ar)}{r^2} + \frac{k \cos(ar)}{r} \right) \mathrm{d}r \, \mathrm{d}\theta \right] \tag{A.50}$$

where $a = k + k_v \cos\theta$. Defining the sine and cosine integrals

$$\mathrm{Si}(x) = \int_0^x \frac{\sin x'}{x'} \, \mathrm{d}x' \tag{A.51}$$

$$\mathrm{Ci}(x) = \gamma + \log x + \int_0^x \frac{\cos x' - 1}{x'} \, \mathrm{d}x' \tag{A.52}$$

where γ is Euler's constant, and noting that

$$\frac{\mathrm{dCi}(x)}{\mathrm{d}x} = \frac{\cos x}{x} \tag{A.53}$$
$$\frac{\mathrm{dSi}(x)}{\mathrm{d}x} = \frac{\sin x}{x} \tag{A.54}$$
$$\frac{\mathrm{d}^2\mathrm{Ci}(x)}{\mathrm{d}x^2} = -\frac{\cos x}{x^2} - \frac{\sin x}{x} \tag{A.55}$$
$$\frac{\mathrm{d}^2\mathrm{Si}(x)}{\mathrm{d}x^2} = -\frac{\sin x}{x^2} + \frac{\cos x}{x} \tag{A.56}$$
$$\tag{A.57}$$

the radial integral in Eq. A.48 may be evaluated in terms of the sine and cosine integral so that

$$\tilde{H} = \delta\varphi(\mathbf{y}) \lim_{\epsilon \to 0} \left(-\frac{1}{2\epsilon} + \frac{1}{4\pi} \int_0^{2\pi} \left[(k-a)\,\mathrm{Si}(ar) - \frac{\cos(ar)}{r} \right]_\epsilon^{R(\theta)} \mathrm{d}\theta \right.$$
$$\left. + \frac{j}{4\pi} \int_0^{2\pi} \left[(k-a)\,\mathrm{Ci}(ar) + \frac{\sin(ar)}{r} \right]_\epsilon^{R(\theta)} \mathrm{d}\theta \right) \tag{A.58}$$

For small arguments, Ci and Si may be expanded as

$$\mathrm{Ci}(x) = \gamma + \log(x) + O(x^2) \tag{A.59}$$

$$\mathrm{Si}(x) = O(x) \tag{A.60}$$

so that the $r = \epsilon$ contribution in Eq. A.58 may be replaced by

$$\begin{aligned} &\frac{1}{4\pi}\int_0^{2\pi}\left[(k-a)[\mathrm{Si}(a\epsilon) + j\mathrm{Ci}(a\epsilon)] - \frac{e^{-ja\epsilon}}{\epsilon}\right]\,\mathrm{d}\theta \\ &= \frac{1}{2\epsilon} - \frac{jk}{2} + \frac{jk_v}{4\pi}\int_0^{2\pi}\log(k + k_v\cos\theta)\,\cos\theta\,\mathrm{d}\theta \qquad +O(\epsilon) \end{aligned} \tag{A.61}$$

Substituting this result back into Eq. A.58 and taking the limit as $\epsilon \to 0$ then gives the final form of the reduced surface integral as

$$\begin{aligned} \tilde{H} = \delta\varphi(\mathbf{y})\Bigg\{ &-\frac{jk}{2} - \frac{1}{4\pi}\int_0^{2\pi}\Bigg(\frac{e^{-j\{k+k_v\cos\theta\}R(\theta)}}{R(\theta)} \\ &+ k_v\cos\theta\Big[\mathrm{Si}(\{k + k_v\cos\theta\}R(\theta)) \\ &+ j\mathrm{Ci}(\{k + k_v\cos\theta\}R(\theta)) - j\log(k + k_v\cos\theta)\Big]\,\mathrm{d}\theta\Bigg)\Bigg\} \end{aligned} \tag{A.62}$$

Since the singular behavior of the $\mathrm{Ci}(x)$ function at $x = 0$ is removed by subtraction of the log term, the integrand is a regular smooth function when the integral is expressed in this form. Standard gaussian quadrature rules may therefore be used to evaluate the remaining angular integral.